HIGH VOLTAGE PARTIAL DISCHARGE MEASUREMENTS - IMPROVING THEIR SIGNIFICANCE

A THESIS SUBMITTED

TO

THE VICTORIA UNIVERSITY OF MANCHESTER

FOR

THE DEGREE OF DOCTOR OF PHILOSOPHY

IN

THE FACULTY OF TECHNOLOGY

BY

JOHN HOWARD REEVES, B.Sc.(Lond.), M.Sc.(Man.)

OF

THE DEPARTMENT OF ELECTRICAL ENGINEERING AND ELECTRONICS

MAY 1979

ProQuest LLC.
789 East Eisenhower Parkway
P.O. Box 1346
Ann Arbor, MI 48106 – 1346

To my wife, Lizanne

ACKNOWLEDGEMENTS

The author wishes to thank Professor L.M. Wedepohl and Professor H.C.A. Hankins of the Department of Electrical Engineering and Electronics for providing facilities in the Radio Techniques Laboratory and the Electricity Council for the award of a scholarship.

The author is most grateful to his supervisor, Dr. A.G. Heaton, for his guidance and encouragement and his section leader, Mr. W.P. Baker, for introducing him to the field of high voltage engineering and supporting this study.

The author is indebted to Professor A. Wexler of the Electrical Engineering Department, University of Manitoba, Winnipeg, Canada for allowing him free use of the finite element program MANFEP and its associated documentation. The latter was referred to frequently when modifying the program and during the writing of section 2.3 . The author is also indebted to Dr. R.C. Gibson of E.C.R.C. for his Gaussian Elimination scheme.

The author wishes to thank Dr. D.K. Paul of U.M.I.S.T. and Mr. S.J. Kearley and Dr. R. MacKinlay of E.C.R.C. for their invaluable help on many occasions, Mr. A.T. Sandiford for the detailed design and the construction of the artificial discharge source and Mr. C.P. Hopley for the construction of the discharge measurement and location instrument. Finally the author wishes to record his thanks to all his colleagues at U.M.I.S.T. and E.C.R.C. and within the Electricity Supply Industry who have helped in so many different ways.

CONTENTS

ABSTRACT

The potential / stress distributions in and around 'pill box', spheroidal and 'wedge' shaped voids contained within dielectric regions between plane, parallel electrodes are given. The results were predominantly obtained by a finite element method which uses higher order interpolatory polynomials to considerably reduce the time and effort required to define the field regions. In those cases where the field distribution was found to be non-polynomic, a finite difference method with linear interpolation was utilized. The sets of simultaneous equations so generated were solved by a Gaussian elimination scheme that takes full advantage of the banded nature of the coefficient matrices. The methods are used to solve both two and three dimensional axi-symmetric problems and can accommodate both inhomogeneous and anisotropic dielectrics. In complex form, they are used to determine the electro-static effects of dielectric loss and finite resistivity of the void surfaces. The effects of voids on the capacitance and loss tangent of a test specimen are also given. The analysis is extended to include the electro-static effects of a partial discharge on the potential and charge distributions in and around a void and this is used to establish the apparent / real charge transfer ratio for a wide range of void shapes and sizes and for differing degrees of discharge.

Measurements of the microwave noise emitted from spark discharges made using both a simple crystal detector and a sensitive radiometer are reported. It is shown that these could be used to accurately locate spark discharges but the technique is insensitive to partial discharges.

A versatile travelling wave method is described that has been used to accurately locate partial discharge sources in metal-clad switchgear and short cables. Details of an instrument, that can both locate and measure the magnitude of a discharge source from a single event, are then given. An artificial discharge source suitable for calibrating both the location and the magnitude measurements is also described.

Keywords: partial discharges, discharge detection, discharge calibrator, insulation measurements, fault location, cable insulation, switchgear insulation, travelling waves, high voltage engineering, voids, sparks, dielectrics, dielectric loss, conducting films, charge transfer, capacitance, inhomogeneous and anisotropic dielectrics, solution of fields, finite difference method, finite element method, higher order interpolatory polynomials, banded matrices, microwave noise measurements, radiometer.

Declaration

With the exception of the introductory part of chapter 5, no portion of the work referred to in this thesis has been submitted in support of an application for another degree or qualification of this or any other university or other institution of learning. The extent of the previously reported work is clearly indicated.

Curriculum Vitae

Since obtaining an honours degree in physics at University College London in 1967, the author has been employed as a Research Officer at the Electricity Council Research Centre, Capenhurst, Chester in their Distribution Research section. He obtained his Master's degree at U.M.I.S.T. in 1972 following the submission of a thesis entitled 'The location of partial discharges in metal-clad switchgear'. The author was awarded an Electricity Supply Industry Scholarship to undertake this work.

The author is married with one small son!

CHAPTER 1

Introduction

The rising cost of capital equipment has forced the electricity supply industry to reduce its reserve plant capacity to a minimum. Additional demand must now be met, where possible, by increasing the loading of existing equipment and delaying the replacement of obsolete equipment. As a consequence, the detection of incipient faults is of paramount importance, especially in high voltage equipment where the cost penalties of a breakdown are high.

A significant proportion of the faults occurring in high voltage equipment due to ageing are attributable to insulation failures, and so considerable effort has been directed to obtaining methods for assessing the soundness of insulation. The choice of methods currently available is sufficient to enable inherent insulation weakness to be detected in most cases. This is not adequate however as most insulating structures leave something to be desired and a more accurate assessment is required before decisions regarding replacement or reconditioning can be made. These are major decisions as failure to act when necessary can have serious consequences whilst replacement or reconditioning will incur heavy expenditure which may not be necessary. To resolve the problem detailed information on the nature, extent and location of the defects is required. In the light of such information it may then be possible to defer work on the equipment or recondition only part of it in lieu of total replacement. Accurate diagnoses are particularly required when reconditioning as labour costs are high and disturbance of equipment must be kept to a minimum to avoid precipitating further failures. This is especially important when older gear is involved.

This thesis describes methods of incipient fault detection that

enable more accurate assessment to be made of the soundness of insulating structures. The thesis can be divided into three parts. The first part concerns the effect of voids within insulation and the interpretation of the consequent electrical phenomena observable at the test terminals of the equipment. The second part describes the extension of radio interference measurements upto microwave frequencies where highly directional aerials with large gains yet moderate dimensions are available and the third part describes a method of accurately locating discharges by a time of travel measurement. The technique is particularly useful for the location of discharges in metal-clad switchgear and short cables and an insturment capable of locating and measuring the magnitude of discharges from a single-shot event is described. Firstly though a brief resumé of the causes of solid insulation failure is given followed by a review of the methods employed when testing equipment for incipient insulation faults.

1.1 Causes of solid electrical insulation failure

Electrical

Insulation is required to withstand the working electric stress for many years. In addition it is required to withstand stresses considerably in excess of this for brief periods during surges. These surges can result from switching operations and lightning during service and proof-testing during testing. As these requirements differ widely it is not surprising that electrical failure can occur in a variety of ways.

Failure would inevitably occur if the intrinsic breakdown strength of the insulation were to be exceeded. In the case of solid insulation this condition is reached when the conduction electrons gain more energy from the electric field than they can dissipate to the lattice structure. However this type of breakdown does not arise in practice as the other breakdown mechanisms occur at lower electrical stresses. A more likely cause of failure is breakdown of the ambient medium. This can manifest

itself in a variety of ways. Firstly an arc may form directly between the high voltage and earth electrodes resulting in total breakdown. Secondly, if the direct paths between the electrodes are either long or absent altogether, breakdown of the ambient medium can produce discharge channels between the electrodes and the surface of the insulation. These channels create intense localized electric fields at the point of impingement and can cause erosion or puncture of the insulation. Thirdly, if the surrounding medium is subject to highly non-uniform fields corona will occur. This constitutes a loss of energy and a source of radio interference and is therefore most undesirable but it plays only a minor role in insulation deterioration.

A further cause of insulation failure is surface contamination by industrial polution, salt etc.[1] When moistened by atmospheric precipitation etc. this can produce leakage paths over the surface of the insulation. Stress concentrations may result causing surface discharges with subsequent erosion and tracking leading to failure.[2,3] Solar radiation and atmospheric oxidation and erosion can further aggravate the situation. Defective subsidiary insulation (such as a shroud) can also cause failure by creating excessive surface stress concentrations.

Insulation can fail internally due to the presence of voids and other inclusions. Voids can be responsible for insulation failure since, having a permittivity less than that of the surrounding dielectric, they are subjected to stresses in excess of those experienced by the bulk of the dielectric under a.c. conditions. As their breakdown strength is less than that of the surrounding dielectric anyway, internal discharges occur within them at stresses well below the breakdown strength of the overall insulation and often below the working stress. Under d.c. conditions similar stress enhancement occurs if the conductivity of the void is less than that of the surrounding dielectric. However, as displacement currents are no longer available to sustain the discharges, repetition rates are

much lower.

The insulation surfaces provide the instantaneous cathode and anode for the discharges which will include electrons with energies upto the first ionization potentials of the included gases. Cobine[4] lists these potentials for some of the common inorganic gases. They range from 9.5 e.v. for nitric oxide to 15.57 e.v. for nitrogen. As Baker[5] points out many of the electrons arriving at the anode will have more than sufficient energy to rupture chemical bonds in the surface of the insulation. The C - H bond found in many insulants is particularly vulnerable. As a result erosion of the insulation can take place enlarging the void and further weakening the insulation. Bombardment of the cathode by positive ions aggravates the situation by raising the surface temperature. In fact Mayoux[6] considers positive ion bombardment (especially by the O^+ ion) to be primarily responsible for the erosion damage caused by partial discharges. He came to this conclusion after examining the surface damage caused to polyethylene following bombardment by electronic, ultra-violet and ionic beams. He observed that only the ionic beams produced erosion of the kind produced by discharges and considers that the mass of the ions plays a significant part in the erosion process.

During studies on the long term breakdown of polyethylene containing voids, Mason[7] observed the formation of pits with microscopic conducting channels extending from them into the insulation. These channels propagated as a consequence of the intense local stress concentrations at their ends and led finally to failure of the insulation. He also observed chemical and mechanical degradation of the void surface due to cumulative heating by the discharges and chemical attack. The latter probably resulted from the formation of gases such as ozone and the oxides of nitrogen within the voids. Such degradation rendered the surfaces partially conducting causing tracking. In some cases the conductivity was sufficient to effect-

ively short circuit the void preventing further discharges. This conduction must always be born in mind when discharge testing as it can lead to false confidence in the soundness of insulation.

Voids can be formed either during manufacture or subsequently. In the latter case this can be the result of localized breakdown of the insulation in the vicinity of included stress sharing foils and foreign particles. Voids also arise around imperfectly fitting electrodes and at interfaces within the insulation. The degree of stress enhancement occurring within a void depends on various parameters but is especially pronounced in dielectrics of high permittivity. It is also greater in voids with small dimensions parallel to the electric field and large dimensions normal to it. A detailed study of the stress distributions in and around voids is given in chapter 3.

Thermal

Heat is generated in high voltage equipment due to resistive losses in the conductors and dielectric loss in the insulation. In the medium term this can cause failure of the insulation due to 'thermal runaway'.[8] This will occur if the heat generated in part of the insulation exceeds the rate at which it can be dissipated. The consequent increase in temperature results in breakdown by causing the insulation to melt, decompose or suffer loss of mechanical strength. Alternatively the intrinsic electric strength of the insulation at elevated temperature may be insufficient to withstand the working stress. Thermal instability is effectively restricted to lossy dielectrics.[9,10] It may be precipitated by externally applied heat including that from solar radiation. This failure mechanism must be guarded against when conducting accelerated life tests on equipment using higher frequency excitation and/or increased electric stress levels.

Long term failure can occur due to ageing. As Dakin[11] demonstrates this can be treated as a chemical process where the time to failure (t_f)

is given by

$$\ln(t_f) = C + B/T \qquad (1.1\text{-}1)$$

This equation shows the temperature dependence of the ageing processes. It is derived from Guldberg and Waage's law of mass action (or the theory of rate processes)

$$\frac{d}{dt}(n_o - n) = kn \qquad (1.1\text{-}2)$$

where k is given by the Arrhenius equation

$$k = A \exp(-E/RT) \qquad (1.1\text{-}3)$$

E is the activation energy for the particular reaction and R is the gas constant. From equation (1.1-1) if $\ln(t_f)$ is plotted against $1/T$ a straight line should be obtained which can be used to predict the life expectancy at different temperatures. Use of the equation, including ageing at varying temperatures, is described by Allen and Tustin.[12]

Ageing results in deterioration of the physical properties of the insulation[13,14] and is commonly associated with chemical changes[15] such as the depolymerization and carbonization of cellulose and synthetic resins.[16,17]

Mechanical

Vibration due to electro-mechanical and magnetostrictive forces, wind, motor vehicles, trains, machinery etc. can cause insulation failures. Transformer insulation can fail due to the large electro-mechanical forces applied whilst supplying system fault current. However the greatest incidence of mechanical failures occurs in cables through third party and subsidence damage.

Chemical, electro-chemical and other causes

External chemical degradation due to oxidation can result in surface discharging and erosion. Similarly degradation can occur in voids due to chemical attack by ozone and the oxides of nitrogen formed by dis-

charges. Water is also produced when hydrogen, liberated from the insulation surface, combines with oxygen contained in the void and this water, plus any already present within the insulation, can combine with the oxides of nitrogen to form nitrous and nitric acids. This mechanism is considered responsible for the pin holing sometimes found in the paper insulation of cables especially in vertical runs adjacent to either heat shrinkable terminations or conventional end boxes.[18] Aside from the chemical effects, the presence of water will reduce the electrical performance of the insulation whether it remains predominantly in the void or whether it disperses into the surrounding insulation. Preventing the ingress of external moisture into insulation has always been a requirement of insulation engineering. Traditionally hydrostatic pressure, capillary action and diffusion were considered the causes of ingress but more recently water treeing[19] has been observed in polyethylene. Warm damp conditions can cause polyethylene terephthalate, cellulose esters and other polyesters to hydrolyse with rapid loss of strength and similar conditions can leach sodium to the surface of high sodium content glass fibres considerably reducing their mechanical strength.

Electrochemical degradation arises due to the presence of ions within the insulation. Under the influence of the applied electric field, these migrate creating an ionic conduction current. On arrival at the electrodes the ions produce reactions with by-products that are harmful to both the insulation and electrodes. The effect is more pronounced under d.c. conditions than a.c.

Other causes of insulation failure include fungal growths, attack by insects and rodents and bridging by birds. Insulation systems commonly employ liquid and gaseous dielectrics and vacua. These possess additional failure mechanisms which will not be discussed in this thesis.

1.2 Methods of testing equipment for incipient insulation faults

.2.1 D.C. resistance measurements

Though d.c. resistance measurements are traditionally used to test insulation, great care must be exercised when using them to test high voltage equipment as the measurements become critically dependent on the elimination of stray leakage paths. Surface leakage in particular must be guarded against when making measurements in a damp atmosphere.

Measurements may be made directly or using a Wheatstone bridge with unequal arms. As both methods require a stabilized high voltage supply, however, the latter can be reduced to a potential divider circuit. An attractive form of this is the virtual earth circuit shown in figure 1.2.1-1 .

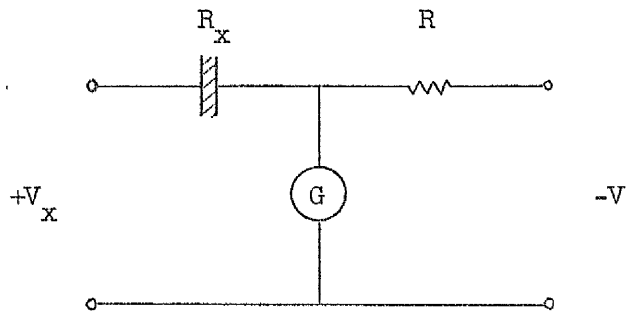

Figure 1.2.1-1 Virtual earth circuit for the measurement of resistivity

In use R and V (both of relatively low impedance) are adjusted to obtain a null on the galvanometer giving $R_x = R\ (V_x/V)$. The circuit has the advantage that, at balance, the voltage across the galvanometer is negligible and any stray leakage paths associated with it are consequently immaterial. In all resistivity measurements a sensitive current/voltage detector is required. The limiting sensitivity achievable with a galvanometer is approximately 100 pA which enables 100,000 Mohms to be measured to an accuracy of one percent at 1 kV. Using an electrometer valve, the sensitivity can be increased by three orders of magnitude and, at least, a further order of magnitude can be realized by the use of a solid state varactor

diode amplifier.

Interpretation of the results is complicated by two factors. Firstly the conductivity of most insulating materials approximately doubles for each ten degrees Celcius rise in temperature and secondly the measured conductivity is found to decrease by three or four orders of magnitude with time of stressing. Baker[20] demonstrates that both these effects are manifestations of the theory of rate processes as applied to dielectric relaxation[21] and emphasizes that close control of the test temperature and stressing voltage is required if meaningful results are to be obtained. The method is of limited use on small, highly ordered insulation systems when, for example, a thin layer of air adjacent to one electrode would produce a high value of resistance and yield no indication of the soundness of the bulk of the insulation. Such orderliness is however unlikely to occur in a large item of equipment and so the method can often provide a fair assessment of the overall soundness of the insulation.

.2.2 Dielectric loss and permittivity measurements

As the loss tangent of insulation is a dimensionless quantity, measurement of the dielectric loss has obvious advantages especially for simple structures. For more complicated systems though the results may be misleading. To illustrate this consider the ingress of moisture into the surface of an insulating slab adjacent to an electrode. Representing the composite system by two capacitors in series, one a low-loss component corresponding to the sound fraction of the insulation and the other a lossy component corresponding to the damp insulation abutting the electrode. Baker[5] shows that the maximum loss tangent will be recorded when the moisture penetrates two thirds of the way through the slab. Any further penetration will not produce an increase in loss tangent. This surprising result would appear somewhat damming of loss measurements. However, had permittivity measurements been conducted at the same time, a steady increase

would have been observed exposing the real condition of the insulation. Despite such shortcomings, loss tangent measurements are of considerable value when testing high voltage structures. Permittivity measurements are dimensional and, as a consequence, are generally only of use for relative measurements.

An instrument designed by Douglas et al[22] for the testing of bushings and busbars uses a Wien series resistance bridge operating at 80 Hz. Though this imposes increased charging current demands on the battery powered instrument (approximately 550 volts are applied to the sample) this disadvantage is more than offset by the high degree of immunity to mains frequency interference. This is achieved by using a highly selective detector amplifier with a rejection ratio of 54dB at 50 Hz relative to 80 Hz. When balanced the capacitance and loss tangent of the sample can be read directly from the instrument.

As a consequence of dielectric relaxation phenomena, the loss tangent and permittivity are functions of both temperature and measurement frequency. If at all possible therefore measurements should be conducted under similar conditions to those occurring in service. If measurements are required at high frequency, allowance must be made for the inductance of the connecting leads.[23] Failure to make the necessary corrections would result in an apparent increase in capacitance with frequency thereby conflicting with the theory of dielectric relaxation.

The variation of permittivity and loss tangent with applied voltage is of considerable importance when testing insulation as the onset of partial discharges is marked by an increase in both apparent permittivity and loss tangent. Discharge measurements obtained in this way yield general information on the total discharge activity rather than specific information on individual discharges. They are particularly suitable for mica based insulation in which the damage caused by discharges is related to the total discharge activity rather than the magnitude of individual

discharges. This is a consequence of the compound nature of this insulation, with discharges occurring readily in the organic bonding but being effectively halted by the highly discharge resistant mica flakes.

Measurement of capacitance and loss tangent at high voltages can be made using the long established Schering bridge circuit shown in figure 1.2.2-1 . The combination of C_x and R_x represents the lossy test specimen and C_s is a high voltage, low-loss standard capacitor. Though C_3 is not normally included in the circuit, Baker points out that it will inevitably be present in any practical realization of the bridge. At balance

$$C_x = \frac{C_s R_4 (1 + \omega^2 C_3^2 R_3^2)}{R_3 (1 + \omega^2 C_3 R_3 C_4 R_4)} \qquad (1.2.2\text{-}1)$$

and

$$R_x = \frac{R_3 (C_4 R_4 - C_3 R_3)}{C_s R_4 (1 + \omega^2 C_3^2 R_3^2)} \qquad (1.2.2\text{-}2)$$

As $\tan\delta_x = \omega C_x R_x$ this gives

$$\tan\delta_x = \frac{(C_4 R_4 - C_3 R_3)\omega}{1 + \omega^2 C_3 R_3 C_4 R_4} \qquad (1.2.2\text{-}3)$$

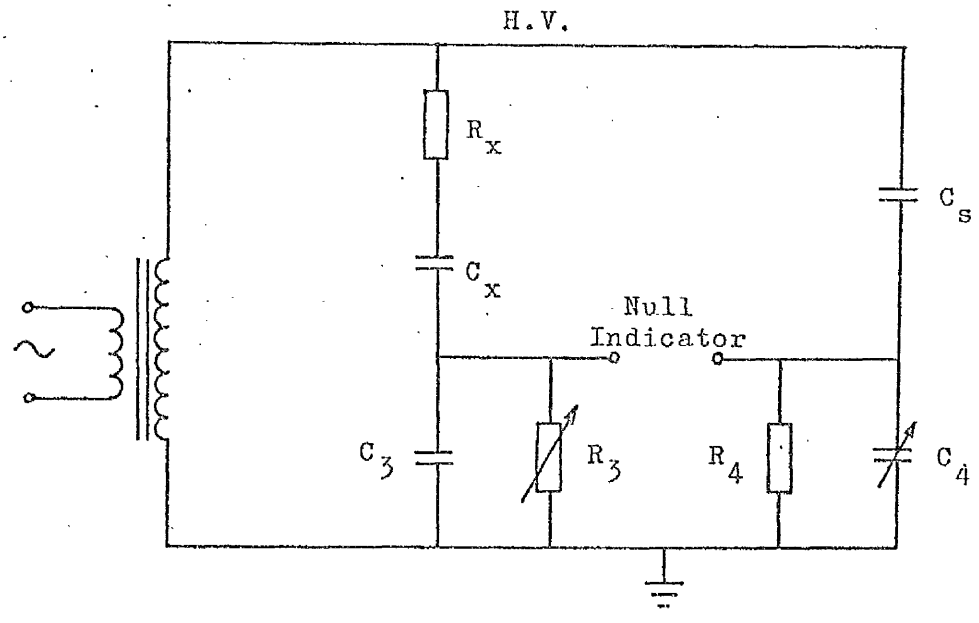

Figure 1.2.2-1 Practical Schering bridge circuit

A circuit capable of greater sensitivity is the transformer ratio arm bridge shown in figure 1.2.2-2. When balanced the ampere turns in the two opposing primary sections of the output transformer are equal resulting in zero overall magnetomotive force. In addition to producing a null in the detector output this results in there being no potential across the primary windings and therefore renders any stray capacitance associated with long leads connected to these points unimportant. At balance

$$C_x = C_s N_2 / N_1 \qquad (1.2.2\text{-}4)$$

$$R_x = \frac{N_1 R_1 (C_1 + C_s)}{N_2 C_s} \qquad (1.2.2\text{-}5)$$

and

$$\tan\delta_x = \omega R_1 (C_1 + C_s) \qquad (1.2.2\text{-}6)$$

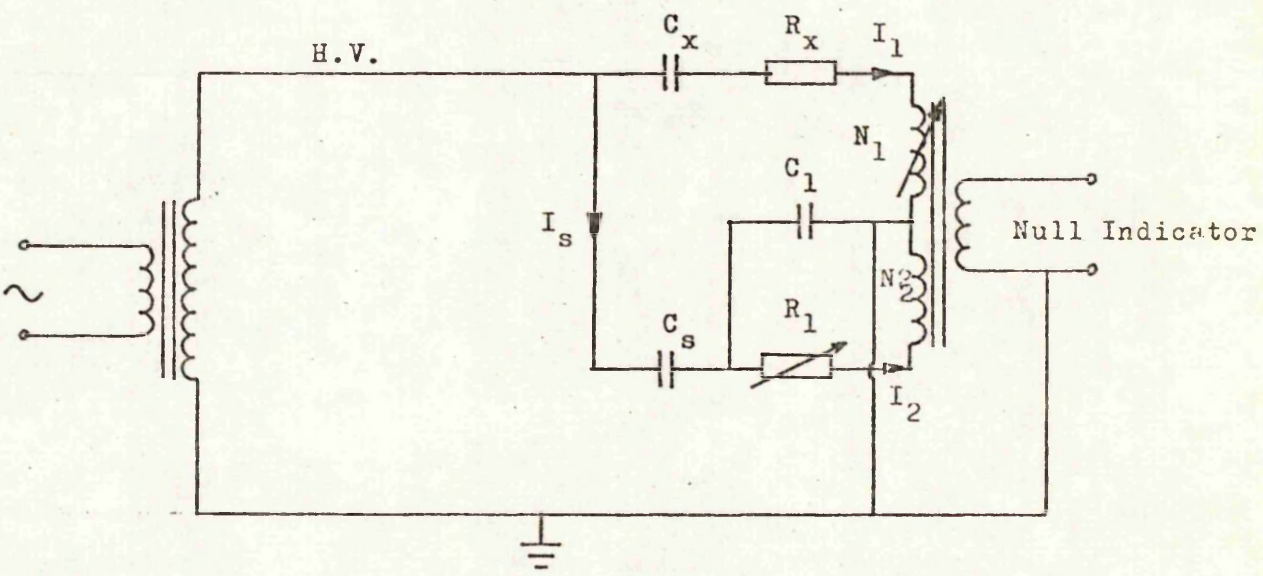

Figure 1.2.2-2 High voltage transformer ratio arm bridge

A further instrument in general use for dielectric loss is that due to Simons.[24] From the circuit given in figure 1.2.2-3 it is seen to be basically a capacitance bridge with adjustment for loss in the specimen.

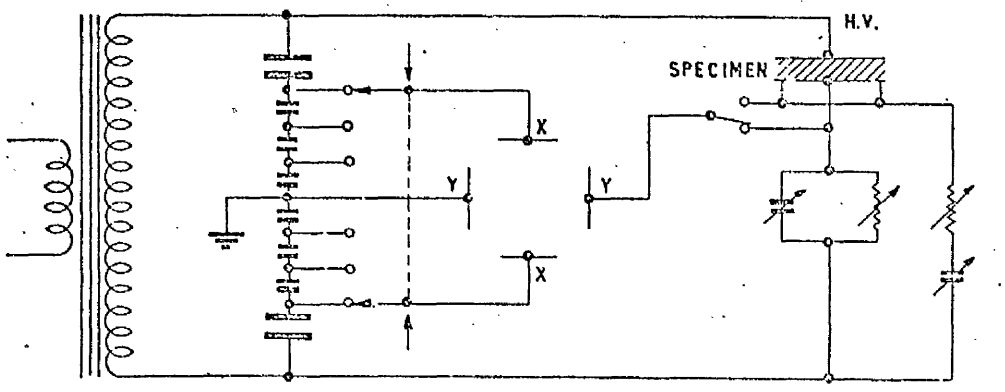

Figure 1.2.2-3 Dielectric loss analyser

The output is in the form of a loop display on a cathode ray oscilloscope and shows the instantaneous unbalance of the bridge as a function of the stressing voltage. Though less sensitive than the previous methods, it is ideal for routine testing because it yields four important parameters in a single measurement:- the low voltage capacitance and loss tangent from the initial balance conditions, the discharge inception voltage and the increase in loss tangent with voltage from the trace.

It has been pointed out that the measured value of the conductance of insulation decreases with time of stressing and that the permittivity falls with increasing frequency. Both these effects are the result of dispersion in the dielectric due to dielectric relaxation. Dispersion is defined as the fractional change in permittivity $(\epsilon_1 - \epsilon_2) / \epsilon_1$ where ϵ_1 and ϵ_2 are the values at two specified frequencies f_1 and f_2. As the the above observations suggest, it can be measured in the frequency or the time domain. The former involves measurement of the capacitance at the two specified frequencies whereas the latter involves the application of d.c. stresses for fixed times. The instrument described by Mole[25] is of this

latter type. The sample is stressed for a period τ and then short circuited for a period $\tau/100$. The maximum voltage attained on recovery when expressed as a percentage of the initial stressing voltage then yields the dispersion.

1.2.3 Partial discharge measurements

For the thirty years prior to the middle 1950's, discharge testing was limited to a stipulation that all synthetic resin bonded paper (s.r.b.p.) bushings were to be free from audible hiss upto $1\frac{1}{4}$ times working voltage. Under favourable conditions a skilled listener can detect discharges of as little as 40 pC in magnitude and the 'in service' record of bushings tested in this way proved excellent. With the advent of sensitive and non-subjective electrical methods, the hissing test was discontinued for batch testing and acoustic methods are now primarily used for the remote detection and location of discharges in installed equipment. Ultrasonic detectors are used to reduce the level of background interference and locations are obtained by scanning the defective equipment to find the position of maximum noise level. Wilson[26,27] gives plots of the frequency spectra typically obtained due to background noise and in the vicinity of a source of partial discharges and shows the power density of the latter to be appreciably greater than the former in the higher audible and ultrasonic regions. He concludes that detection within the frequency band 25 - 40 kHz provides the best signal to noise ratio. Sensitivity depends on whether air borne noise is being detected using a directional microphone with horn / reflector or a contact microphone is being used. The former can give a sensitivity as good as 50 - 100 pC when used to detect discharge sites in the end windings of an 11 kV motor or in a polymeric cable termination whereas the latter can achieve a sensitivity of 250 pC on the sheath of an installed 11 kV cable.

An alternative method adopted by Allan et al[28] for the location of discharges in transformers involves measuring the travel time delay of

the acoustic impulses. Either multiple microphones or combined electrical / acoustic detection is used and location is effected by triangulation. In addition to the detection and location of discharges, information regarding the nature of the discharge source could be possible following work by Harrold.[29] He observed that the spectral content of the acoustic impulses generated by oil immersed discharges bears a distinct relationship to the discharge dimensions.

Optical methods are capable of detecting discharges of a few pico-coulombs using long film exposures. However detection is restricted to surface discharges and internal discharges in transparent insulation. The use of photo-multipliers as detectors has been mainly restricted to discharge research applications[30,31] but Teich[32] has proposed their use with a scintillator for detection at ultra-violet wave-lengths. Less background interference is experienced at these frequencies and, with the scintillator coupled to the photomultiplier by a length of insulating light guide, a sensitivity of better than 40 pC is claimed. Strong et al[33] have compared the visual, ultra-violet and ultra-sonic emissions of corona discharges in air. They used both photography and a special low-light-level isocon television camera for their ultraviolet studies and found the technique provided a sensitive means of locating corona sources that could be used in day light. The correlation with the ultra-sonic emissions detected at 40 kHz was found to be good. The ultra-violet pictures were found to render the electric field visible and could therefore be used to investigate insulation structures. Daniel[34] used a similar television camera to observe the corona from overhead transmission lines and concluded that the technique was particularly suitable for the scanning of such circuits as corona could be detected at distances upto 400 metres. Individual corona sources could be detected at 30 - 40 metres but these sensitivities could only be achieved when the ambient illumination level was below 10 lm/m^2 . (i.e. from dusk onwards)

Of the electrical methods of discharge detection, loss tangent measurements have already been described. After deducting the solid loss of the dielectric these measurements yield the total energy loss per cycle in the equipment under test due to discharges. Experiments by Meats[35] indicate that all discharges contribute to breakdown irrespective of their size and that the rate of breakdown (expressed in terms of insulation thickness / time to failure) is proportional to the product of the total charge transfer and the electric stress to which the sample is subjected. Dielectric loss measurements therefore provide an indication of the total damage, attributable to discharges, that is occurring within the specimen. When testing equipment however, the condition of any weak spots in the insulation is generally of more interest than that of the insulation as a whole and, for this reason, the magnitude of the largest discharge is considered more appropriate in many cases.

The Schering bridge circuit of figure 1.2.2-1 may be used to make such measurements by replacing the null indicator with a differential amplifier having a high pass filter at its input to render it insensitive to 50 Hz voltages. The magnitude of individual discharges can be ascertained by viewing the output of the amplifier with an oscilloscope. Initially detectors with fairly large pass-bands (5 - 20 kHz) were used and the bridge was balanced to minimize the residual 50Hz voltage but by increasing the 50Hz rejection and balancing the bridge at the middle frequency of the pass-band, improved immunity to noise on the high voltage supply was achieved. A much greater improvement is obtained by replacing the broad-band detector with a narrow-band tuned type such that each discharge impulse produces a damped oscillatory wavetrain. Some loss of resolution results but this disadvantage is more than offset by the improved noise immunity.

E.R.A. discharge detector

The E.R.A. model 3 discharge detector developed by Mole[36] is of

this type. Figure 1.2.3-1 shows the test circuit most commonly used with this instrument. Discharges occurring within the test specimen C_x cause the circuit to ring at a frequency determined by the inductance of the input unit and the effective capacitance of the test specimen C_x in series with the coupling capacitor C_b. The resultant damped train of oscillations is transformer coupled to an amplifier contained in the discharge detector which typically has a pass-band from 20 - 80 kHz. The output is displayed on a cathode ray tube using an elliptical time-base running at the high voltage energization frequency thereby yielding the relationship between the timing of the discharge pulses and the phase of the high voltage supply. This is further facilitated by the provision of zero crossing markers on the trace derived from the voltmeter circuit. Test specimens of widely different capacitance can be accommodated by changing the input unit.

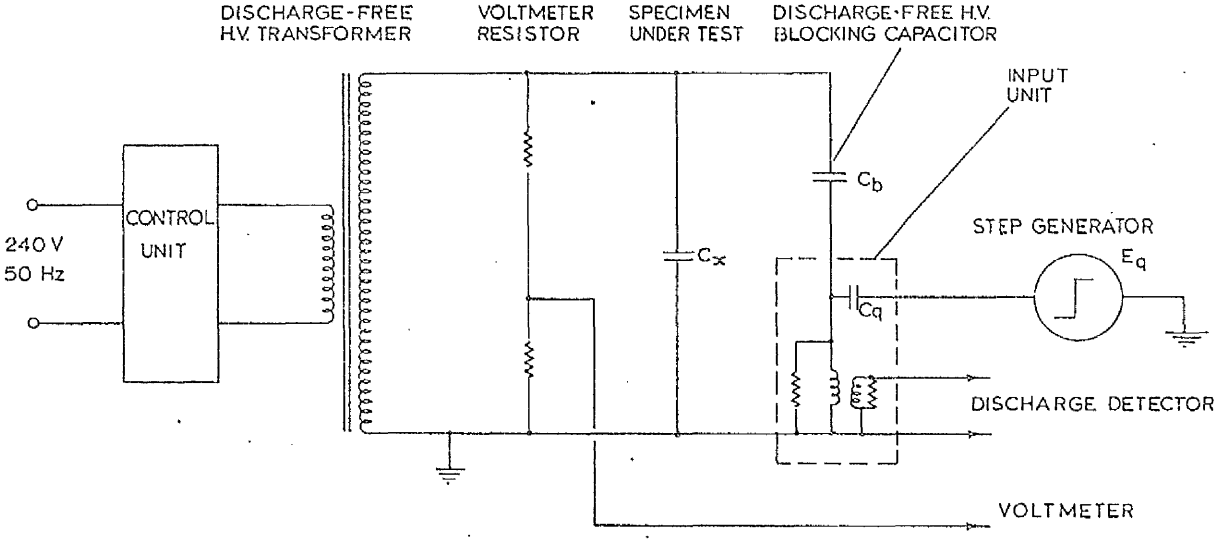

Figure 1.2.3.-1 Unbalanced test circuit most commonly used with the E.R.A. model 3 discharge detector

To measure the magnitude of the detected discharges a known charge is synchronously injected into the low voltage end of the blocking capacitor through the capacitor C_q by means of a step-wave generator contained within the detector. The resultant calibration pulses are adjusted

to match the discharge pulses by attenuating the step-wave generator's output. The discharge magnitude is then given by

$$Q_x = E_q C_q (1 + C_x / C_b) \qquad (1.2.3.-1)$$

To achieve good sensitivity the capacitance of C_b should not be less than one tenth of that of C_x and preferrably should be about equal to it.

Equation (1.2.3-1) does not include the capacitance of the high voltage transformer, a parameter that is frequency dependent and not generally known. To avoid this error it is customary to inject pulses of known charge into the high voltage side of the measurement system and this can be done with the system either live or dead. The latter is preferrable for production type measurements. However it requires the connection of a second high voltage discharge-free capacitor which increases the cost and weight of the test system, increases the system capacitance and also extends the time taken to set-up the test circuit. The use of a low voltage calibrator is therefore preferable when making measurements on small numbers of test specimens in the laboratory or when conducting measurements on installed equipment in the field. A further disadvantage of using equation (1.2.3-1) is that, each time a discharge measurement is made, the discharge magnitude can only be ascertained by calculation or use of the specially designed circular 'slide rule' provided with the instrument. In contrast, if the output attenuation setting of the step-wave generator corresponding to a discharge magnitude of, say, 100 pC is ascertained by means of the low voltage calibrator, the discharge magnitude can be read off directly from a simple look-up table containing the voltage ratios corresponding to 1,2,3,.....,20 dB. The model 3 discharge detector has now been superceded by the transistorized model 5 . This is substantially similar in its operation to the model 3 but with the addition of a direct reading discharge magnitude meter. A gating facility enables the magnitude of a particular discharge to be read in the presence of others.

Discharge detection under noisy conditions

The model 5 discharge detector is capable of detecting discharges as small as 0.005 pC with the circuit of figure 1.2.3-1 and a tuning capacitance of 25 pF. This figure increases to 0.04 pC with C = 1500 pF. However these sensitivities can only be realized under conditions of very low ambient noise. In fact, when conducting discharge measurements on installed equipment under unfavourable conditions, the sensitivity can be reduced by a thousand fold. To reduce the effect of external interference, various techniques can be employed. These include screening and filtering together with the elimation of as many extraneous discharge sources as is possible. Once this has been done, the sensitivity can be further improved by the use of signal-recovery equipment. Wilson[37] describes the use of both a 'box-car' instrument and a time averaging computer to improve the signal to noise ratio. The former is much the simpler instrument but, for a sample time equal to $1/n^{th}$ of the repetition period, it takes n times as long to achieve the same signal enhancement. This is a serious disadvantage when attempting to detect discharges that are liable to self-extinction. Both instruments rely on the discharges occurring at similar phase angles of the energizing high voltage during successive cycles and so can give little enhancement of discharges lacking this stability.

A further technique advocated by Wilson[38] is the use of a frequency-adjustable narrow-band radio interference meter as the detector rather than the non-adjustable tuned detector. With the ability to change the detection frequency, it is usually possible to significantly improve the signal to noise ratio by selecting a 'quiet' part of the interference spectrum. By combining this with signal recovery using a time averaging computer, Wilson claims to have improved the detection sensitivity by as much as a hundred times in some cases.

An alternative solution is the pulse discrimination system proposed by Black.[39,40] Referring back to the test circuit of figure 1.2.3-1,

he replaces the inductive input unit with a capacitive one. This then forms a potential divider with C_b but, because the capacitance of the unit is kept to a minimum, the attenuation of the discharge pulses is small. Each discharge pulse results in a step change in the voltage across the measuring unit capacitance but this decays exponentially due to a shunting resistor. The resultant pulse is fed to an emitter follower circuit to buffer the input circuit from the loading of the coaxial cables connecting the measuring unit to the main instrument. The time constant of the input circuit is arranged to be a few microseconds only in order that discharges occurring in rapid succession can be resolved. A shunting inductor is also connected to the input circuit to reduce the residual 50 Hz voltage to negligible proportions but its value is chosen to be sufficiently large that the resultant resonant period is considerably greater than the circuit's time constant. The inductor therefore plays little part in determining the characteristics of the discharge pulses.

By using a capacitive input circuit, discharge pulses free from overshoot can be produced. These unidirectional pulses can therefore be used to yield the sign of the discharge transients as well as their magnitude. If a similar measuring unit can be inserted in the earth lead of the test specimen C_x the sign information is of considerable benefit because, if a discharge occurs within either the test specimen or the blocking capacitor C_b, the discharge transients detected by the two measuring units will be of opposite polarity whereas they will be of the same polarity if a discharge occurs externally to both of them. Thus by a suitable logic system, discharge sources external to C_x and C_b can be rejected. Black claims a rejection ratio of 7000:1 . This brings considerable advantages because it obviates the need for a discharge free supply with all its inevitable expense and inconvenience. Black also demonstrates its effectiveness when making a measurement on a cable sample using guard rings for, any discharges associated with the guard rings, will be treated as originating

externally and so will be rejected by the instrument. A further advantage of the system can be realized by furnishing the logic circuitry with the sign of dV/dt of the high voltage supply. With this information discharges occurring in C_x can be distinguished from those occurring in C_b and vice-versa. Thus C_b need not be discharge free and can, for instance, be a second test specimen.

Black describes schematically the logic circuitry required to achieve satisfactory operation free from spurious responses due to, for instance, overshoot signals. He then describes the method used to produce a display on a cathode ray tube using an elliptic time-base. Alternatively the pulse can be recorded on a transient recorder and then plotted graphically later. A disadvantage of the pulse discrimination system so far described is the need to interpose a measuring unit between the low voltage end of C_x and earth. For installed equipment this is often not possible. To overcome this difficulty, Black has developed a battery operated measuring unit that can be interposed between the high voltage end of C_x and the supply. It is coupled to the main instrument by light guides to achieve the necessary isolation, two being used to indicate the polarity. In this application only the polarity of the discharges is required from the unit, because the magnitude of the discharge can be determined from the other channel. However, using an optically isolated analogue circuit the discharge magnitude could also be obtained from this unit. Bleys[41] describes an optically isolated analogue circuit with a rise-time of 80 ns that could possibly be adapted for this purpose. With such an arrangement the second measuring unit and the blocking capacitor could be dispensed with, discrimination between internal and external discharges being effected purely by comparison of the polarities of the discharge transients with that of the dV/dt of the energizing voltage. The circuit would however be dependent on the self-capacitance of the high voltage source being adequate. For non-earthed

test specimens a low voltage measuring unit could be used in a similar manner but connected to the earthy side of the test specimen.

Calibration of discharge detection system

Calibration of the discharge detection system has already been discussed in terms of injecting known quantities of charge using 'ideal' step-wave generators. Mole[42] discusses the merits of direct and indirect calibration and derives expressions for the deviation from the ideal case occasioned by the use of 'non-idealized' step-wave generators. He concludes that satisfactory calibration can be achieved provided the following requirements are satisfied. (a) Direct calibration is used either on its own or in conjunction with indirect calibration. (b) The risetime of the transition is less than a given value. (e.g. The error will be less than 10% if $f_o T_1 < 0.08$ for a narrow-band detector where f_o is the centre frequency of the detector's pass band and T_1 is the time constant of the step-wave transition. For a wide-band detector with $f_2 / f_1 = 10$, the requirements are more stringent and $f_o T_1 < 0.06$. This figure relates to an ideal wide-band detector having upper and lower limits to its pass-band of f_2 and f_1 respectively.) (c) The rate of decay of the step change is sufficiently small. (This requirement is readily satisfied, the error being less than 1% provided $f_o T_2 > 1.2$ for a narrow-band detector and $f_o T_2 > 1.75$ for the wide-band detector where T_2 is the time constant of the decaying waveform.) (d) The time interval T_3 between successive discharges is adequate. (The maximum error is given by $Y = G / T_3 \Delta f$ where Y is the difference in the response between the first and second calibration pulses expressed as a fraction of the peak response of the first, $\Delta f = f_2 - f_1$ and G is a function of $\Delta f / f_o$. $G = 1/\pi$ for small values of $\Delta f / f_o$ rising to 0.38 with $\Delta f / f_o = 1$ and 1.3 with $\Delta f / f_o = 5$. Again it is not onerous to satisfy this requirement.) The I.E.E.E. guide to the calibration of discharge measurements[43] stipulates

that the rise time of the step-wave from the calibrator must be less than 100 ns. It also suggests that, if the rate of decay of the step change is less than that required to reduce the applied voltage to half its initial value in 1 ms, the effect of the tail on the calibration will be negligible.

Discharge measurements on cables

Special problems arise when discharge testing cables because, being physically long, they can support travelling and stationary waves which can provoke erroneous responses from discharge detectors. In addition they tend to suffer from high levels of interference especially in the case of installed cables. When testing drum lengths in the factory, the provision of discharge free terminations can also be a problem.

Mole[44] discusses the response of narrow-band and wide-band detectors when making measurements on long cables (i.e. cables greater than approximately a quarter of a wavelength at f_o, the centre frequency of the detector's pass-band) not terminated in their characteristic impedance at the remote end. He also considers the effect of connecting the two ends of a cable together in order to conduct a discharge test on, say, a completed drum length after manufacture. He demonstrates that when two or more, discharge transients arrive at the detector from the same discharge (but by different routes) serious super-position errors can arise in the case of narrow-band detectors (β response). The effect is less serious in the case of wide-band detectors (α response) but can still be significant. Super-position errors can be avoided by connecting the discharge detector to one end only of the test specimen and terminating the remote end in its characteristic impedance. As the characteristic impedance of a cable is low, a series blocking capacitor must be included to limit the power frequency current drawn. The capacitor must be reasonably large however if the termination is not to appear reactive and Mole states that the minimum acceptable capacitance is given approximately by $C_b = 0.25 / R_o f_o$

where R_o is the characteristic impedance of the cable (assumed to be resistive). In many cases it is impracticable to use such a large capacitor but Mole discusses a method of overcoming this difficulty by including an inductor adjusted to make the termination series resonant at f_o. He also describes a method that is suitable for the simultaneous testing of two cables of similar length. The discharge detector is connected to the near ends of both cables and the remote ends are connected through a resistor equal to the sum of the characteristic impedances of the two cables. By this means the reflected and transmitted pulses at the remote end are arranged to be equal and opposite and therefore cancel on arriving at the detector.

Eager and Bader[45] have analysed the response of a tuned detector to a typical discharge transient from a long cable. They also extended their analysis to include discharge transients from shorter cables where multiple reflections are significant. They conclude that the use of a low frequency detector (30kHz centre frequency with a band-width of 10kHz) has advantages both in terms of insensitivity to the position of the discharge sites and reduction in extraneous noise. They give experimental results that show the sensitivity to decrease almost linearly as the cable length is increased upto 500 metres and thereafter to remain constant to beyond 2000 metres, the longest length tested. A sensitivity of 4 pC is claimed to be typically achievable on long lengths of cable under factory conditions.

To investigate super-position errors Lukaschewitsch and Puff[46] used a model consisting of 2000 metres of 60 ohm polyethylene insulated coaxial cable fitted with multiple tapping points. Five different types of discharge detector were tested. The results are plotted and show that, in all cases, significant errors can arise. However in the case of one, a narrow-band detector with a pass-band of 195 - 205 kHz, serious loss of sensitivity was experienced at certain locations. The situation could,

however, be improved considerably by terminating the far end of the cable. (e.g. At 1750 metres from the measuring end the sensitivity was reduced by 89% compared with 51% with the far end of the cable terminated.) A further investigation was conducted using a double-pulse generator which was less cumbersome and provided greater flexibility. Measurements upto the equivalent of 10,000 metres of cable were made. They conclude that calibrations pulses should be injected at both ends of the test specimen for each measurement and that measurements should be made from each end of the cable in turn. Also, where possible, measurements of each discharge should be made at several different detection frequencies and the largest value taken to be correct. It can be assumed that this value will be the least in error because the error is always negative.

Beneke[47] discusses the merits of scanning and full reel measurements on cables during manufacture. The former has the advantage of greater sensitivity and high locational accuracy but it cannot be applied to the finished product. When using full reel detection he stresses the need for caution if a detector with a β-type response is used. If a very wide-band (0.1 - 10 MHz) detector is used, the discharge transients are individually resolved and so can be used for discharge location.[48] (This type of detection is currently being investigated by the author.) However the method is not suitable for production line measurements because of its high susceptibility to interference and the need for skilled interpretation of the results. Beneke considers the use of a detector with a pass-band below 150 kHz and an α- type response to be the most satisfactory in this situation. He refers to the detection system of Eager and Bader but points out that with an integration time as long as 9 microseconds positive errors are likely to arise due to the overlapping of successive discharges.

As regards providing discharge free terminations for cables during test Beneke reports that, upto 15 kV, insulating or semi-conducting paste has proved satisfactory. Immersion in oil extends this to 40 kV without the

need for field control devices. Using de-ionized water for stress relief and insulation he claims satisfactory results at over 100 kV. However this method necessitates the provision of a continuous supply of de-ionized water and the stripping of a moderate length of cable and is not therefore suitable for routine measurements.

Blodgett and Eigen[49] report discharge measurements made on a cable containing various discharge producing defects that had been specially included during manufacture. They found that, in some cases, the discharge magnitudes increased with increasing stress whereas, in other cases, they remained unchanged. With such uncertainties they consider that cable sections displaying even the lowest discernable level of discharge should be rejected pending the availability of more accurate information regarding the expected life of insulation containing discharge sources. They also assembled a coaxial cable model approximately 300 metres long with tapping points and injected signals from a swept frequency oscillator into the cable via a 10 pF capacitor. The voltage signal appearing at one end of the cable was examined using a spectrum analyser for various injection positions. Connection to the end of the cable was made through a 600 pF capacitor to simulate a typical coupling capacitor. As would be expected from transmission line theory, considerable variation in the magnitude of the received signal was observed with change of frequency and injection position. For these and other reasons, the authors consider a scanning method preferable for manufacturing applications. They then outline a suitable scanning system employing a de-ionized water trough with careful control of the stress distribution. Pick-up is by means of two electrodes arranged to reject extraneous interference and a sensitivity of 0.01 mV is claimed.

Eager, Bahder and Silver[50] report their experience of discharge detection in commercial production of power cables with extruded insulation. They propose the use of a corona factor relating the apparent discharge magnitude to the applied electric stress as a measure of the soundness of insul-

ation. They also advocate making tanδ measurements to detect screen imperfections. Shimoguchi et al[51] similarly report their experience of testing installed cables. Their results are drawn from tests on about 1500 circuits rated from 6.6 to 77 kV using both d.c. insulation and partial discharge tests. For the partial discharge tests they used low frequency high voltage excitation with an approximately triangular waveform and were able to locate discharge sources using the wide-band travelling-wave method. The discharge sources included those arising from resealed faults. This technique has also been used by the author and found particularly effective, for instance, at finding joints in 11 kV paper insulated cables with defective sealing. In this situation a fault will occur sooner or later but, if the cable is protected by, for example, a fast unit protection scheme, the fault current will be tripped before a solid fault is established. In many cases the heat of the fault can dry out the joint sufficiently for it to withstand a subsequent pressure test and so the fault cannot be located by conventional fault location techniques. However the fault results in considerable charring of the insulation papers and there is usually sufficient conductivity present for the site to discharge at an appreciable rate under a high voltage d.c. stress.

The test arrangement used by the author is shown in figure 1.2.3-2 and the trace to be expected with the discharge in the position indicated is shown in figure 1.2.3-3 . From this trace the discharge site can be located. Figure 1.2.3-4 shows the trace actually obtained when locating a resealed fault in an 11 kV cable 1140 metres in length. The trace was obtained by maintaining the high voltage for sufficient time to allow the discharges associated with the voids that are ubiquitously present in M.I.N.D. paper insulated cables to die away. This particular discharge site then became readily identifiable as the site of the fault. The discharge pulses were of positive polarity but, because the detector circuit was underdamped, substantial negative overshoots were produced.

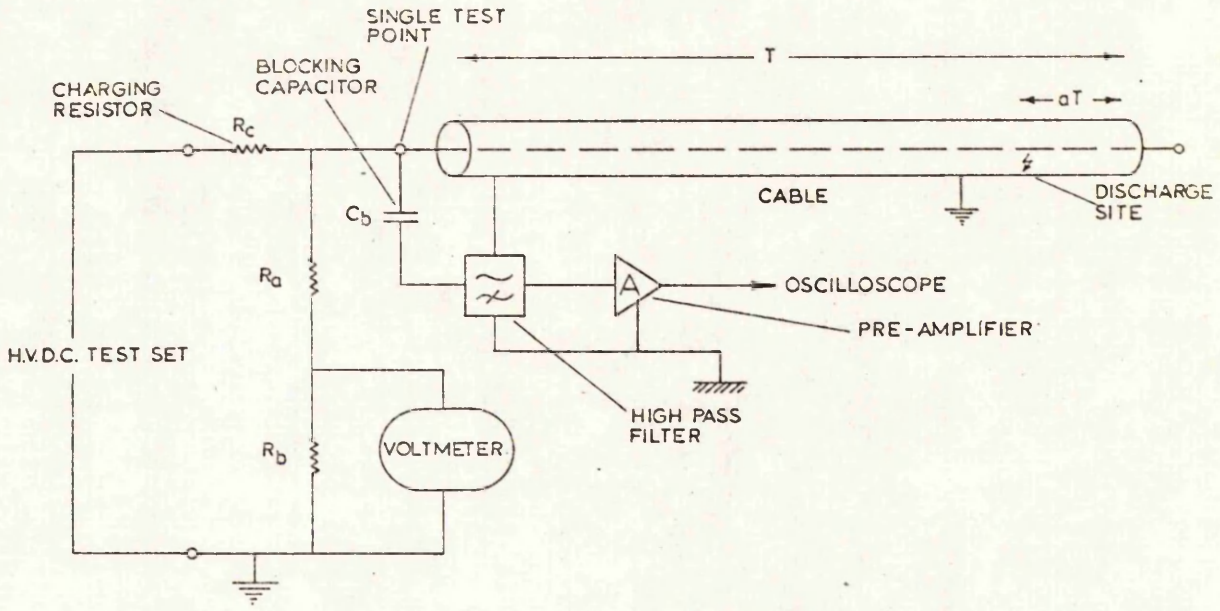

Figure 1.2.3-2 Single-ended travelling wave method of partial discharge location

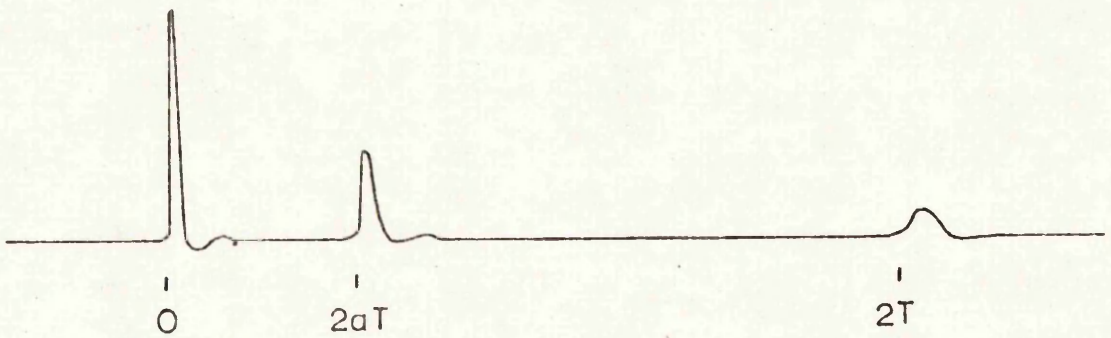

Figure 1.2.3-3 Trace to be expected with discharge site at position shown in figure 1.2.3-2

In figure 1.2.3-2 the low voltage side of the coupling capacitor was connected, via a high-pass RC type filter, to a transmission system of 50 ohms characteristic impedance. Nigol[52] reports the use of a similar detection system for the location of dicharges but using a higher detection impedance. (10 kohms) He also describes stationary wave measurements made in the frequency domain (rather than the time domain) similar to those

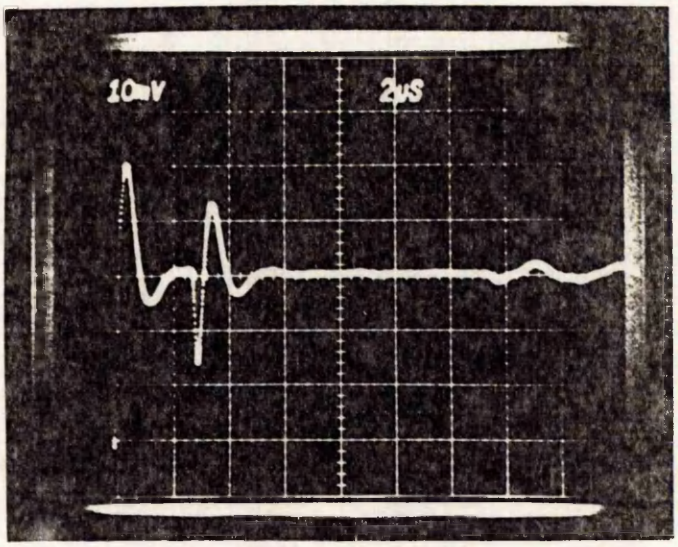

Figure 1.2.3-4 Trace obtained when locating a resealed fault on an 11 kV cable 1140 metres in length

of Blodgett and Eigen. However from a typical spectral analysis trace given in the paper it would appear that he used impulses as the signal source rather than a swept frequency oscillator though this is not clear from the text. The location of a discharge site in an 11 kV cable by this method is described by Galand.[53] However it would appear that the method is not suitable for the location of multiple sites in a cable. The preceding discussion relates to the location of partial discharge sources in cables. Corresponding techniques have been used to effect locations in high voltage transformers but these will not be discussed in this thesis.

Very low frequency testing

The use of very low frequency high voltage sources has already been referred to in connection with the discharge testing of cables. The purpose of reducing the test frequency is to reduce the charging current required to achieve a specified voltage on a given test specimen. As this can be substantial for high capacitance test specimens the technique has considerable appeal. The energizing voltage waveforms used vary but include

sinusoidal, triangular and exponential forms. These can be generated using electro-mechanical modulators or by using resistors or electronic valves in series with high voltage supplies.

Miller, Black and Gray[54] describe a generator of this type using series valves which, because the grids of the valves are at considerable potentials with respect to earth, utilizes fibre optic control lines. An alternative method is the use of a high frequency (40 kHz) Cockroft-Walton multiplier driven from a power oscillator. A generator of this type, capable of supplying a current of 1mA at 25kV peak is described by Hilder, Gray and Black.[55] The high voltage output is controlled by electronically varying the oscillator's output voltage. Smoothing of the high voltage output is required to reduce the 40 kHz ripple. Both these methods are capable of providing high voltage sources of considerable flexibility. In both cases the VA requirements can be halved by reversing the output polarity of the generator at the zero crossing point. However this necessitates the use of a high voltage switch which can present difficulties.

Virsberg and Kelen[56] discuss the change in the stress distributions to be expected within insulation when testing at very low frequencies with particular reference to high voltage machine insulation. They show that, for volume resistivities less than 10^{11} ohm-metre, the stress distribution at 0.1 Hz can deviate markedly from that at 50 Hz. This resistivity is well exceeded by new insulation but might not be attained in the case of the insulation of older machines, especially if they are damp.

Miller and Black[57] give the results of partial discharge measurements on epoxy resin and polyethylene samples, a short length of cross-linked polyethylene cable and part of an epoxy-resin bonded mica-insulated stator bar over the frequency range 0.1 to 50 Hz. They used the pulse discrimination system to reject extraneous pulses and a pulse height analyser to assist in the interpretation of the results. From the results obtained they conclude that the inception voltage is largely independent of the

excitation frequency over this frequency range (for materials such as epoxy resin). There is also little variation in the most probable discharge magnitude but, at the lower end of the frequency range, there is an increase in the number of smaller discharges. Taylor[58] gives the results of bridge measurements on machine insulation made at 50 Hz and 0.1 Hz and shows the loss tangent to be increased by approximately a factor of three at the lower frequency. He also found the increase in capacitance to vary from 3 (for epoxy bonded mica) to 27 percent (for Copal mica), the increase being roughly proportional to the loss tangent. This finding is to be expected from the theory of dielectric relaxation.[21]

Other methods of partial discharge detection

There is an increasing demand for the detection of discharges in live transmission / distribution equipment. In this situation it is not allowable to make direct connection to the high voltage conductor or to break the connection to the earth foil of a bushing. An instrument designed by Wilson[59,60] overcomes this difficulty by using a split, ferrite-cored current transformer to detect the discharge transients flowing in the earth, or neutral, connection of the system it is required to test. The ferrite used responds in the frequency band 0.5 to 10 MHz and so is insensitive to currents at the power frequency and its harmonics. A narrow band detection system is used with a centre frequency that can be adjusted, on site, to a suitably quiet part of the interference spectrum. The peak level of the received pulses is continuously recorded and an alarm condition is initiated if a pre-determined level is exceeded. A sensitivity of 5 pC has been measured.

Radio frequency interference measurements have been much used for the detection of partial discharges[61] but attempts to locate discharge sources by this method have, in general, not been successful. This can be attributed to the lack of sufficiently directional aerials at the detection frequencies normally employed and confusing re-radiation by other metal

objects. However Loftness[62] reports the successful location of discharge sources on overhead lines using detection frequencies upto 500 MHz. Allan and Kashani[63] made measurements of the radiated radio frequency noise and ultra-sonic levels from 11 kV and 33 kV insulators and found reasonable correlation between them. They therefore conclude that discharge sources causing radio frequency interference can be satisfactorily located using an ultra-sonic (40 kHz) probe but assessment of the level of interference would be difficult.

Other methods of discharge detection include gas-in-oil analysis and the measurement of the physical and chemical properties of insulating papers. The latter is normally conducted on paper samples removed from a cable following a fault, especially if the cause of the fault is unknown. The extent of any discharge activity can be estimated from the amount of carbonization and waxing present. This can normally be ascertained directly by visual examination but, in some instances, a 'magenta dye' test may be required to assist the observation. This test involves the degreasing of the paper samples (preferrably in a Soxhlet apparatus) followed by colouring with a water based dye. (N.B. Magenta is no longer used as it has been established that it can be carcinogenic.) Areas that have been exposed to discharge activity are high-lighted by their inability to absorb the dye due to the presence of the wax. Discharge activity is also considered to result in degradation of the paper similar to that resulting from thermal ageing. This being the case, the discharge activity / thermal ageing to which paper insulation has been exposed can be ascertained by measuring the degree of degradation of the paper. Lawson et al[64] have investigated various methods for achieving this measurement and consider the following six to give meaningful results.

1) Tensile strength

2) Extension to break

3) and 4) Burst strength and degree of polymerization

5) Tear strength

6) Folding strength

These methods are given in increasing order of sensitivity according to Lawson et al but not, in the author's experience, increasing order of reproducibility. Measurement of the degree of polymerization is being used by the author with satisfactory results. This technique measures a mean molecular weight of the cellulose by a viscometric method involving dissolving the paper in a special solution. To date cupri-ethylene diamine solution, in accordance with the I.E.C. specification No. 450 [65] has been used but this solution is difficult to produce and has a limited shelf life even when stored at 1.5 molar concentration in a refrigerator. The use of cupra-ammonium hydroxide solution as an alternative is currently being investigated. Lawson et al consider the insulation to have reached the end of its useful life when any of the six physical or chemical parameters has fallen to one tenth of its original value.

1.2.4 Analysis of results of discharge measurements and their relationship to degradation

Dakin et al[66] consider that in many instances the utilization of a meter is preferable to the use of an oscilloscope when conducting discharge tests as this provides a simple quantitative answer. They favour an instrument indicating the peak value of the apparent charge rather than an 'average discharge current' instrument because the former relates primarily to the greatest depth of void present whereas the latter is principally a measure of the overall volume subject to discharge activity. They are of the opinion that it is the former which presents the greatest danger to an insulation system's integrity. For their measurements they used a radio frequency interference set capacitively connected to the test specimen but via a loosely coupled radio frequency transformer.

To further improve the significance of discharge measurements

Reynolds[67] advocates the use of a multi-channel pen recorder to provide a permanent record of the variation with time of four parameters:

1) The peak value of the apparent charge in pC averaged over 0.1 to 1 second.
2) The average value of the pulses expressed as a current in microamperes.
3) The average power obtained by multiplying the equivalent discharge current by the applied voltage.
4) The applied voltage.

He claims that by recording these four parameters a more realistic assessment of the soundness of insulation can be made.

Other workers in the field favour the use of pulse height analysers. The work of Miller and Black[57] has already been discussed. The technique and practice of 'pulse height analysis' is described by Bartnikas[68] who then gives experimental results obtained with various test specimens including X.L.P.E. and E.P.R. cable when stresses at different voltages or for different periods of time. The pulse height analyser used had 1024 channels.

Megahed et al[69] report the use of a simple six channel pulse height analyser to study the temporal variation of the discharge activity in epoxy resin and polyethylene samples. Their results show considerable variations in the discharging rate over a period of 200 hours with wide variations in behaviour between the two materials and between measurements on the same material but at different discharge magnitudes.

Franke and Czekaj[70] describe a simple wide-band partial discharge detector where all pulses over a pre-determined level are counted. By combining several of these simple instruments a low-resolution amplitude-distribution analyser was produced which proved useful for monitoring the discharge activity in submarine telecommunication cables. (These cables are series powered using a high voltage d.c. supply.) The author has

designed a similar instrument for the continuous monitoring of the partial discharge activity in high voltage metal-clad switchgear. The discharge pulses are capacitively coupled to the instrument either through the capacitor bushings or using a metal electrode placed under the lid of a chamber. The rate at which discharges occur over the set threshold level is continuously monitored and, in the event of this exceeding a given level, an alarm relay is operated. The instrument operates in the 30 - 100 MHz frequency band where attenuation adequately restricts the search area and, by making the integration period sufficiently long, the instrument is rendered largely insensitive to system disturbances. The results obtained so far have shown that if a switch-board is subject to discharges, the discharging will often occur for several hours before extinguishing. The ensuing dormant period can then last for tens of hours or even days before discharging recommences. To provide more than one threshold level, pre-attenuators controlled on an hourly cycle have been used. This work will be reported shortly.

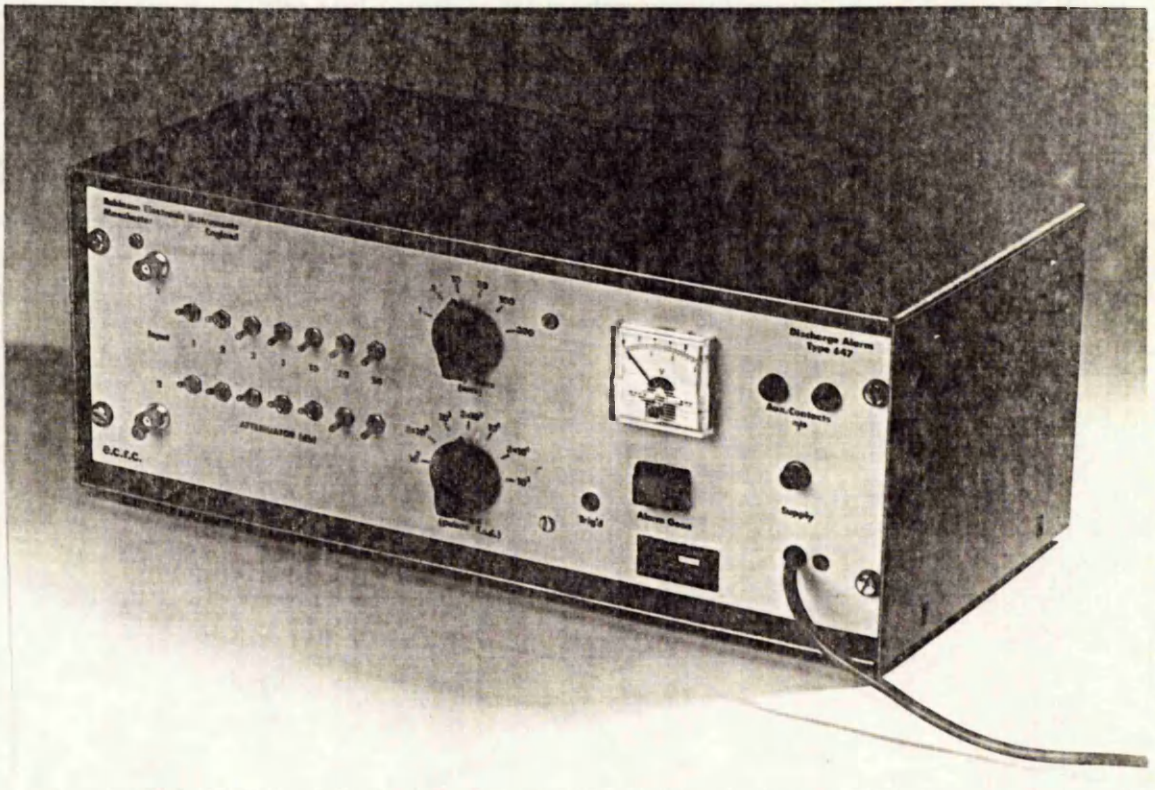

Figure 1.2.4-1 Discharge alarm

Instead of measuring the rate at which discharges occur, Lacoste et al[71] measured the time between consecutive discharges. The number of discharges per minute was then plotted as a function of the time between discharges to yield what they describe as a 'chronogramme'. The experimental results given show the chronogrammes to have well defined peaks and these are claimed to be reproducible. The authors propose a simple explanation for this phenomenon.

Relating partial discharge activity to degradation and prospective life is not easy even with laboratory test specimens and it is especially difficult where high voltage plant is concerned. Constandinou[72] gives the results of tests on model bushings aimed at predicting the behaviour of oil-impregnated paper bushings. His results were obtained by stressing the bushings at 3.25 kHz rather than the power frequency to accelerate the ageing process. This technique is currently being used by the author (but using 400 Hz three phase excitation) to conduct an accelerated life-test on an installed 33 kV metal-clad busbar. Constandinou found that the most critical factor in determining the failure of bushings of this type when operated at a stress of 3 kV/mm was the ability of the oil to dissolve any trapped gas. Inability to do this will result in, otherwise sound, bushings failing in 12 to 20 years at 50 Hz. The deleterious effects of small discharges in oil-impregnated paper bushings is reflected in the I.E.C. Publication 137 [73] which recommends that the maximum partial discharge magnitude should not exceed 10 pC for this type of bushing. Discharges upto twice this figure are considered acceptable in cast insulation bushings and ten times in synthetic resin bonded paper capacitor type bushings. All these values relate to the largest discharge magnitude at $0.63\ U_N$.

Guidance regarding the acceptable magnitude of discharges in 11 kV mass-impregnated cables is given in a report by Mole.[74] He details the discharge characteristics and fault statistics of twenty five installed cables and concludes that:

1) New cables can be expected to have discharge inception voltages of 70 - 90 percent of the working voltage and discharge levels at working voltage of 100 - 1000 pC.

2) Most cables that have been in service for some years can be expected to have an inception voltage below 50% of working voltage and exhibit discharges in the range 500 - 10,000 pC at working voltage.

3) A few cables may be found with discharge levels at working voltage in excess of 10,000 pC. However discharges exceeding 100,000 pC are unlikely.

4) Provided discharge levels greater than 2000 pC are not maintained for appreciable periods, no significant deterioration due to discharges would arise.

The degradation of samples of polyethylene by partial discharges under laboratory conditions has been investigated by Toriyama et al.[75] They measured various parameters to assess the effect of discharges including weight variations, infra-red absorption spectra (both reflected and transmitted) and chemical analysis of the samples and any evolved gases. In addition the samples were examined by optical and electron microscopes. They concluded that the polyethylene was oxidized by activated oxygen. Degradation due to ozone and the oxides of nitrogen was also apparent. Reynders[76] conducted accelerated life tests on polythene samples using 4 kHz high voltage excitation. He found the degradation to follow one of two distinct patterns. Both patterns showed large discharges initially (Upto 1500 pC in some cases) but in the first pattern these reduced to a low level (10 - 30 pC) fairly rapidly and remained at this level until just prior to failure. At this point the discharge magnitude increased rapidly. Failure occurred after a total of 400 - 800 hours had elapsed. In the second pattern the initial high level of discharge activity was maintained for longer. This was followed by a long period during which

only extremely small discharges occurred. Nevertheless degradation continued and, once more, a rapid increase in discharge magnitude was observed just prior to failure. (700 - 1300 hours) Infra-red examination of samples showing the first pattern of degradation revealed oxidation similar to that obtained by thermal or photo oxidation in the presence of excess oxygen. In the case of the second pattern of degradation, the formation of a transparent gel was observed in a similar way to that observed by Mason[77] when testing sealed cavities in polyethylene. Reynder's findings at 4 kHz are considered applicable at 50 Hz because the life-time of his test samples, when multiplied by the acceleration factor of 80, are reasonably in agreement with the 10^5 hours at 50 Hz given by Hogg and Walley.[78] Therefore the low levels of discharge activity displayed by Reynder's samples for most of the stressing time could have serious repercussions when discharge testing polyethylene insulated cables, for instance, as they could lead to false confidence in the soundness of the insulation.

Having outlined the mechanisms of insulation failure and the various techniques of prophylactic testing available to the high voltage insulation engineer, it is evident that there still remains much room for improvement when it comes to supplying reliable quantitative information about the degree of degradation and the prospective life of insulation structures in service. Partial discharge measurements are much used for the detection of incipient faults and work now, to be described, is aimed at improving the significance of these measurements.

CHAPTER 2

Description of the techniques used in this study for the analysis of potential distributions within dielectrics

In chapter 1 the deleterious effects of voids within dielectrics were described and it was pointed out that they are likely to be the limiting factor in the performance and life expectancy of high voltage insulation structures. To quantify these effects an analysis of the electrical stress in dielectrics containing voids was undertaken. The results provide detailed information on the stresses in and around voids and enable more accurate assessment of the condition of insulation to be made by interpretation of the discharge characteristics. The effect of void size, shape and condition on the inception voltage and discharge magnitude is analysed and the variation in the bulk properties, capacitance and loss tangent, is also quantified.

In this chapter a brief review of the mathematical background is given followed by details of the numerical techniques employed to effect solutions. The application of these techniques to the analysis of the electric fields in dielectrics containing voids is described in chapter 3.

2.1 Mathematical background

The electrostatic field intensity $\underline{E}$ at a point is related to the potential $\emptyset$ by the equation

$$\underline{E} = -\nabla\emptyset \qquad (2.1\text{-}1)$$

and, in an isotropic region, the electrostatic flux density $\underline{D}$ is given by

$$\underline{D} = k\underline{E} = -k\nabla\emptyset \qquad (2.1\text{-}2)$$

where

$$k = \epsilon_o\epsilon_r \qquad (2.1\text{-}3)$$

and ϵ_o, ϵ_r are the free space and relative permittivities respectively. Now from the differential form of Gauss's theorem

$$\nabla.\underline{D} = \rho \qquad (2.1\text{-}4)$$

where ρ is the electrostatic charge contained within the differential

volume and so, combining these equations,

$$-\nabla.(k\nabla\phi) = \rho \qquad (2.1\text{-}5)$$

This is Poisson's equation for an isotropic dielectric. For a homogeneous region where k is not a function of position this reduces to the familiar form

$$-\nabla^2\phi = \rho/k \qquad (2.1\text{-}6)$$

If $\rho = 0$, this reduces further to Laplace's equation.

For an anisotropic region k is a function of direction. (Such a situation would arise if, for instance, the dielectric were laminated with a greater value of k along the laminations than perpendicular to them.) In this case the scalar k must be replaced with a tensor $\underline{\underline{k}}'$ given by

$$\underline{\underline{k}}' = \begin{bmatrix} k_{x'} & 0 \\ 0 & k_{y'} \end{bmatrix} \qquad (2.1\text{-}7)$$

where x' and y' are the local axes parallel to the laminations and perpendicular to them (or vice versa) and $k_{x'}$ and $k_{y'}$ are the corresponding values of k. Equation (2.1-2) can then be written as

$$\underline{D}' = \underline{\underline{k}}'\underline{E}' \qquad (2.1\text{-}8)$$

or

$$\begin{bmatrix} D_{x'} \\ D_{y'} \end{bmatrix} = \begin{bmatrix} k_{x'} & 0 \\ 0 & k_{y'} \end{bmatrix} \begin{bmatrix} E_{x'} \\ E_{y'} \end{bmatrix} \qquad (2.1\text{-}9)$$

Expanded this gives

$$D_{x'} = k_{x'}E_{x'} \quad \text{and} \quad D_{y'} = k_{y'}E_{y'} \qquad (2.1\text{-}10)$$

as expected.

Since the directions of the local axes x' and y' can change from point to point, it is necessary to rewrite equation (2.1-8) in terms of the global axes x and y. This can be achieved as shown in appendix 1 by relating the local axes to the global axes through the unitary tensor

$$T = \begin{bmatrix} \cos\alpha & \sin\alpha \\ -\sin\alpha & \cos\alpha \end{bmatrix} \qquad (2.1\text{-}11)$$

where α is the angle, measured in an anti-clockwise direction, between the global coordinates and the local coordinates. This gives

$$\underline{D}' = \underline{\underline{T}}\underline{D} \qquad \underline{E}' = \underline{\underline{T}}\underline{E}$$

and $$\underline{\underline{D}} = \underline{\underline{k}}\,\underline{E} \qquad (2.1\text{-}12)$$

where $$\underline{\underline{k}} = T^{-1}\underline{\underline{k}}'T = \begin{bmatrix} a & b \\ b & c \end{bmatrix} \qquad (2.1\text{-}13)$$

with $$a = k_{x'}\cos^2\alpha + k_{y'}\sin^2\alpha \qquad (2.1\text{-}14)$$

$$b = (k_{x'} - k_{y'})\sin\alpha\cos\alpha \qquad (2.1\text{-}15)$$

$$c = k_{x'}\sin^2\alpha + k_{y'}\cos^2\alpha \qquad (2.1\text{-}16)$$

Thus, from equation (2.1-5), the general form of Poisson's equation for an inhomogeneous and anisotropic dielectric is

$$-\begin{bmatrix} \frac{\partial}{\partial x} & \frac{\partial}{\partial y} \end{bmatrix}\begin{bmatrix} a & b \\ b & c \end{bmatrix}\begin{bmatrix} \frac{\partial \phi}{\partial x} \\ \frac{\partial \phi}{\partial y} \end{bmatrix} = \rho \qquad (2.1\text{-}17)$$

or $$-\frac{\partial}{\partial x}\left(a\frac{\partial \phi}{\partial x} + b\frac{\partial \phi}{\partial y}\right) - \frac{\partial}{\partial y}\left(b\frac{\partial \phi}{\partial x} + c\frac{\partial \phi}{\partial y}\right) = \rho \qquad (2.1\text{-}18)$$

Assuming a,b and c to be functions of position this gives

$$a\frac{\partial^2 \phi}{\partial x^2} + 2b\frac{\partial^2 \phi}{\partial x \partial y} + c\frac{\partial^2 \phi}{\partial y^2} + \left(\frac{\partial a}{\partial x} + \frac{\partial b}{\partial y}\right)\frac{\partial \phi}{\partial x} + \left(\frac{\partial b}{\partial x} + \frac{\partial c}{\partial y}\right)\frac{\partial \phi}{\partial y} + \rho = 0 \qquad (2.1\text{-}19)$$

Methods of solving field problems

Solution of equation (2.1-19), with the appropriate boundary conditions, yields the potential distribution within a field region. In some circumstances this equation can be solved analytically by separation of the variables.[79] Failing that, the problem may be rendered soluble by the use of conformal transformations.[80] For most practical problems however the boundary conditions and charge distributions will not be amenable to solution by these methods and resort to other methods must be made.

Graphical, electroconductive and numerical methods are used principally.[81] Graphical methods using the curvilinear square technique enable approximate solutions to be quickly obtained by hand but the accuracy is limited. More accurate solutions can be obtained experimentally using an electroconductive analogue of the field region it is wished to study. The conducting medium can be an electrolytic tank, a graphite loaded paper, a thin metal film or a resistor/capacitor/inductor net. The net provides

potential values only at the nodes and therefore cannot strickly represent the continuous medium in the field region. However, provided the mesh size is sufficiently small, the field value at the node points is yielded with negligible error. The potential at other points can be obtained by interpolation. Numerical methods are capable of still greater accuracy and, in addition, can provide more flexibility. For these reasons all the field problems in this study were solved numerically.

Two methods are in common usage. The first involves formulating finite difference equations relating the potential at each of many specified nodes to the potentials of its neighbours. The resultant set of simultaneous equations must then be solved to give the potentials at the nodes. Like the network analogue, the potential at other points can be obtained by interpolation. The second method exploits the well known principle that the solution to electrostatic problems is such that the overall potential energy of the system is minimized. The field is approximated by combinations of trial functions chosen by variational techniques with the aim of achieving this minimisation. However only a limited number of functions can be included so large complicated regions are divided into elements. This is quite acceptable provided the boundary conditions between elements are satisfied and enables regions containing discontinuities in permittivity etc. to be accurately represented. This is known as the method of finite elements.

Both methods were used during the course of this study because, in many cases, one method was more suitable than the other. Also, where practicable, the solutions were cross checked using the alternative method. Details of the methods will now be given.

2.2 Method of finite differences

Finite difference equations

The Laplace and Poisson equations are examples of second order partial differential equations of the elliptic type. Approximate solutions using the finite difference method are obtained by representing the field

region as a grid of points. Difference equations are generated relating the potential at each of these points, or nodes, to those at neighbouring nodes and the resulting set of equations is then solved to obtain the overall solution.

For the symmetrical five-point star shown in figure 2.2-1, the finite difference form of equation (2.1-6) is[81]

$$\nabla^2\phi = (\phi_{i-1,j} + \phi_{i+1,j} + \phi_{i,j-1} + \phi_{i,j+1} - 4\phi_{i,j})/h^2 = -\rho/k \qquad (2.2\text{-}1)$$

This assumes the dielectric to be both homogeneous and isotropic. Only terms involving the fourth and higher powers of h have been ignored in the derivation of this equation which is thus of high accuracy provided h is small.

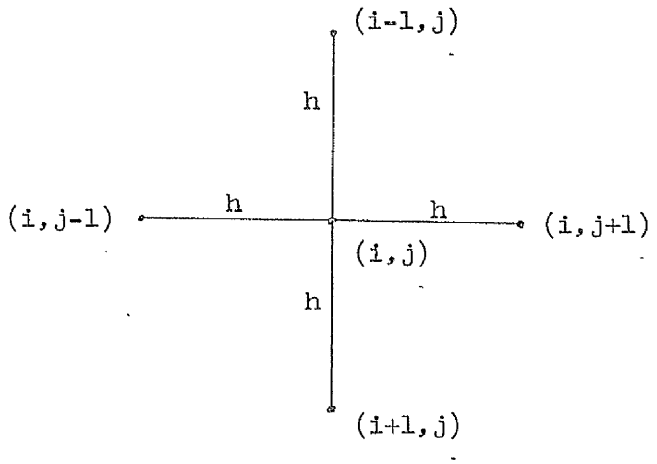

Figure 2.2-1 Symmetrical five-point finite difference nodal star

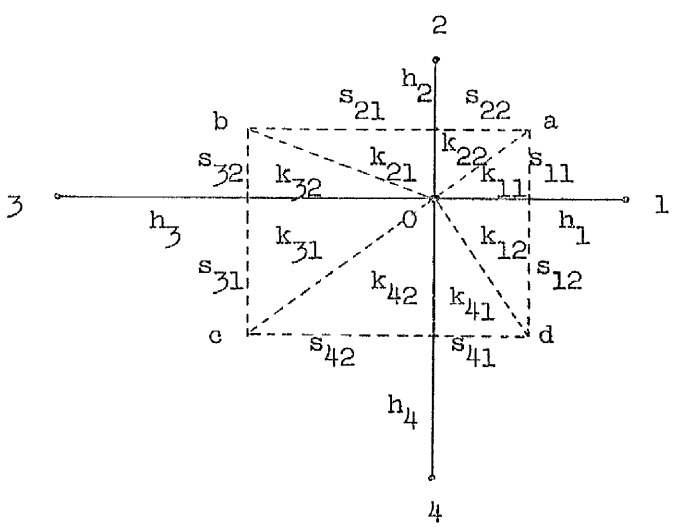

Figure 2.2-2 Asymmetric five-point finite difference nodal star

Wensley and Parker[82] demonstrated that a finite difference equation for the asymmetrical star shown in figure 2.2-2 can be obtained using the integral form of Gauss's theorem

$$\int_S \underline{D}.d\underline{S} = \int_\tau \rho d\tau \qquad (2.2\text{-}2)$$

Integration around abcd, assuming the cell to have unit depth, gives

$$\sum_{n=1}^{4} \frac{(\phi_o - \phi_n)}{h_n} (k_{n1}s_{n1} + k_{n2}s_{n2}) = \rho_{abcd} \qquad (2.2\text{-}3)$$

where $s_{11} = \frac{1}{2}h_2$; $s_{12} = \frac{1}{2}h_4$ etc. (In contrast to equation 2.2-1 local, rather than global, node numbers have been used to simplify the notation.) For an electrostatic problem the k's represent the permittivities of the respective sectors and ρ_{abcd} is the charge contained within the cell abcd. Using this equation dielectric boundaries and anisotropic/inhomogeneous dielectrics can be accommodated. It will be noticed that this equation reduces to the simpler equation (2.2-1) if the star is symmetrical and the permittivity uniform.

Boundary conditions

Dirichlet boundary conditions (specified potential) are readily accommodated by placing the outermost nodes on the boundary at the points of intersection with the nodal grid. If these nodes can be arranged to coincide with the regular grid the disruption of the computing algorithms used to obtain a solution will be minimal. Furthermore the accuracy of the difference equations will be greater.

The generalized Neumann boundary condition (specified potential gradient normal to the surface) is less easy to handle. Wexler[83] describes a method using the same boundary node positions as would be used for a Dirichlet boundary whereas Fox[84] employs nodes that lie on the regular nodal grid but outside the boundary. These additional nodes are referred to as 'fictitious nodes'. Homogeneous Neumann boundaries ($\partial\phi/\partial n = 0$) arise at lines of symmetry etc. and are therefore frequently encountered. In this study they could be arranged to be parallel to the nodal grid in

each case and so were easily represented using a reduced form of equation (2.2-3). Mixed boundary conditions of the form

$$k(s)\left.\frac{\partial \phi}{\partial n}\right|_s + \sigma(s)\,\phi(s) = h(s) \qquad (2.2\text{-}4)$$

are also possible but were not needed in this study.

Axially - symmetric fields

Three dimensional field problems having symmetry about an axis can be analysed in two dimensions as the circumferential variation is known. In cylindrical coordinates Poisson's equation for an inhomogeneous medium is[85]

$$-\frac{1}{r}\frac{\partial}{\partial r}\left(rk\frac{\partial \phi}{\partial r}\right) - \frac{1}{r}\frac{\partial}{\partial \theta}\left(\frac{k}{r}\frac{\partial \phi}{\partial \theta}\right) - \frac{\partial}{\partial z}\left(k\frac{\partial \phi}{\partial z}\right) = \rho \qquad (2.2\text{-}5)$$

Rearranging this equation and taking the field to be constant with respect to θ (which is normally the case)

$$-\frac{\partial}{\partial r}\left(rk\frac{\partial \phi}{\partial r}\right) - \frac{\partial}{\partial z}\left(rk\frac{\partial \phi}{\partial z}\right) = r\rho \qquad (2.2\text{-}6)$$

Comparing this with equation (2.1-18) it is evident that axisymmetric problems may be solved by working in the $r - z$ plane with $a = c = rk$. (This is a mathematical justification for the use of wedge shaped electrolytic tanks to solve axisymmetric problems.) $b = d = 0$ and ρ suitably redefined. Again the dielectric need not be isotropic and a general form of (2.2-6) analogous to (2.1-18) can be written. For the particular case where the dielectric laminations are concentric, $a = rk_r$, $c = rk_z$ and $b = d = 0$.

Dielectric loss

Under alternating field conditions the current through a capacitor containing a lossy dielectric includes a resistive component in phase with the applied voltage. This can be the result of finite dielectric conductivity and/or finite dielectric relaxation time. It is most conveniently accommodated mathematically by ascribing a complex value to the relative permittivity

$$\epsilon_r = \epsilon' - j\epsilon'' \qquad (2.2\text{-}7)$$

where

$$\epsilon'' = \epsilon' \tan \delta \qquad (2.2\text{-}8)$$

By this means the problem is reduced once more to the solution of equation (2.1-5) though the operator (and therefore the answers) will now be complex.

Semiconducting films

A film of small, but finite, thickness δ having a relative permittivity $(\epsilon_r)_f$ can be attributed a film coefficient k_f where $k_f = \epsilon_o(\epsilon_r)_f\delta$. Referring to figure 2.2-2 if a film with coefficient $(k_f)_i$ connects the central node to node i, Gauss's theorem can be satisfied by the addition of a term $(k_f)_i (\phi_o - \phi_i)/h_i$ to equation (2.2-3). Providing δ is negligible compared with the mesh dimensions the other terms in the equation remain unaltered.

Like ϵ_r, k_f can be complex and, in particular, has no real part for a purely resistive film. To determine what value must be specified for k_f to represent a film of given admittance, consider a square of film with a voltage $V = V_o e^{j\omega t}$ applied across opposite faces. The current through the film will be given by $I = YV = (G + jS)V$. But

$$I = \frac{\partial D}{\partial t} = \frac{\partial}{\partial t}\left\{\epsilon_o(\epsilon_f' - j\epsilon_f'')\, V_o e^{j\omega t}\right\} \qquad (2.2\text{-}9)$$

Therefore

$$k_f = (S - jG)/\omega \qquad (2.2\text{-}10)$$

where S and G are the values per square.

Solution of finite difference equations

Iterative methods

Either iterative or direct methods can be used for the solution of the large sets of first order simultaneous equations generated by the finite difference method. The iterative solution of n equations using relaxation is best explained by considering the i^{th} equation

$$\sum_{j=1}^{n} a_{ij}\,\phi_j = b_i \qquad (2.2\text{-}11)$$

This can be rearranged to express the i^{th} unknown in terms of the others

$$\phi_i^{(m)} = \frac{b_i}{a_{ii}} - \sum_{j=1}^{i-1} \frac{a_{ij}\phi_j^{(m)}}{a_{ii}} - \sum_{j=i+1}^{n} \frac{a_{ij}\phi_j^{(m-1)}}{a_{ii}} \qquad (2.2\text{-}12)$$

where $\phi_i^{(m)}$ is the value of ϕ_i after the m^{th} iteration. The procedure is to guess the first set of solutions and apply (2.2-12) to each of the n equations in turn to produce an improved set. The values obtained after this first iteration are then further improved by successive iterations. This, the Gauss Seidel method, uses the latest available values for ϕ_j in every case and typically produces the same accuracy of solution in half the number of iterations required by the straight Jacobi method where only node values from the previous interation are used.. The method has the additional advantage that it requires less computer store as the newly calculated node values can displace the old.

The method so far described is refered to as 'level relaxation'. The difference between $\phi_i^{(m)}$ and $\phi_i^{(m-1)}$ represents a correction term that must be added to $\phi_i^{(m-1)}$ to update the solution. By increasing the correction by a factor α, the convergence rate can be greatly increased. The new estimate is given by

$$\phi_i^{(m)} = \phi_i^{(m-1)} + \alpha(\phi_i^{(m)} - \phi_i^{(m-1)}) \qquad (2.2\text{-}13)$$

Ostrowski's theorem states that, for $0<\alpha<2$, convergence to the solution is guaranteed[86] provided matrix A is symmetric and positive definite. In practice α is always set greater than unity so the method is referred to as successive over-relaxation. (S.O.R.)

Choosing the optimum value for α is not easy. Explicit formulae can be written for square and rectangular regions[87] but not for general regions. For these it can however be shown that[81]

$$\alpha_{opt} = \frac{2}{1+\sqrt{(1-\lambda)}} \qquad (2.2\text{-}14)$$

where

$$\lambda = \lim_{n\to\infty} \frac{R^{n+1}}{R^n} \qquad (2.2\text{-}15)$$

and R^n is the modulus of the maximum residual (see next paragraph) after the n^{th} iteration with α equal to unity. Using these formulae, Carre[88] describes a method of updating α as the computation progresses. When using such a method though, it is wise to check that the computational

effort involved in improving α does not exceed the time saved by the improved rate of convergence. In the authors's experience α_{opt} lies between 1.7 and 1.8 for many field problems and the savings in computing time effected by accurately optimising α are not great.

To assess the accuracy with which the solutions fit the set of simultaneous equations the residual at each node can be evaluated. This is given by the difference between the value calculated for a node by the appropriate equation and the current solution at that node. Hence for the i^{th} node after the m^{th} iteration the residual is

$$R_i^{(m)} = \frac{b_i}{a_{ii}} - \sum_{j=1}^{i-1} \frac{a_{ij}\phi_j^{(m)}}{a_{ii}} - \sum_{j=i+1}^{n} \frac{a_{ij}\phi_j^{(m)}}{a_{ii}} - \phi_i^{(m)} \qquad (2.2\text{-}16)$$

When using the S.O.R. method the iterations are terminated when either the sum of the residuals or the magnitude of the largest or preferrably both are reduced below a specified level.

When either a complex source term or a complex operator is involved the solution is less straightforward. Stoll[89] shows that the optimum accelerating factor will, in general, be complex and points out that, if α is real, the solution may not converge even with a value as low as 1.5. He gives curves for a two dimensional region of 11 x 11 nodes that show the behaviour of the solution to be tolerant of small underestimates of the real part of α and small overestimates of the imaginary part but to oscillate violently if the reverse is the case. Oscillations attributable to overestimating the real part of α can however be damped down to some extent by increasing the imaginary part of α. He used a complex form of the method used by Carre[88] to obtain his estimates.

In view of the difficulties that can be experienced obtaining convergence of complex solutions it was considered unwise to pursue iterative methods especially as adequate direct methods are now available. This opinion was endorsed by the claims of Galloway, Ryan and Scott[90] that convergence, even for real fields, can be elusive if large differ-

ences in mesh size or permittivity are involved. A direct method was therefore adopted.

Direct methods

The traditional method of Gaussian elimination is still probably the most used method of solving sets of simultaneous equations. The matrix A of the equation

$$A\,\underline{x} = \underline{b} \qquad (2.2\text{-}17)$$

is converted to upper triangular form with the elements on the leading diagonal equal to unity by systematic elimination of the elements below the diagonal. The solution is then obtained by backward substitution. To obtain the highest solution accuracy, especially if the equations are ill conditioned due to matrix A being nearly singular, pivotting strategies can be used.[91] When dealing with the sparse, banded coefficient matrices generated by the finite difference method this can produce a considerable increase in the bandwidth of the matrix. As this greatly increases the computational effort involved in the solution it is best avoided even if double precision arithmetic has to be used to maintain accuracy.

Other methods of solution are available that enable substantial economies in computing time to be effected in particular circumstances. For symmetric matrices savings of upto fifty percent can be made by the use of symmetric Choleski factorisation.[92] The coefficient matrix is expressed as

$$A = L\,L^{T} \qquad (2.2\text{-}18)$$

where L is a lower triangular matrix and the elements of L are given by

$$e_{ij} = \left(a_{ij} - \sum_{k=1}^{j-1} e_{ik}e_{jk}\right)/e_{jj} \qquad j<i \qquad (2.2\text{-}19)$$

$$e_{ii} = \left\{a_{ii} - \sum_{k=1}^{i-1} e_{ik}^{2}\right\}^{\frac{1}{2}} \qquad (2.2\text{-}20)$$

Applying (2.2-18) to (2.2-17)

$$L\,L^T\,\underline{x} = \underline{b} \qquad (2.2\text{-}21)$$

or $$L\,\underline{y} = \underline{b} \qquad (2.2\text{-}22)$$

where $$L^T\,\underline{x} = \underline{y} \qquad (2.2\text{-}23)$$

Vector $\underline{y}$ is readily obtained using equation (2.2-22) and $\underline{x}$ likewise using (2.2-23).

Providing A is positive definite the term under the square root sign in equation (2.2-20) is always positive and therefore all the elements of L are real. However, if A is not positive definite, there is no such guarantee and Walsh[93] claims the method can be numerically unstable. In view of the nature of the field problems that were to be tackled it was considered prudent not to pursue the method but to use a form of Gaussian elimination specially adapted to banded systems. Before describing it mention of matrix inversion should be made. Several efficient numerical methods are available including Crout factorization, Zollenkopf bi-factorization,[94] partitioning and the method of Shipley and Coleman. However unless solutions for more than one right hand side vector are required the increased computational effort cannot be justified.

The Gaussian elimination scheme used was a modified form of the method developed by Gibson[95] for studying the heating of metal slabs in induction furnaces. His difference equations also involved complex coefficients as the magnetic parts of the calculations required differentials with respect to time of time harmonic quantities. The method makes full use of the symmetrical and banded nature of the matrix to reduce computation time and storage to the minimum.

Figure 2.2-3 illustrates the arrangement of the nodes used and the form of the boundary conditions. The upper and lower boundaries are Dirichlet and the axis of symmetry c - d is homogeneous Neumann. As the regions analysed are unbounded, the fourth boundary is placed sufficiently far from all non uniformities that the field in its vicinity can be considered uniform. The outward flux through it is therefore zero and the boundary can also be considered homogeneous Neumann.

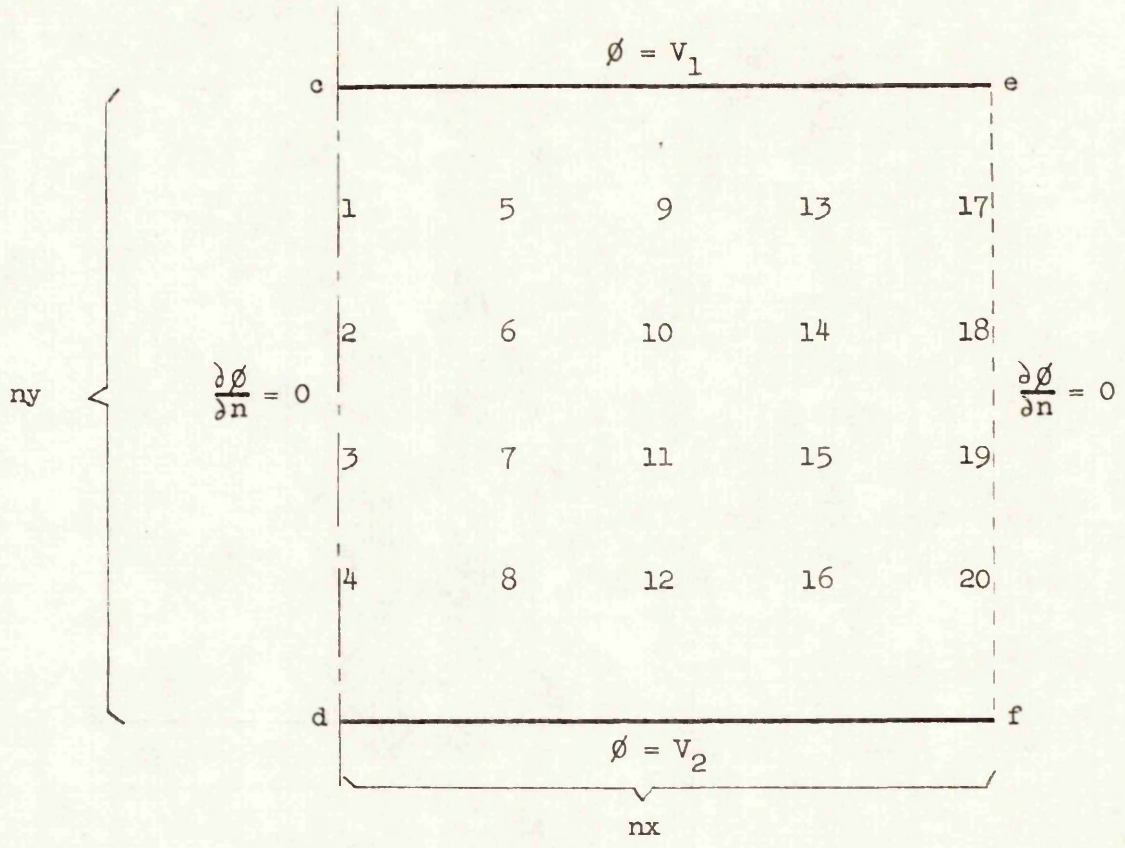

Figure 2.2-3 Arrangement of finite difference nodes.

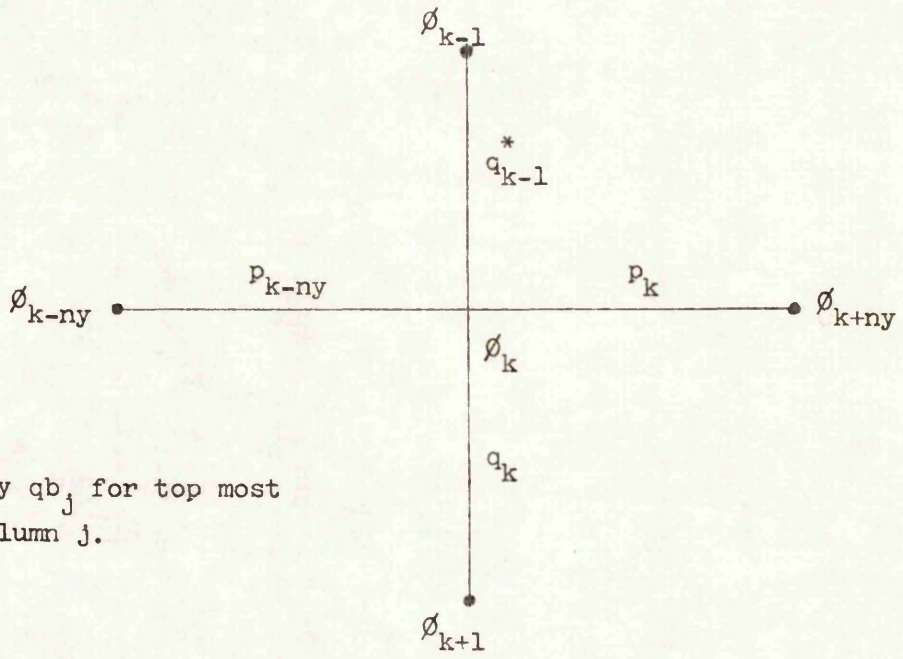

* Replaced by qb_j for top most node in column j.

Figure 2.2-4 General nodal star of figure 2.2-3

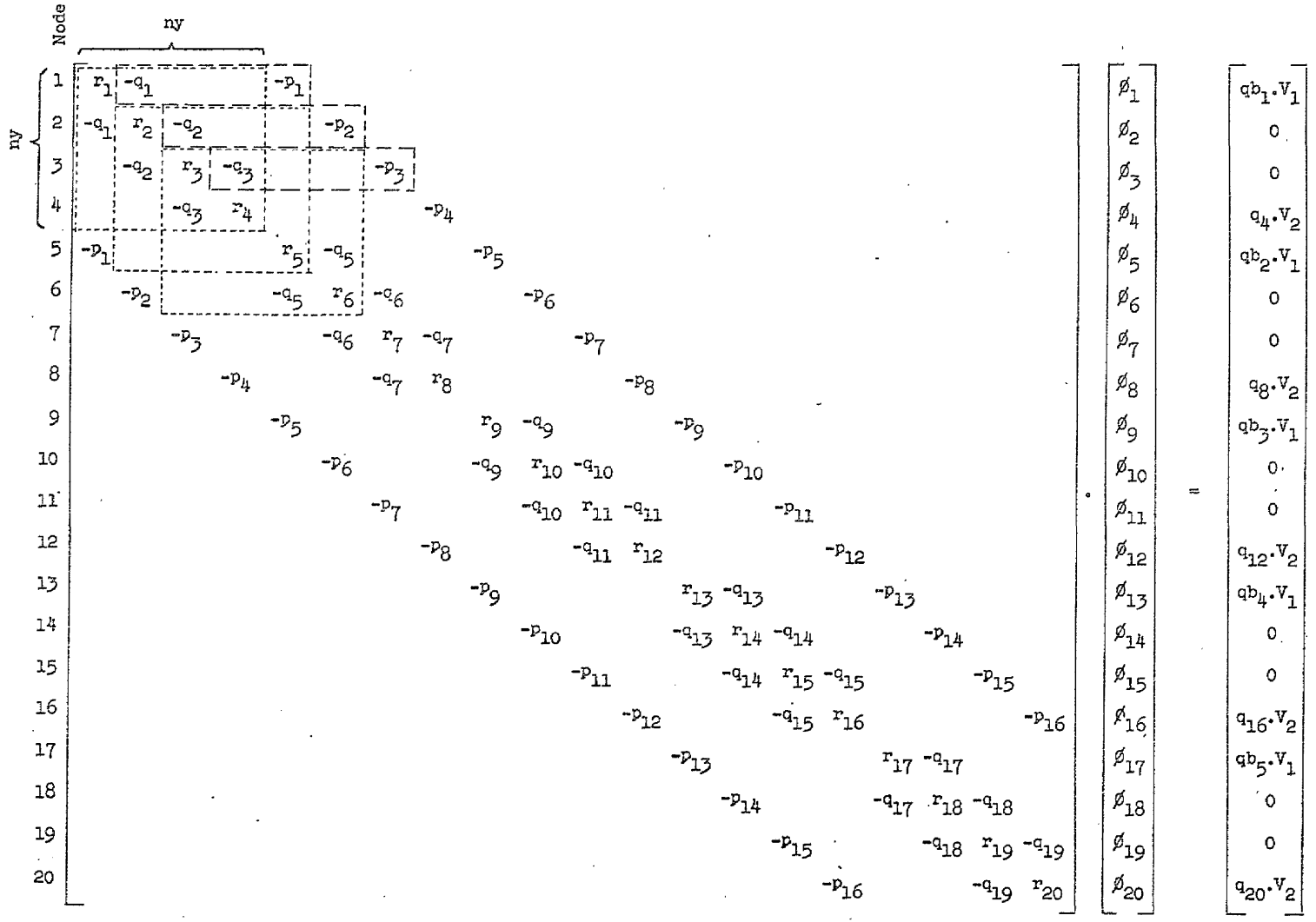

Figure 2.2-5 Matrix representation of the finite difference equations.

With reference to figure 2.2-4 the finite difference equation for the general node k, assuming a Laplacian field, can be seen to be

$$-p_{k-ny}\phi_{k-ny} - q_{k-1}\phi_{k-1} + r_k\phi_k - q_k\phi_{k+1} - p_k\phi_{k+ny} = 0 \qquad (2.2\text{-}24)$$

where $$r_k = p_{k-ny} + p_k + q_{k-1} + q_k \qquad (2.2\text{-}25)$$

These equations require modification at nodes adjacent to boundaries as some terms will be absent whilst others will generate the source terms that constitute the vector $\underline{b}$ of equation (2.2-17). The complete matrix representation of the finite difference equations is shown in figure 2.2-5. The symmetric and banded nature of the coefficient matrix is clearly apparent and the elements can be seen to form a regular pattern. It will also be noticed that the simple node numbering scheme produces a constant bandwidth rendering variable bandwidth techniques, such as that given by Jennings and Tuff,[96] unnecessary.

To effect a solution the algorithm commences by forming a square submatrix W (shown dotted) of dimension ny containing the elements in the top left hand corner of matrix A. The first equation, including the right hand side, is divided by a_{11} to reduce the diagonal element to unity and the resulting elements $a_{1,2}$ to $a_{1,1+ny}$ (shown dashed) are stored. Using the first equation all elements in the first column of A are now reduced to zero by elimination and, at the same time, W is moved one step down the diagonal of A to accommodate the new values of the elements of A so generated. The procedure is then repeated to reduce the second diagonal element of A to unity and the resulting coefficients a_{23} - $a_{a,a+ny}$ are stored as before. The second column of A can thus be cleared of non-zero elements by elimination and the algorithmic loop can be continued until W has travelled down the entire length of the diagonal and rests in the bottom right hand corner of matrix A. As the dimension of W is so much less than that of A, standard Gaussian elimination can be used to eliminate the remaining non-zero elements below the diagonal whereupon all the node values can be rapidly obtained by back substitution.

The largest computational array is that required to store the elements of the banded, upper triangular matrix. This contains $ny^2(nx - 1)$ elements and, for large problems, needs to be transferred to the large core memory of the computer. It is more efficient to do this using block transfers and so an additional array of dimension $(ny)^2$ is used to permit the transfer of ny lines at a time, the large core memory requirement being reduced correspondingly. A further point to note is that no array is needed to store the matrix $\emptyset$ as the solutions can displace the elements of b as back substitution proceeds. It is clear that for efficiency in terms of both computer time and store requirements ny should be kept as small as possible and certainly less than nx. This is checked by the subroutine in addition to comprehensive checks on array bounds. Using a CDC 7600 computer a typical solution time was approximately 1.5 seconds for a 920 node problem. (nx = 40, ny = 23) The machine has a 60 bit word length and the maximum value of residual obtained for the above solution was less than 1 part in 10^{13}. The algebraic sum of the residuals was less than 1 part in 10^{11}.

Diagonal links in finite difference grid

It has already been pointed out that semiconducting films can be accommodated by including additional terms in equation (2.2-3). It is not necessary to restrict these to the directions of the four arms of the basic finite difference star and diagonal films such as those shown in figure 2.2-6 are easily included.

Equation (2.2-24) now takes the form

$$-g_{k-ny-1}\emptyset_{k-ny-1} - p_{k-ny}\emptyset_{k-ny} - f_{k-ny+1}\emptyset_{k-ny+1} - q_{k-1}\emptyset_{k-1} + r_k\emptyset_k - q_k\emptyset_{k+1} - f_k\emptyset_{k+ny-1} - p_k\emptyset_{k+ny} - g_k\emptyset_{k+ny+1} = 0 \qquad (2.2\text{-}26)$$

where

$$r_k = p_{k-ny} + p_k + q_{k-1} + q_k + f_{k-ny+1} + f_k + g_{k-ny-1} + g_k \qquad (2.2\text{-}27)$$

If either g_{k-ny-1} or g_k are non-zero the bandwidth of the coefficient matrix (and hence the solution time) is increased. This is clearly illus-

trated in figure 2.2-7 which also shows the increased size of the computational arrays needed to effect a solution.

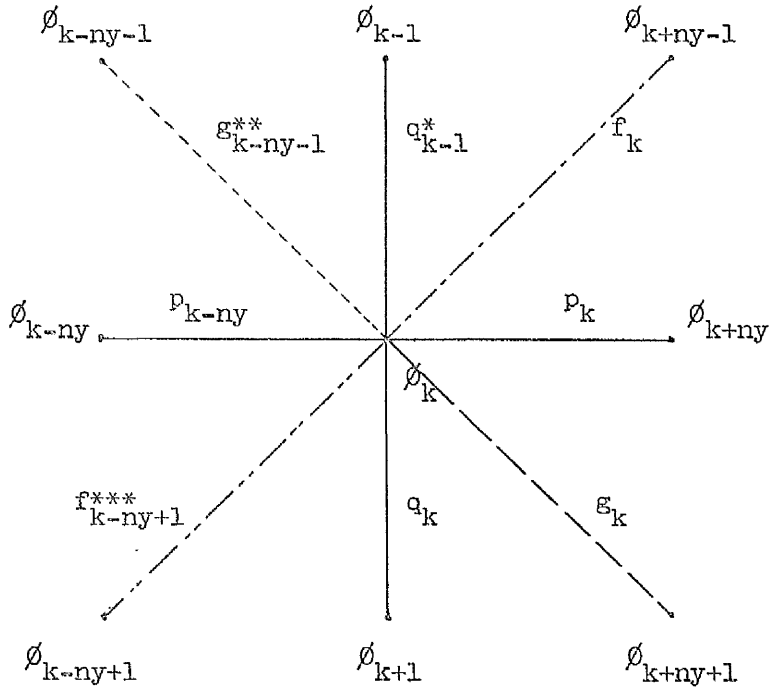

* Replaced by qb_j for top-most node in column j

** Replaced by gb_{j-1} for top-most node in column j

*** Replaced by fb_{j-1} for bottom-most node in column j

Figure 2.2-6 General node of figure 2.2-3 with diagonal links.

When diagonal elements dictate an increase in matrix bandwidth, this can be put to good effect by using the nine node finite difference representation of the Laplacian operator.[97] Such a representation enables additional terms in the Taylor series expansion of the field at each node to be included with consequent reduction of the truncation error. However the additional complication proved unnecessary for the field problems solved in this study.

Calculation of capacitance and loss

The net charge on a conductor in a field region can be obtained using Gauss's theorem (equation 2.2-2) and, for loss-less problems, the overall capacitance of that conductor, with respect to the other conductors of the system, is given by $C = Q/V$ where V is the voltage required to

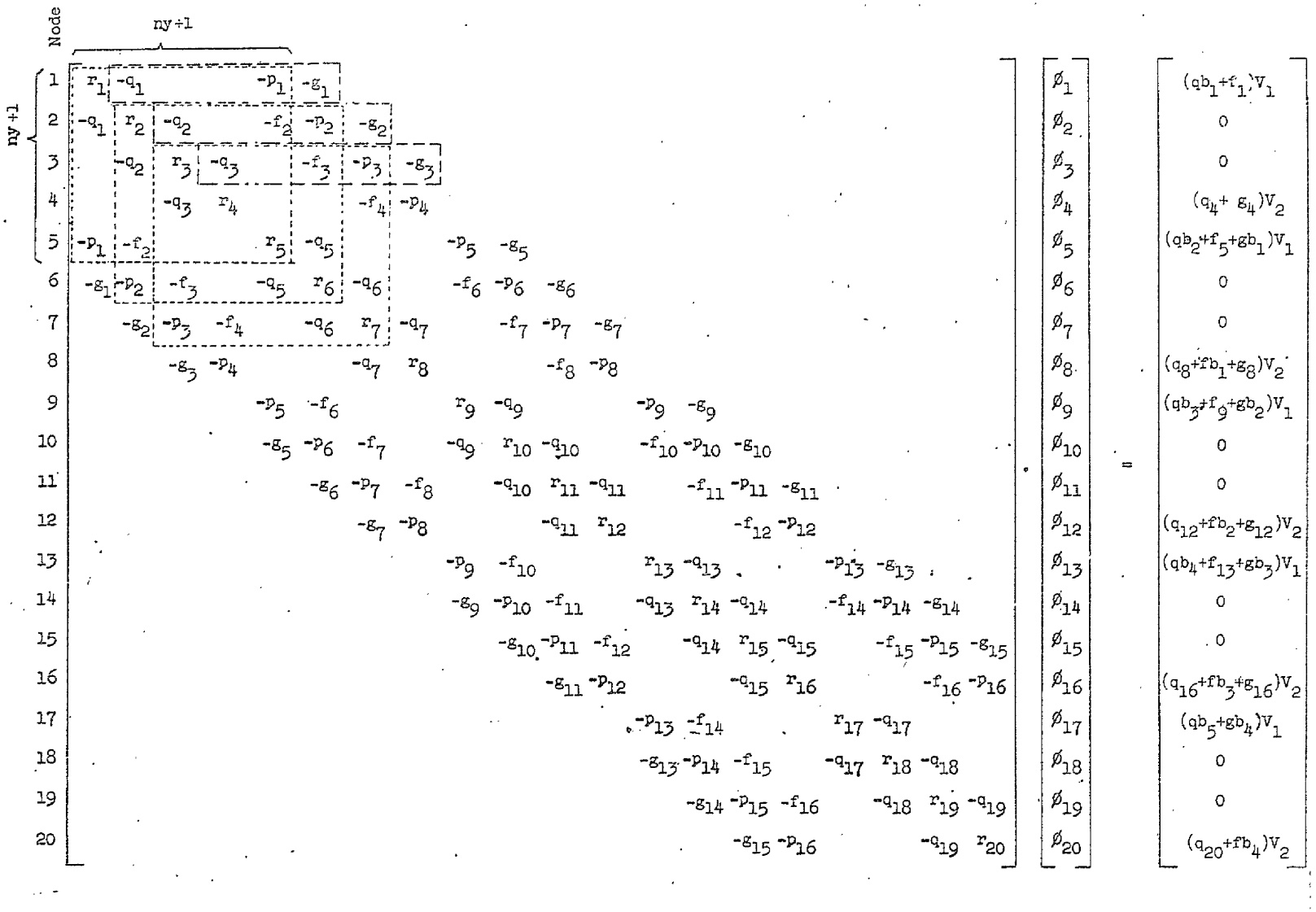

Figure 2.2-7 Matrix representation of the finite difference equations with diagonal elements.

impress the net charge Q. As the displacement flux between node i and adjacent node j is given by $-a_{ij}(\phi_i - \phi_j)$ the integral can be obtained by summation along any contour enclosing the conductor.[98] However for accuracy the contour should be arranged to avoid regions with high rates of change of flux density.

For time harmonic problems involving loss, the flux will, in general, be complex. If the net flux leaving a conductor is represented by

$$\text{div } D = D_o e^{j(\omega t+\phi)} \qquad (2.2\text{-}28)$$

the displacement current

$$I = \frac{\partial(\text{div}D)}{\partial t} = j\omega D_o e^{j(\omega t+\phi)} \qquad (2.2\text{-}29)$$

If the impressed voltage is

$$V = V_o e^{j(wt + \theta)} \qquad (2.2\text{-}30)$$

then the admittance is given by

$$Y = \frac{I}{V} = \frac{j\omega D_o}{V_o} e^{j(\phi - \theta)} \qquad (2.2\text{-}31)$$

But $Y = G + jS = G + j\omega C$.

Therefore $$C = S/\omega \qquad (2.2\text{-}32)$$

and $$\tan\delta = G/S \qquad (2.2\text{-}33)$$

2.3 Method of Finite Elements

The solution of the differential equation describing a field problem can be approximated by combinations of known functions with suitable coefficients. These coefficients can be determined by the methods of weighted residuals[99] of which the collocation and Galerkin methods represent particular choices of weighting function. Alternatively variational principles may be used. The former involves working directly with the differential equation and boundary conditions whereas solution by the latter is obtained through the use of a functional related to the differential equation and boundary conditions. The variational approach, involving the maximizing or minimizing of some physical parameter, is not universally applicable but, for those problems where it is, it provides a

powerful method of solution. This is the case with electrostatic field problems where the functional, representing the potential energy, is minimized to obtain a solution. As the functional has a stationary point at its minimum, small deviations from the true solution have a minimal effect on its value. Therefore values for the system capacitance obtained directly from the functional are inherently more accurate than those obtained by contour integration within the field region.

The principle disadvantage of the variational method when used on its own stems from the limited number of trial functions that it is practical to include when approximating the solution. This results in poor field representations especially along boundaries and in the vicinity of abrupt changes of permittivity within the dielectric. The former may be overcome by limiting trial functions to ones that fit the specified boundary conditions but this is possible in relatively few cases. The method of finite elements overcomes these difficulties by dividing the field region up into elements and applying the variational technique to each of these in turn. Provided the elements are suitably chosen, accurate representations of the field in each can be achieved with only a small number of trial functions. The 'creases' in the 'potential surface' at abrupt changes in permittivity are readily accommodated by making these discontinuities coincide with element boundaries. The problem then reduces to relating the corresponding boundary conditions on either side of the discontinuities. A further important advantage of the method is that regions of interest can be examined in greater detail by locally using smaller elements. If, at the same time, larger elements can be tolerated in other regions the computational effort required need not increase. For these reasons the method is favoured for the solution of field problems. Its use is described by Desai and Abel,[100] Strang and Fix,[101] Wexler[83] and Zienkiewicz[102] whilst many of the mathematical concepts employed are treated by Mikhlin.[103]

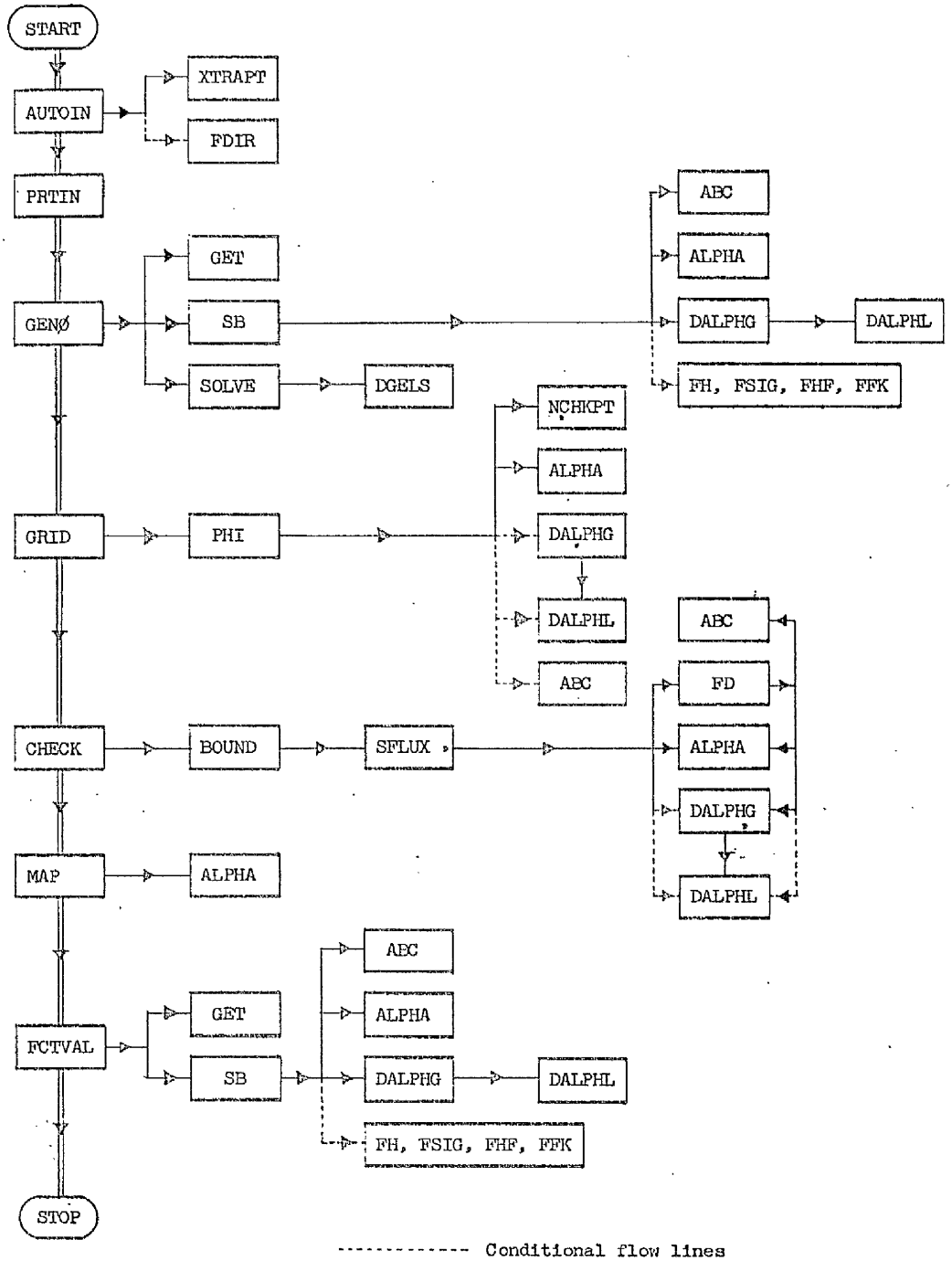

Figure 2.3-1 Subprogram flow diagram of MANFEP for deterministic problems.

Description of basic program

The programs used were modifications of MANFEP (University of Manitoba Finite Element Program) so a description of this program will be given. The flow diagram for deterministic problems having only one solution (i.e. not eigenvalue problems) is given in figure 2.3-1.

Specification of field region

The first subroutine to be called, AUTOIN, reads the input data and concurrently writes it on the output file for reference. The field region is divided up into triangular elements and the input data specifies the positions of the nodes, numbers them and establishes which nodes form the vertices of the respective triangular elements. The boundary conditions are also specified for each triangle side forming part of the problem boundary. These can be of three types:

Dirichlet $$\phi(s) = g(s) \qquad (2.3\text{-}1)$$

Neumann $$k(s)\left(\frac{\partial \phi}{\partial n}\right)_s = h(s) \qquad (2.3\text{-}2)$$

or Mixed $$k(s)\left(\frac{\partial \phi}{\partial n}\right)_s + \sigma(s)\,\phi(s) = h(s) \qquad (2.3\text{-}3)$$

With a Dirichlet boundary, the potential is specified as a function of position whereas, for a Neumann boundary the flux density normal to the surface is given. ($\hat{n}$ is the outward pointing unit vector normal to the boundary.) A mixed boundary condition arises if the normal flux density is proportional to the difference between the potential on the surface and that external to the surface. Thus

$$k(s)\left(\frac{\partial \phi}{\partial n}\right)_s = \sigma(s)\,(\phi(s) - \phi_o(s)) \qquad (2.3\text{-}4)$$

which is of the form given by (2.3-3). In the program Neumann boundaries are treated as mixed ones with $\sigma(s) = 0$. Also any boundary that is not specified to the contrary is assumed to be homogeneous Neumann with $h(s) = 0$.

Isoparametric elements

The field in each element is approximated by an N^{th} order interpolatory polynomial

$$\phi(x,y) = \sum_{i+j\leq N} c_{ij} x^i y^j \qquad (2.3\text{-}5)$$

and the program is required to calculate the values of the coefficients c_{ij} that provide the closest approximation to the true solution. The number of coefficients is given by

$$M = (N+1)(N+2)/2 \qquad (2.3\text{-}6)$$

Equation (2.3-5) can be rewritten to express the potential $\phi(x,y)$ in terms of the potentials at M nodes within the element. If these are given by

$$\phi_i = \phi(x_i,y_i) \qquad i = 1,2,\ldots,M \qquad (2.3\text{-}7)$$

substituting the cooordinates of each node into (2.3-5) in turn yields a set of equations from which the c's can be eliminated. Equation (2.3-5) now becomes

$$\phi(x,y) = \sum_{i=1}^{M} \alpha_i(x,y)\, \phi_i \qquad (2.3\text{-}7a)$$

where the coefficients α are known as shape functions. The shape functions derived by the method just described are not the only ones to be acceptable, in fact, any set of functions capable of representing a linear variation of the field and possessing the property

$$\alpha_i(x_j,y_j) = \delta_{ij} \qquad (2.3\text{-}8)$$

is acceptable. Shape functions of the Lagrange[102] type are used in the program.

The numerical aspects of the finite element technique are greatly eased if the analysis can be restricted to a single, standard element and this can be achieved if suitable transformations are available to transform between the standard element and the actual elements. Equation (2.3-7a) defines the potential at the point (x,y) in terms of the potentials at the nodes. This suggests that a similar equation can be written defining the position (x,y) of the point (ξ,η) in the standard element in terms of the coordinates (x_i,y_i) of the nodes. We have then

$$x = \sum_{i=1}^{M} \alpha_i(\xi,\eta)\, x_i \qquad (2.3\text{-}9a)$$

$$y = \sum_{i=1}^{M} \alpha_i(\zeta,\eta) y_i \qquad (2.3\text{-}9b)$$

The standard, or local, triangular element is normally chosen to be the simplex (0,1), (0,0), (1,0) in the ζ, η plane and this can be transformed to a triangular element in the x,y (or global) plane using three nodes only. However global elements with curved sides can be mapped if more nodes are used. Depending on whether the number of nodes used to map the elements is less than, equal to or greater than the number used to interpolate the field potentials, the elements are described as subparametric, isoparametric or superparametric. Isoparametric elements are used in this program and, since the same nodes are used for both mapping and field interpolation, the same shape functions can be employed.

The choice of node positions is governed by the need for continuity of potential at the interface between two adjacent elements. For elements described by N^{th} order interpolatory polynomials, this condition is met if there are (N+1) common nodes along the boundary. The node positions used are shown in figure 2.3-2. A square grid is used in the local plane for convenience and corresponding Lagrange shape functions are given in table 2.3-1. These shape functions are calculated by subroutine ALPHA in the program. In the global plane, the node positions of straight sided elements are chosen to maintain the same proportions as those used in the local plane. The extra nodes required for the specified value of N are generated automatically by subroutine XTRAPT from the coordinates of the vertex nodes. The subroutine establishes which nodes are common to two elements and also sets the appropriate values for nodes where Dirichlet boundary conditions are enforced.

Having established in the program the number and position of all the nodes required to represent the field region, the position of individual nodes may be altered to accommodate curved boundaries. The new coordinates are read from the data by AUTOIN. Following this details are read of any nodes, common to more than one element, that can assume

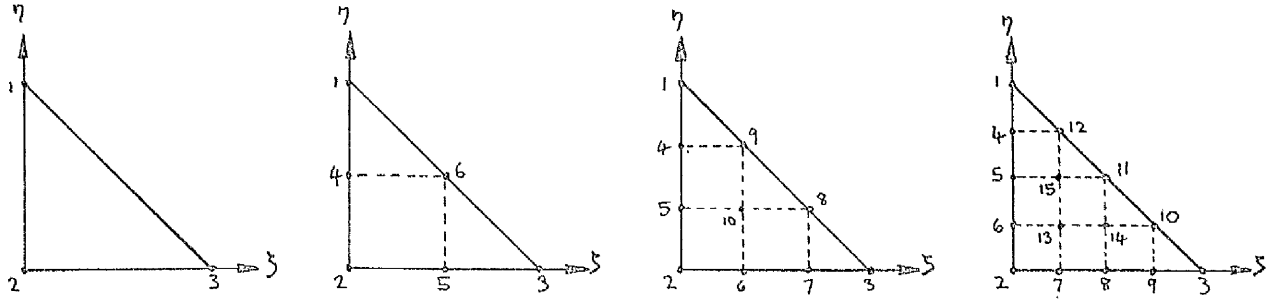

N=1, M=3 N=2, M=6 N= 3, M=10 N=4, M=15

Figure 2.2-2 Position of nodes in local element.

Table 2.3-1 Shape functions $\alpha_i(\xi,\eta)$

i	N = 1	N = 2	N = 3	N = 4
1	L_1	$L_1(2L_1-1)$	$\frac{1}{2}L_1(3L_1-1)(3L_1-2)$	$L_1(4L_1-1)(4L_1-2)(4L_1-3)/6$
2	L_2	$L_2(2L_2-1)$	$\frac{1}{2}L_2(3L_2-1)(3L_2-2)$	$L_2(4L_2-1)(4L_2-2)(4L_2-3)/6$
3	L_3	$L_3(2L_3-1)$	$\frac{1}{2}L_3(3L_3-1)(3L_3-2)$	$L_3(4L_3-1)(4L_3-2)(4L_3-3)/6$
4		$4L_1L_2$	$9L_1L_2(3L_1-1)/2$	$8L_1L_2(4L_1-1)(4L_1-2)/3$
5		$4L_2L_3$	$9L_1L_2(3L_2-1)/2$	$4L_1L_2(4L_1-1)(4L_2-1)$
6		$4L_3L_1$	$9L_2L_3(3L_2-1)/2$	$8L_1L_2(4L_2-1)(4L_2-2)/3$
7			$9L_2L_3(3L_3-1)/2$	$8L_2L_3(4L_2-1)(4L_2-2)/3$
8			$9L_3L_1(3L_3-1)/2$	$4L_2L_3(4L_2-1)(4L_3-1)$
9			$9L_3L_1(3L_1-1)/2$	$8L_2L_3(4L_3-1)(4L_3-2)/3$
10			$27L_1L_2L_3$	$8L_1L_3(4L_3-1)(4L_3-2)/3$
11				$4L_1L_3(4L_1-1)(4L_3-1)$
12				$8L_1L_3(4L_1-1)(4L_1-2)/3$
13				$32L_1L_2L_3(4L_2-1)$
14				$32L_1L_2L_3(4L_3-1)$
15				$32L_1L_2L_3(4L_1-1)$

where $L_1 = \eta$, $L_2 = 1 - \xi - \eta$, $L_3 = \xi$

different values in the respective elements. (Such a situation will arise, for instance, with a 180 degree bend in a flow channel when nodes occupying nominally the same position but on different sides of the bend have different

values.) The subroutine then reads details of any filamentary elements included in the field region (to be discussed later) and any groups of nodes which are to be forced to assume the same potential. The latter situation would arise, for instance, in electrostatic problems when there are foil inclusions in insulation for stress sharing purposes. Finally, for Dirichlet boundaries not having a constant value along their length, the subroutine establishes the required node values using the function subprogram FDIR. Subroutine PRTIN prints the node coordinates and gives the numbers of the nodes in each element. It also details the specified boundary conditions and the parameters of any filamentary elements.

Minimization of the functional

Equation (2.1-18) can be expressed as

$$L\phi = \rho \qquad (2.3\text{-}10)$$

where L is given by

$$L = -\frac{\partial}{\partial x}\left(a\frac{\partial \phi}{\partial x} + b\frac{\partial \phi}{\partial y}\right) - \frac{\partial}{\partial y}\left(b\frac{\partial \phi}{\partial x} + c\frac{\partial \phi}{\partial y}\right) + d\phi \qquad (2.3\text{-}11)$$

The additional term, $d\phi$, has been included to cover time harmonic wave propagation problems involving solutions of the Helmholtz equation.

Using Euler's theorem a corresponding functional can be written for equation (2.3-10) such that the function $\phi(x,y)$ required to minimize the functional is the solution of the differential equation. The functional, given by Wexler,[83] is

$$F = \iint\left[a\left(\frac{\partial \phi}{\partial x}\right)^2 + 2b\frac{\partial \phi}{\partial x}\frac{\partial \phi}{\partial y} + c\left(\frac{\partial \phi}{\partial y}\right)^2 + d\phi^2 - 2\phi\rho\right]dxdy + \int_c(\sigma\phi^2 - 2h\phi)ds \qquad (2.3\text{-}12)$$

The line integral includes all sections of the field region boundary where Neumann or mixed boundary conditions are specified as given by equations (2.3-2) and (2.3-3). It will be noticed that any Dirichlet boundary conditions of the form given in equation (2.3-1) do not enter into the expression for the functional. Instead they restrict the range of trial functions as any function chosen must satisfy these conditions.

For a Laplacian problem in a homogeneous isotropic region with only Dirichlet and homogeneous Neumann (h = 0) boundary conditions the expression for the functional reduces to

$$F = a\iint \left[\left(\frac{\partial \phi}{\partial x}\right)^2 + \left(\frac{\partial \phi}{\partial y}\right)^2\right] dxdy \qquad (2.3\text{-}13)$$

As the energy within a dielectric region is given by

$$U = \tfrac{1}{2}\int \underline{D} \cdot \underline{E}\, d\tau \qquad (2.3\text{-}14)$$

it is evident that the value obtained for the two dimensional functional using (2.3-13) is equal to twice the energy stored in unit depth of a three dimensional region with ϕ independent of the z-coordinate. The capacitance of the system can therefore be obtained directly from the value of the functional. Returning to equation (2.3-12) the similarity in the contributions to the functional of the source term (ρ) (involving ρ) and the Neumann term (h) (involving h) will be noticed. This is to be expected as the former represents a distribution of charges within the region and the latter the equivalent of a charge distribution along the boundary.

From (2.3-7a) and (2.3-9a/b) for each finite element

$$\phi(x,y) = \sum_{i=1}^{M} \alpha_i(\xi,\eta)\, \phi_i \qquad 2.3\text{-}15)$$

Substituting this expression in (2.3-12) gives the functional in terms of the node potentials. The resultant approximation can be minimized using [83] the Rayleigh - Ritz procedure whereby the functional is differentiated with respect to each node potential in turn and the resultant expressions set equal to zero. Thus

$$\frac{\partial F}{\partial \phi_i} = 0 \qquad i = 1,2,\ldots\ldots,M \qquad (2.3\text{-}16)$$

where

$$\frac{\partial F}{\partial \phi_i} = 2\iint \left\{ a(x,y)\left(\sum_{j=1}^{M} \frac{\partial \alpha_j}{\partial x}\phi_j\right)\frac{\partial \alpha_i}{\partial x} + b(x,y)\left[\left(\sum_{j=1}^{M} \frac{\partial \alpha_j}{\partial x}\phi_j\right)\frac{\partial \alpha_i}{\partial y} + \left(\sum_{j=1}^{M} \frac{\partial \alpha_j}{\partial y}\phi_j\right)\frac{\partial \alpha_i}{\partial x}\right] + \right. \qquad (2.3\text{-}17)$$

$$\left. c(x,y)\left(\sum_{j=1}^{M} \frac{\partial \alpha_j}{\partial y}\phi_j\right)\frac{\partial \alpha_i}{\partial y} + d(x,y)\left(\sum_{j=1}^{M} \alpha_j \phi_j\right)\alpha_i - \rho(x,y)\alpha_i \right\} dxdy + 2\int \left\{ \sigma(s)\left(\sum_{j=1}^{M} \alpha_j \phi_j\right)\alpha_i \right.$$

$$\left. - h(s)\alpha_i \right\} ds$$

As each equation involves the potentials of the nodes associated with the particular element a set of simultaneous equations is produced

$$\sum_{j=1}^{M} s_{ij} \phi_j = b_i \qquad i = 1,2,\ldots,M \qquad (2.3\text{-}18)$$

or, in matrix form, $$s \underline{\phi} = \underline{b} \qquad (2.3\text{-}19)$$

The elements of the vector $\underline{b}$ originate from the source distribution and inhomogeneous Neumann terms. Also, where a node is located on a Dirichlet boundary its value is specified and it cannot therefore act as a variational parameter. As a consequence, if the boundary is inhomogeneous additional terms will be contributed to $\underline{b}$.

All integrations are performed in the local plane over the simplex (0,1), (0,0), (1,0) using the Gaussian Quadrature method.

In order to transform (2.3-17) to $\zeta - \eta$ coordinates the global derivatives of the shape functions require transformation to local derivatives. Now

$$\begin{bmatrix} \frac{\partial \alpha_i}{\partial x} \\ \frac{\partial \alpha_i}{\partial y} \end{bmatrix} = J^{-1} \begin{bmatrix} \frac{\partial \alpha_i}{\partial \zeta} \\ \frac{\partial \alpha_i}{\partial \eta} \end{bmatrix} \qquad (2.3\text{-}20)$$

where the Jacobian matrix J is given by

$$J = \begin{bmatrix} \frac{\partial x}{\partial \zeta} & \frac{\partial y}{\partial \zeta} \\ \frac{\partial x}{\partial \eta} & \frac{\partial y}{\partial \eta} \end{bmatrix} = \begin{bmatrix} J_{11} & J_{12} \\ J_{21} & J_{22} \end{bmatrix} \qquad (2.3\text{-}21)$$

Substituting for x and y using (2.3-9), this may be expressed as

$$J = \begin{bmatrix} \frac{\partial \alpha_1}{\partial \zeta} & \frac{\partial \alpha_2}{\partial \zeta} & \cdots & \frac{\partial \alpha_M}{\partial \zeta} \\ \frac{\partial \alpha_1}{\partial \eta} & \frac{\partial \alpha_2}{\partial \eta} & \cdots & \frac{\partial \alpha_M}{\partial \eta} \end{bmatrix} \begin{bmatrix} x_1 & y_1 \\ x_2 & y_2 \\ \vdots & \vdots \\ x_M & y_M \end{bmatrix} \qquad (2.3\text{-}22)$$

The local derivatives can be obtained from table 2.3-1 using

$$\frac{\partial \alpha_i}{\partial \zeta} = \sum_{j=1}^{3} \frac{\partial \alpha_i}{\partial L_j} \frac{\partial L_j}{\partial \zeta}$$

$$\frac{\partial \alpha_i}{\partial \eta} = \sum_{j=1}^{3} \frac{\partial \alpha_i}{\partial L_j} \frac{\partial L_j}{\partial \eta} \qquad (2.3\text{-}23)$$

Expressing the Jacobian in the form of (2.3-22) has the advantage that the matrix of local derivatives need only be evaluated once for each Gauss integration point in the local plane. The Jacobian can then be found for any point in the global plane from post multiplication by the appropriate node coordinates. Using (2.3-20) the transformation from global to local derivatives is given by

$$\begin{bmatrix} \frac{\partial \alpha_i}{\partial x} \\ \frac{\partial \alpha_i}{\partial y} \end{bmatrix} = \frac{\begin{bmatrix} J_{22} & -J_{12} \\ -J_{21} & J_{11} \end{bmatrix}}{\det|J|} \begin{bmatrix} \frac{\partial \alpha_i}{\partial \zeta} \\ \frac{\partial \alpha_i}{\partial \eta} \end{bmatrix} \qquad (2.3\text{-}24)$$

The differential area dxdy can be transformed into local coordinates by considering the differential cell formed by the vectors $d\bar{r}_\zeta$ and $d\bar{r}_\eta$ in the x - y plane where

$$d\bar{r}_\zeta = \hat{i}\frac{\partial x}{\partial \zeta}d\zeta + \hat{j}\frac{\partial y}{\partial \zeta}d\zeta = \hat{i}\,J_{11}d\zeta + \hat{j}\,J_{12}d\zeta \qquad (2.3\text{-}25)$$

$$d\bar{r}_\eta = \hat{i}\frac{\partial x}{\partial \eta}d\eta + \hat{j}\frac{\partial y}{\partial \eta}d\eta = \hat{i}\,J_{21}d\eta + \hat{j}\,J_{22}d\eta \qquad (2.3\text{-}26)$$

The differential area is

$$d(\text{area}) = d\bar{r}_\zeta \times d\bar{r}_\eta = \hat{k}\,(J_{11}J_{22} - J_{21}J_{12})d\zeta d\eta \qquad (2.3\text{-}27)$$

which is numerically equal to $\det|J|\,d\zeta d\eta$.

When performing the contour integration the transformation of ds depends on which side of the simplex is being traversed. Between (0,0) and (1,0) $d\eta = 0$ and

$$ds = \left\{J_{11}^2 + J_{12}^2\right\}^{\frac{1}{2}}d\zeta \qquad (2.3\text{-}28)$$

from (2.3-25). Similarly between (0,0) and (0,1) $d\zeta = 0$ and

$$ds = \left\{J_{21}^2 + J_{22}^2\right\}^{\frac{1}{2}}d\eta \qquad (2.3\text{-}29)$$

from (2.3-26). When integrating along the hypotenuse $d\zeta = -d\eta$ and

$$d\bar{r} = \hat{i}\,(J_{11} - J_{21})\,d\zeta + \hat{j}\,(J_{12} - J_{22})\,d\zeta \qquad (2.3\text{-}30)$$

Therefore $$ds = \left\{\left[(J_{11} - J_{21})^2 + (J_{12} - J_{22})^2\right]/2\right\}^{\frac{1}{2}}ds' \qquad (2.3\text{-}31)$$

where ds' is the differential distance along the boundary in the local plane.

Referring to the flow diagram, the local derivatives of the shape

functions are generated by subroutine DALPHL. The Jacobian is calculated by DALPHG using DALPHL and the result is then used to transform the local derivatives to global. DALPHG also calculates the transforms required for the contour integration. The parameters a,b,c,d and ρ at any point in the global plane are generated by the subroutine ABC which is specific to the particular problem in hand. Likewise functions FH and FSIG supply the values of h and σ along those boundaries where the parameters are a function of position. Using these various subprograms, SB generates the s and $\underline{b}$ matrices of equation (2.3-19) for the individual elements. Subroutine GET prepares the input data required by SB.

Finite Elements

The analysis described so far enables the matrix equation (2.3-19) to be formulated for any given element and, if solved, would yield the node values required in (2.3-15). Furthermore the solution would be such that, for the limited number of trial functions used, the root mean square error in the energy would be minimised. However the inadequacies of attempting to represent the whole of a field region by one set of functions have already been enumerated. To overcome such limitations the region is divided into finite elements. This is acceptable provided continuity of potential and normal flux density can be obtained at the inter-element boundaries. For the choice of node positions used in the program, the former is ensured by constraining the nodes, common to two or more elements, to have the same values in each and Wexler[83] shows that the latter condition is satisfied as a consequence.

From (2.3-12) it is evident that the overall value of the funtional is equal to the sum of the values obtained for the individual elements.

Thus
$$F = \sum_{k=1}^{N} F_k \qquad (2.3\text{-}32)$$

where N is the number of elements and

$$\frac{\partial F}{\partial \phi_i} = \sum_{k=1}^{N} \frac{\partial F_k}{\partial \phi_i} \qquad (2.3\text{-}33)$$

It follows that the individual contributions to the overall S and $\underline{B}$ matrices can be accumulated as the computation proceeds through the separate elements. Though the summation in (2.3-33) includes all elements, ϕ_i is a variational parameter only in those elements containing node i. The other elements therefore make no contribution to the summation.

The construction of the overall S and B matrices is performed by subroutine GENO. When these are complete, subroutine SOLVE manipulates them to take account of any Dirichlet boundaries and/or equipotential node groups and then calls subroutine DGELS. This subroutine solves the resultant set of simultaneous equations by Gaussian elimination with complete pivotting and yields the potential values at the nodes.

Value of potential at any given point

In order to find the value of the potential at a point (x_o, y_o) in the global plane it is necessary to ascertain which global element contains the point and to determine the corresponding coordinates (ζ_o, η_o) in the local simplex. These requirements are satisfied by transforming the global coordinates to local for each element in turn and assigning the point to the first element that causes the transformed point to lie within, or on, the local simplex.

A linear transformation is used for elements with three straight sides but it is necessary to resort to an iterative, two dimensional Newton - Raphson method in the case of curved elements. In the latter case the error terms F_r and G_r given by

$$F_r = x_r - x_o = \left\{ \sum_{i=1}^{M} \alpha_i(\zeta_r, \eta_r)\, x_i \right\} - x_o$$

$$G_r = y_r - y_o = \left\{ \sum_{i=1}^{M} \alpha_i(\zeta_r, \eta_r)\, y_i \right\} - y_o \qquad (2.3\text{-}34)$$

are calculated. From these, improved estimates of ζ_o and η_o can be obtained by setting

$$\zeta_{r+1} = \zeta_r - (\Delta\zeta)_r; \qquad \eta_{r+1} = \eta_r - (\Delta\eta)_r \qquad (2.3\text{-}35)$$

where $(\Delta\xi)_r$ and $(\Delta\xi)_r$ are solutions to

$$\left(\frac{\partial x}{\partial \xi}\right)_{\xi_r,\eta_r} (\Delta\xi)_r + \left(\frac{\partial x}{\partial \eta}\right)_{\xi_r,\eta_r} (\Delta\eta)_r = F_r$$

$$\left(\frac{\partial y}{\partial \xi}\right)_{\xi_r,\eta_r} (\Delta\xi)_r + \left(\frac{\partial y}{\partial \eta}\right)_{\xi_r,\eta_r} (\Delta\eta)_r = G_r \qquad (2.3\text{-}36)$$

The initial estimates of ξ and η are obtained by linear transformation.

Once the global element containing the required point has been identified and the corresponding local coordinates established, the potential can be calculated from equation (2.3-15). Alternatively the x and y derivatives of the potential can be obtained from

$$\left(\frac{\partial \phi}{\partial x}\right)_{x_o,y_o} = \sum_{i=1}^{M} \left(\frac{\partial \alpha_i}{\partial x}\right)_{\xi_o,\eta_o} \phi_i$$

$$\left(\frac{\partial \phi}{\partial y}\right)_{x_o,y_o} = \sum_{i=1}^{M} \left(\frac{\partial \alpha_i}{\partial y}\right)_{\xi_o,\eta_o} \phi_i \qquad (2.3\text{-}37)$$

If the x and y components of the flux are required they are calculated from

$$\text{Flux}_x = -a \frac{\partial \phi}{\partial x} - b \frac{\partial \phi}{\partial y}$$

$$\text{Flux}_y = -b \frac{\partial \phi}{\partial x} - c \frac{\partial \phi}{\partial y} \qquad (2.3\text{-}38)$$

where all the parameters are evaluated at (x_o, y_o).

Subroutine GRID generates a regular grid of points in the (x,y) plane and the field values at these points are calculated by function PHI. Logical function NCHKPT is used to check if a point lies within or on the simplex in the local plane.

Flux calculations

Through the entry point CHECK located in subroutine AUTOIN, subroutine BOUND may be called. This calculates the potential and normal flux density at equi-spaced points along any specified element boundary and, in addition, integrates the total flux crossing the boundary. This enables the capacitance of individual electrodes in a multi-electode problem to be determined. The facility can also be used to check the accuracy of the flux

balances achieved by the final solution to a problem and therefore provides an important check of the solution accuracy.

To effect the calculations BOUND calls SFLUX. This establishes the coordinates of the points at which the flux is to be calculated in both the local and global planes and it also calculates the direction cosines n_x and n_y of the outward going normal for points on straight sided elements. FD is called to calculate the normal flux density. This subroutine calculates the x and y components of the flux density using (2.3-38) and obtains the normal flux density from

$$\text{Flux}_n = n_x.\text{Flux}_x + n_y.\text{Flux}_y \qquad (2.3\text{-}39)$$

The direction cosines of straight sided elements are determined by SFLUX from the vertex coordinates using simple trigonometry. When the element side is curved however it becomes necessary to obtain the orientation of the global boundary at each point separately. This is achieved by FD using the derivatives of x and y with respect to ξ and η. The direction cosines of the outward facing unit normal are then readily obtained by simple transformation.

The total flux crossing a boundary is calculated in SFLUX by one dimensional contour integration using either the trapezoidal or the Gaussian quadrature method. Integration is performed along the appropriate simplex boundary. As a curved boundary in the global plane does not, in general, transform to a straight boundary in the local plane this is not strictly permissible. However the error introduced is small provided the deviation is modest. If greater accuracy is required then, prior to integration, the source of each global point in the local plane must be traced by the Newton-Raphson technique previously mentioned.

To check the fit of a curved global element boundary to the real boundary, subroutine MAP can be called. This outputs the (x,y) coordinates corresponding to equispaced points along the straight sides of the simplex. The calculations are made using equations (2.3-9).

Calculation of functional value

Examination of equations (2.3-12) and (2.3-17) reveals that the value of the functional can be obtained from the S and B matrices of (2.3-19). The contribution to the functional of the k^{th} element by s is given by the double summation

$$ {}^{s}F_k = \sum_{i=1}^{M} \left(\phi_i \sum_{j=1}^{M} s_{ij} \phi_j \right) \qquad (2.3\text{-}40) $$

whereas that by b is

$$ {}^{b}F_k = \sum_{i=1}^{M} b_i \, \phi_i \qquad (2.3\text{-}41) $$

To obtain the value of the functional, subroutine FCTVAL is called. This procures the values of the elements of the s and b matrices using subroutines GET and SB and performs the necessary summations. It also sums the s and b terms for each element and totals the contributions to give the overall functional value.

Filamentary elements

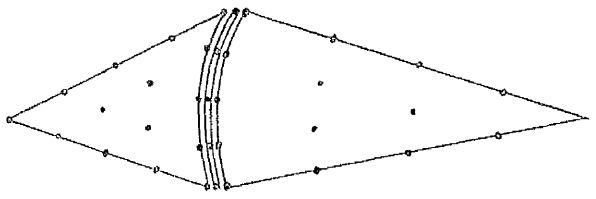

Figure 2.3-3 Filamentary element between two regular elements.

Referring to figure 2.3-3 the filamentary region of vanishing width δ can be considered a separate finite element. The value of its functional is given by the isotropic form of equation (2.3-12) namely

$$ F = \iint \left[k(\nabla\phi)^2 - 2\phi\rho \right] dxdy + \int_c (\sigma\phi^2 - 2h\phi) ds \qquad (2.3\text{-}42) $$

with d = 0. As the element is narrow it can be assumed that field variations occur only along the length of the element with the result that the surface integrals of (2.3-42) can be reduced to line integrals multiplied by δ

and the contour integrations become identically zero. Thus

$$F = \int_s \left[k_f(\nabla\phi)^2 - 2\phi\rho_f\right] ds \qquad (2.3\text{-}43)$$

where $k_f = k\delta$, $\rho_f = \rho\delta$ and the integration path s is along the element. Both k_f and ρ_f will, in general, be functions of s.

With no field variation across the element only a one dimensional array of nodes is required. Furthermore if the positions of these nodes are chosen to align with those of the adjacent elements, the values of the nodes in each 'triplet' will be identical. Thus one common set of nodes can be used and an increase in the number of variational parameters avoided. In MANFEP, for programming convenience, the filamentary element is considered to be attached to one or other of the adjoining elements. When formulating the matrices s and b for the host element using (2.3-17) additional terms are included from the derivatives of (2.3-43). These are given by

$$\frac{\partial F}{\partial \phi_i} = 2\int \left\{ k_f(s)\left[\frac{\partial \alpha_i}{\partial x}\left(\sum_{j=1}^{M} \phi_j \frac{\partial \alpha_j}{\partial x}\right) + \frac{\partial \alpha_i}{\partial y}\left(\sum_{j=1}^{M} \phi_j \frac{\partial \alpha_j}{\partial y}\right)\right] - \rho_f(s)\alpha_i \right\} ds \qquad (2.3\text{-}44)$$

where summation is over all nodes in the filamentary element.

CHAPTER 3

The electrostatic effects of voids in dielectrics

In chapter 2 the techniques used to study the potential distributions in dielectrics were described and in this chapter their application to dielectric regions containing voids is discussed. Both two dimensional and three dimensional axisymmetric problems are handled for a wide range of void shapes and sizes in dielectrics of different permittivity. As a special case d.c. potential distributions are also included. The effect of dielectric loss is then considered followed by a study of the influence of conducting films deposited on the surface of the voids. The latter is considered largely responsible for the self extinction of partial discharges, a phenomenum that is so frequently encountered when discharge testing. This work serves to quantify the effect.

In addition to giving the potential distributions, the changes in capacitance and loss tangent, as measured at the electrodes, are also given. Finally the effects of the rapid charge transfer that occurs during a partial discharge are discussed and quantitative results given.

3.1 Cases with neglible loss

If a dielectric region containing gaseous inclusions is subjected to an electric field the stress in the voids is, in general, greater than that experienced by the surrounding dielectric. This is a consequence of the low (approximately unity) value of the relative permittivity of the gas compared with that of the surrounding dielectric. For a pair of large plane parallel electrodes of separation t containing a laminar void of large dimensions perpendicular to the field direction, the degree of stress enhancement is given by

$$\frac{E_v}{E_i} = \frac{\epsilon_r t}{t + (\epsilon_r - 1)d} \qquad (3.1\text{-}1)$$

where d is the thickness of the lamina. This equation shows that, for $d \ll t$,

the stress enhancement approaches ϵ_r. The enhancement is less for voids of smaller dimensions perpendicular to the field direction and larger dimensions parallel to it.

The electric fields within elliptic cylindrical and oblate spheroidal cavities located in infinite dielectric regions are shown by Smythe[105] to be uniform. His analysis shows the stress enhancement to be given by

$$\frac{E_v}{E_i} = \frac{\epsilon_r(1 + m/n)}{\epsilon_r + m/n} \qquad (3.1\text{-}2)$$

for an eliptic cylindrical cavity where m and n are the semi-major and semi-minor axes respectively and the latter is parallel to the applied field. In the case of a circular cylindrical cavity $m = n$ and this reduces to

$$\frac{E_v}{E_i} = \frac{2\epsilon_r}{\epsilon_r + 1} \qquad (3.1\text{-}3)$$

For an oblate spheroidal cavity the equivalent expression is

$$\frac{E_v}{E_i} = \frac{\epsilon_r}{1 + (\epsilon_r - 1)f} \qquad (3.1\text{-}4)$$

where $$f = \frac{b^2}{a^2\left(\frac{b^2}{a^2} - 1\right)^{3/2}} \sec^{-1}\left(\frac{b}{a}\right) - \frac{1}{\frac{b^2}{a^2} - 1} \qquad (3.1\text{-}5)$$

b is the radius and a the semi axis. For a spherical void $a = b$, $f = \frac{2}{3}$ and equation (3.1-4) becomes

$$\frac{E_v}{E_i} = \frac{3\epsilon_r}{2\epsilon_r + 1} \qquad (3.1\text{-}6)$$

Under d.c. conditions, the potential distribution is determined by the conductivities of the constituent materials instead of their permittivities. However the governing equations remain the same so solutions are readily obtained by replacing the values of the permittivities with the corresponding conductivities. In the case of a gas filled void, the conductivity can be assumed to be negligible. This situation therefore yields the same potential distribution as that for a void in a dielectric of infinite permittivity under a.c. conditions. Thus a good approximation to the d.c. solution can

be obtained by solving the a.c. problem assuming the permittivity to be large. Applying this reasoning to equations (3.1-1) to (3.1-4) and (3.1-6) gives E_v/E_i = t/d; 1 + m/n; 2; 1/f; 3/2 respectively. For the numerical solutions obtained in this study a value of 10,000 was taken for the permittivity, this being large enough to reduce the errors to negligible proportions yet not so large as to create computational difficulties.

Equations (3.1-2) to (3.1-6) relate to single voids in infinite dielectric regions. Salvage[106] extends the analysis to include single voids located centrally between two infinite plane parallel electrodes. He makes use of a technique, devised by Rayleigh for the solution of Laplace's equation in a dielectric region containing an infinite array of circular cylinders or spheres, to solve the field in and around an infinite array of voids. The voids can be of either elliptic cylindrical or oblate spheroidal shape, with circular cylindrical and spherical voids as special cases. The analysis assumes the voids to be equally spaced with their minor axes colinear along a line parallel to the impressed electric field. It is clear from symmetry considerations that an equipotential plane must exist centrally between adjacent voids and so an interposed conducting sheet will not disturb the field pattern. Using this fact he is able to give formulae for the electric stresses in single voids between plane parallel electrodes but with the proviso that, for the approximations used to be valid, the major axis/diameter of the void must not exceed the electrode separation. His results show the stresses in the voids to be reduced by the proximity of the electrodes and to be no longer uniform. Along the (minor) axis stresses are least at the two ends increasing to a maximum at the centre. However this value is the least on the major axis/diameter where the stress is shown to reach a maximum at the extremities. These findings have been confirmed by measurements using an electrolytic tank.[107]

Cylindrical voids between plane parallel electrodes

The void shapes discussed so far, excluding the first, are most

likely to approximate to those found in isotropic dielectrics in which gas bubbles can be formed during manufacture, installation, service or repair. In the case of laminated dielectrics however the voids are more likely to be 'pill box' shaped or rectangular in cross section. The former is likely to occur if a layer of the insulation has been punctured and the latter arises at the butt gaps in tape insulation. The two shapes are conveniently analysed together as the former is merely the axisymmetric case of the latter. Because this geometry is not amenable to analytical treatment resort to numerical methods must be made. Again Salvage was active in the field using the finite difference technique to evaluate potential distributions.[108] He gives curves for the mean axial stress in cylindrical voids with axes parallel to the applied field as a function of their size and shape for different dielectric permittivities.

It was considered that more detailed information would provide a better appreciation of the fields within a void prior to breakdown and that this information could be used to predict the likely situation after breakdown. Since it is the change between these two conditions that produces the externally detectable evidence most commonly used by discharge detectors it was considered that such a study could improve the interpretation of discharge measurements.

The arrangement of the generalized cylindrical void is shown in figure 3.1-1. From symmetry is is evident that the solution to only one quadrant need be found as the others can be obtained by reflection in the two axes. This enables a considerable reduction to be made in the computational effort. The fields were primarily solved using the finite element method with fourth order polynomials. This had the advantage that the number of nodes that were required to be input as data was minimal, the program generating the remaining nodes automatically. The total number of nodes for any problem was limited to a maximum of 100 for which the solution time on a CDC 7600 computer was approximately 1.5 seconds. Solutions were obtained for $r/d = 0.25, 0.5, 1, 2$ and 5 with $d/t = 0, 0.1,$

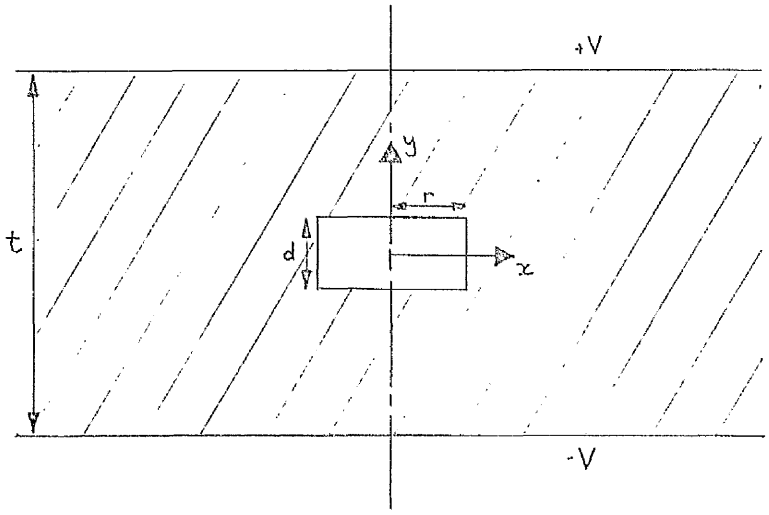

Figure 3.1-1 Generalized cylindrical void between plane parallel electrodes

0.2, 0.4, 0.6 and 0.8 . Relative permittivity values of 2, 4, 10 and 10,000 were considered, the last yielding a close approximation to the d.c. solution as previously mentioned.

The arrangement of the finite elements in each case is shown in figure 3.1-2. It can be seen that in areas expected to have highly non-uniform electric stresses smaller elements were used to permit more accurate representation of the field. It would have simplified the computation considerably if the same basic configuration of elements could have been used in each case but this clearly was not possible with such a wide range of void shapes and sizes. However, by adopting four basic arrangements, a reasonable set of elements could be found for each problem.

The voids are located in an infinite region bounded above and below by plane parallel electrodes. If these electrodes are assumed to be at potentials of +1000 and -1000 volts respectively then the upper and lower boundaries of the quadrants shown in figure 3.1-2 are of the Dirichlet type equal to 1000 and 0 volts respectively. The left hand boundary is a homogeneous Neumann type ($\partial\phi/\partial n = 0$) since there can be no flux crossing the axis of rotation. At positions well removed from the void the electric stress is uniform with the field lines running normal to the electrodes. Therefore by making the right hand boundary sufficiently far removed from the field disturbances caused by the void it too can be treated as homo-

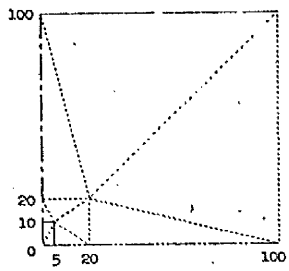

No. 1 r/d = 0.25 d/t = 0.1

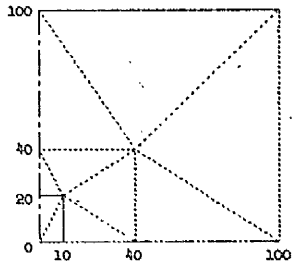

No. 2 r/d = 0.25 d/t = 0.2

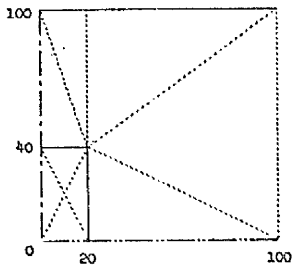

No. 3 r/d = 0.25 d/t = 0.4

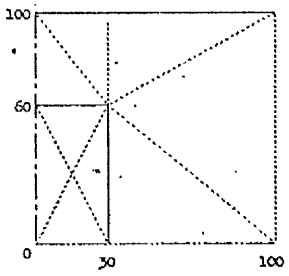

No. 4 r/d = 0.25 d/t = 0.6

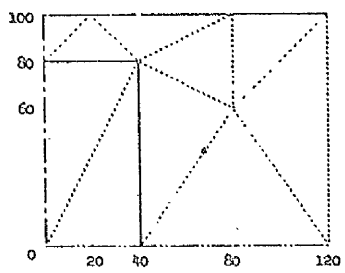

No. 5 r/d = 0.25 d/t = 0.8

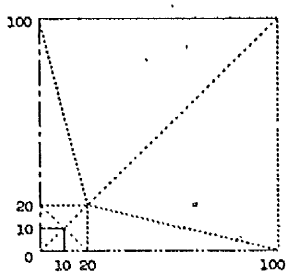

No. 6 r/d = 0.5 d/t = 0.1

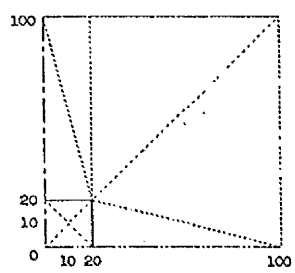

No. 7 r/d = 0.5 d/t = 0.2

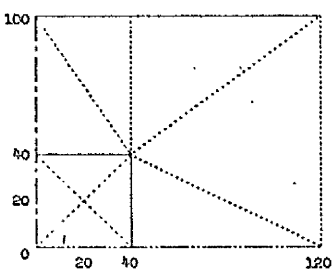

No. 8 r/d = 0.5 d/t = 0.4

Figure 3.1-2 Arrangement of finite elements for 'pill box' shaped voids.

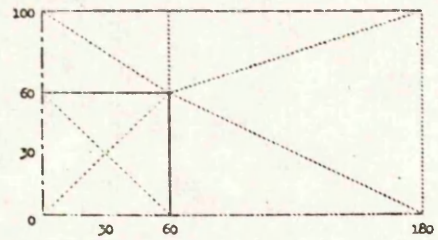

No. 9 r/d = 0.5 d/t = 0.6

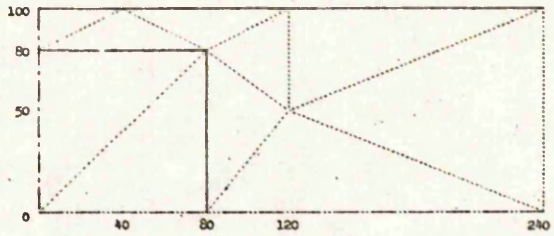

No. 10 r/d = 0.5 d/t = 0.8

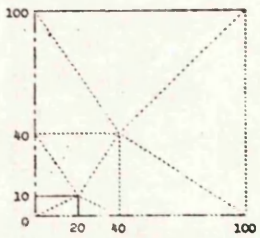

No. 11 r/d = 1 d/t = 0.1

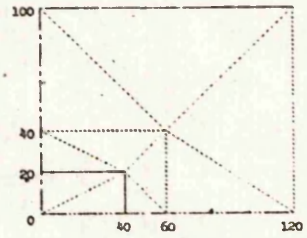

No. 12 r/d = 1 d/t = 0.2

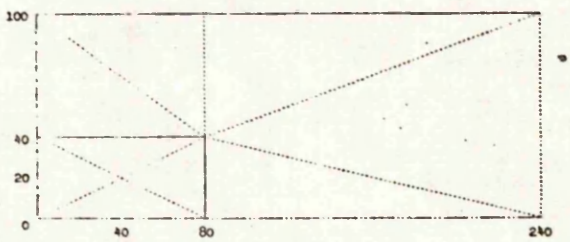

No. 13 r/d = 1 d/t = 0.4

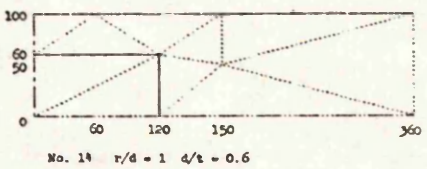

No. 14 r/d = 1 d/t = 0.6

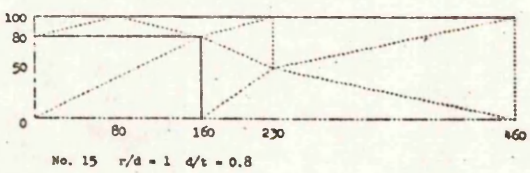

No. 15 r/d = 1 d/t = 0.8

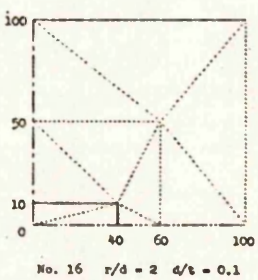

No. 16 r/d = 2 d/t = 0.1

Figure 3.1-2 continued.

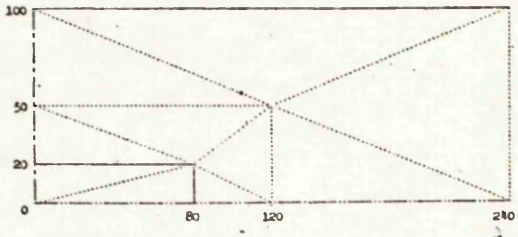

No. 17 r/d = 2 d/t = 0.2

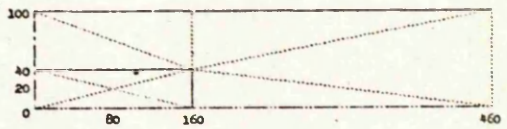

No. 18 r/d = 2 d/t = 0.4

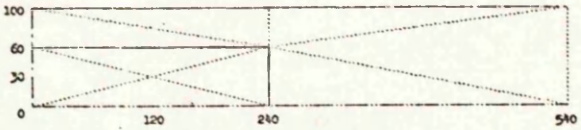

No. 19 r/d = 2 d/t = 0.6

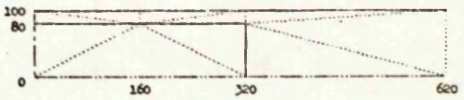

No. 20 r/d = 2 d/t = 0.8

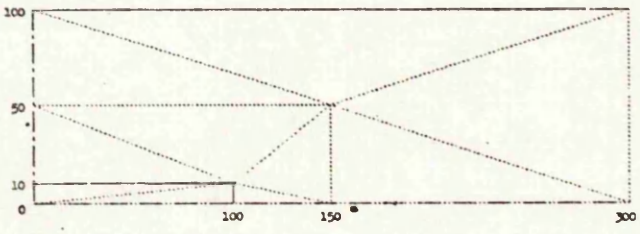

No. 21 r/d = 5 d/t = 0.1

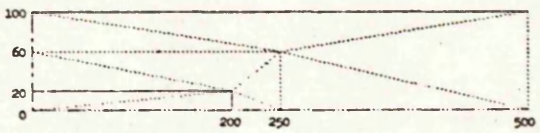

No. 22 r/d = 5 d/t = 0.2

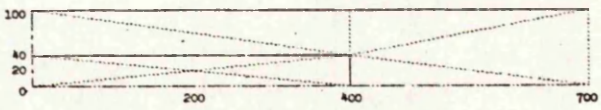

No. 23 r/d = 5 d/t = 0.4

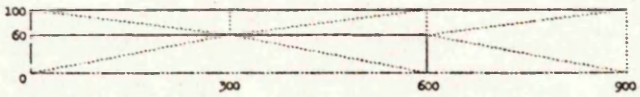

No. 24 r/d = 5 d/t = 0.6

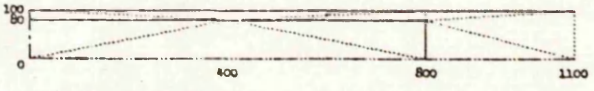

No. 25 r/d = 5 d/t = 0.8

Figure 3.1-2 (continued)

geneous Neumann. In this way the difficulty of an unbounded field region is overcome. To determine the potential distributions with d/t = 0, the program was re-run for quadrants 1, 6, 11, 16 and 21 in figure 3.1-2 with the upper Dirichlet boundary respecified as inhomogeneous Neumann. For these axisymmetric problems h(s) is, from equation (2.3-2)

$$h(x) = \epsilon_o \epsilon_r x E_i \qquad (3.1\text{-}7)$$

The results show that the mean electric stress experienced by a 'pill box' shaped void is greatest along the axis. The extent to which this exceeds the impressed electric field is shown in figures 3.1-3(a) to (d) for the full range of values of d/t and r/d. The top curve with r/d = ∞ represents the case of a lamina void for which the stress enhancement is given by equation (3.1-1). At the other extreme a needle shaped void aligned with the field for which r/d = 0 undergoes no stress enhancement and is therefore represented by the d/t axis in these figures. The curves are generally in agreement with those given by Salvage[108] but minor differences are apparent for small values of d/t where his values were obtained by extrapolation.

The variation in potential along the void surfaces is shown in figures 3.1-4(a) to (d) for the voids in dielectrics of permittivity 2, 4, 10 and 10,000 respectively. The left hand side of each graph gives the radial variation in potential on the upper and lower surfaces of the voids ($y = \pm d/2$) whereas the right hand side shows the variation on the cylindrical surfaces. ($x = \pm r$) The potentials are given as a fraction of that applied to the high voltage electrode. To obtain the ratio of the mean electric stress along the void at a give radius to the impressed electric stress remote from the void, the curves on the left hand side should be multiplied by t/d. The curves show the mean stress experienced by a void to be greatest on its axis and to decrease steadily reaching a minimum on the periphery. This decrease is more marked in voids having a large value of r/d. The potential variation along the cylindrical surfaces is approximately linear indicating a nearly constant surface electric stress slightly in excess of E_i. It is interesting

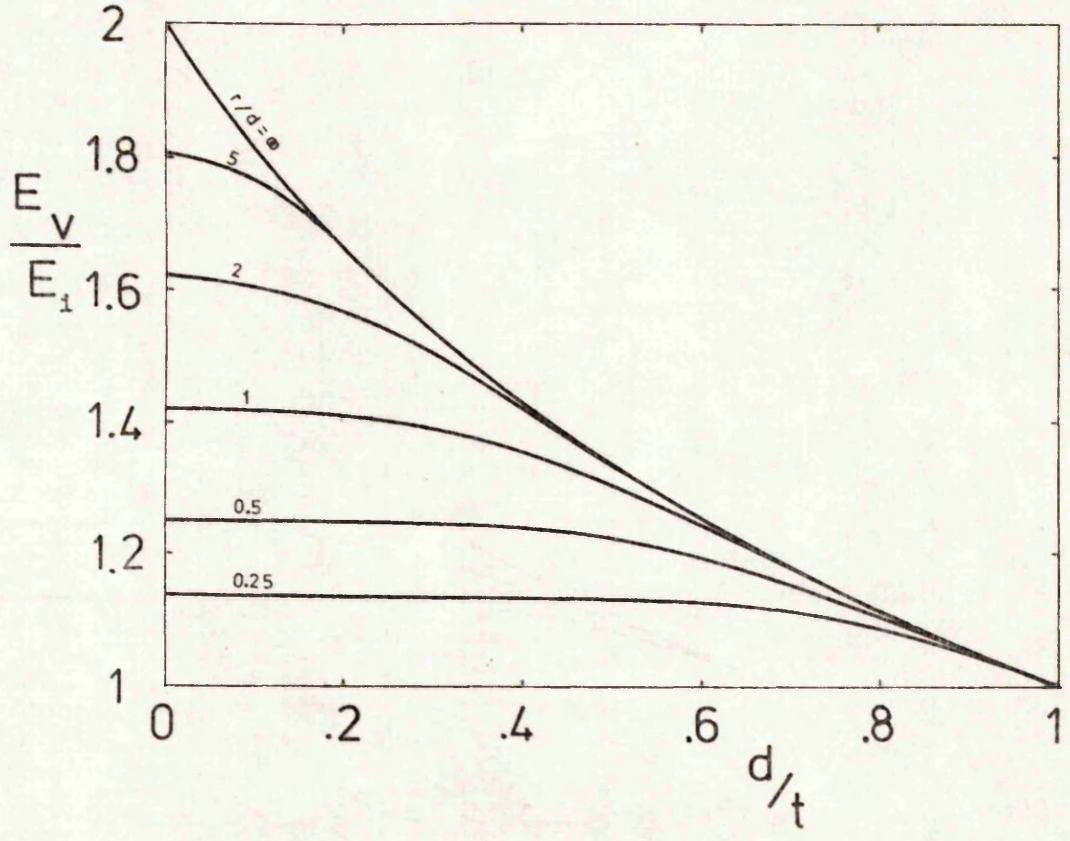

Figure 3.1-3(a) Enhancement in the mean axial electric stress across a circular cylindrical void. (Permittivity of dielectric = 2)

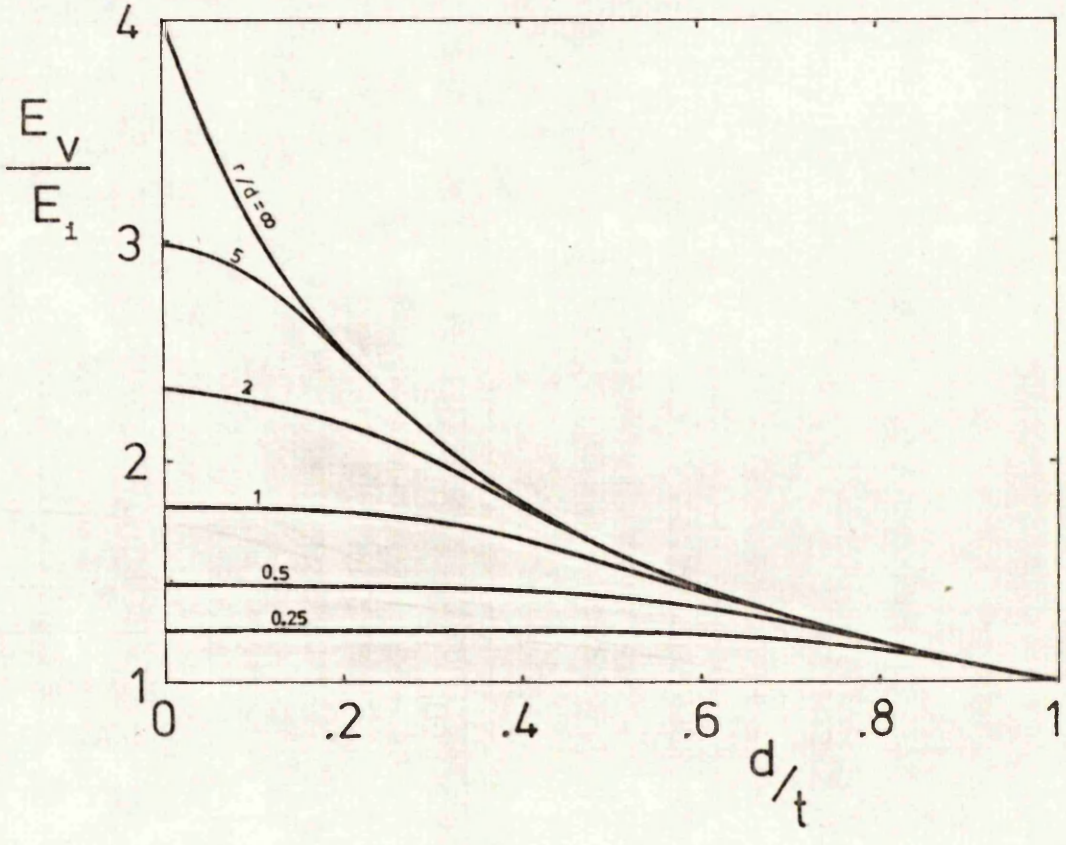

Figure 3.1-3(b) As per figure 3.1-3(a) but with $\epsilon_r = 4$

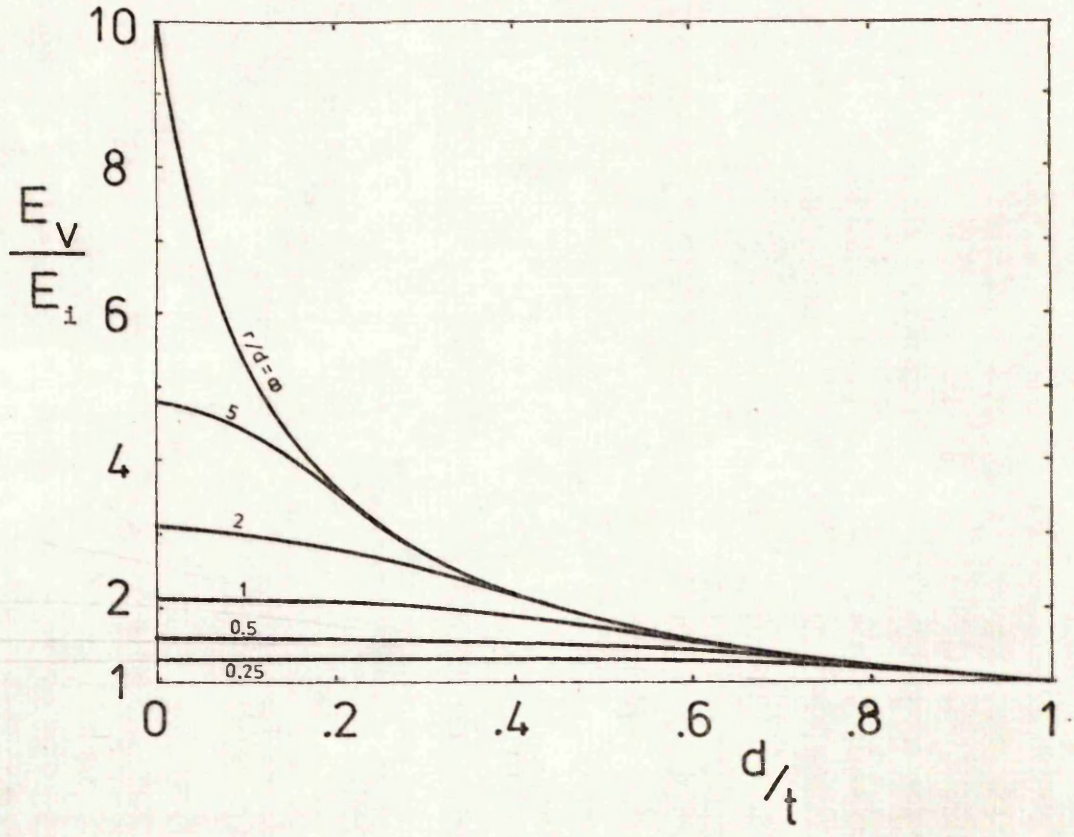

Figure 3.1-3(c) As per figure 3.1-3(a) but with ϵ_r = 10

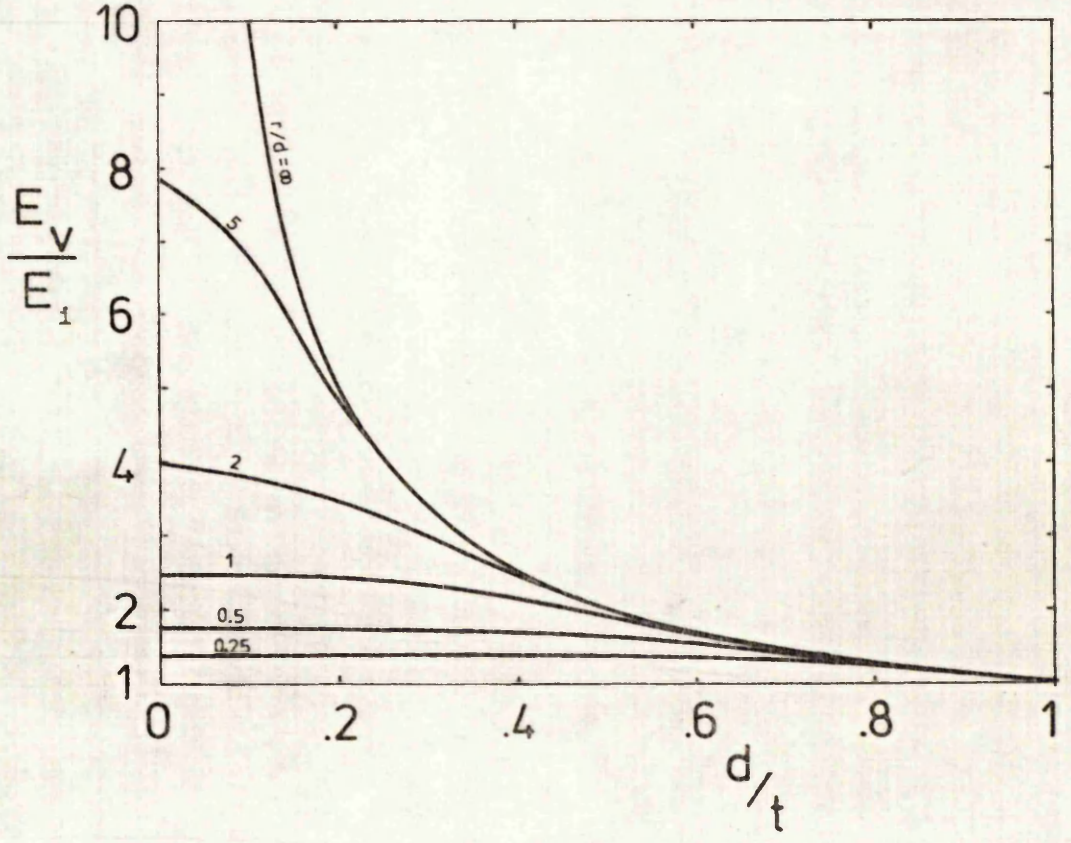

Figure 3.1-3(d) As per figure 3.1-3(a) but with ϵ_r = 10,000

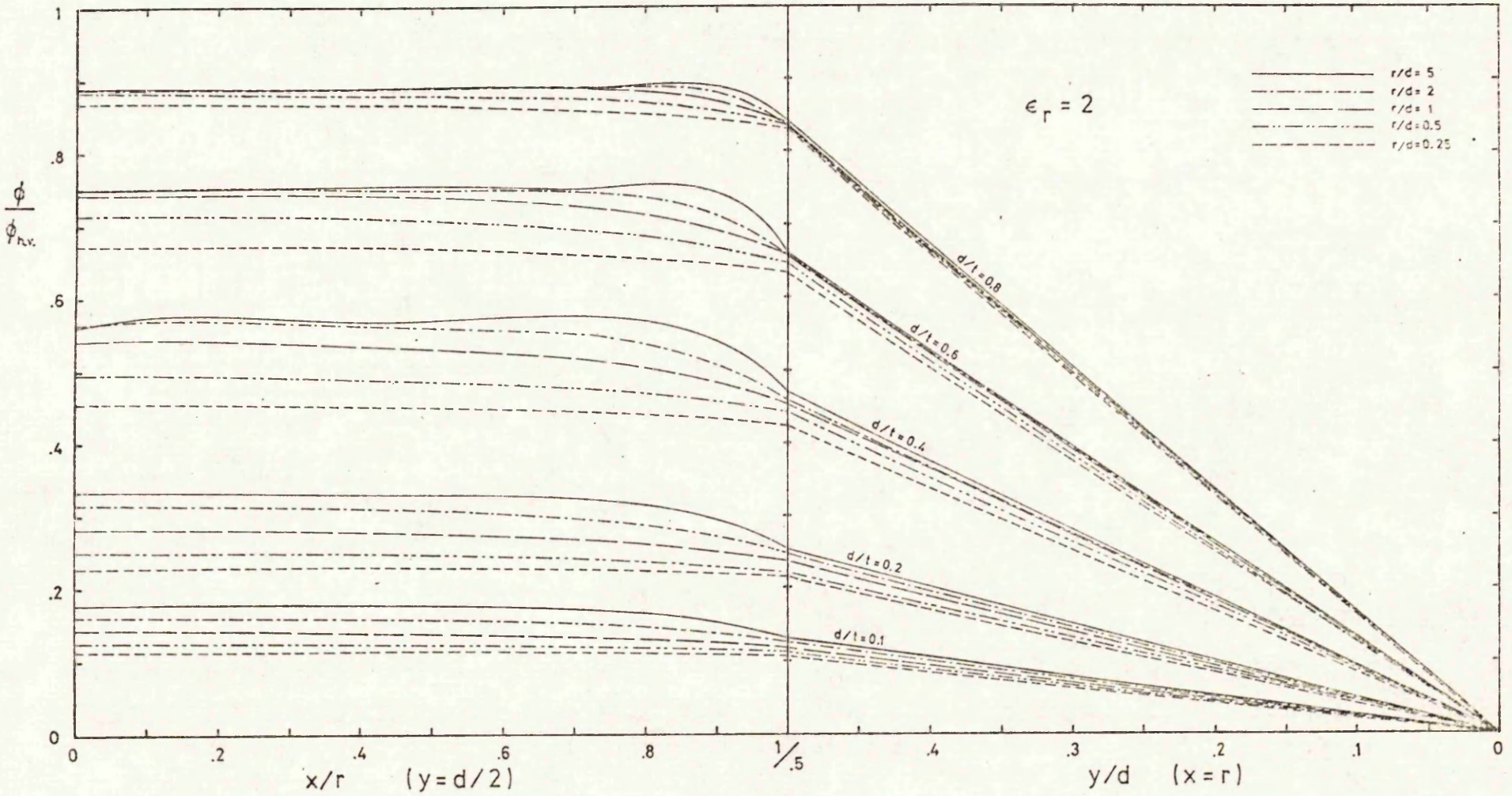

Figure 3.1-4(a) Potential variation along surfaces of voids. Left-hand side of graph shows variation across end faces and right-hand side shows variation along cylindrical faces. (Permittivity of dielectric = 2)

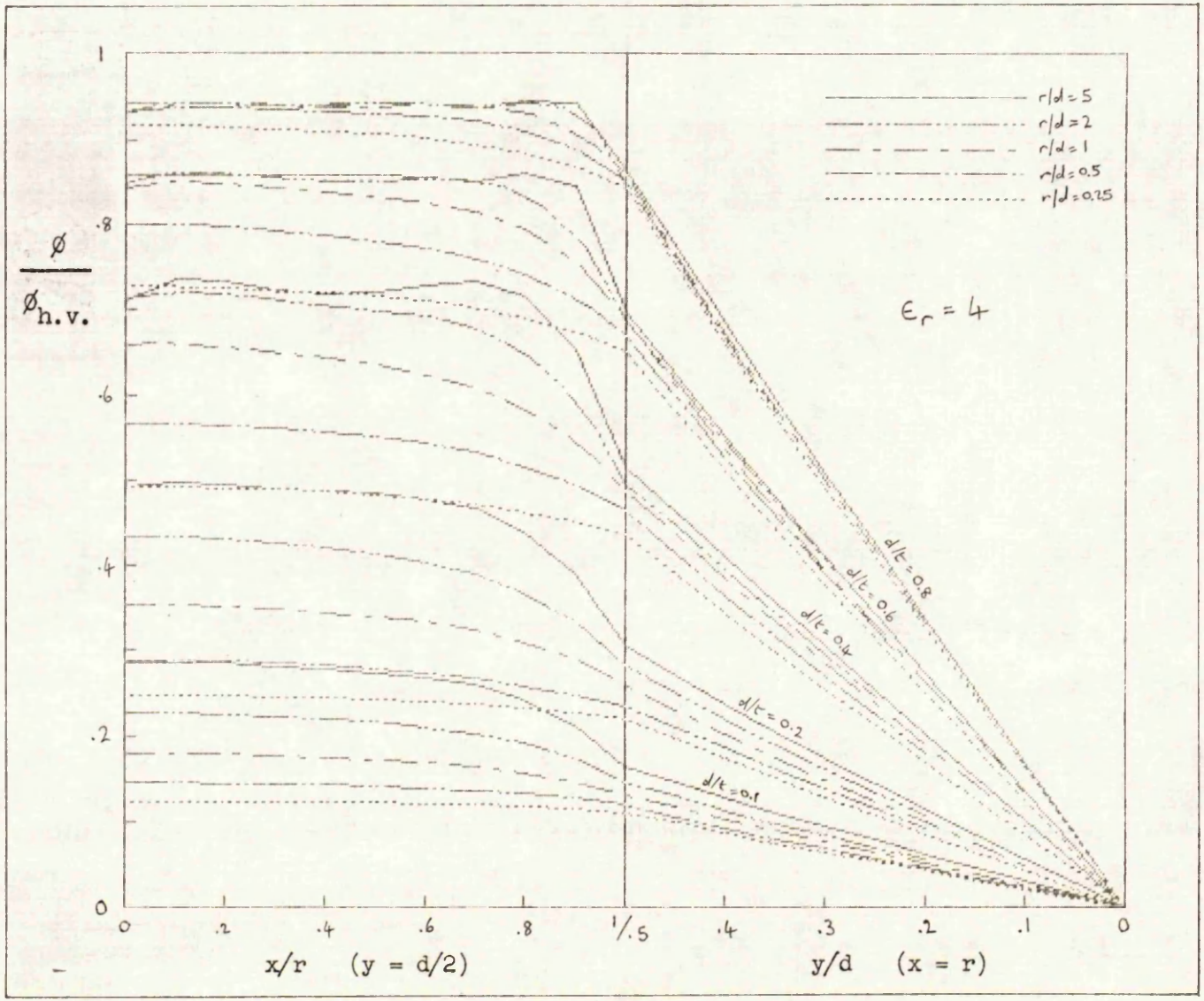

Figure 3.1-4(b) As per figure 3.1-4(a) but with $\epsilon_r = 4$

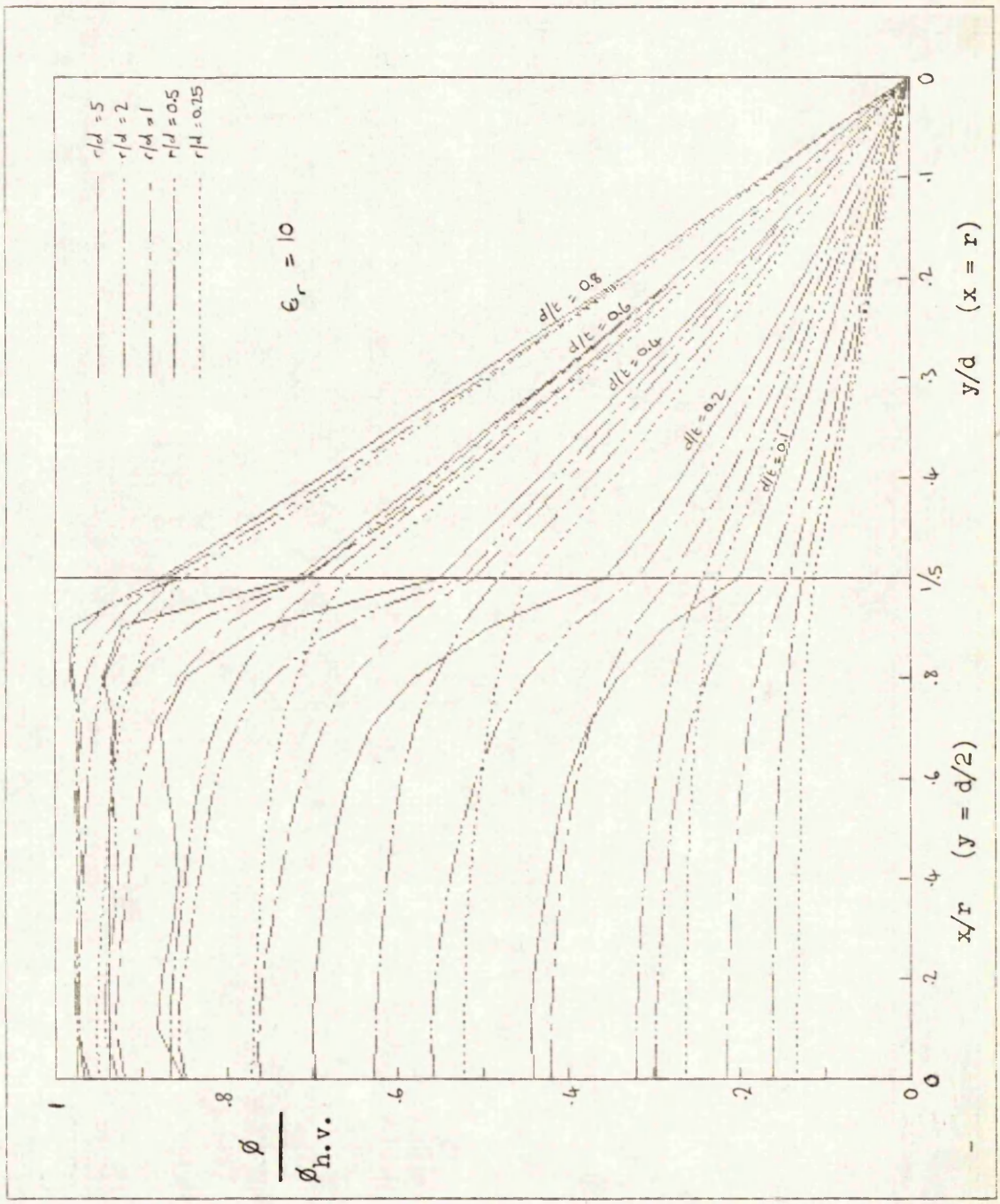

Figure 3.1-4(c) As per figure 3.1-4(a) but with $\epsilon_r = 10$

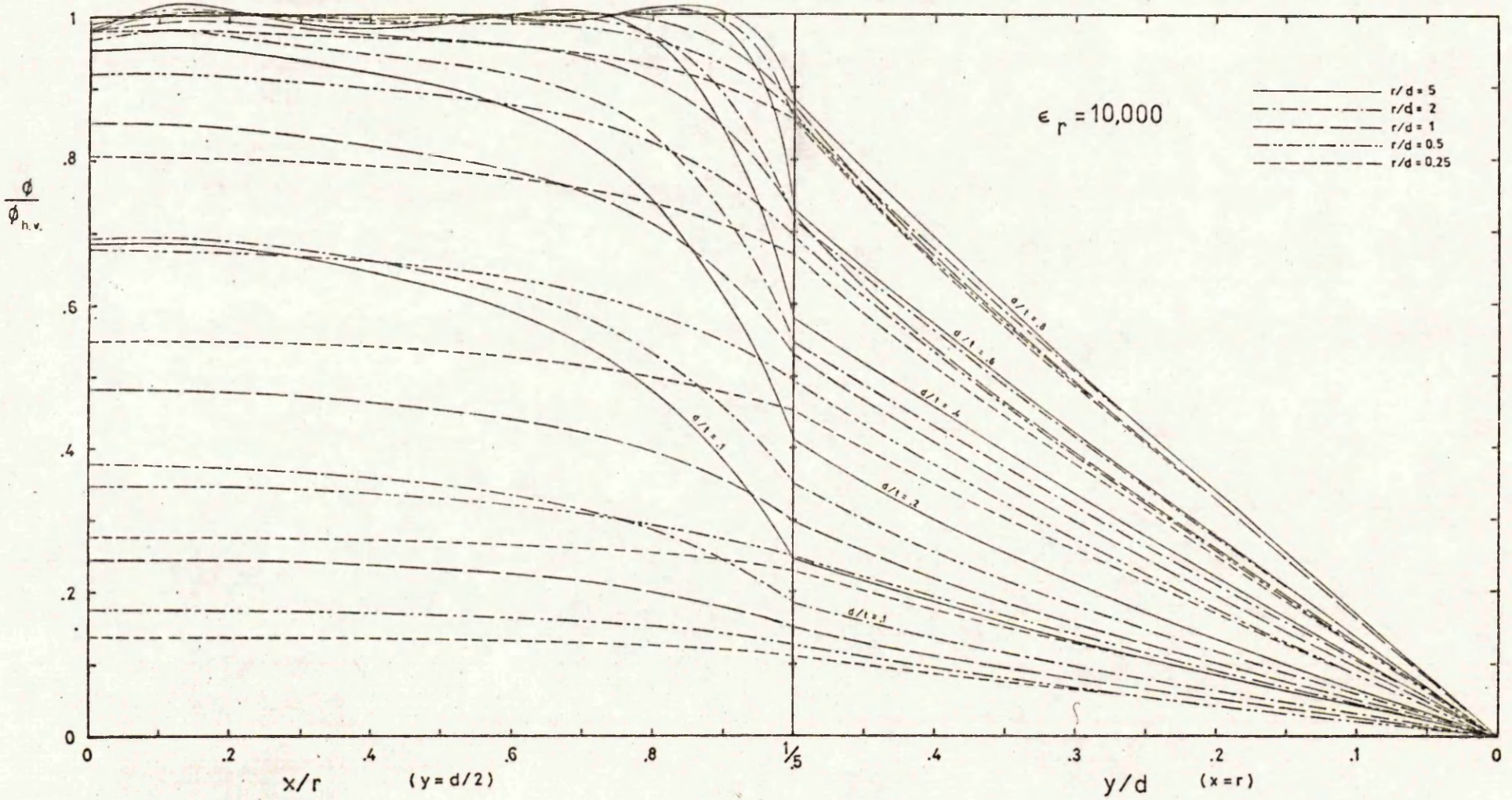

Figure 3.1-4(d) As per figure 3.1-4(a) but with ϵ_r = 10,000

to note that, for a void with d/t = 1, this stress would be exactly constant and equal to E_i since, in this case, the cylindrical faces of the void would be homogeneous Neumann boundaries. The corresponding curve would be a straight line drawn diagonally across the right hand side of each graph from the top-left to the bottom-right.

The curves show the limitations of representing fields by fourth order polynomials where an abrupt change of potential occurs within an element. When an attempt is made to represent such a field with a polynomial of limited order, overshooting occurs and the calculated solution oscillates about the true one. This is particularly noticeable, for instance, with the curves obtained for r/d = 5, d/t = 0.4 i.e. figure 3.1-2(23). The remedy would have been to increase the number of elements but this was not considered justified as the errors were modest. Checks were made of the flux balances between elements for both the total integrated flux and the flux at spot points on the boundary. Good agreement was found with the lower values of permittivity, especially when considering the total flux, but the results were disappointing with ϵ_r = 10,000.

The computation further showed the stresses within the voids to vary according to the void size, shape and the permittivity of the surrounding dielectric. Nevertheless the following general characteristics were evident.

a) At any given radius the electric stress in the y direction (E_y) is a minimum on the axis of symmetry y = 0 and increases progressively toward the void ends. The effect is most marked in voids with small values of r/d and d/t. It was also noticed that the ratio of the end stress to the centre stress was greatest on the rotational axis for voids having a small value of r/d but greatest on the periphery for those with a large value.

b) The magnitude of E_y at any given distance from the axis of symmetry y = 0 is a maximum on the rotational axis and falls progressively towards the void periphery. The effect is greatest in voids with a large value of r/d and a small value of d/t.

c) An exception to (b) arises in the void corner (x = r, y = d/2)

where a local enhancement of both E_y and E_x can occur. It is interesting to note that, in common with E_y, E_x can exceed the impressed electric stress E_i.

d) The magnitude of E_y is greatest in voids for which d/t is small.

e) As expected, in any given void the stress enhancements are most pronounced if the permittivity of the surrounding dielectric is high.

Effects of voids on sample capacitance

In chapter 2 it was established that the value of the two dimensional functional for a region with only Dirichlet or homogeneous Neumann boundaries is equal to twice the energy stored in unit depth of the corresponding three dimensional region assuming the field to be independent of the third co-ordinate. For the axisymmetric regions shown in figure 3.1-2, equation (2.3-13) becomes

$$F = \int_0^{\frac{t}{2}} \int_0^R \epsilon_o \epsilon_r r \left\{ \left(\frac{\partial \phi}{\partial r} \right)^2 + \left(\frac{\partial \phi}{\partial z} \right)^2 \right\} dr dz \qquad (3.1\text{-}8)$$

where R is the maximum radius included in the integration. The energy stored overall is

$$U = \tfrac{1}{2} \int_0^{2\pi} \int_{-\frac{t}{2}}^{\frac{t}{2}} \int_0^R \underline{D} \cdot \underline{E} \; r \; dr \; dz \; d\theta \qquad (3.1\text{-}9a)$$

and so

$$U = \int_0^{2\pi} F \; d\theta = 2\pi F \qquad (3.1\text{-}9b)$$

From this the capacitance is given by

$$C = 4\pi F / V^2 \qquad (3.1\text{-}10)$$

where V is the voltage across the whole specimen. (2,000 volts in this analysis)

Voids with non-conducting surfaces.

To assess the reduction in the specimen capacitance resulting from the presence of a void with non-conducting surfaces, the capacitance C_T' of each of the arrangements shown in figure 3.1-2 was calculated from the functional value. In addition the capacitance C_T was calculated assuming the void to be absent. The latter was considered to consist of two parts.

The first was that attributable to a cylinder of dielectric running normal to the electrodes with a plan area equal to that of the void and the second was the capacitance of the remainder. These correspond to C_B and C_A respectively in figure 3.1-5(a). C_A was deducted from C_T' to yield C_B' of figure 3.1-5(b). The ratio C_B'/C_B gives a dimensionless assessment of the change in capacitance resulting from the void and is therefore universally applicable.

a) Without void

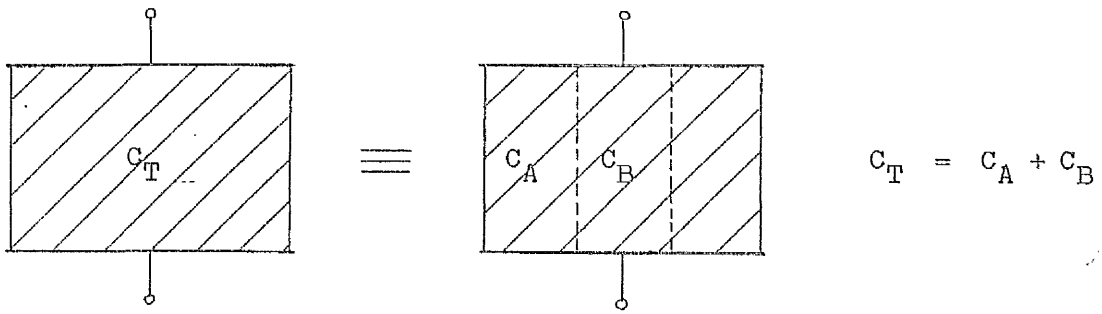

b) With void

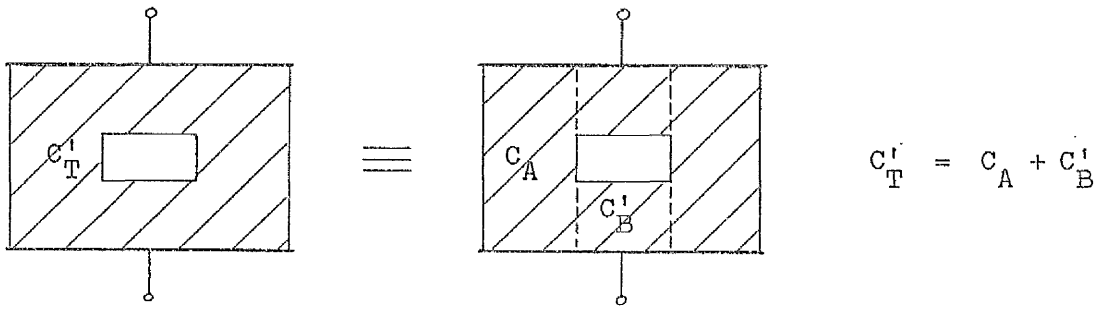

Figure 3.1-5 Assessment of specimen capacitance change when void present.

Curves showing the variation in C_B' / C_B with change of d/t are given in figure 3.1-6 for values of ϵ_r = 2, 4, 10 and 10,000 and r/d = 0.25, 0.5, 1, 2 and 5. Referring to the figure, all the curves must clearly tend to unity as d/t tends to zero. At the other extreme, as d/t = 1 represents a cylindrical void bridging the two electrodes, the curves must, in this case, be equal to the reciprocal of the relative permittivity. At intermediate values of d/t, the curves show C_B' / C_B to be between these two values. They also show that, for any given value of permittivity the values of C_B' / C_B are less for voids with high ratios of r/d than for voids having a low ratio. Furthermore this effect is especially pronounced when the void is surrounded by dielectric of high permittivity.

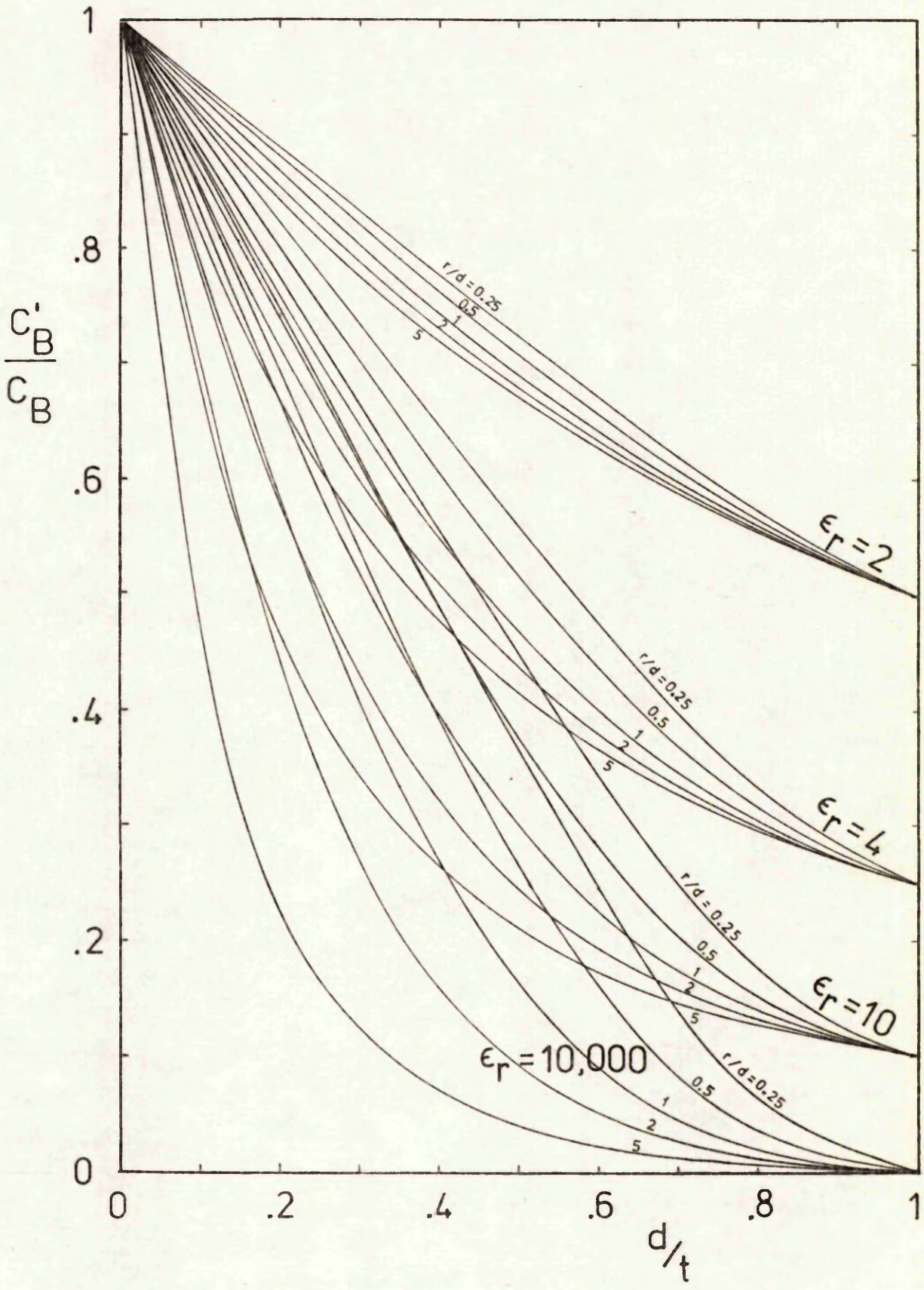

Figure 3.1-6 Effect of non-conducting cylindrical voids on specimen capacitance

Voids with perfectly conducting surfaces

If a semiconducting layer forms on the surface of the void the loss of the specimen capacitance will be reduced and, beyond a certain conductivity, the overall capacitance will show an increase rather than a decrease. Such cases result in loss and will be analysed in the next section. However, in the limit when the film can be considered perfectly conducting, the system becomes loss-less once more and so will be discussed here.

A perfectly conducting void always results in an increase in the specimen capacitance for the configurations shown in figure 3.1-2. To determine the extent of this increase the program was re-run with a homogeneous Dirichlet boundary specified along the void sides. In this situation, though the permittivity does determine the flux density and capacitance, C_B' / C_B, being dimensionless, is not affected. The program was therefore run with the relative permittivity equal to unity. The curves corresponding to figure 3.1-6 are given in figure 3.1-7 . Again all the curves tend to unity as d/t tends to zero but, in contrast, they tend to infinity as d/t tends to unity. The curves show C_B' / C_B to rise most rapidly for small values of r/d.

As the surface conductivity of a void increases (possibly as the result of internal discharges) the stress within the void decreases. A stage is therefore reached when the stress is insufficient for breakdown to occur within the void and the discharges will self extinguish. This can lead to over confidence in the condition of the insulation, a situation that is particularly insidious as the insulation is now subject to increased stressing. Figure 3.1-8 shows the stress that the insulation adjacent to a perfectly conducting void would experience. The left hand side of the figure gives the variation of E_y across the end of the cylinder and the right hand side gives the variation in E_x along its length. The curves show the stress enhancement to be appreciable especially in the vicinity of the void 'corners'.

Accuracy of solutions

To check the accuracy of the solutions obtained by the finite element method, finite difference solutions were also obtained in the case of the

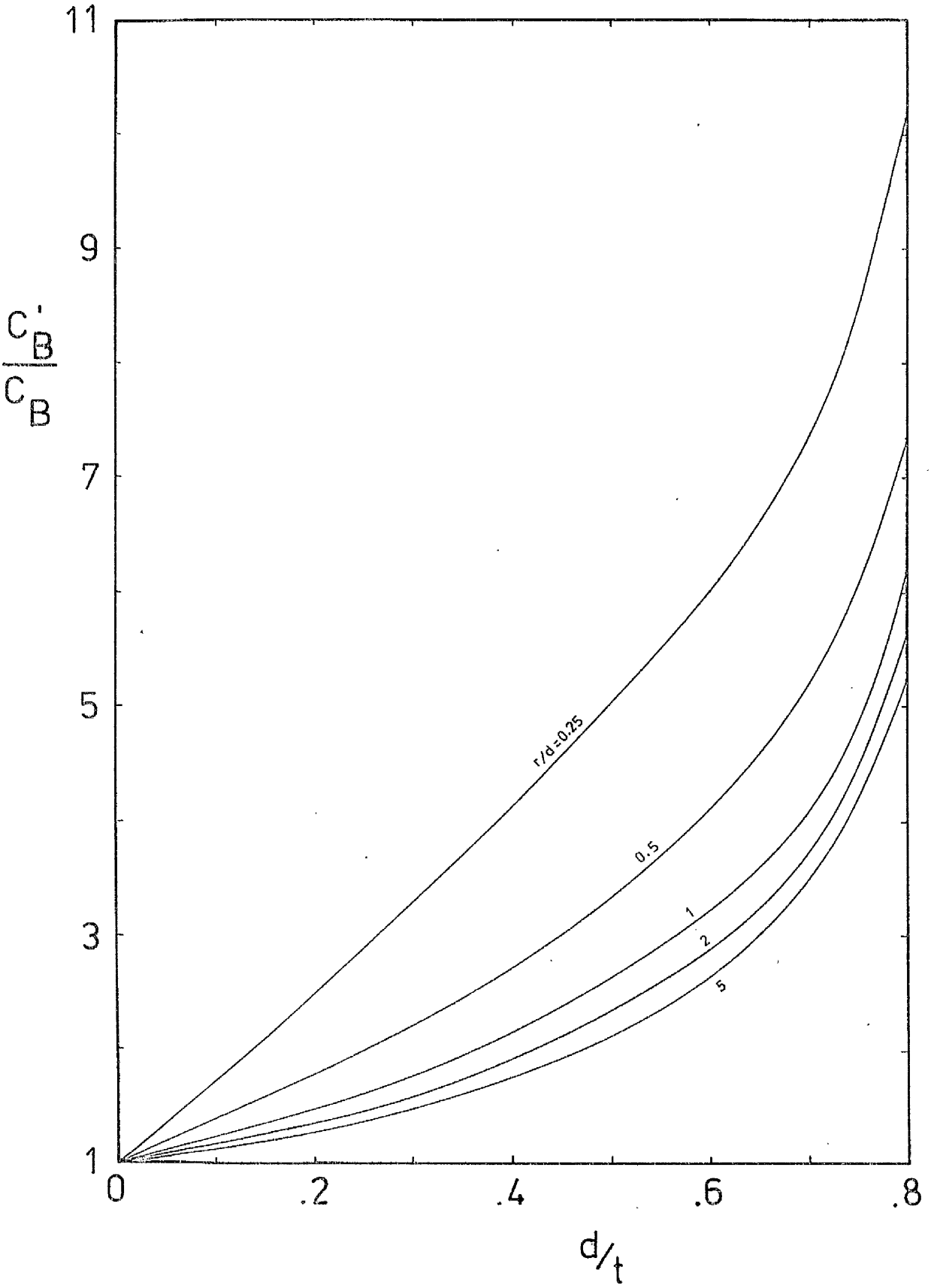

Figure 3.1-7 Effect of perfectly conducting cylindrical voids on specimen capacitance

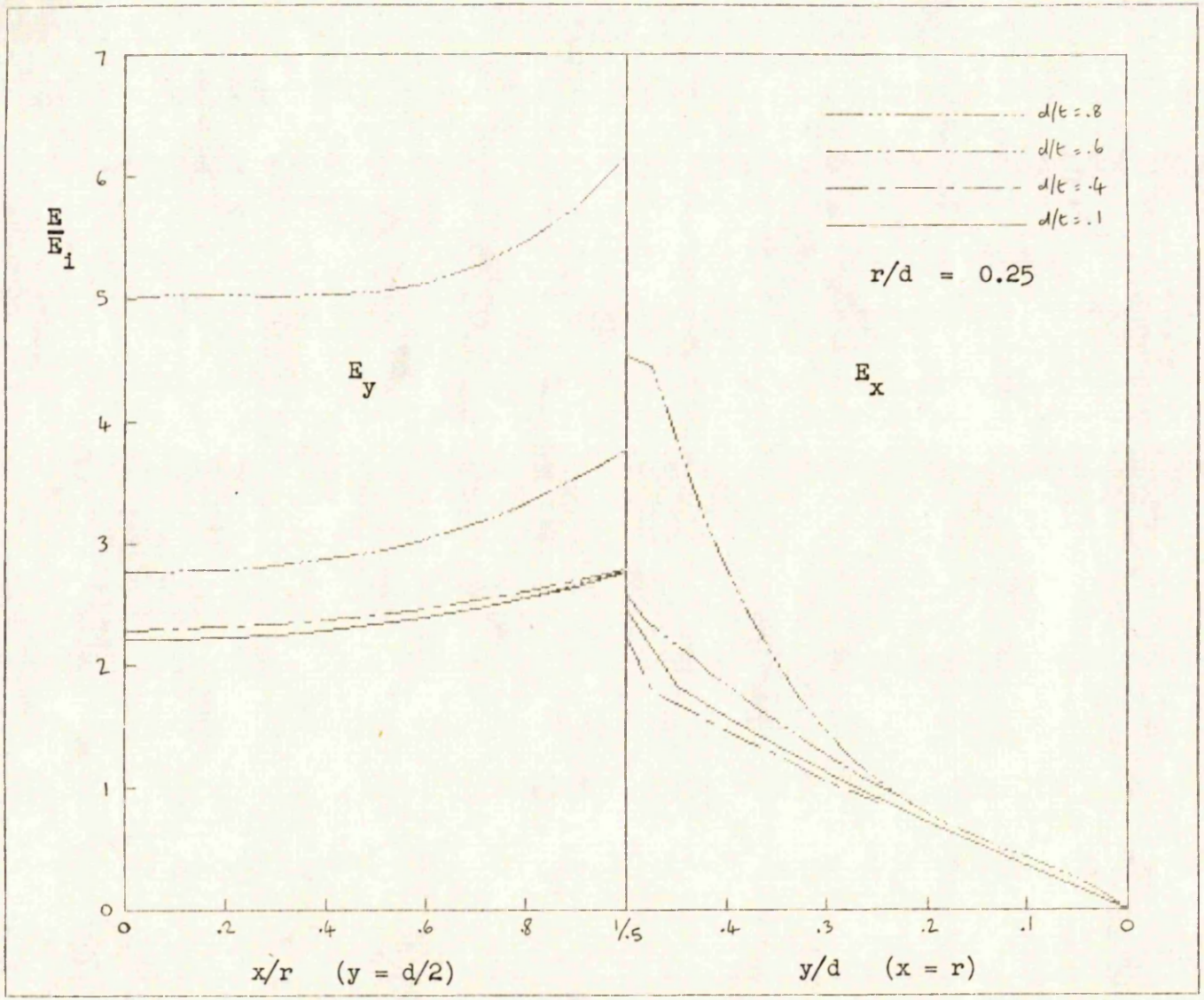

Figure 3.1-8 Electric stress adjacent to a perfectly conducting cylindrical void

(a) r/d = 0.25

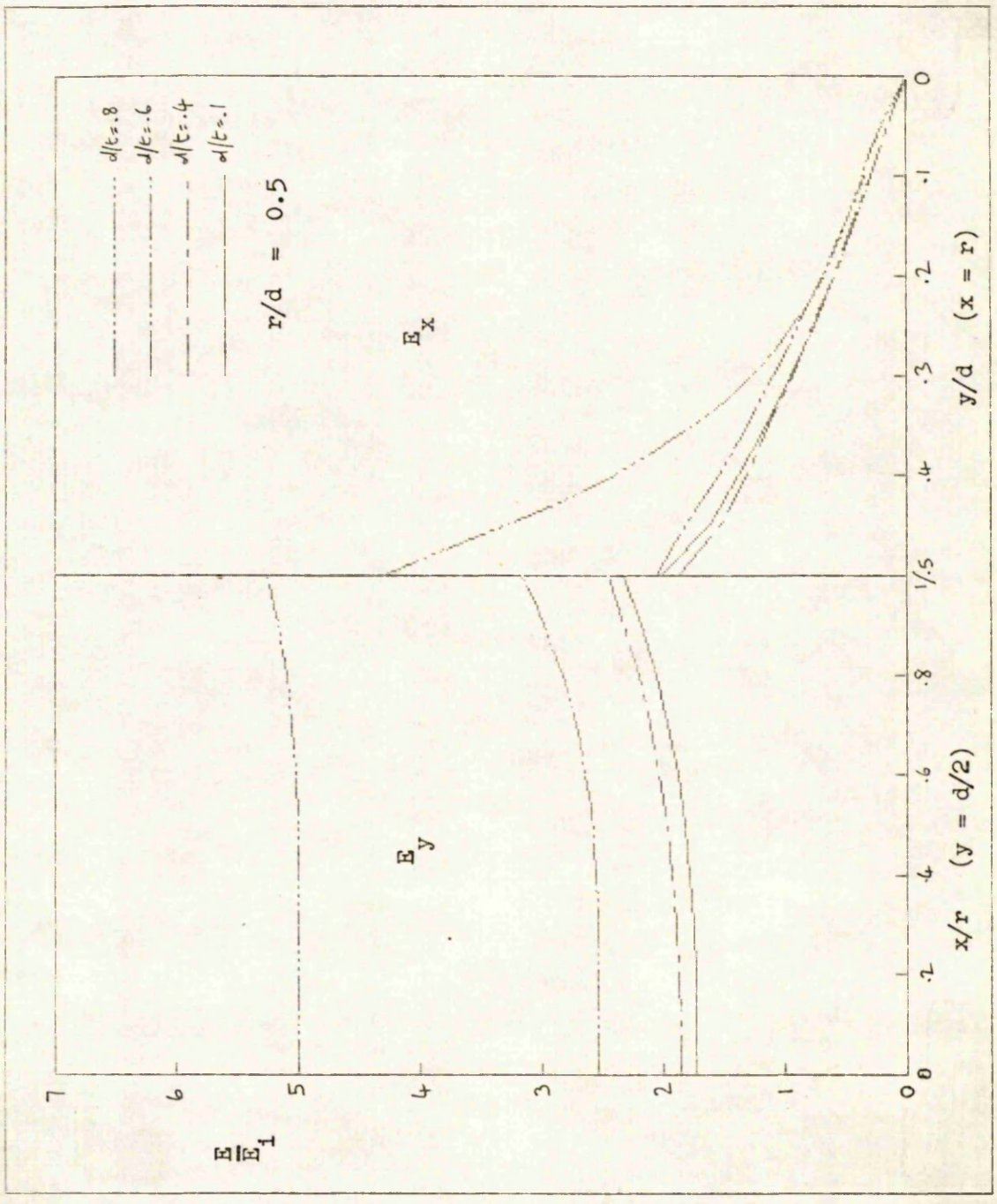

Figure 3.1-8(b) As per figure 3.1-8(a) but with r/d = 0.5

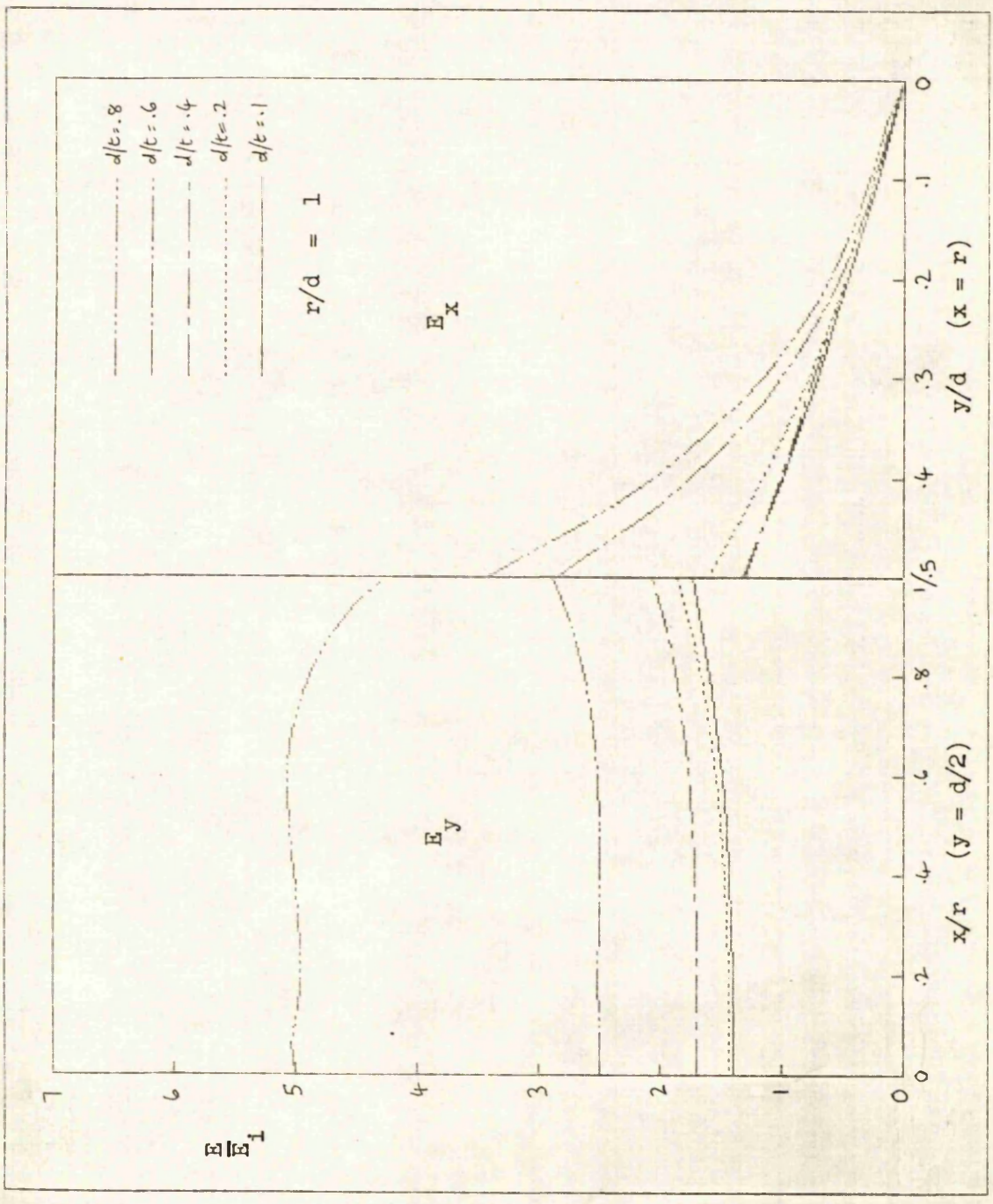

Figure 3.1-8(c) As per figure 3.1-8(a) but with r/d = 1

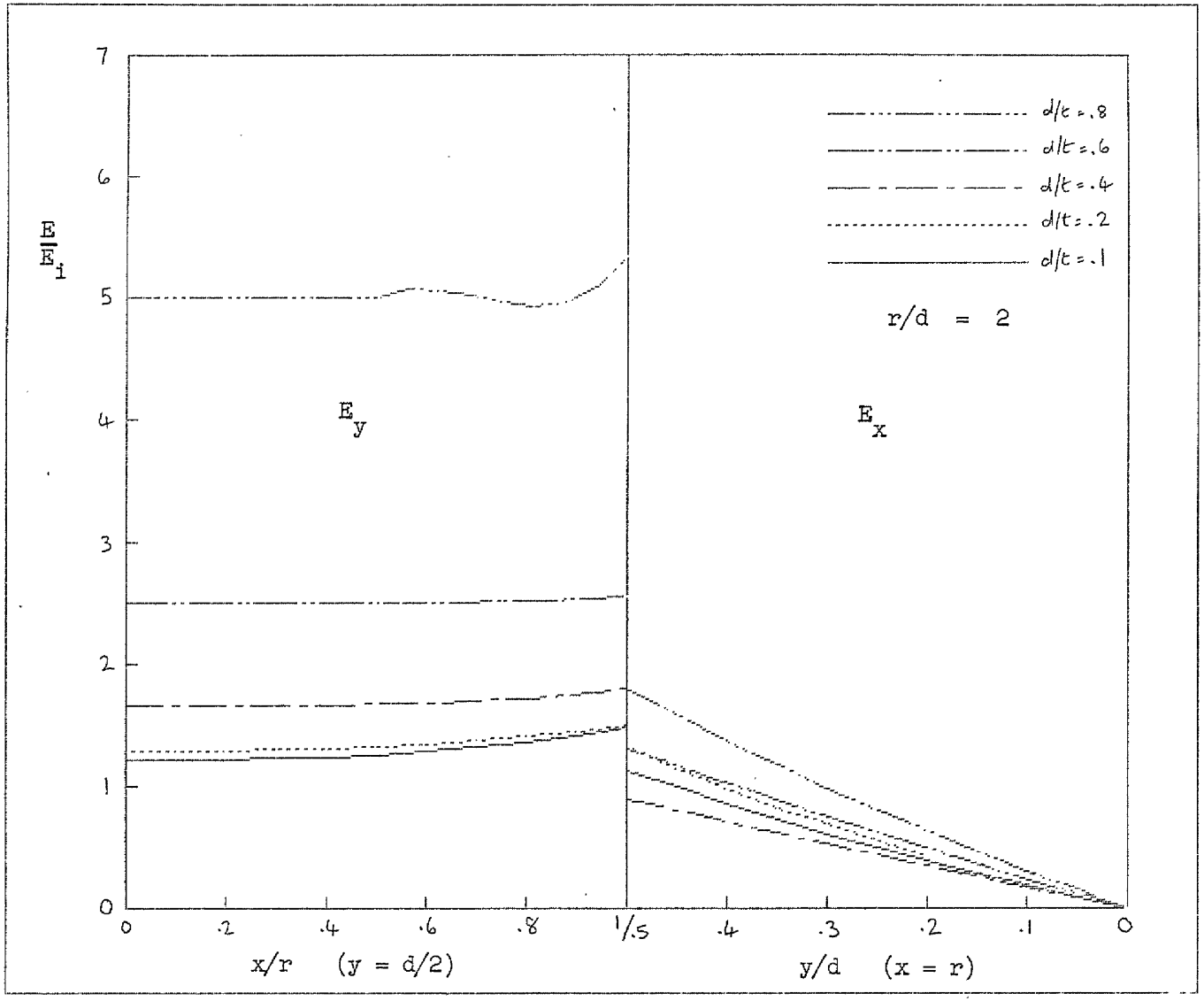

Figure 3.1-8(d) As per figure 3.1-8(a) but with r/d = 2

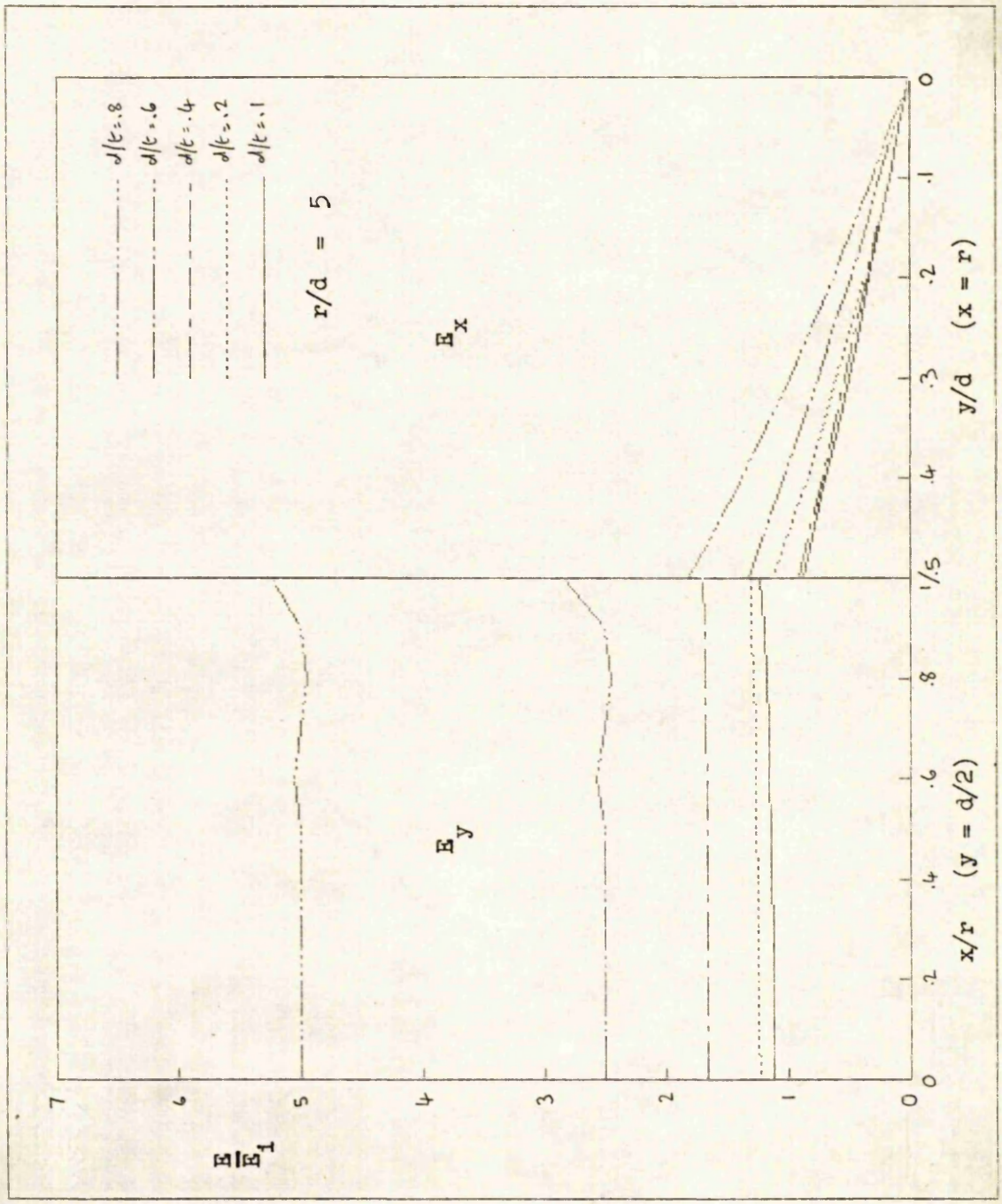

Figure 3.1-8(e) As per figure 3.1-8(a) but with r/d = 5

rectangular/cylindrical void with $r/d = 2$ and $d/t = 0.2$ (No. 17, figure 3.1-2). The nodal mesh used for this is shown in figure 3.1-9 where it can be seen that 920 nodes were used, excluding those on the Dirichlet boundaries. This was a substantial increase on the 79 used for the finite element solution. Execution time on a CDC 7600 computer was increased from 1.57 to 2.35 seconds. The two solutions are compared in figure 3.1-10 where it can be seen that agreement is almost perfect except in the vicinity of the void 'corner'. Here the change in potential is too abrupt to be represented by a fourth order polynomial. As a result, the finite element solution shows slight 'rounding' of the solution together with minor oscillatory over-shoots elsewhere. However, at maximum, the solutions differ by less than 1.5 percent. The numerical accuracy of the finite difference solution was high with the magnitude of the largest residual equal to only 0.65×10^{-10} and the algebraic sum of the residuals -0.55×10^{-8}. These figures reflect the high accuracy of the machine with its 60 bit word length.

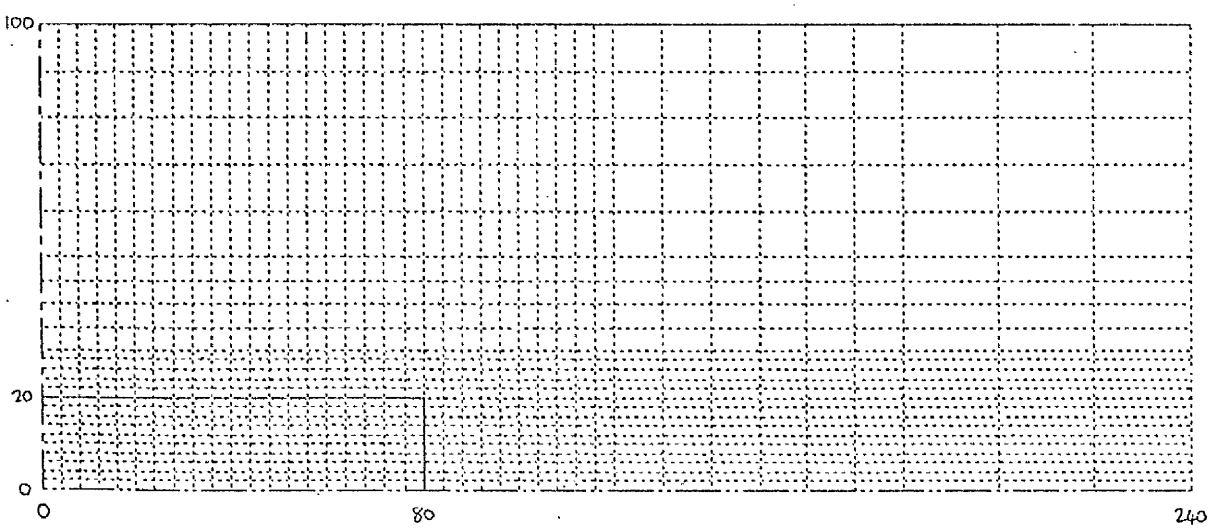

Figure 3.1-9 Nodal mesh used for finite difference solution of rectangular/cylindrical voids with $r/d = 2$ and $d/t = 0.2$

Comparison of axi-symmetric case with corresponding two dimensional rectangular shaped void

Figure 3.1-10 also shows the potential distribution obtained for the same configuration when a two dimensional problem is assumed. The stress

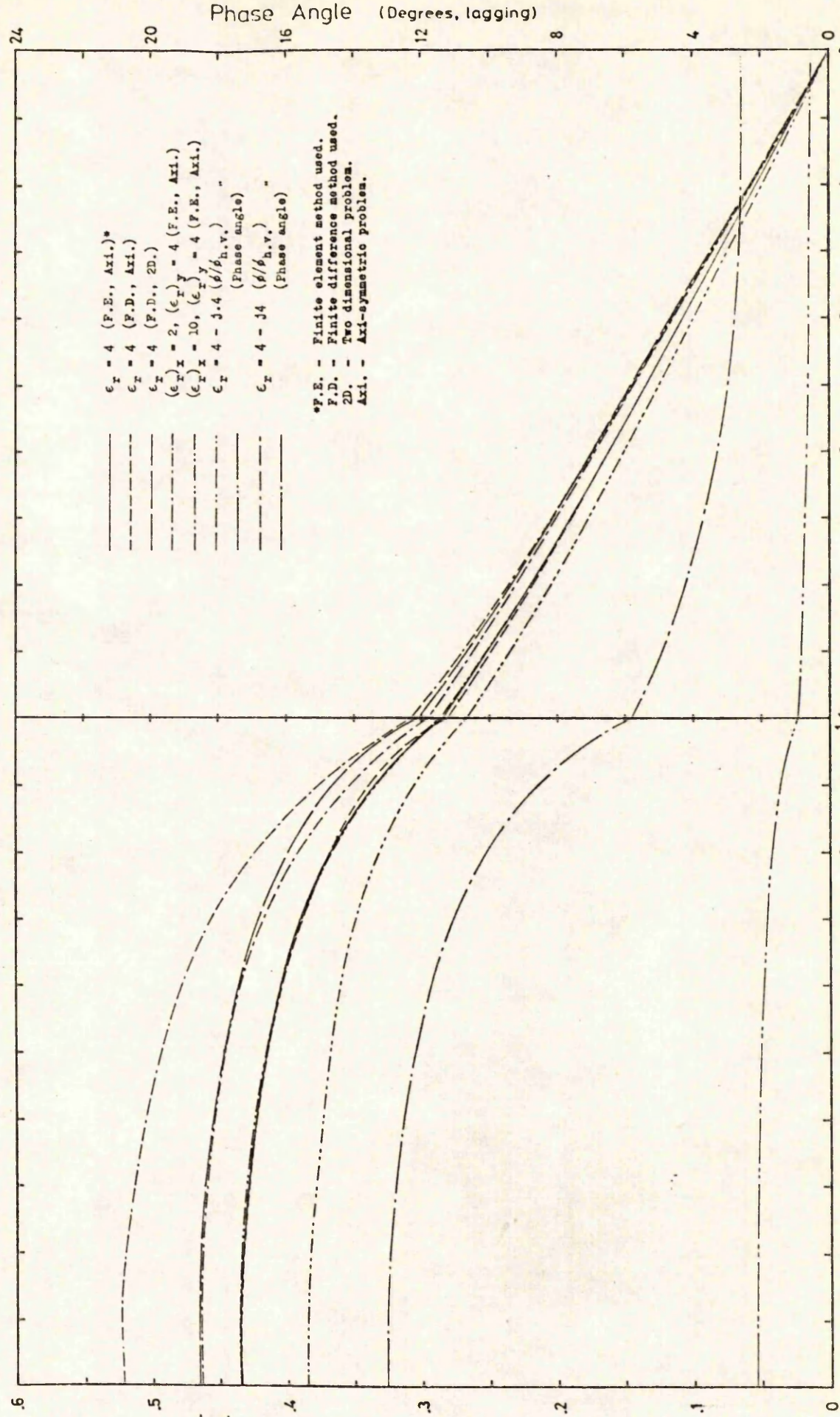

Figure 3.1-10 Compendium of results obtained for rectangular / cylindrical void with r/d = 2 and d/t = 0.2

enhancement is increased with $E'_V/E_i = 2.33$ and the effect on the capacitance is also greater with $C'_B/C_B = 0.678$. (c.f. $E'_V/E_i = 2.17$ and $C'_B/C_B = 0.716$ for the axisymmetric problem with $\epsilon_r = 4$)

Effect of dielectric anisotropy

The effect of dielectric anisotropy for the axisymmetric problem is shown in figure 3.1-10 as well. Maintaining the relative permittivity in the y direction at 4 but reducing it to 2 in the x direction results in an increase in the stress enhancement with $E'_V/E_i = 2.32$ and $C'_B/C_B = 0.697$ for an axi-symmetric problem. Conversely increasing the permittivity in the x direction to 10 results in less stress enhancement with $E'_V/E_i = 1.93$. The effect on the capacitance is also less with $C'_B/C_B = 0.745$.

Elliptic/oblate spheroidal void

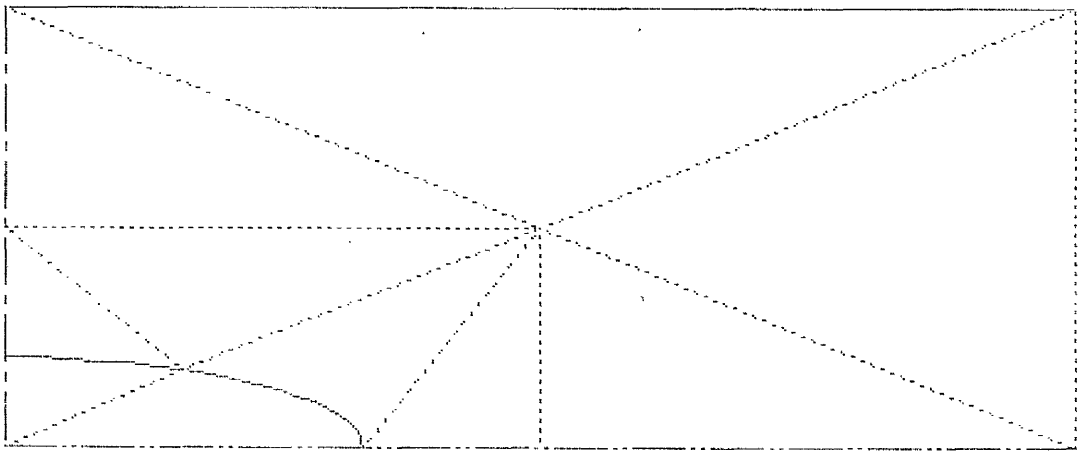

Figure 3.1-11 Elliptic/oblate spheroidal void analysed for comparison purposes. Finite element boundaries shown.

For comparison purposes the elliptic/oblate spheroidal void shown in figure 3.1-11 was investigated. This has major and minor axes equal to the depth and diameter respectively of the rectangular/cylindrical void just discussed and was analysed using the finite element method. The arrangement of the finite elements used is shown and it can be seen that the position of six intermediate nodes had to be re-specified. (Fourth order polynomials) For the axisymmetric case with $\epsilon_r = 4$, $E'_V/E_i = 2.04$ which is slightly less

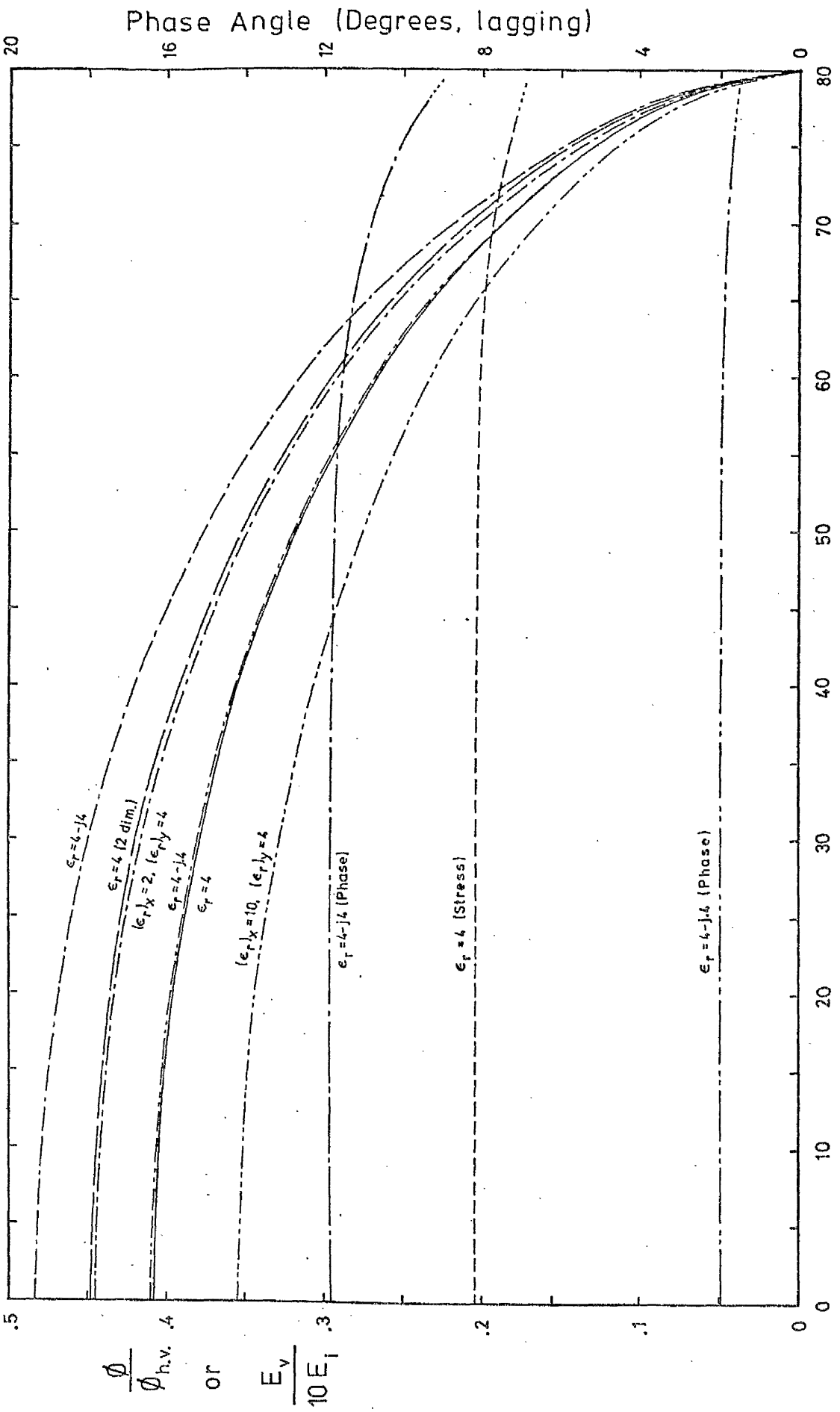

Figure 3.1-12 Results obtained for the elliptic / oblate spheroidal void shown in figure 3.1-11

than the corresponding figure for the cylindrical void. Not surprisingly C'_B/C_B is slightly higher than its counterpart with a value of 0.801 . Reducing $(\epsilon_r)_x$ to 2 but retaining $(\epsilon_r)_y = 4$, increases E'_v/E_i to 2.23 with C'_B/C_B reduced to 0.783 . In contrast, with $(\epsilon_r)_x = 10$, E'_v/E_i is reduced to 1.77 and C'_B/C_B increased to 0.827 . For the two dimensional problem with $\epsilon_r = 4$ the values for E'_v/E_i and C'_B/C_B are 2.24 and 0.739 respectively. Figure 3.1-12 shows the variations in potential along the void surface in each case and, in addition, gives the stress across the void for the axi-symmetric case with $\epsilon_r = 4$. The stress can be seen to be effectively constant across the void with just a slight reduction at the extremities.

The analysis of figure 3.1-11 required the solution of 79 non-Dirichlet nodes and took approximately 4.6 seconds of computer time. This substantial increase in computation time arose because resort to the Newton-Raphson technique was necessitated in order to transform the curved elements in the global plane to the simplex in the local plane. To check the fidelity of the global elements generated on transformation from local coordinates the void boundaries were mapped out. The results were favourable with a maximum error of less than 1 part in 10^5 for $x \leqslant 40$ and less than 1% for $x \leqslant 64$. However this increased to 18% with x = 76. This figure does not do justice to the accuracy of the representation as at this point on the ellipse the gradient is high. Viewed as an error in the x coordinate, the accuracy is better than 2%.

Two dimensional wedge - shaped void

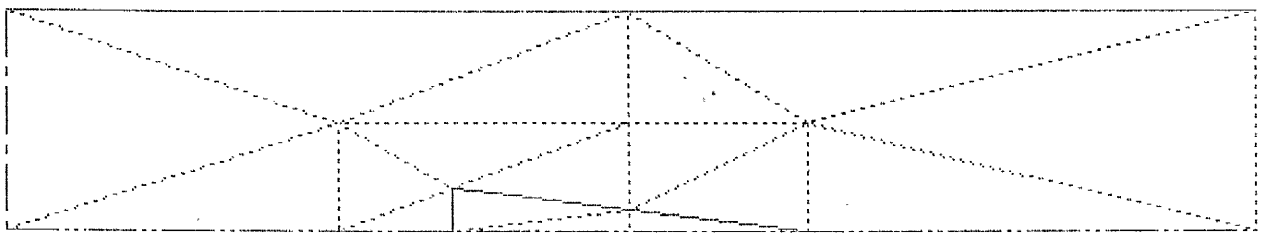

Figure 3.1-13 Wedge shaped void analysed for comparison purposes. Finite element boundaries shown.

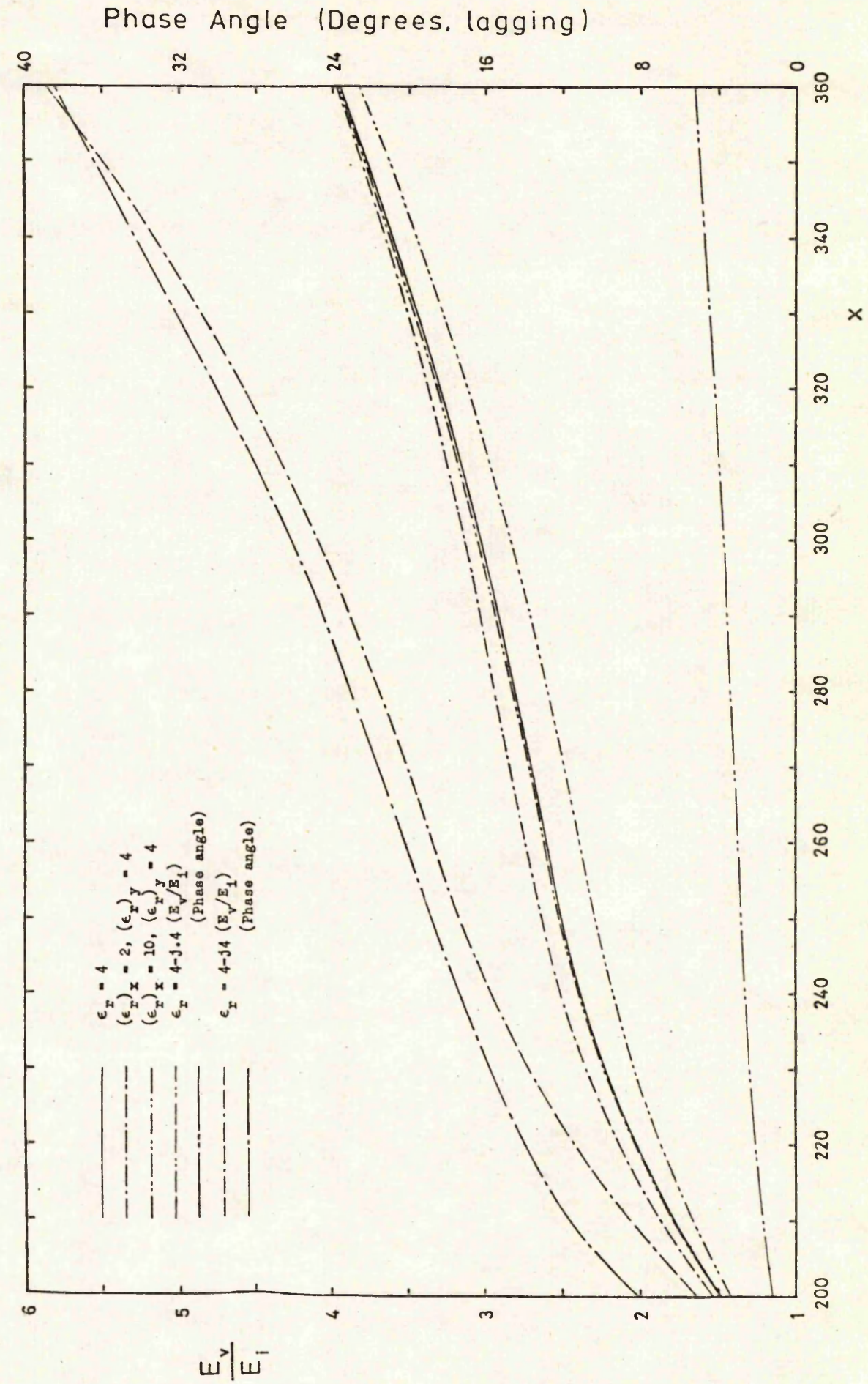

Figure 3.1-14 Results obtained for the wedge shaped void shown in figure 3.1-13

As a further comparison, the wedge shaped void shown in figure 3.1-13 was analysed. A void of this shape is potentially likely to arise in wrapped insulation and was therefore considered of interest to this study. The results obtained are shown in figure 3.1-14 where it can be seen that the stress enhancement, in each case, increases steadily towards the thin end of the void. It will be noticed that with $\epsilon_r = 4$ the stress enhancement at the void tip rises almost to 4, the value obtained for a lamina void normal to the field in an infinite dielectric region. Values for C'_B/C_B of 0.807, 0.815 and 0.829 are yielded with $(\epsilon_r)_y$ equal to 4 and $(\epsilon_r)_x$ equal to 2, 4 and 10 respectively. The solution was effected more satisfactorily in this instance by increasing the number of elements to 17 though this necessitated reducing the order of the approximating polynomials to 3. The problem required the solution of 68 non-Dirichlet nodes and typically took 1.46 seconds execution time. The results for figures 3.1-2(17), 3.1-11 and 3.1-13 are summarized in table 3.2-1 .

Equi-potential plots

To illustrate the effect of a void on the potential distribution, plots of the equi-potentials obtained for the void configurations of figures 3.1-2(17) and 3.1-11 are given in figures 3.1-15 and 3.1-16 respectively. In each case the dielectric is taken to have $\epsilon_r = 4$ and both the x - y and axisymmetric cases are plotted for comparison.

The curves demonstrate the increase in electric stress that occurs within the void and that the effect is greater for an x - y problem than for the corresponding axi-symmetric problem. The 'almost uniform' stress obtained in the case of the elliptic/spheroidal voids is also apparent.

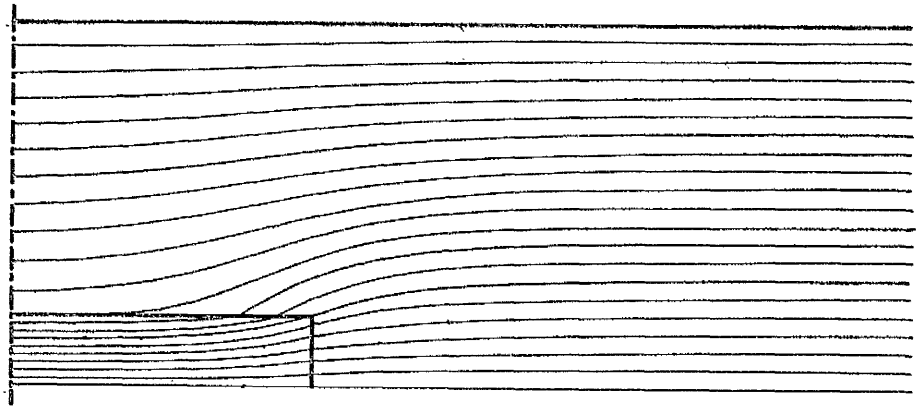

Figure 3.1-15(a) Plot of the equi-potentials obtained for the rectangular void of figure 3.1-2(17) with $\epsilon_r = 4$

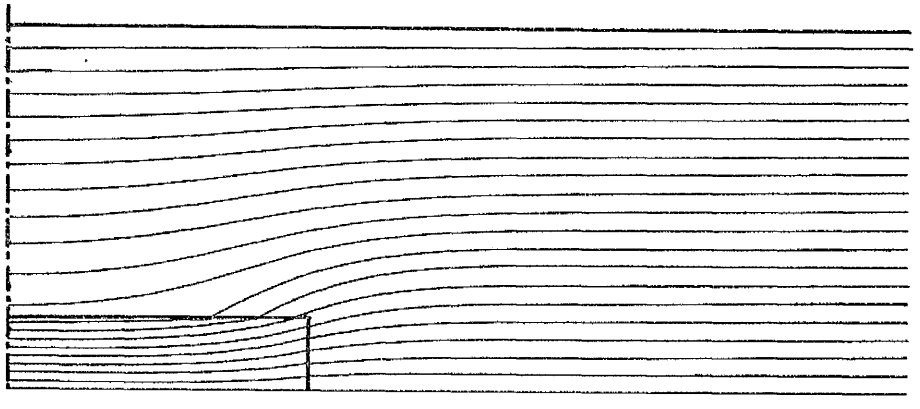

Figure 3.1-15(b) Plot of the equi-potentials obtained for the cylindrical void of figure 3.1-2(17) with $\epsilon_r = 4$

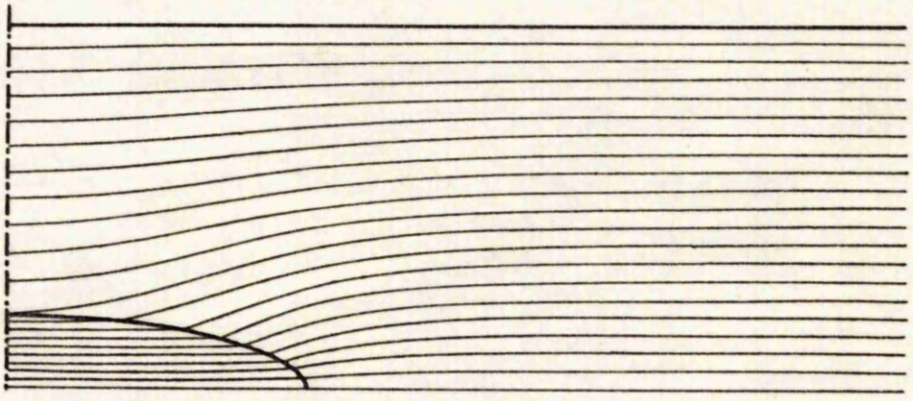

Figure 3.1-16(a) Plot of the equi-potentials obtained for the elliptic void of figure 3.1-11 with $\epsilon_r = 4$

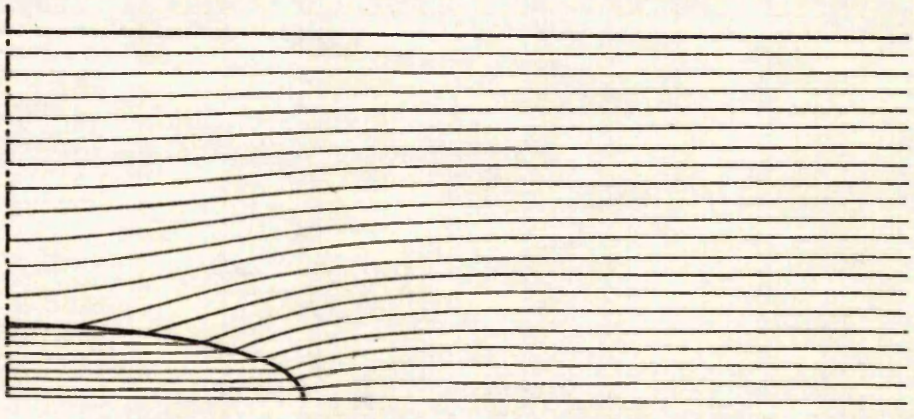

Figure 3.1-16(b) Plot of the equi-potentials obtained for the spheroidal void of figure 3.1-11 with $\epsilon_r = 4$

3.2 Cases with loss

When loss is involved the operator of equation (2.1-5) becomes complex and Wexler[83] points out that the operator will in general not be self adjoint. Since, without this property, stationarity at the solution point cannot be expected, the problem appears not to be amenable to solution by variational techniques. However Wexler shows this not to be the case by introducing the adjoint of the operator. This has the same solution as the original when applied to the adjoint of the problem in hand. By combining the two equations a new problem can be formulated, of dimension one greater than the original, that does have a self adjoint operator. The problem can be solved variationally but, in general, the operator will not be positive definite and so no guarantee of convergence can be given. Wexler points out though, that the chances of success are high if a methodical approach is adopted. The numerical errors will be smallest for those operators that are closest to being positive definite.

For the problem (of the Helmholtz type)

$$-(\nabla^2 - d)\,\phi = f \qquad (3.2\text{-}1)$$

with homogeneous Neumann or Dirichlet boundary conditions Wexler demonstrates that the matrix equation for the new, higher order, problem is of the form

$$\begin{bmatrix} [0] & S + d^*T \\ S + dT & [0] \end{bmatrix} \begin{bmatrix} \underline{\phi} \\ \underline{\phi}_a \end{bmatrix} = \begin{bmatrix} \underline{b}_a \\ \underline{b} \end{bmatrix} \qquad (3.2\text{-}2)$$

where

$$S = \iint \nabla\underline{\alpha}.\nabla\underline{\alpha}^T \, dxdy \qquad (3.2\text{-}3)$$

$$T = \iint \underline{\alpha}.\underline{\alpha}^T \, dxdy \qquad (3.2\text{-}4)$$

$$\underline{b} = \iint \underline{\alpha} \, f \, dxdy \qquad (3.2\text{-}5)$$

$$\underline{b}_a = \iint \underline{\alpha} \, f_a \, dxdy \qquad (3.2\text{-}6)$$

$\underline{\phi}_a$ and $\underline{b}_a$ relate to the adjoint problem. $[0]$ is a square matrix of zeros having the same order as the other matrices. The solution to the adjoint problem is not of interest. It is an arbitrary field as the source function

f_a does not need to be specified and the only requirement is that it must satisfy the same boundary conditions as the true field. It may therefore be discarded leaving, from equation 3.2-2, the solution of

$$(S + dT)\,\underline{\phi} = \underline{b} \qquad (3.2\text{-}7a)$$

For the fields solved in this study $d = 0$ and this equation therefore reduces to

$$S\,\underline{\phi} = \underline{b} \qquad (3.2\text{-}7b)$$

This is identical in form to equation 2.3-19 and may therefore be extended to include inhomogeneous and mixed boundary conditions in a similar manner. It differs from equation 2.3-19 in that the vectors $\underline{\phi}$ and $\underline{b}$ are complex if the source function is complex. In addition matrix S will be complex if the operator is complex as the full expression for S is

$$S = \iint \nabla\underline{\alpha} \cdot (\underline{\underline{k}}\,\nabla\underline{\alpha}^T)\,dxdy + \iint d\,\underline{\alpha}\cdot\underline{\alpha}^T\,dxdy + \int_c \sigma\,\underline{\alpha}\,\underline{\alpha}^T\,ds \qquad (3.2\text{-}8a)$$

Adapting MANFEP (see figure 2.3-1) to solve complex problems involves changing a number of variables and arrays from real to complex notation. Firstly the S and B arrays must be changed together with the various arrays that contain the nodal solutions. The value of the field at any point will, in general, be complex as will its spatial derivatives and flux components. Complex boundary conditions (Dirichlet, Neumann or mixed) demand that the corresponding variables be complex and, in the case of variable boundary conditions, so also must the associated functions. The same applies to the variables and functions required when specifying any filamentary elements. The complex operator manifests itself through the coefficients a, b and c of Poisson's equation (equation 2.1-18) and these will therefore, in general, be complex. The source function ρ can also be complex as can the coefficient d in the Helmholtz equation. When evaluating the functional of an element both the contribution from the line integration and that from the surface integration can be complex. Therefore all variables denoting functional

values or sums thereof must be specified as complex. During the operation of the program it is convenient in many cases to store the variables relating directly to the element that is being computed at that particular instant in local arrays. These arrays are smaller than their global counterparts and are reused during the computation of subsequent elements. These local arrays must be designated as complex if the global array is such. Finally some variables used for summation, efficiency and general computation purposes require to be made complex.

Other minor changes are required. For instance the final system of simultaneous equations is solved for the nodal function values by Gaussian elimination. To maintain numerical accuracy a pivotting strategy is employed and, in order to find the largest diagonal element, the moduli of the elements must be compared rather than their complex values. Format statements must also be altered to make allowance for the increase in the number of characters transferred during reading and writing operations.

Calculation of capacitance and loss tangent from functional

Under steady-state time harmonic excitation the mean energy stored in a dielectric region is given by (two dimensional problem)

$$U = \tfrac{1}{2}\,\mathrm{Re}\left\{\iint \underline{D} \cdot \underline{E}^{*}\, dxdy\right\} \qquad (3.2\text{-}8b)$$

If the coefficients b, d and ρ of the second order elliptic equation are zero, in matrix form

$$\underline{D} = \begin{bmatrix} D_x \\ D_y \end{bmatrix} = \begin{bmatrix} a & 0 \\ 0 & c \end{bmatrix} \begin{bmatrix} E_x \\ E_y \end{bmatrix} = \begin{bmatrix} aE_x \\ cE_y \end{bmatrix} \qquad (3.2\text{-}9)$$

and

$$\underline{D}^{T}\,\underline{E}^{*} = a\,E_x\,E_x^{*} + c\,E_y\,E_y^{*} \qquad (3.2\text{-}10)$$

Taking

$$a = \epsilon_o(\epsilon_x' - j\epsilon_x'') \quad \text{and} \quad c = \epsilon_o(\epsilon_y' - j\epsilon_y'') \qquad (3.2\text{-}11)$$

the real part of equation 3.2-10 gives the stored energy namely

$$\mathrm{Re}\,(\underline{D}^{T} \cdot \underline{E}^{*}) = \epsilon_o\left\{\epsilon_x'\,E_x\,E_x^{*} + \epsilon_y'\,E_y\,E_y^{*}\right\} \qquad (3.2\text{-}12)$$

Thus the matrix form of equation (3.2-8b) is

$$U = \tfrac{1}{2}\,\mathrm{Re}\left\{\iint \underline{D}^T\,\underline{E}^*\,dxdy\right\} \qquad (3.2\text{-}13)$$

Hence by replacing ϕ_i with ϕ_i^* for the second summation in equation 2.3-40 the real part of the surface integral in the expression for the functional is made equal to twice the mean energy stored in the dielectric. Summing the results over all the elements and dividing by the square of the r.m.s. voltage then yields the overall capacitance. ($C = 2\,U_{mean}/V^2_{r.m.s.}$)

The power dissipated overall is given by

$$W = 2\omega\iint \tan\delta_x\,U_x + \tan\delta_y\,U_y\,dxdy \qquad (3.2\text{-}14)$$

where the x and y subscripts denote the components attributable to the x and y directions respectively. Since $\tan\delta_x = \epsilon''_x/\epsilon'_x$, $U_x = \tfrac{1}{2}\epsilon_o\epsilon'_x E_x E_x^*$ etc

$$W = \epsilon_o\omega\iint \epsilon''_x E_x E_x^* + \epsilon''_y E_y E_y^*\,dxdy \qquad (3.2\text{-}15a)$$

or

$$W = -\omega\,\mathrm{Im}\left\{\iint \underline{D}^T\,\underline{E}^*\,dxdy\right\} \qquad (3.2\text{-}15b)$$

and

$$\tan\delta = \frac{W}{2\omega U} = \frac{-\,\mathrm{Im}\left\{\iint \nabla\phi.(\underline{k}\,\nabla\phi)dxdy\right\}}{\mathrm{Re}\left\{\iint \nabla\phi.(\underline{k}\,\nabla\phi)dxdy\right\}} \qquad (3.2\text{-}16)$$

Thus the overall loss tangent is given by the negative of the quotient of the imaginary and real parts of the surface integral contribution to the functional.

This analysis can be extended to axially symmetric problems in the same way as before (see equation 3.1-9) However the expression for the loss tangent is independent of any multiplying constant and is therefore equally applicable to both two dimensional and axisymmetric problems.

Once more, to reduce the numerical answers to dimensionless constants, the change in sample capacitance due to the presence of the void was expressed through the ratio C'_B / C_B. (See figure 3.1-5) The change in the loss tangent could be similarly expressed as the ratio of the loss tangents of C'_B and C_B i.e. $(\tan\delta)'_B / (\tan\delta)_B$. To evaluate this ratio, $(\tan\delta)'_B$ was calculated using the expression

$$C'_T\,(\tan\delta)'_T = C_A\,(\tan\delta)_A + C'_B\,(\tan\delta)'_B \qquad (3.2\text{-}17)$$

which is immediately obtained from consideration of the equivalent conductivities

of the individual components.

Table 3.2-1 Summary of electric stress, capacitance and loss tangent changes for figures 3.1-2(17), 3.1-11 and 3.1-13

Figure No.	Config.	Permittivity		Stress enhancement		Reduction in tanδ	Reduction in capacitance
		$(\epsilon_r)_x$	$(\epsilon_r)_y$	E'_V/E_i		$\frac{(\tan\delta)'_B}{(\tan\delta)_B}$	C'_B / C_B
3.1-2(17)	x - y	4	4	2.33		-	0.678
	axi.	4	4	2.17		-	0.716
	axi.	2	4	2.32		-	0.697
	axi.	10	4	1.93		-	0.745
	axi.	4-j0.4	4-j0.4	2.17		0.743	0.717
	axi.	4-j4	4-j4	2.61		0.705	0.758
3.1-11	x - y	4	4	2.24		-	0.739
	axi.	4	4	2.04		-	0.801
	axi.	2	4	2.23		-	0.783
	axi.	10	4	1.77		-	0.827
	axi.	4-j0.4	4-j0.4	2.05		0.832	0.802
	axi.	4-j4	4-j4	2.41		0.777	0.833
				(I)	(II)		
3.1-13	x - y	4	4	3.95	1.49	-	0.815
	x - y	2	4	3.98	1.53	-	0.807
	x - y	10	4	3.82	1.42	-	0.829
	x - y	4-j0.4	4-j0.4	3.96	1.49	0.803	0.816
	x - y	4-j4	4-j4	5.85	1.64	0.701	0.892

(I) Thin end of wedge:- x = 360 (II) Thick end:- x = 200

Results obtained with a lossy dielectric

From figures 3.1-10, 3.1-12 and 3.1-14 it is evident that the modulus of the potential distribution in and around a void is virtually unaltered on increasing the loss tangent from zero to 0.1 . A change in the argument of the potential on the void surface does however occur but this is small. The minimum and maximum deviations are -0.96, -2.17; -1.64, -1.97 and -1.22, -5.04 degrees for the 'pill box', spheroid and 'wedge' respectively. On further increasing the loss tangent to 1.0 a noticeable increase in the modulus of the electric stress across the void occurs, the maximum stresses being, respectively, 20.3%, 18.1% and 48.1% up on those with $\tan\delta = 0$. The increase is less away from the areas of maximum stress. With $\tan\delta = 1.0$ the arguments are also considerably increased with minimum and maximum deviations of -5.81, -13.07; -9.87, -11.80 and -8.13, -36.86 degrees respectively. In all cases dielectric loss results in lagging phase angles for the potential distribution.

Semiconducting films

Discharge activity in a void can result in the formation of a carbonized layer within the surface of the void. This will have a finite conductivity and will therefore affect the potential distribution in and around the void. Similarly water vapour can be formed in the void as a result of discharge activity and this can then condense on the void surface to form a semiconducting layer. This layer will have a similar effect to the carbonized layer but with the exception that it will be less permanent because the water will tend to diffuse away from the void into the surrounding dielectric. In both cases conduction currents will flow in the film under a.c. conditions resulting in a resistive loss which will manifest itself at the high voltage measurement terminals as an apparent dielectric loss. In this section the effect on the potential distribution, capacitance and loss tangent of films of different conductivity is calculated for the void shapes of figures 3.1-2(17), 3.1-11 and 3.1-13.

For the purpose of analysis by the finite element method the conducting film can be treated as a filamentary element of infinitessimal thickness yet with a finite film coefficient as discussed in chapter 2. The analysis there assumed the coefficient to be real but, by extending to the complex case, lossy films may also be included.

If the film coefficient is

$$k_f = k_f' - jk_f'' \qquad (3.2\text{-}18)$$

then the susceptance per square is

$$S = \omega k_f' \qquad (3.2\text{-}19)$$

and the conductance per square

$$G = \omega k_f'' \qquad (3.2\text{-}20)$$

Therefore in the case of a purely resistive film $S = 0$ and

$$k_f = 0 - jG/\omega \qquad (3.2\text{-}21)$$

To investigate the effect of surface conductivity on the three different shapes of void, the required filamentary elements were established and equation (3.2-21) applied over a wide range of conductivities. Unfortunately the results were disappointing with the variations in the potentials along the void surfaces exhibiting pronounced oscillations both in magnitude and phase. It was concluded that the solutions were non-polynomic and therefore not amenable to the use of a simple element structure with higher order interpolatory polynomials. Two ways of overcoming this difficulty were apparent. Either the element structure could be increased in complexity and linear interpolation used or a finite difference approach could be adopted again using linear interpolation. The latter was considered preferable as the coefficient matrix could be banded more simply thereby easing the computational requirements and permitting a greater number of nodes to be used.

The finite difference representations of figures 3.1-2(17), 3.1-11 and 3.1-13 are shown in figures 3.1-9, 3.2-1 and 3.2-2 respectively. The

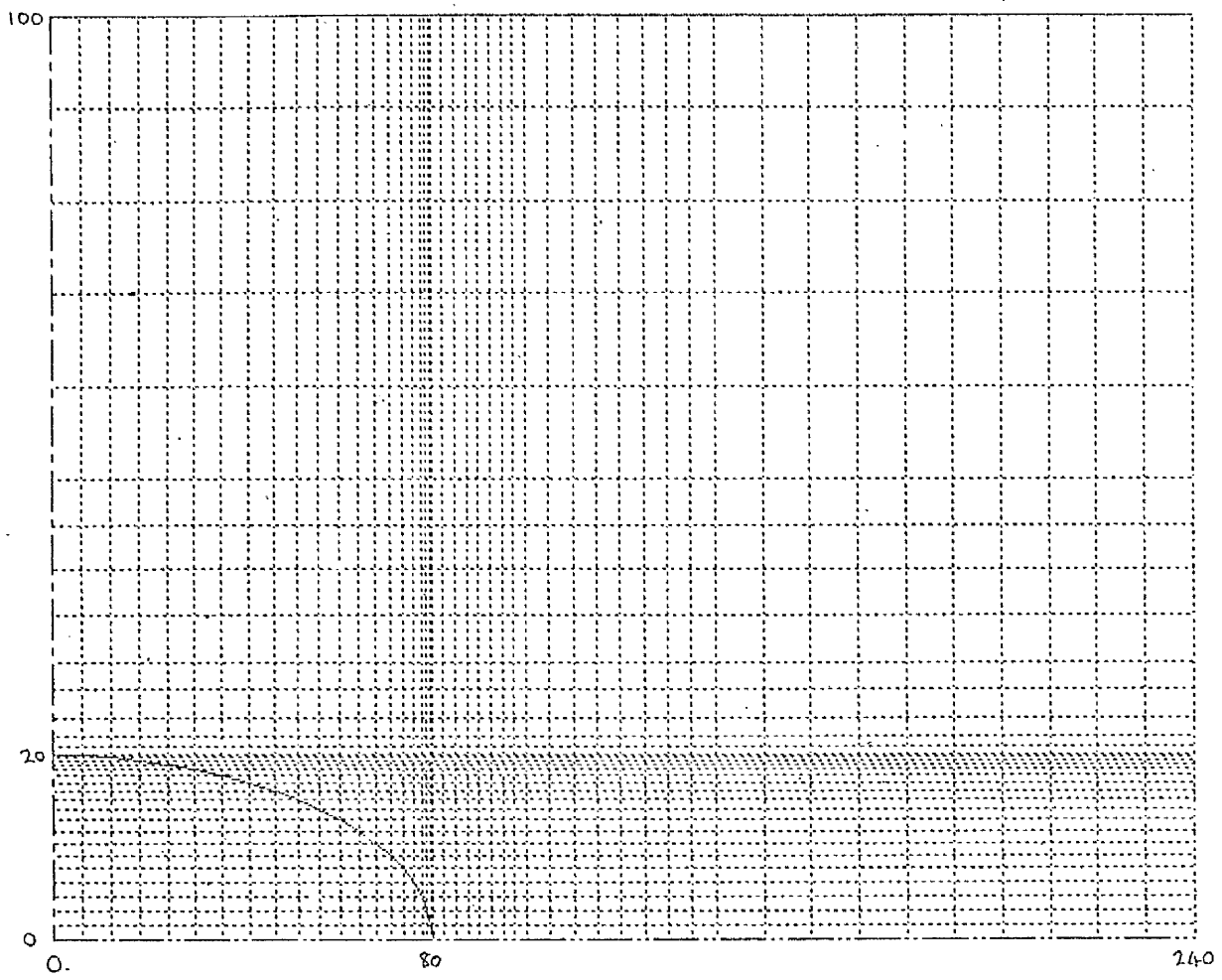

Figure 3.2-1 Finite difference representation of oblate spheroidal cavity given in figure 3.1-11

presence of the conducting films necessitated the addition of extra components to the complex coefficient matrix and, in the cases of the oblate spheroid and the wedge, these resulted in diagonal links that increased the overall bandwidth of the matrix as discussed in chapter 2. As figures 3.1-9 and 3.2-1 represent axi-symmetric problems all 'admittance' values between nodes were multiplied by their mean distance from the axis of rotation in an analogous manner to that used with the finite element method. By this means the capacitance and conductance of the overall system (all four quadrants) could be obtained by simply multiplying the result calculated using equations (2.2-31) and (2.2-32) by the factor π. The loss tangent however was given

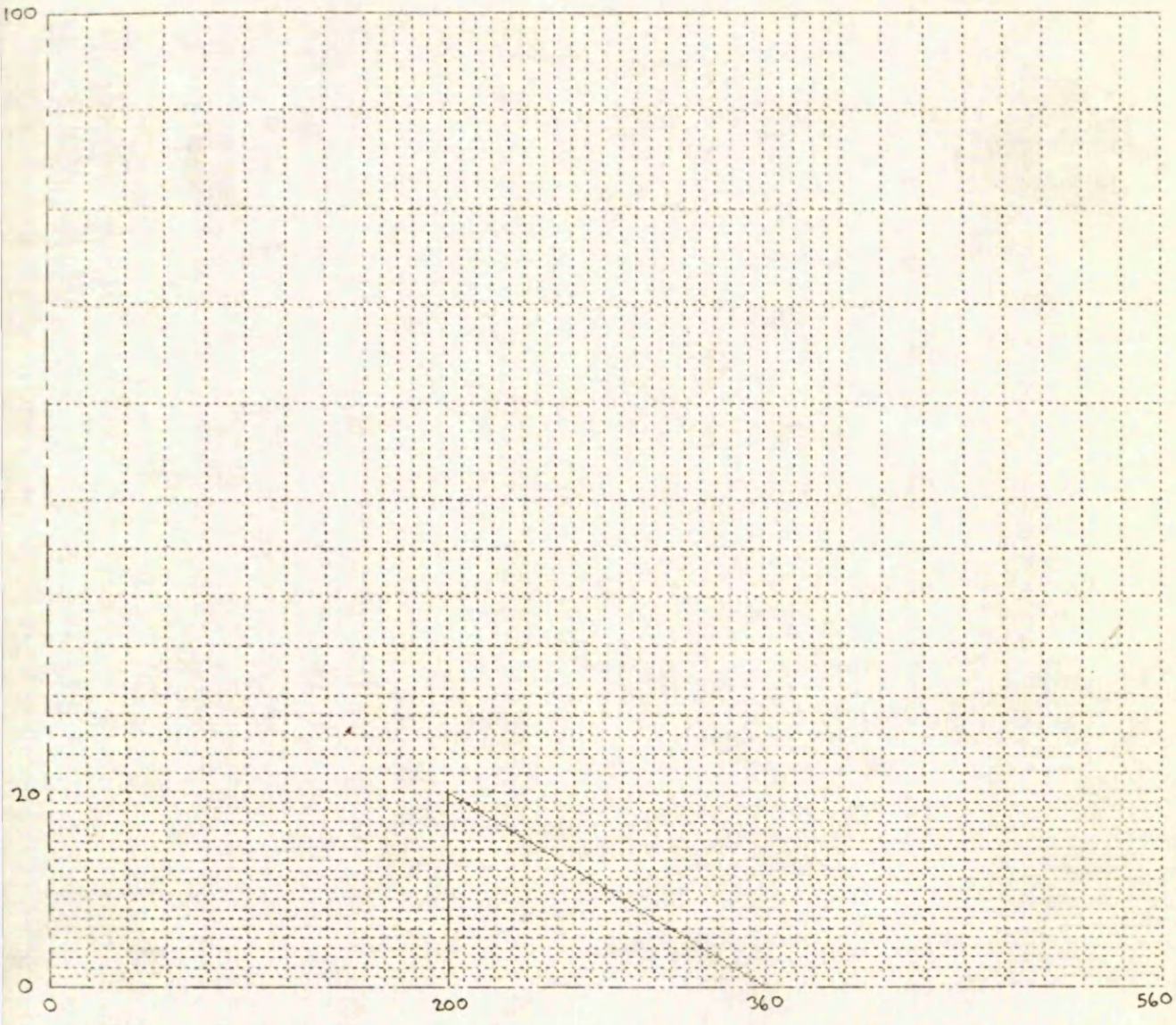

Figure 3.2-2 Finite difference representation of 'wedge' shaped void shown in figure 3.1-13

directly by equation (2.2-33).

Effect on electric stress distribution - 'pill box' shaped void

The effect of a conducting film on the electric stress across the 'pill-box' shaped void is shown in figure 3.2-3 . The mean axial stress is given relative to that obtained for the same void but with no conducting film, over a wide range of void surface conductivities. The stress is expressed as a ratio to demonstrate the effect of surface conductivity on the discharge inception voltage which will vary in inverse proportion to the stress ratio. The curves confirm the experimental observation that discharge activity ceases when there is appreciable surface conductivity. However

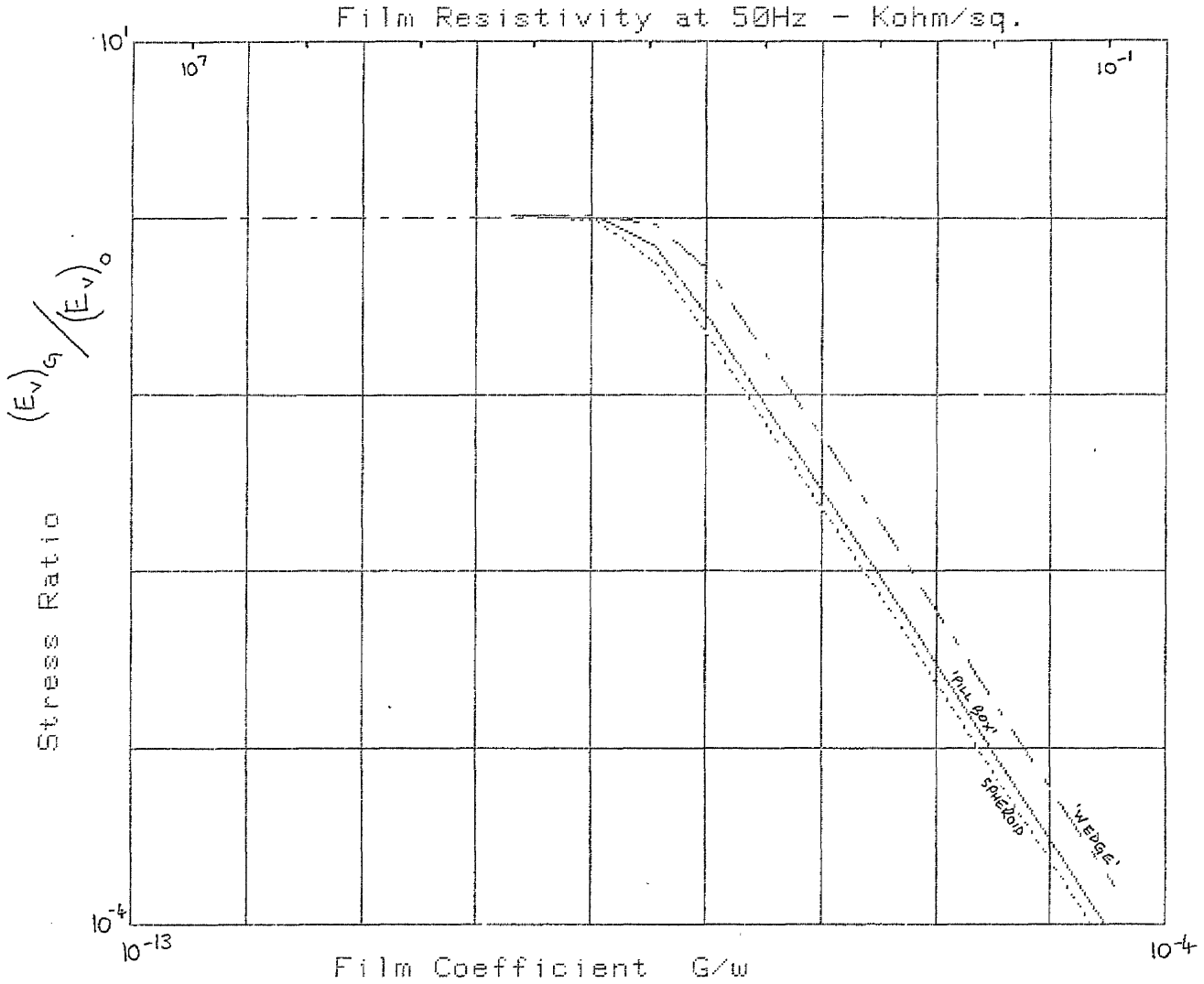

Figure 3.2-3 The effect of surface conductivity on the modulus of the mean electric stress across the three different void shapes. (Axial stress given for 'pill box' and spheroid. Central stress given for 'wedge'.)
i.e. x = 280

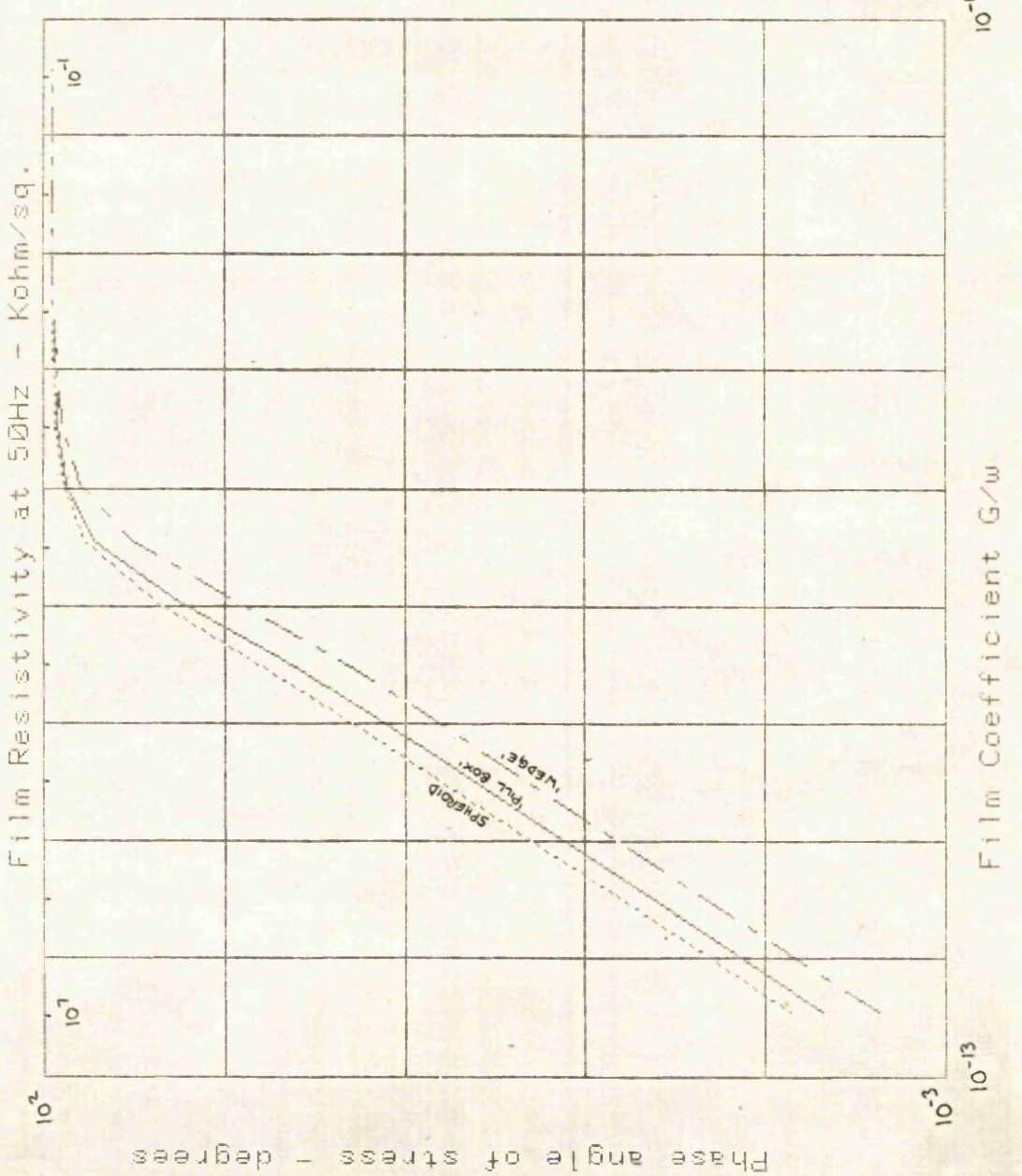

Figure 3.2-4 The effect of surface conductivity on the argument of the mean electric stress across a void

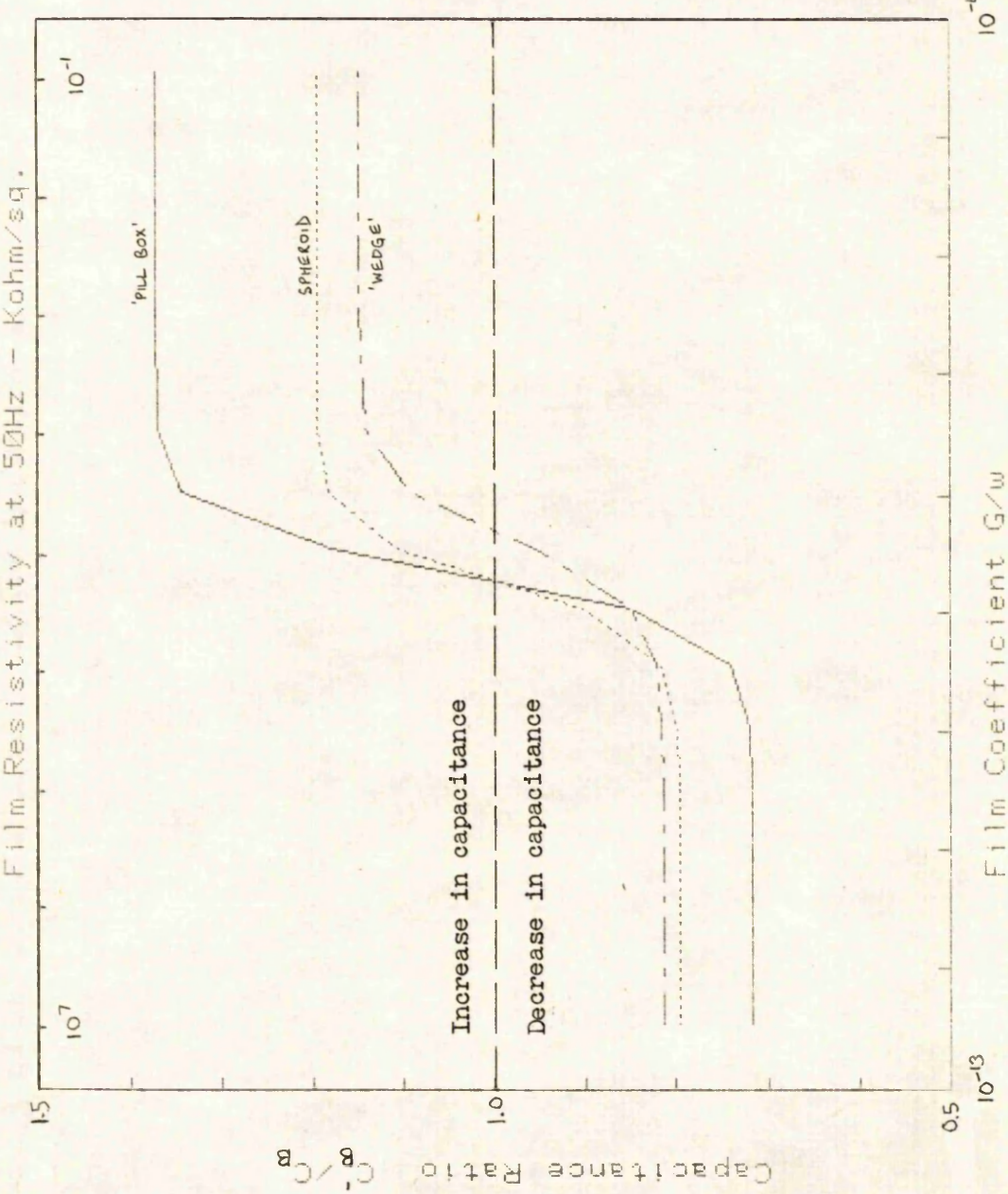

Figure 3.2-5 The effect of void surface conductivity on the capacitance of the test specimen

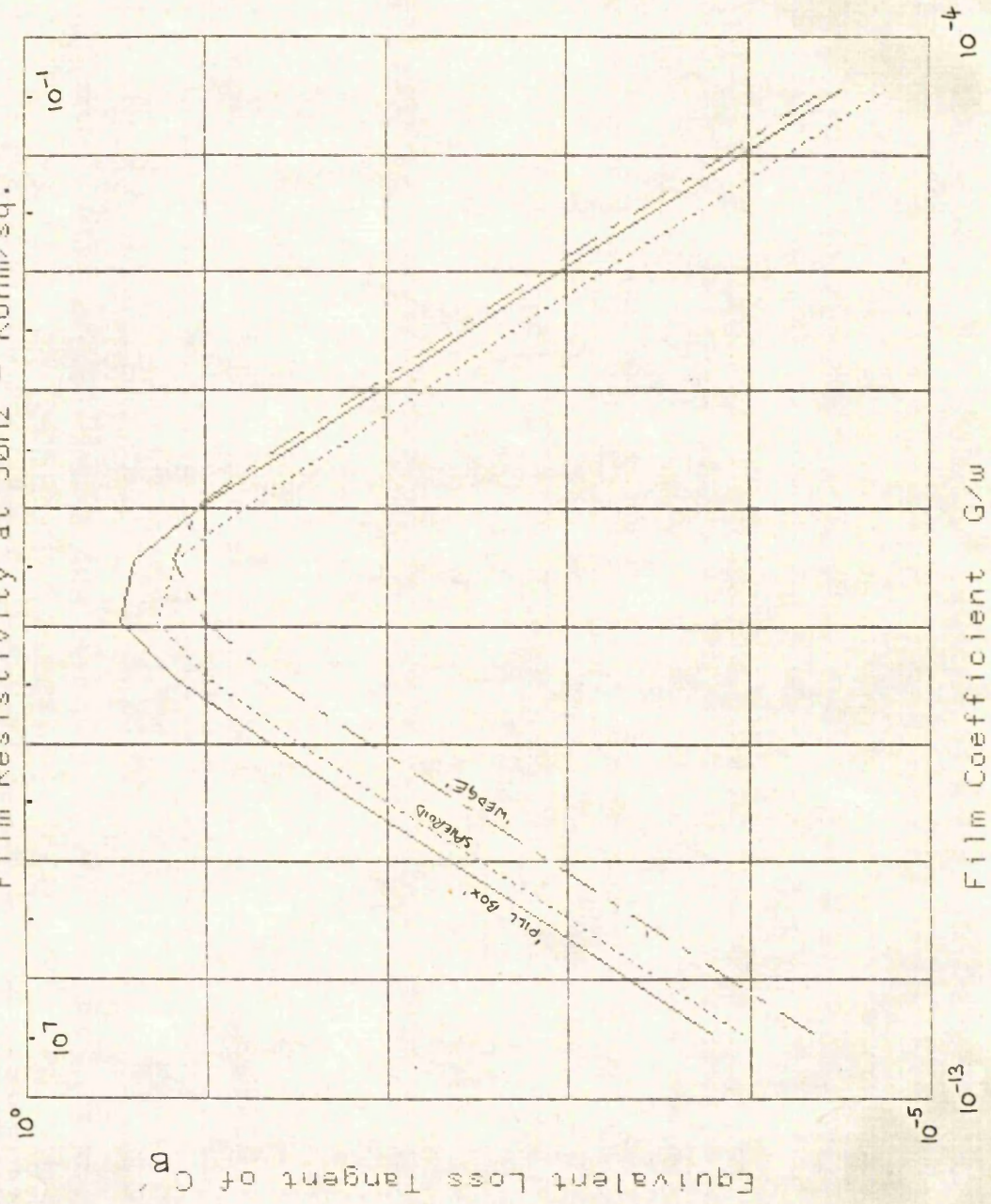

Figure 3.2-6 The effect of void surface conductivity on the loss tangent of the test specimen

a surprising observation from the curves is that, for some conductivities, the stress is increased rather than decreased. This is a consequence of the rapid increase in the phase angle of the electric stress across the void relative to the applied voltage. Though the in-phase component of the stress falls monotonically as the conductivity increases, the quadrature component increases rapidly and, as a consequence, the resultant electric stress can show a small, but definite, increase in magnitude. The plot of the phase angle of E_v given in figure 3.2-4 shows the stress to be virtually in phase with the applied voltage for small values of conductivity but to increase rapidly in an intermediate range of conductivities finally approaching quadrature (E_v leading) for high values of conductivity.

Effect on capacitance and loss tangent

Figure 3.2-5 shows the effect of surface conductivity on the overall capacitance. Again the change in capacitance is expressed through the dimensionless ratio C_B' / C_B and the curves show the manner in which this ratio increases from 0.716, the value with no conductivity of the void surface, to 1.376, the value with a perfectly conducting void.

For this example the loss tangent of the dielectric is taken as zero and therefore the loss is attributable solely to the conducting film. To quantify this loss in a dimensionless form (including being independent of frequency) the loss is expressed as an effective loss tangent of the capacitance C_B'. The values thus obtained are plotted in figure 3.2-6 and it can be seen that, for small values of conductivity, the loss tangent increases linearly with increase in conductivity. The loss tangent peaks at an intermediate value of conductivity and then starts to decrease with further increase in the conductivity, the rate of decrease becoming linear for large values of conductivity.

Comparison with spheroidal and 'wedge' shaped voids

The magnitude and phase angle plots of the mean axial stress across the oblate spheroidal void are also given in figures 3.2-3 and 3.2-4 for the same range of void surface conductivities and the corresponding capacitance

and loss tangent variations are given in figures 3.2-5 and 3.2-6.

The node points defining the void / dielectric interface of figure 3.2-1 were obtained from the parametric equations for an ellipse

$$x = a \cos \theta \; ; \quad y = b \sin \theta \qquad (3.2\text{-}22)$$

where a and b are the semi-major and semi-minor axes respectively, by dividing the quadrant into twenty equal increments of θ. By this means a reasonably even distribution of node points was established along the whole void surface. The lines of the finite difference grid that were adjacent to the void but did not cut it were chosen to have a fixed, small separation. This separation was then increased to a somewhat larger value for the next group of lines away from the void and beyond this group the separation was further increased. By this means a reasonably simple and economical grid was formed that could accommodate the sample's geometry and provide a concentration of nodes in the areas with the least uniform fields. The results show that the effect of the conductivity on the axial stress across the void is more pronounced than it is for the 'pill-box' shaped void. The capacitance variations however are similar and the values of the effective loss tangent smaller.

For comparison purposes the modulus and argument of the stress across the centre (i.e. x = 280) of the wedge shaped void have been plotted as well in figures 3.2-3 and 3.2-4 . In common with the other two shapes of void, the modulus of the electric stress increases slightly as the conductivity increases to a level where significant phase shifting of the stress vector occurs and then decreases for further increases in conductivity. The phase of the vector once more approaches quadrature for large conductivities and the modulus falls linearly. It is interesting to note that for all three voids as the conductivity increases the quadrature component of the electric stress rises linearly for small values of conductivity but falls linearly for large values. In contrast the in-phase component falls continuously, the change being only small for the lower values of conductivity but increasing to a square law for large conductivities. From figures 3.2-5 and 3.2-6 it can be seen that the variations in capacitance and loss tangent follow

a similar pattern for the wedge to those for the other two void shapes.

Execution time on the CDC 7600 computer was approximately 5.5 seconds for both the wedge and the spheroidal shaped voids compared with only 2.5 seconds for the pill-box shaped void. These figures reflect the larger number (1551) of non-Dirichlet nodes used for the wedge and the spheroid compared with the 920 used for the pill-box and also the increase in the coefficient matrix bandwidth occasioned by the presence of diagonal links in the finite difference grid.

Figures 3.2-3 to 3.2-6 show the variations in the various parameters as a function of G/ω this quantity having the dimension Siemen second. For ease of interpretation the corresponding values of conductivity at 50 Hz are also given and these may be used at other frequencies provided the conductivity is scaled pro-rata. Thus it is apparent that at very low frequencies even the most modest surface conductivity can seriously alter the stress distribution in a void. For these three examples surface conductivity of the voids is shown to have little effect provided the surface resistivity is greater than 10^6 ohm/square with 50 Hz excitation but below this it has a considerable effect. As this figure must be increased to 5×10^8 ohm/square with 0.1 Hz excitation, it is evident that care must be taken when analysing the results of discharge measurements obtained using very low frequency excitation.

3.3 The effect of a partial discharge

The work so far has described in some detail the electrostatic effects of voids in insulation both for lossless and for lossy cases. The interest in the potential distributions derived is primarily concerned with establishing under what circumstances partial discharges are likely to occur. When a partial discharge does occur the stress distribution within the insulation is left considerably different from that prior to the discharge and it is this difference that results in the externally detectable changes in the

electrical parameters of the insulation structure that are most commonly used for partial discharge detection. Discharge detectors in this category include both narrow and broadband types, and those involving the measurement of dielectric loss but exclude those measuring the electromagnetic or acoustic emissions associated with the breakdown process. At present only a qualitative measure of the relationship between the externally detectable effects and the actual discharge can be made which is inadequate if an accurate assessment of the condition of insulation is to be made. To illustrate this point consider the three capacitor model shown in figure 3.3-1, where b is the

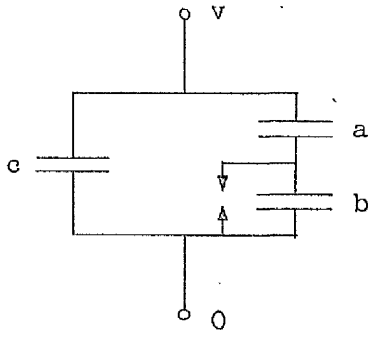

Figure 3.3-1 Three capacitor model of discharging insulation structure

capacitance of the discharging void, a is its series capacitance and c is the capacitance of the remainder of the insulation structure. If a constant voltage v is maintained across the structure, the actual charge transferred during the breakdown of the void is given by

$$\Delta Q_r = C.\Delta V = (a + b)\, v \frac{a}{a + b} = va \qquad (3.3\text{-}1)$$

assuming b to be completely discharged. However the charge supplied by the external circuit to maintain v constant is given by

$$\Delta Q_a = \Delta C.V = \left\{(c + a) - \left[c + \frac{ab}{a + b}\right]\right\} v = \frac{a^2}{a + b} v \qquad (3.3\text{-}2)$$

ΔQ_a, the apparent charge transferred, can be measured in the external circuit and is related to the real charge by

$$\Delta Q_a / \Delta Q_r = a / (a + b) \qquad (3.3\text{-}3)$$

Unfortunately neither a nor b are normally known and so there is a degree of uncertainty associated with assessing the magnitude of discharges from the

apparent charge transfer. This is not the case however if the discharge energies are measured for, the energy supplied by the external circuit is given by

$$\Delta E = \tfrac{1}{2}\Delta C.\, V^2 = \tfrac{1}{2}\left\{(c + a) - \left[c + \frac{ab}{a + b}\right]\right\} v^2 = \tfrac{1}{2}\frac{a^2 v^2}{a + b} \qquad (3.3\text{-}4)$$

and this is equal to the energy dissipated in the discharge namely

$$E = \tfrac{1}{2} C V^2 = \tfrac{1}{2}(a + b)\left[\frac{av}{a + b}\right]^2 = \tfrac{1}{2}\frac{a^2 v^2}{a + b} \qquad (3.3\text{-}5)$$

It would therefore appear that measurement of the loss of energy, rather than charge, would be more satisfactory but this alternative, in general, presents difficulties. For an insulation structure containing a single discharge site that breaks down a fixed number of times per cycle under high voltage a.c. excitation with all the discharges of equal magnitude, the magnitude of the discharge energy is readily obtained from measurements of the loss tangent. However if there is more than one discharge site or the discharges at the one site are of differing magnitudes, such a measurement will yield the mean energy dissipated per cycle rather than details of the individual discharges. Though this information is satisfactory for assessing the state of some types of insulation (e.g. micaceous) it is not very satisfactory in general. As an alternative, in some instances the apparent charge transfer can be multiplied by the instantaneous energising voltage to yield the discharge energy but this will not normally be true when a.c. testing because the voltage across a void can be considerably out-of-phase with the h.v. excitation owing to previous discharge activity. Because of these difficulties it is normal to measure ΔQ_a when discharge testing.

Ratio of apparent / real charge transfer

As the magnitude of the ratio $\Delta Q_a/\Delta Q_r$ is so important it was considered worthwhile to extend the computational work of this study to include the effects of partial discharges in the void configurations of figure 3.1-2 . The principle of the method used is as follows. Initially the nodal voltages are calculated as before to establish the nodal voltages prior to discharge. (i.e. assuming the upper and lower electrodes to be at +1000 and -1000 volts

respectively) The computation is then repeated with equal and opposite charges assumed to be deposited on each end of the void and the electrodes at zero potential. This second computation yields a new set of nodal voltages, of which any multiple may be added to or subtracted from the previous set by the law of superposition. Thus by suitable choice of multiplying factor (a_o) any given nodal voltage in the first set can be reduced to zero.

The node located centrally on the end face of the void (and hence on the axis of rotation) was chosen to be set to zero in order to represent the condition just after the discharge has extinguished. At this point in time the potentials at the centres of the end faces of the void will have been reduced substantially to zero as a result of the discharge yet, because the conducting channel will have disappeared, the potential along the axis will be able to float. The computation assumes the discharge to occur along the axis of the void this being considered the most probable site as the stress is greatest here. The rate at which the charge density falls-off the axis is debateable, but for this study the distribution was assumed to have the Gaussian form

$$\rho(r) = a_o e^{-r^2/R_o^2} \qquad (3.3\text{-}6)$$

Three fall-off rates were considered to cover different relative void and conducting channel sizes namely $R_o/R = 0.25$, 0.5 and 1.0 where R is the radius of the void. As the configurations were axisymmetric the charge density was multiplied by r in-line with the other parameters. The actual charge transfer required to reduce the voltage across the void to zero could be calculated from

$$Q_n = \int_0^{2\pi}\int_0^{R} a_o r\, e^{-r^2/R_o^2}\, dr d\theta \qquad (3.3\text{-}7)$$

i.e.

$$Q_r = a_o \pi R_o^2 (1 - e^{-R^2/R_o^2}) \qquad (3.3\text{-}8)$$

To calculate the apparent charge transfer the capacitance of the

system prior to the discharge was first evaluated from the functional value in the usual way. The node values obtained from the second computation, (i.e. with all the Dirichlet nodes homogeneous and charges on the void ends) after being increased or decreased by the multiplying factor a_o, were added to the initial node values to yield the node values following the occurrence of the discharge. The value of the new functional could now be obtained by recalling subroutine FCTVAL. In contrast to the previous evaluation of the functional with no stored charge, a non-zero contribution by the B matrix was obtained from equation (2.3-41) in addition to that by the S matrix from equation (2.3-40). The former represented, for a two dimensional problem, twice the work done in establishing the charge distribution whereas the latter represented twice the energy stored within the dielectric.

N.B. For the second computation made with all the Dirichlet boundaries homogeneous the S and B contributions are equal confirming that the energy stored in the field is equal to the work done in establishing the charge distribution.

From the latter the new overall capacitance could be calculated and from the change in capacitance the apparent charge transfer was given by $Q_a = V.\Delta C$.

Figure 3.3-2(a) shows the variation in the ratio of the apparent charge transfer to the real charge transfer as a function of the void aspect ratio r/d with d/t = 0.1 and $\epsilon_r = 2$. The results for the three different charge distributions (R_o/R = 0.25, 0.5 and 1.0) representing the discharge of different fractions of the void end surfaces are plotted together for comparison. Figures 3.3-2(b) - (e) show the corresponding variations with d/t equal to 0.2, 0.4, 0.6 and 0.8 respectively. The curves are repeated in figure 3.3-3 with $\epsilon_r = 4$ and in figure 3.3-4 with $\epsilon_r = 10$.

The figures show that, with a few exceptions, the ratio of $\Delta Q_a/\Delta Q_r$ is larger with R_o/R equal to 1.0 than it is with R_o/R equal to either 0.25 or 0.5 and in many instances the difference is appreciable. Surprisingly the other two curves do not follow this trend the curve with R_o/R = 0.5

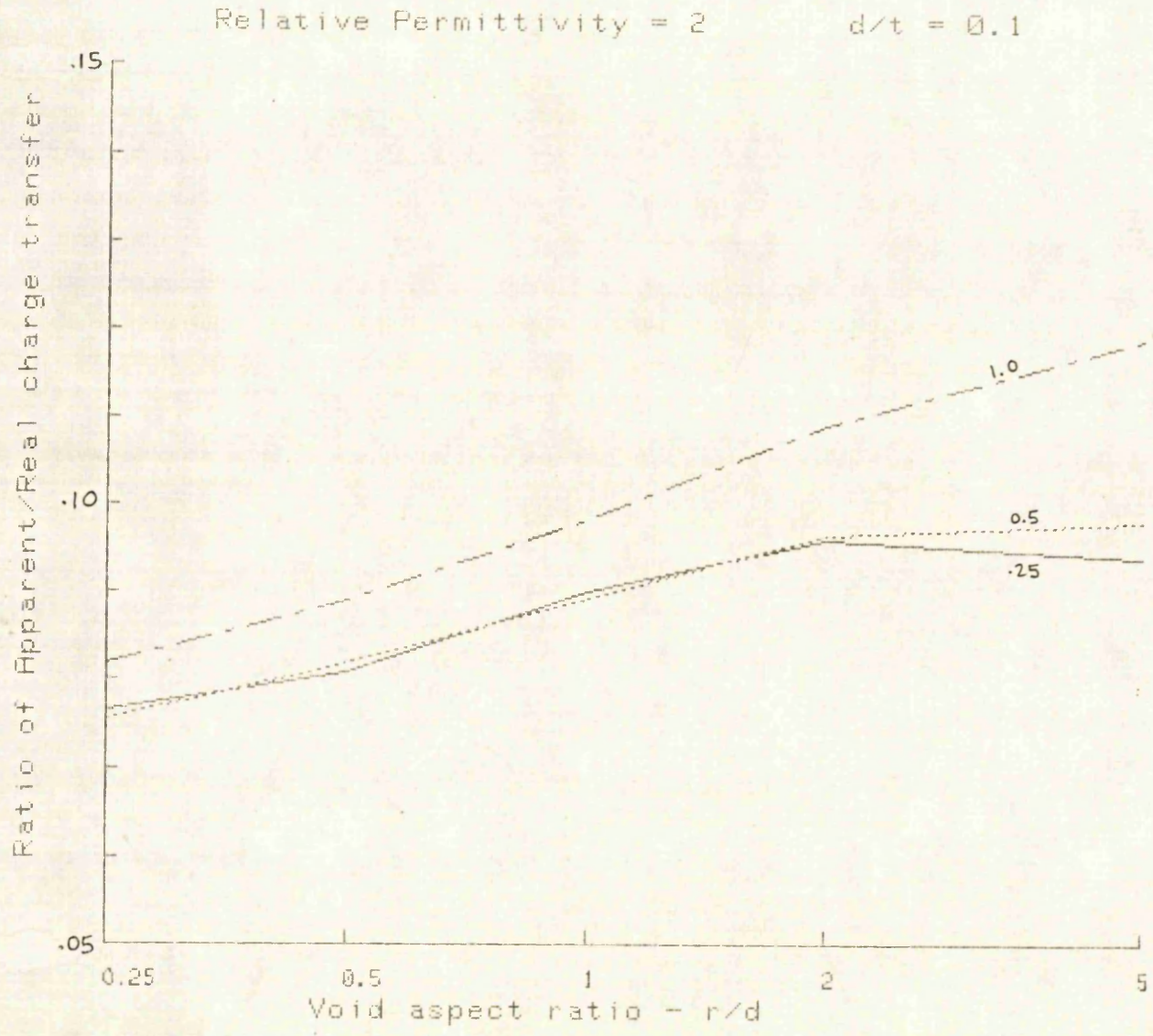

Figure 3.3-2 Apparent charge transfer / actual charge transfer ratios obtained for the 'pill box' shaped voids of figure 3.1-2 ($\epsilon_r = 2$; $R_o/R = 0.25$, 0.5 and 1.0) (a) $d/t = 0.1$

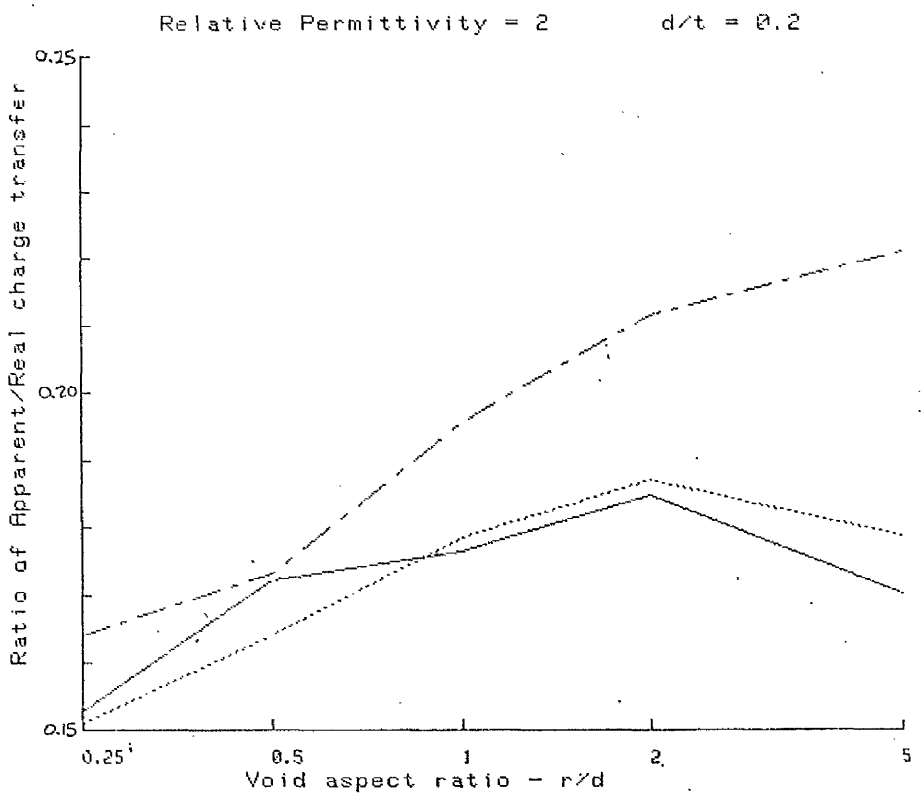

(b) $\epsilon_r = 2$; $d/t = 0.2$

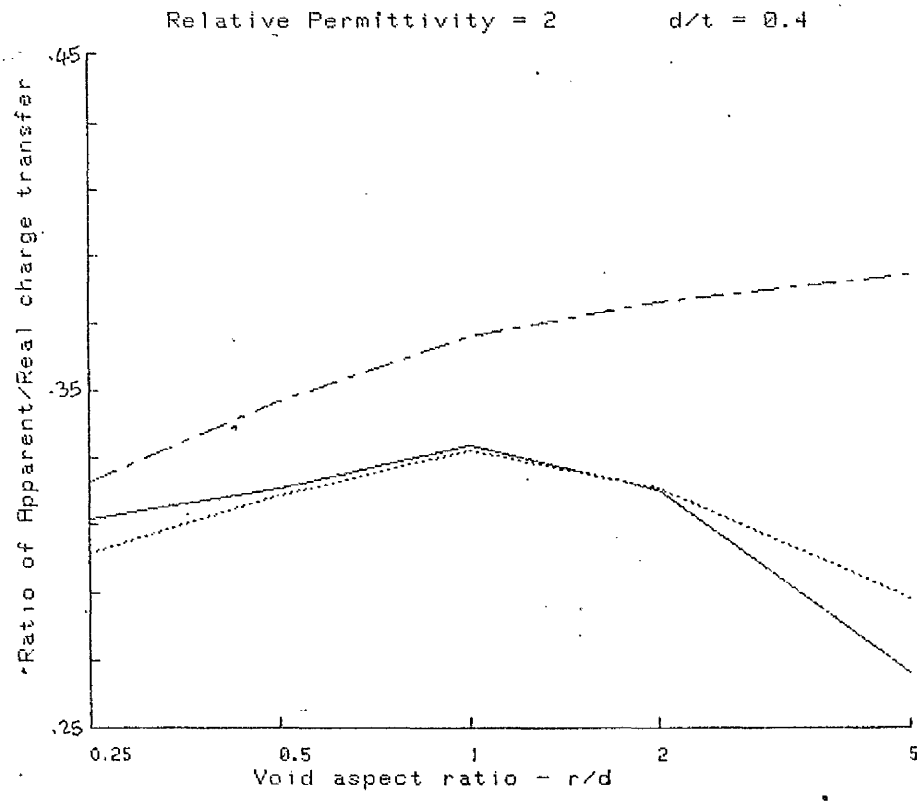

(c) $\epsilon_r = 2$; $d/t = 0.4$

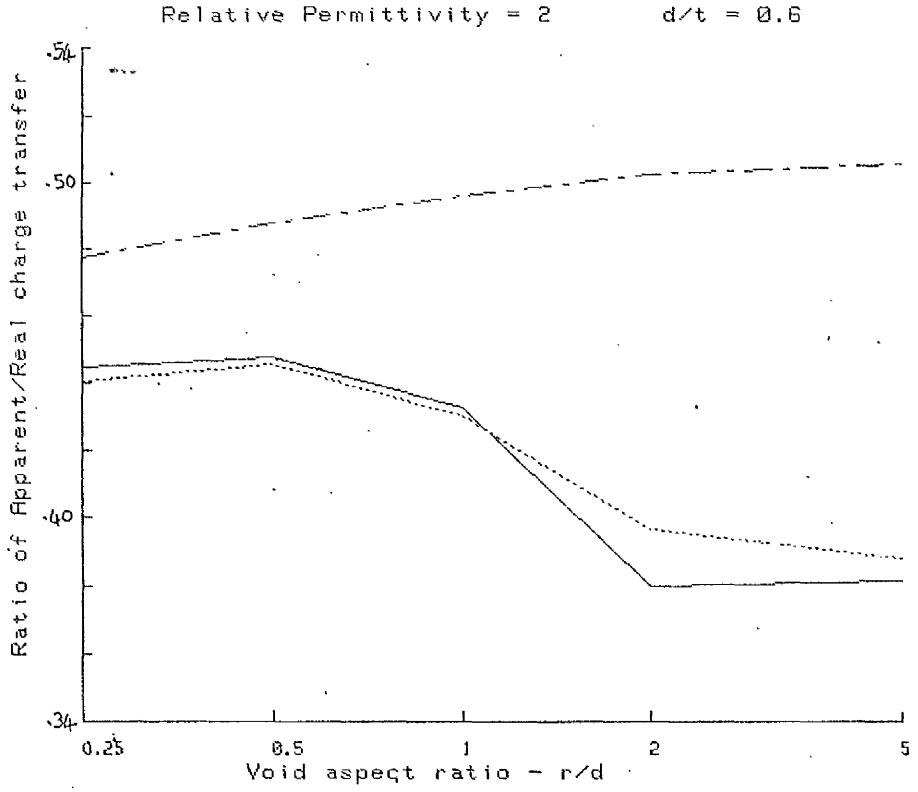

(d) $\epsilon_r = 2$; $d/t = 0.6$

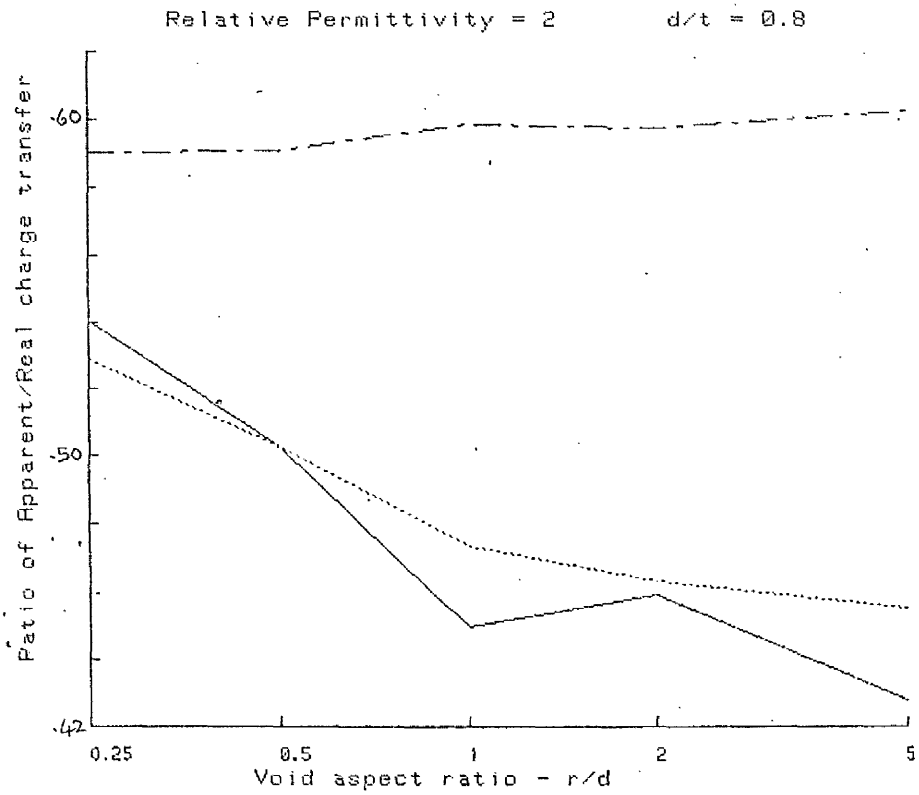

(e) $\epsilon_r = 2$; $d/t = 0.8$

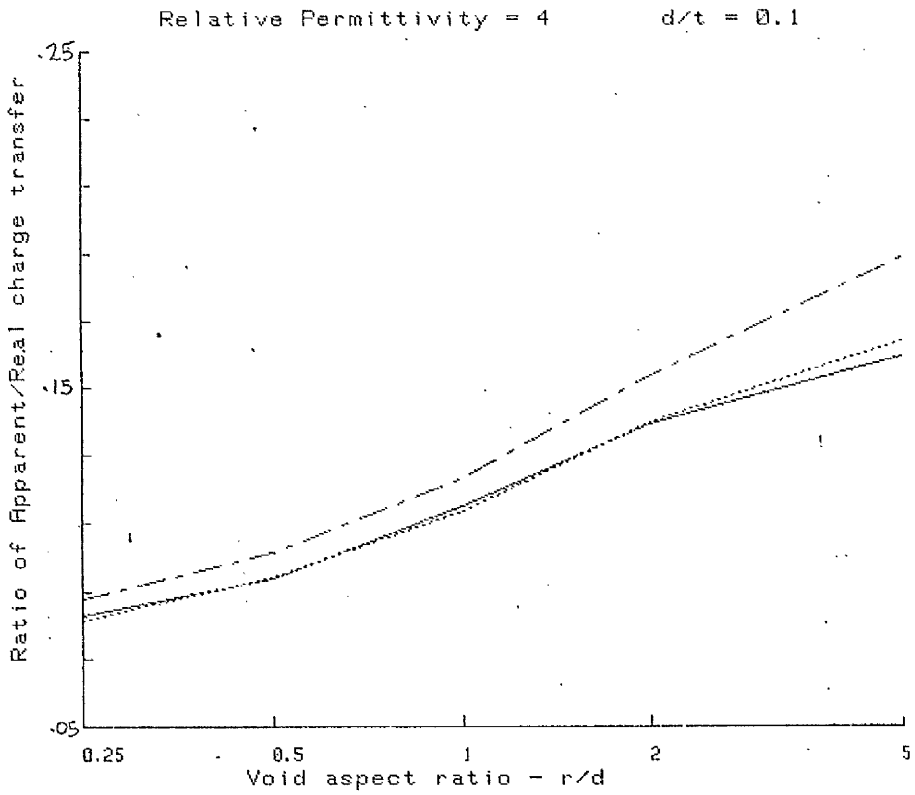

Figure 3.3-3 As per figure 3.3-2 but with $\epsilon_r = 4$. (a) d/t = 0.1

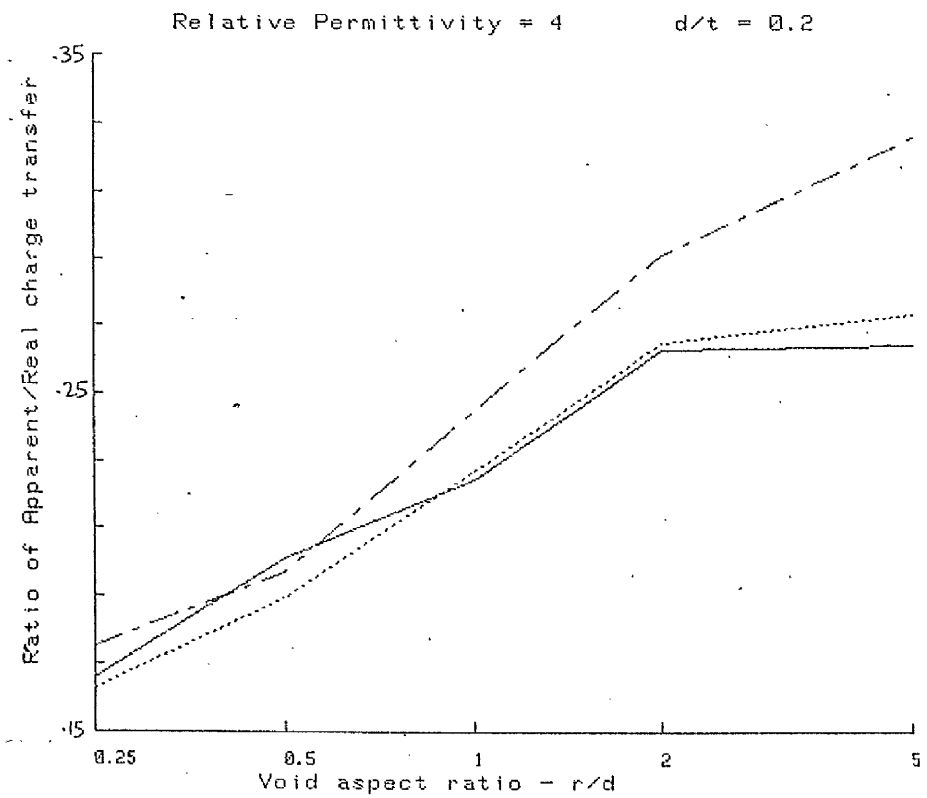

(b) $\epsilon_r = 4$; d/t = 0.2

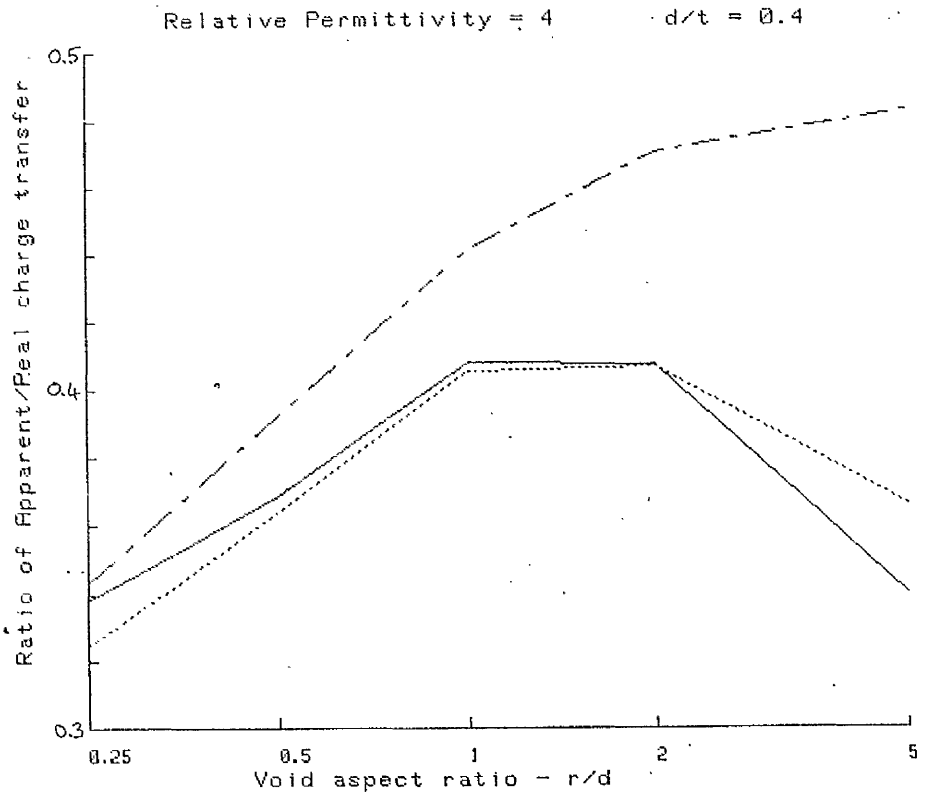

(c) $\epsilon_r = 4$; $d/t = 0.4$

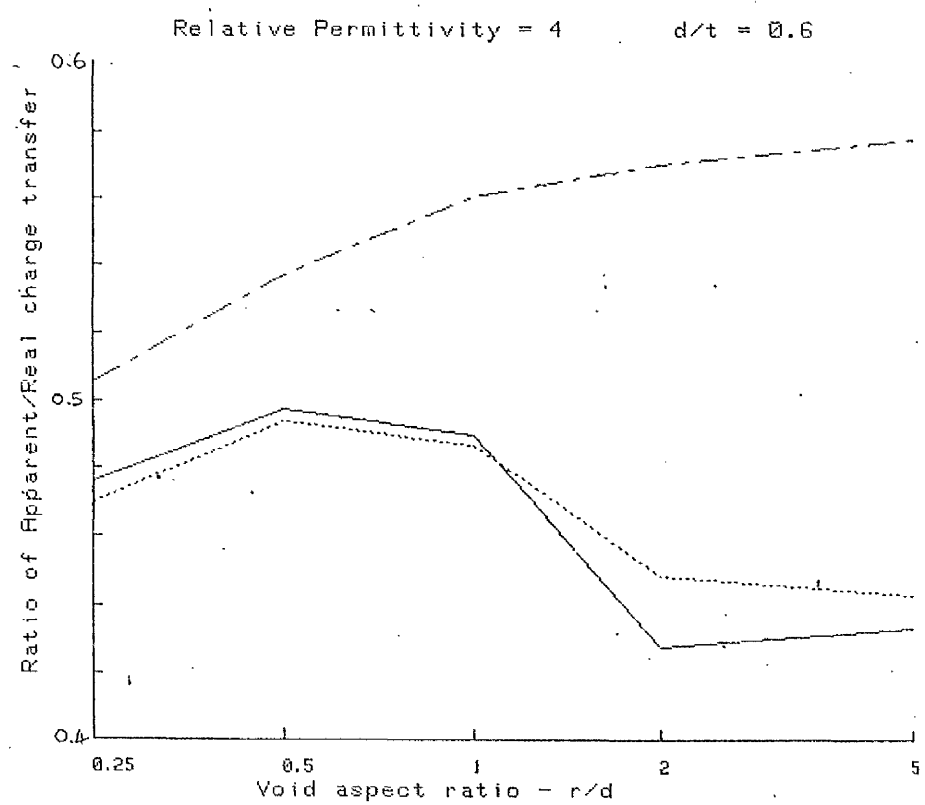

(d) $\epsilon_r = 4$; $d/t = 0.6$

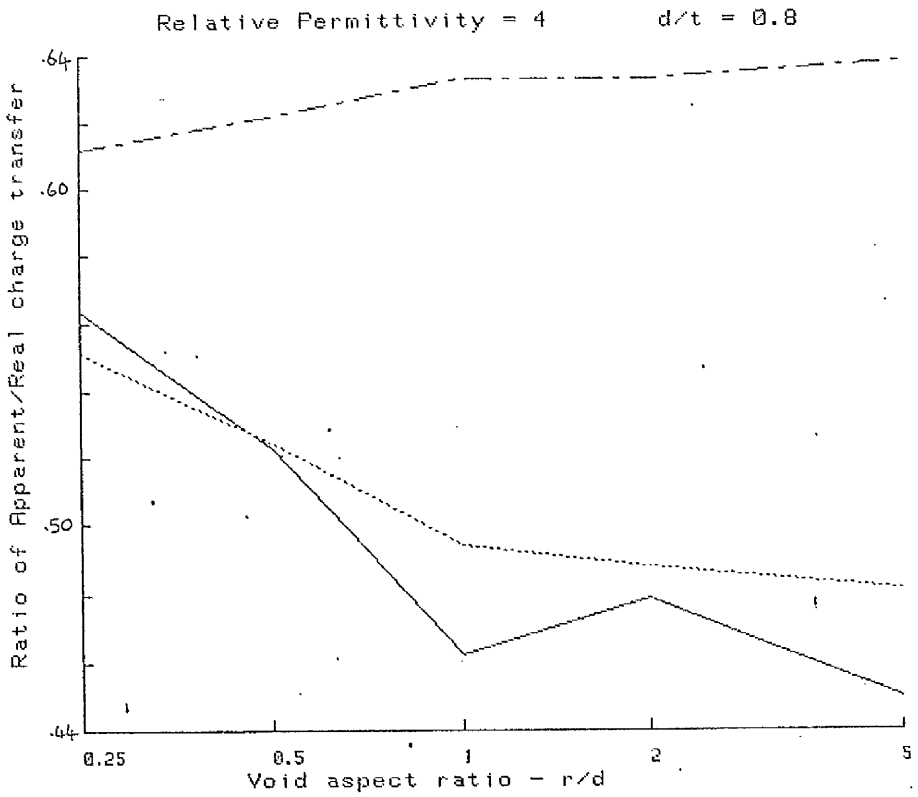

(e) $\epsilon_r = 4$; d/t = 0.8

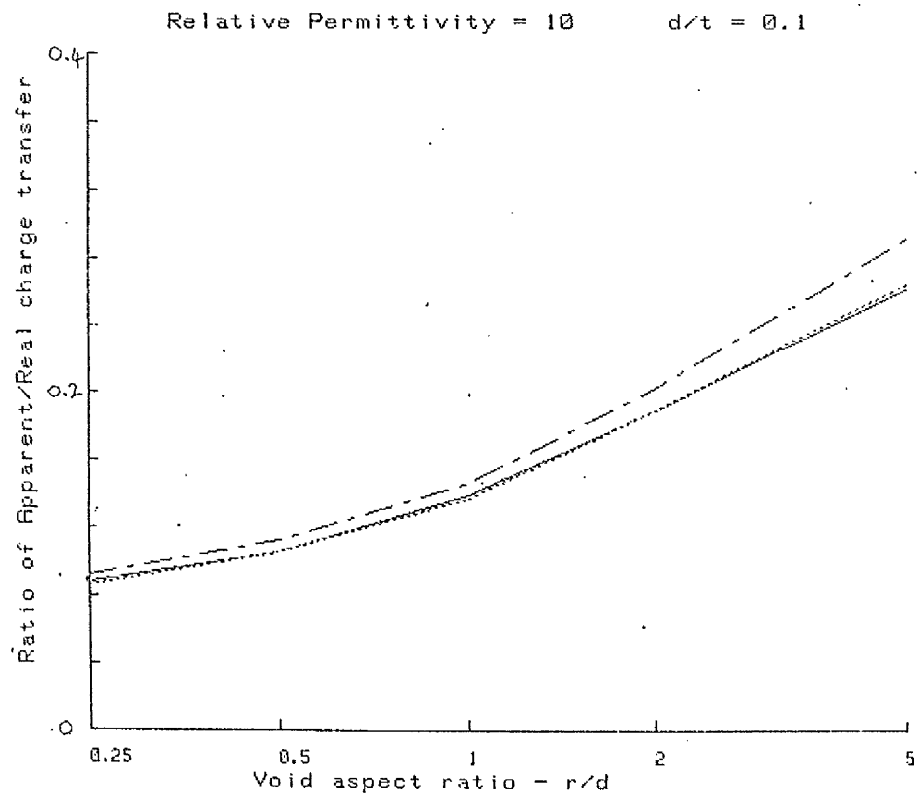

Figure 3.3-4 As per figure 3.3-2 but with $\epsilon_r = 10$. (a) d/t = 0.1

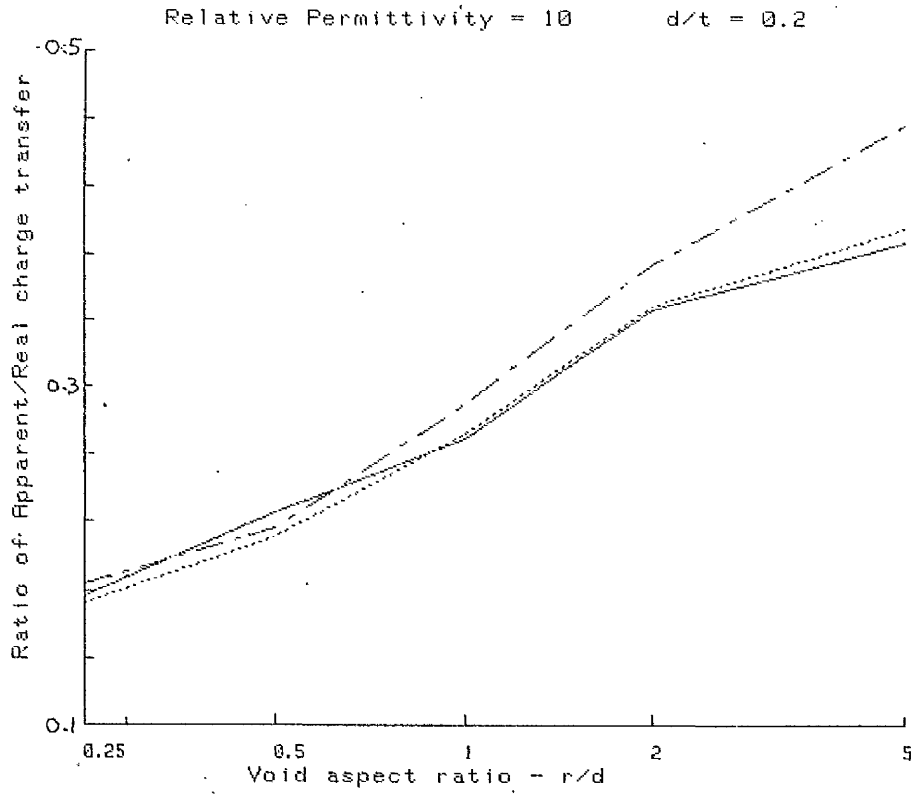

(b) $\epsilon_r = 10$; $d/t = 0.2$

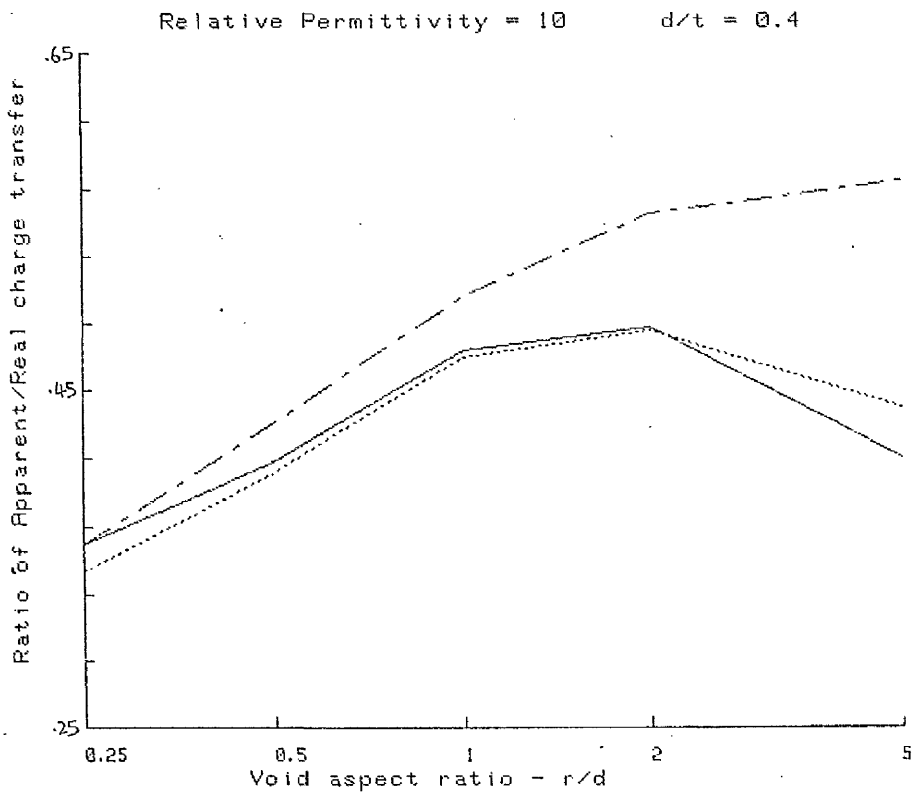

(c) $\epsilon_r = 10$; $d/t = 0.4$

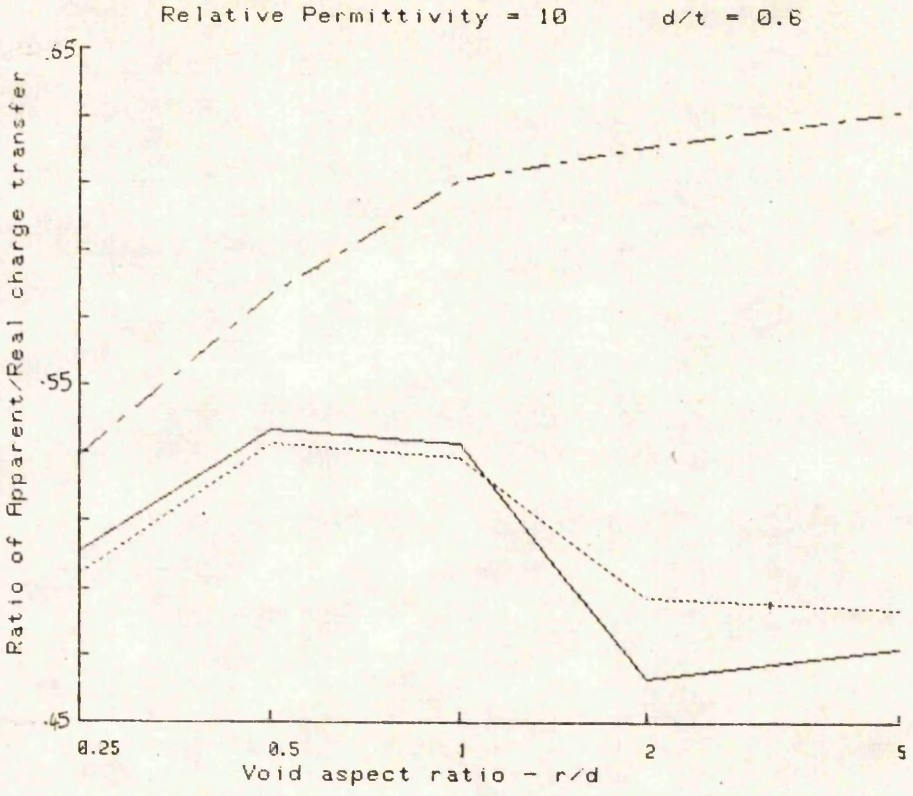

(d) $\epsilon_r = 10$; $d/t = 0.6$

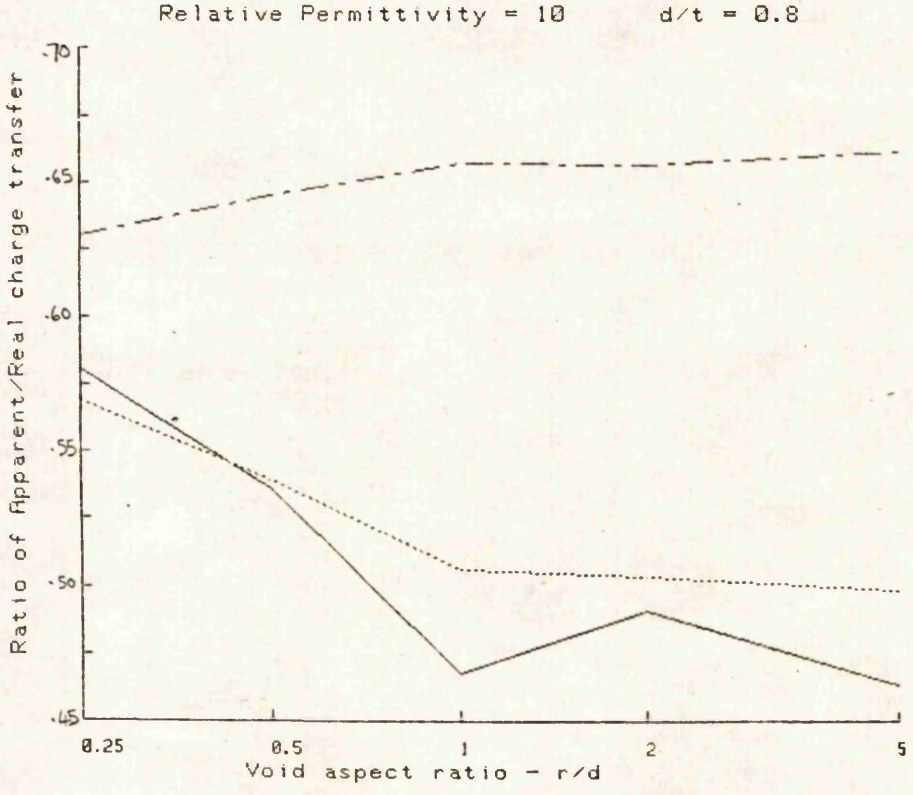

(e) $\epsilon_r = 10$; $d/t = 0.8$

consistently being above that for $R_o/R = 0.25$ when $r/d = 5$ but below when $r/d = 0.25$. The separations are, however, small. The variations in $\Delta Q_a/\Delta Q_r$ with r/d are modest but, again, the curve for $R_o/R = 1$ shows different characteristics from the other two. It consistently increases as r/d is increased (though not always monotonically) whereas the others increase for small values of d/t, decrease for large values and pass through a maximum for intermediate values.

The value of $\Delta Q_a/\Delta Q_r$ is primarily dependent on the value of d/t and the permittivity, an increase in either of these parameters resulting in an increase in $\Delta Q_a/\Delta Q_r$. This is suggested from equation (3.3-3) by considering a and b to be parallel plate capacitors having negligible edge effects. This being the case the ratio $\Delta Q_a/\Delta Q_r$ is given by

$$\frac{a}{a + b} = \frac{\epsilon_r}{\epsilon_r + t/d - 1} \qquad (3.3\text{-}9)$$

A comparison of the values predicted by this rough approximation with those obtained from the computation is given in table 3.3-1 . The computed values given are the largest and smallest that were obtained for each value of permittivity and d/t ratio. (N.B. The largest values were those computed with $r/d = 5$ and $R_o/R = 1$ in each case.) It is interesting to note that the largest computed value is generally about two thirds of that calculated using equation (3.3-9). There is, however, a larger fluctuation in the corresponding ratio for the smallest values of $\Delta Q_a/\Delta Q_r$, it ranging from 0.16 upto 0.51 .

Electric stress distribution after a discharge

As the physical and electrical properties of the problem remain unchanged, the shape functions also remain unchanged and so the potential at any required point can be evaluated directly from the new node potentials. Thus by calling subroutine GRID, the potentials at a grid of points covering the region of interest could be obtained and, from these, the equi-potential contours could be established by interpolation. The results obtained are demonstrated by the equipotential plot given in figure 3.3-5 for the config-

Table 3.3-1 Comparison between the maximum and minimum values obtained for the ratio of apparent / real charge transfer and the values predicted by the simple parallel plate capacitor model using equation (3.3-9).

ϵ_r	d/t	Value of $\Delta Q_a / \Delta Q_r$				
		Calculated using equation (3.3-9)	Obtained from computation			
			Maximum	% of (3.3-9)	Minimum	% of (3.3-9)
2	0.1	0.182	0.119	65.4	.0754	41.4
	0.2	0.333	0.221	66.4	0.151	45.3
	0.4	0.571	0.384	67.3	0.267	46.8
	0.6	0.750	0.506	67.5	0.380	50.7
	0.8	0.889	0.602	67.7	0.428	48.1
4	0.1	0.308	0.189	61.4	.0813	26.4
	0.2	0.500	0.326	65.2	0.163	32.6
	0.4	0.727	0.483	66.4	0.325	44.7
	0.6	0.857	0.578	67.4	0.427	49.8
	0.8	0.941	0.638	67.8	0.449	47.7
10	0.1	0.526	0.291	55.3	.0861	16.4
	0.2	0.714	0.455	63.7	0.172	24.1
	0.4	0.870	0.575	66.1	0.343	39.4
	0.6	0.938	0.632	67.4	0.463	49.4
	0.8	0.976	0.661	67.7	0.463	47.4

uration of figure 3.1-2(17) with $\epsilon_r = 4$ and $R_o/R = 0.5$. The plot shows the perturbation caused by the charge distribution to be considerable with appreciable surface electrical stresses across the end faces of the void.

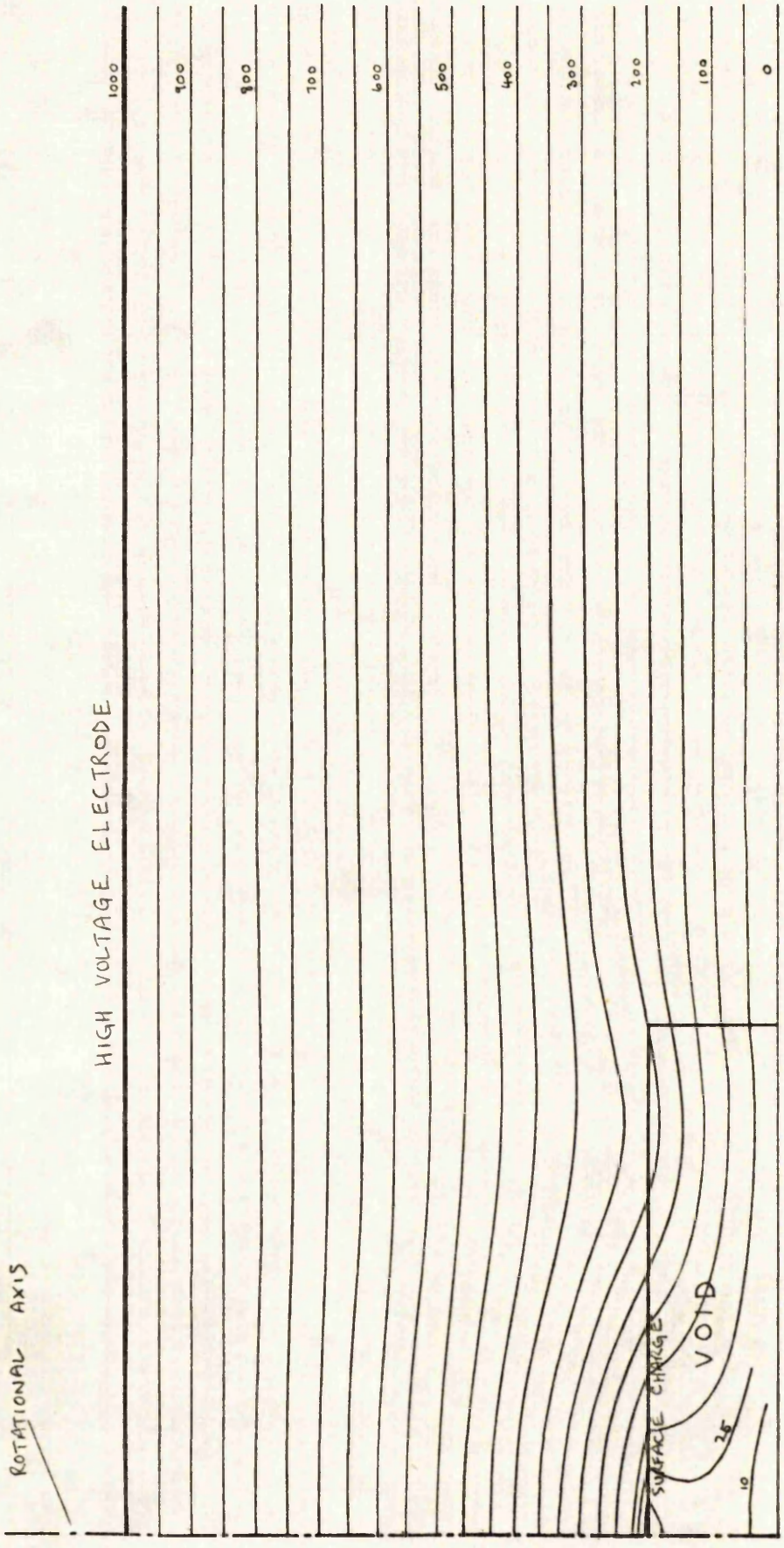

Figure 3.3-5 Plot of the equipotentials obtained for the void configuration of figure 3.1-2(17) after a partial discharge. ($\epsilon_r = 4$; $R_o/R = 0.5$)

To illustrate the fact that the axis of the void is free to float in potential, part of the 10 and 25 volt equipotentials have also been plotted and it can be seen that they both turn back on themselves at the void surface. The former in fact returns to the rotational axis indicating that the potential on the axis within the void exceeds this level for part of its length. The maximum achieved in this example is 19.3 volts at a point 60% up the void from the axis of symmetry.

CHAPTER 4

The emission of microwaves by discharges

Previous work by the author[109] has shown that, when an internal discharge occurs, the rate of charge transfer is sufficient to produce an impulse spectrum extending to several hundred megahertz. The components of such a spectrum bear definite amplitude and phase relationships to each other and can therefore couple to near-by system conductors to produce well defined electrical transients. These transients can be detected by connecting suitable measuring equipment directly to the high voltage structure under test. However, the cost of making such measurements can be high. Additionally, attenuation, dispersion, multiple reflections and multiple transmission paths can severely distort the transients rendering accurate interpretation of the results difficult.

The expense of making direct electrical measurements on high voltage equipment can be obviated by the use of standard radio interference techniques. Measurements are normally made in the medium or high frequency bands. At these frequencies the received radiation is almost entirely attributable to the flow of transient currents in the conductors of the high voltage system. Since, as before, these will be distorted, the method suffers from the same inherent limitations as direct measurements. In practice the complicated structure of the radiating conductors produces further severe distortion rendering the method only suitable for 'noise type' measurements.

If radio interference measurements could be made at microwave frequencies, the conductors of the high voltage system would play a much diminished role since any power coupled to them would be rapidly attenuated. As a consequence direct measurements of the radiation emitted by the discharges could be made which would provide detailed information on individual discharges.

As little information could be found regarding the magnitude or

nature of the microwave radiation emitted by discharges in high voltage power apparatus, a programme of research was undertaken which is described in this chapter.

Previous work

It is well known that discharges produce electro-magnetic radiation in the visible and ultraviolet bands. Visible band techniques are long established[110] and the detection of the ultra-violet emission from corona sources is described in the paper by Strong, Davis and Melville.[33] The description of a more sensitive detector is given by Teich.[32] Discharges also radiate in the infra-red region and to a certain extent in the microwave region.

Historically discharges and microwaves have a long association. At the turn of the century many fundamental experiments were performed on centimetre and sub-centimetre radiation using the damped waves from spark gaps driven by Rumkorff coils. As early as 1894 Lodge[112] attempted waveguide transmission and in 1895 von Lang[113] demonstrated interference effects. Other experiments of a similar nature were performed by Drude[114] and Weber.[115] Bose is credited with the invention of the galena detector in 1901 which enabled him to demonstrate both guided and free space transmission. More recently, microwave techniques have been used extensively to study the physics of discharges.

Physical background

Low pressure discharge tubes are commonly used as noise sources in the microwave laboratory. Their outputs are large with noise temperatures typically greater than 10,000^{o}K. Such temperatures can be identified with the electron temperatures obtained in discharge plasmas. High electron temperatures are to be expected from kinetic theory. They are limited primarily by the ionization energy of the constituent gas atoms since the electrons can continue to accumulate energy and undergo elastic collisions only upto this level. As a consequence the output noise power

from a gas discharge tube is largely independent of the driving current.

Such reasoning may fix the magnitude of the effect but it does not explain the mechanism of generation of the radiation. A free electron is prohibited from radiating of its own accord by the requirement that linear momentum be conserved. However in the field of another particle such as an atom or an ion, the electron will be accelerated and this can result in the emission of a quantum of radiation with a corresponding loss in kinetic energy. The frequency ν of the emitted radiation is given by

$$h\nu = (V_i - V_f)e \qquad (4\text{-}1)$$

where h is Planck's constant, V_i is the initial energy of the electron in electron volts, V_f is the final energy and e is the electronic charge. (An electron at rest at infinity is considered to have zero energy.) For the incident, free electron, V_i is positive and the electron can be considered to be in a positive energy state within the field of the attracting atom or ion. If, after the emission of a photon, V_f is also positive $(V_f < V_i)$ the interaction constitutes an inelastic (non-capturing) collision. Since a continuous distribution of positive energy states exist, the electron may lose any fraction of its initial energy and can, as a consequence, produce radiation of any frequency upto a maximum value corresponding to the loss of its entire energy. The radiation from these so called 'free-free' transitions is referred to as 'bremsstrahlung'. (German for 'braking radiation.) Bremsstrahlung is the principal mechanism of microwave generation by plasmas. If the electron is captured, V_f is negative and the electron remains in a bound orbit around the attracting atom or ion. Such a 'free-bound' transition is referred to as a radiative recombination.

$$H + e \rightleftharpoons H^- + h\nu \qquad (4\text{-}2)$$

It is the reverse of the process of radiative capture.

Measurements of the microwave noise power emitted by a plasma have been made by Bekefi, Hirshfield and Brown.[116] They examined the radiation emitted by a short section of the positive column of a hot-cathode d.c. glow discharge in helium at a pressure of 0.5 torr. Measurements

were made at 3GHz using a sensitive radiometer of the type first described by Dicke.[117] Their results showed the microwave noise power to increase linearly with increasing electron density upto a density of approximately 10^{17} electrons/m^3. Above this level, the plasma is opaque to the radiation. As a consequence it behaves like a black body radiator and there is little further increase in radiated power. Their results also show a localised increase in radiated power at the electron density appropriate to a 'plasma frequency' of 3GHz. The plasma frequency is the frequency of oscillation of a longitudinally displaced electron in the plasma and is given by

$$\omega_p^2 = \frac{ne^2}{m_e \epsilon_o} \qquad (4\text{-}3)$$

where n is the number of electrons per cubic metre, e is the electronic charge, m_e is the electronic mass and ϵ_o is the permittivity of free space. Substituting the values for the constants in equation (4-3) yields

$$f_p = 8.980\, n^{\frac{1}{2}} \qquad (4\text{-}4)$$

So far the discussion has been limited to low pressure discharges where the constituents of the plasma are far from being in thermal equilibrium with each other. Electron temperatures can be upto two orders of magnitude greater than the temperatures of the gaseous atoms and ions with the result that microwave radiation from the plasma arises almost entirely from electron emission mechanisms. As the gas pressure and current increase, there is a greater exchange of energy between the constituent particles. Penning,[118] giving the results obtained from measurements by Elenbaas[119] on the positive column in mercury vapour, illustrates the variation of the electron and gas temperatures as a function of pressure. From an electron temperature of 28,000°K and gas temperature of 290°K at a pressure of 10^{-3} torr the temperatures are shown to converge to a common temperature of 5100°K at 100 torr and thereafter to remain constant. Thus at atmospheric pressure the temperature of the gas rather than the temperature of the electrons is the important parameter. At this pressure the mean free time between

collisions for the ions can be comparable to the period of microwave frequency radiation. Ionic motion may therefore be an important mechanism in the generation of noise in the microwave region.

Since the gas is cooled by its surroundings, the plasma is constrained to a narrow channel. An estimate of the plasma electron density can be obtained by assuming a discharge of 1 amp. to have a radius of 10^{-4}m. For an electron drift velocity of 2×10^{5} m/s the electron density is 10^{21} m^{-3}, showing the plasma to be opaque to microwave radiation. Only surface effects can therefore contribute to the radiation emitted. In view of the limited plasma surface area and reduced electron temperature, less microwave radiation is to be expected, in general, from high pressure discharges.

4.1 Initial investigation [120]

Broad-band measurements

Experimental spark discharges were produced in air at atmospheric pressure between 6mm diameter convex electrodes of coin silver. (95% silver) The electrodes were mounted centrally in a short length of (WG 16) X - band waveguide with the axis of the electrodes parallel to the E-plane of the waveguide when considering propagation in the TE_{10} mode. One electrode was electrically connected directly to the waveguide and the other was connected to a 0 - 4kV r.m.s. 50Hz supply via a chain of high value resistors. In addition to acting as a current limiting resistance, these resistors also decoupled the electrodes from the capacitance of the high voltage supply. In order to minimize the amount of microwave radiation transmitted out of the waveguide along the high voltage supply line a broad-band wave-trap was fitted to the high voltage electrode.

The electrode assembly was connected into the system shown in figure 4.1-1 and crystal current measurements were made at X-band for a range of electrode separations from 0.05 to 0.2mm. The driving voltage was varied and, in addition, the capacitance of the electrode assembly was

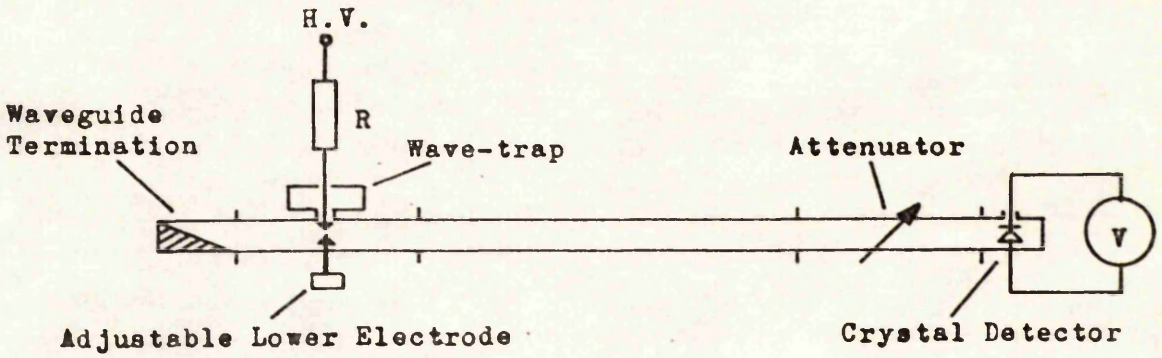

Figure 4.1-1 Arrangement for broadband measurements

altered by attaching lengths of coaxial cable. The calibrated attenuator (0 - 80dB) was used to determine the level of extraneous pick-up at the crystal detector. To reduce the pick-up to an acceptable level careful screening of the high voltage supply, crystal detector and its associated meter was required together with thorough suppression of mains borne interference.

During these measurements the voltage waveform across the electrodes was monitored to yield the number of discharges per cycle, the breakdown voltage and the discharge extinction voltage. From a knowledge of the total capacitance of the electrode assembly, the discharge energy and charge transfer were then estimated. The microwave power was determined from the calibration curve for the crystal detector and the microwave energy emitted per discharge calculated. The bandwidth of these measurements was estimated to be of the order of 8 GHz and the results obtained are shown in figures 4.1-2 and 4.1-3 where the microwave energy radiated per discharge is plotted against the total discharge energy and charge transfer. The latter curve is given as discharge magnitudes are normally measured in terms of the charge transferred though, in this case, the values given relate to the actual charge transferred rather than the, usually measured, apparent charge transferred. The radiation which propagated along the waveguide away from the detector has been allowed for in these figures. Not

unexpectedly, fairly large variations in microwave energy emitted were obtained for a given discharge energy. However the curves show the increase in microwave energy to be less than linear with increase in either discharge energy or charge transfer.

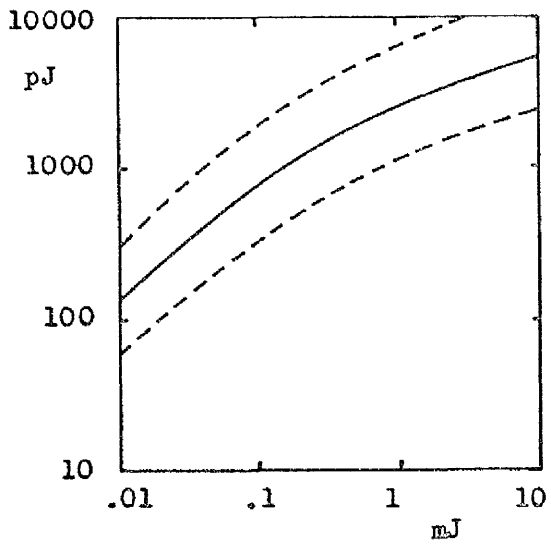

Figure 4.1-2 Variation of microwave energy with discharge energy

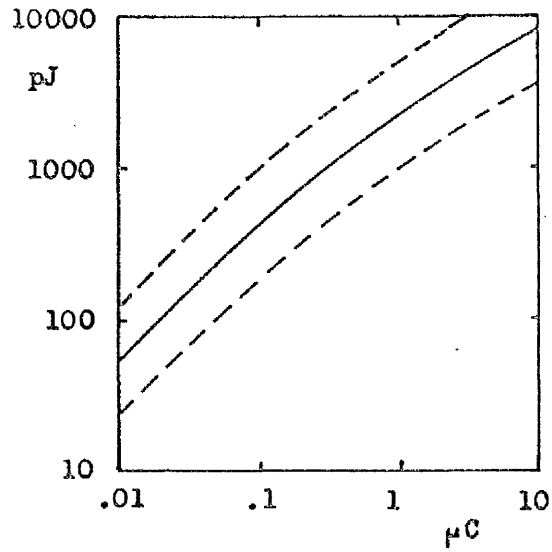

Figure 4.1-3 Variation of microwave energy with charge transfer

Narrow-Band Measurements

The spectral distribution of the microwave radiation was established using the measurement system shown in figure 4.1-4 . The X-band oscillator served, in conjunction with the calibrated attenuator, as a known source of microwave power and enabled absolute measurements to be made. The spectrum analyser was of the triple superheterodyne type employing a first intermediate frequency of 2 GHz. Its input mixing diode was driven by a backward wave oscillator tunable over the frequency range 2 - 4 GHz. As the spectrum analyser possessed no front-end r.f. amplification measurements could be made at X-band by mixing the input signal with either the second or the third harmonic frequency of the local oscillator. The results obtained would however have been ambiguous without the preselector. This voltage controlled, variable frequency, band-pass filter tracked with the spectrum analyser only admitting frequency components appropriate to the band selected.

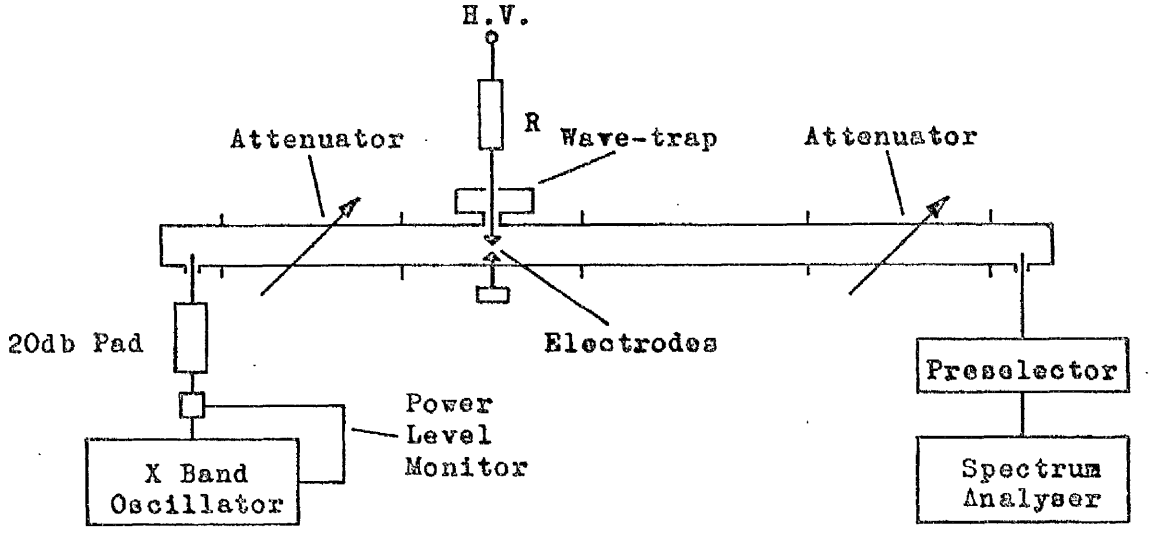

Figure 4.1-4 Arrangement for narrow-band measurements

The spectrum analyser indicated that the microwave radiation consisted of a continuum of incoherent signals stretching from the cut-off

frequency of the waveguide (6.56 GHz) upto beyond the upper limit (12.4 GHz) of the X-band test equipment. The spectrum analyser had an equivalent rectangular filter bandwidth of only 30 KHz which would have allowed any fine structure of preferred emission frequencies to be resolved. However none was observed. Hence it is concluded that continuous radiation, similar to wideband noise exists over the whole of the wave-band. As a consequence of this, measurements can be made over any part of the frequency band and the noise power is a direct function of the band-width.

The previous series of measurements which were performed using the broad-band crystal detector were repeated using the narrow-band detection capabilities of the spectrum analyser. Noise powers per unit bandwidth were obtained and the results are shown in figures 4.1-5 and 4.1-6 where the instantaneous radiated microwave power is plotted against discharge energy and charge transfer for three electrode spacings.

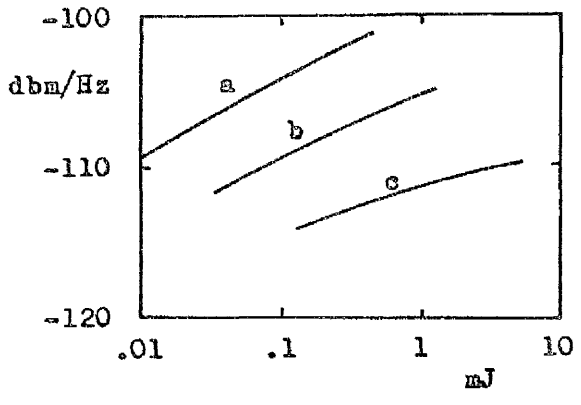

Figure 4.1-5 Variation of microwave power emitted with discharge energy
Electrode spacing: (a) 0.05mm (b) 0.10mm (c) 0.20mm

The values shown are mean values. Peak values were typically 6, 7 and 10dB higher for curves a, b and c respectively. Again the values have been corrected to allow for the radiation that propagated along the waveguide away from the spectrum analyser. The results obtained were independent of the discharge repetition frequency.

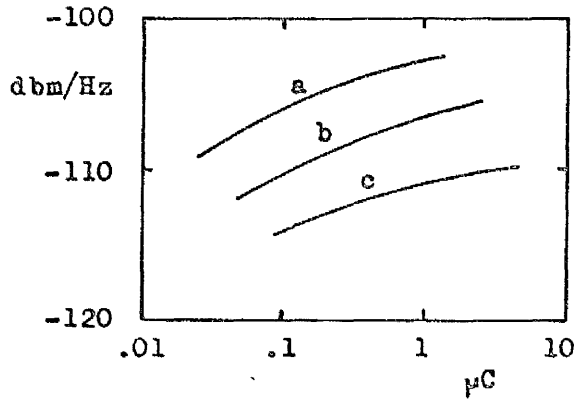

Figure 4.1-6 Variation of microwave power emitted with charge transfer

Ellectrode spacing: (a) 0.05mm (b) 0.10mm (c) 0.20mm

Resonance effects

An additional experiment was conducted using the arrangement shown in figure 4.1-4 but with a movable short circuit behind the discharge source in place of the X-band oscillator and attenuator. The object of this experiment was to determine if resonance effects could be obtained with such a discontinuity. The broad-band radiation was examined with the spectrum analyser and a 'gap' in the spectrum was observed (analogous to the absorption of energy by a wavemeter) when the plane of the short circuit was set to particular distances from the discharge site. The absorption 'gap' corresponding to a distance setting of half a wavelength was especially pronounced and a typical record of the analyser trace obtained is shown in figure 4.1-7 . Such resonance effects could prove useful for locating the position of internal discharges when testing equipment such as bushings. The apparent fine 'gap' structure shown is not of significance. These gaps merely mark the zero crossing points of the high voltage energizing waveform.

Sensitivity

The sensitivity of the spectrum analyser was more than adequate for the detection of the microwave noise emitted by discharges between metal

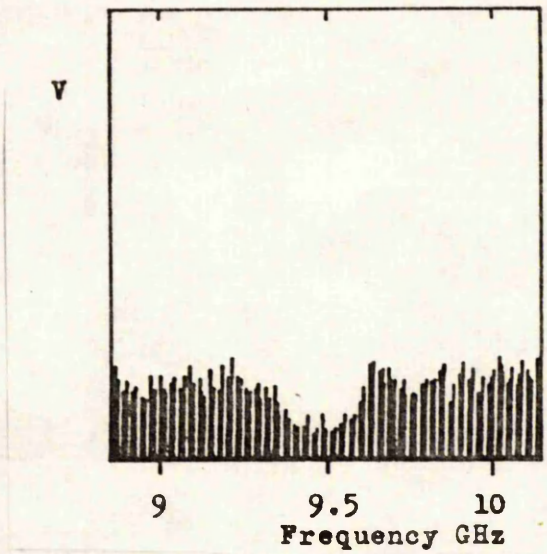

Figure 4.1-7 Resonance absorption of microwave noise

electrodes mounted in a waveguide. The sensitivity could have been increased further over a relatively small bandwidth by prefixing a low-noise X-band parametric amplifier. However, because of the small bandwidth of the spectrum analyser, the sensitivity to the wide-band noise emitted by the discharges would have remained inferior to that of the simple crystal detector. An attractive alternative was the use of a parametric amplifier in conjunction with a crystal detector. Using a parametric amplifier with a bandwidth of 50 MHz and a maximum gain of 22.5 dB, a similar sensitivity to that of the crystal detector was achieved. This allowed measurements to be made over a well defined and relatively narrow bandwidth with a consequent reduction in extraneous interference. The pass-band of the parametric amplifier was centred on 9.47 GHz.

Measurements were made using a discharge source external to the waveguide system by means of the arrangement shown in figure 4.1-8 . The discharges were produced between 6mm diameter, plane, brass electrodes separated by 0.2mm. The discharge energy was 60.3 μJ and the charge transferred 75,300 μC. The discharge repetition frequency was approximately

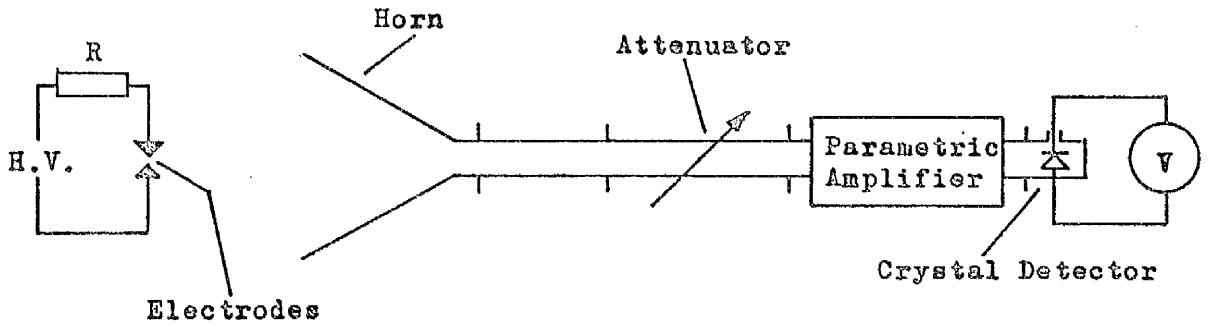

Figure 4.1-8 Arrangement with external discharge source

3600 per second. The horn was of a simple tapered construction and had an aperture of 195mm by 145mm. Figure 4.1-9 shows how the received signal power decreased as the distance of the horn from the discharge was increased. This curve shows that discharges between metal electrodes are easily detected at short range.

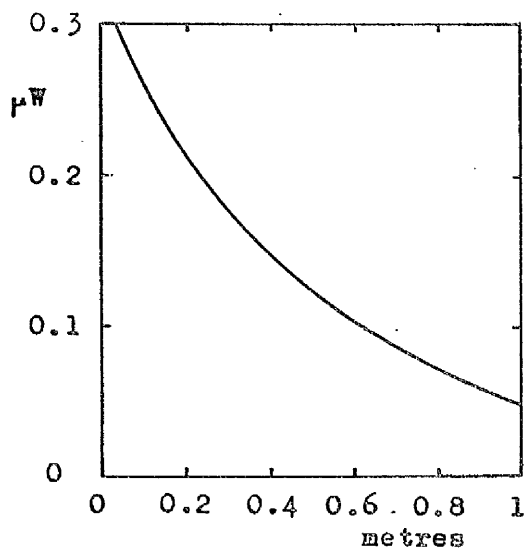

Figure 4.1-9 Microwave power received versus distance using horn antenna

Polarization

On rotating the plane of polarization of the receiver shown in figure 4.1-8 through a right angle, the signal power was found to drop by 11 dB. This indicated that the E vector of the emitted radiation was

mainly parallel to the direction of current flow in the discharge, a fact which could assist in the diagnosis of a faulty high voltage structure.

Conclusions from initial measurements

The results so far obtained show that the broad-band microwave noise radiated by spark discharges between metal electrodes can be detected by using simple, broad-band crystal detectors. Although the discharge levels used could be regarded as high, they are comparable to some cases found when testing, for example, bushings subject to inter-foil breakdown. The values quoted in this study are substantially greater than those normally associated with such measurements because true discharge magnitudes are give instead of the more usual apparent discharge magnitudes.

In common with the other radiative types of measurement used in high voltage partial discharge testing it has the advantage that no connection to the high voltage circuit is required. Furthermore, by using high gain directional aerials (e.g. 300mm in diameter) it should be possible to locate the sites of discharges with a fair degree of accuracy. This would be a major advantage of the method compared with the conventional lower frequency radio interference methods. The method should also be able to detect discharges within insulating structures where optical and ultraviolet methods are not feasible. The polarization of the microwave noise could also assist in the location of discharge sites in insulators which have circular symmetry. With so many possible advantages to discharge detection by microwaves it was decided to construct a sensitive radiometer that should be capable of extending the technique to partial discharges occurring where one electrode (or both) is a dielectric. However before describing the radiometer a brief discussion of the microwave noise levels emitted by a spark discharge as compared to those emitted by a black body will be given to demonstrate that a spark discharge cannot be treated as a black body radiator.

Spark discharge - not a black-body radiator

The total power radiated per unit wavelength interval in all directions in the solid angle 2π by unit area of a total radiator at a temperature of $T^{o}K$ is given by

$$E(T,\lambda) = 2\pi hc^{2}\lambda^{-5}(e^{hc/kT\lambda} - 1)^{-1} \qquad (4.1\text{-}1)$$

where h is Planck's constant $(6.626 \times 10^{-34}$ Joule-seconds)

k is Boltzmann's constant $(1.380 \times 10^{-23}$ Joule / $^{o}K)$

and the other symbols have their usual representations. Since, for microwave frequencies, $hc/kT\lambda << 1$ at non-cryogenic temperatures equation (4.1-1) may be simplified to

$$E(T,\lambda) = 2\pi ckT\lambda^{-4} \qquad (4.1\text{-}2)$$

Integrating between limits λ_a and λ_b the total power emitted in a given frequency band is

$$E(T,\lambda) = (2/3)\pi ckT(\lambda_a^{-3} - \lambda_b^{-3}) \quad \text{Watts/metre}^2 \qquad (4.1\text{-}3)$$

Taking a value of -110 dBm / Hz from figure 4.1-5 for the instantaneous microwave power emitted by a spark discharge yields a power of $80\mu W$ in a band, 8GHz wide, above the waveguide cut-off frequency of 6.56 GHz. Substituting this into equation 4.1-3 gives $T = 88715^{o}K$ for a total radiator area of one square metre. Clearly therefore spark discharges cannot be considered as black-body radiators.

4.2 Radiometric measurement of discharges at X-band

The physical background to the emission of microwaves by discharges has been outlined and experiments described that determined the magnitude and nature of these emissions. Lack of sensitivity of the measuring equipment, however, restricted the study to spark discharges of relatively large magnitude. In this chapter the construction of an X-band radiometer capable of detecting noise powers of 2×10^{-17} W (equivalent to a noise temperature of $\frac{1}{2}$ °K) is outlined and measurements on low level discharges are described. Discharges with one end terminating on the surface of a dielectric are also included in the study.

Sensitivity requirements

Since microwaves can be considered to be infra-red radiation of long wave-length, it is to be expected that hot bodies will radiate thermal noise in the microwave region. From thermodynamic considerations, Dicke[117] shows the power received by an antenna when directed at a black body radiator of temperature T to be equal to the available Johnson noise power from a resistor at that temperature. ($kT\Delta f$) Reference to figure 4.1-9 shows a received microwave noise power of 0.05 W at a distance of one metre from the spark discharge for the particular experimental conditions used. Comparing this to Johnson noise yields a noise temperature at the input to the parametric amplifier of 4×10^{5} °K. This suggests that a sensitive microwave radiometer should be able to detect partial discharges of considerably lower magnitude.

Microwave radiometric techniques

The simplest type of radiometer is the 'straight' receiver shown in figure 4.2-1 .

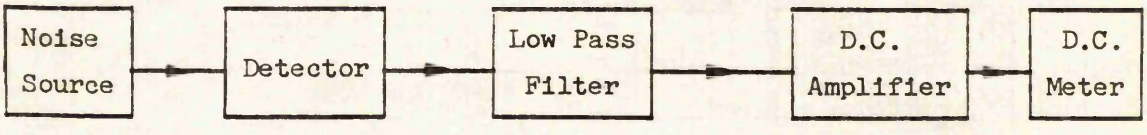

Figure 4.2-1 'Straight' receiver microwave radiometer

The input noise is detected at low level by a square law crystal detector and the resultant signal is fed, via a low-pass filter, to a d.c. amplifier and meter. Nicoll,[121] using a receiver of this type obtained a resolving power of 80°K using a bandwidth of 4GHz and an averaging time of 1 second. Improvements include the addition of low noise r.f. amplification and the provision of d.c. offset facilities for the meter.

The more usual radiometer is the superheterodyne type shown in figure 4.2-2 where it can be seen that the input noise is converted to i.f. noise and amplified before detection. Such an arrangement is inherently more sensitive than the 'straight' receiver.

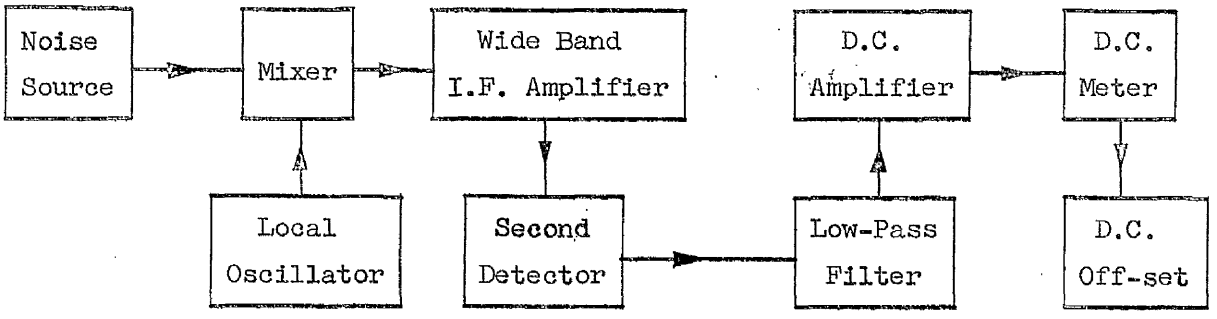

Figure 4.2-2 Superheterodyne receiver microwave radiometer

Gabor[122] has shown that there is a theoretical limit to the resolution attainable with a radiometer given by

$$\Delta T / T = (\nu_b \tau)^{-\frac{1}{2}} \qquad (4.2\text{-}1)$$

where ν_b is the receiver bandwidth and τ is the receiver time-constant. Thus with ν_b = 3.0 MHz, τ = 3 seconds and T = 290 °K, $\Delta T \doteq 0.1$ °K . Such resolution is not achievable in practice primarily due to the noise generated within the radiometer components. Dicke,[117] however, points out that for a receiver with the above parameters and a noise figure of 13 db, the resolution would be reduced to approximately 1°K.

Fluctuations in gain with time would further limit the resolving power of either of the radiometers described so far. In fact to achieve the resolution calculated, the gain would require stabilization to at least one part in three thousand. To avoid this onerous requirement

Goldstein[123] suggested the use of two independent receivers driven from the same signal source. Noise generated in the input stage of either receiver is prevented from reaching the other by isolators. The undetected outputs from the two receivers are fed to a wide-band multiplier and the product passed, via a low-pass filter, to a d.c. meter. Phase stability of the two receivers is essential if correlaton between the two signal outputs is to be maintained. If superheterodyne receivers are used synchronized local oscillators are required so care must be taken not to inject correlated noise into the mixing stages of the receivers. Separate automatic gain control circuits in the receivers ensure that output variations attributable to gain fluctuations are uncorrelated thereby overcoming the difficulties of short term gain fluctuations. Nevertheless long term stability remains important.

Comparison radiometers avoid gain fluctuation problems through comparison of the signal with a reference source. Both signals are handled by a single receiver multiplexed in either the frequency or the time domain. A radiometer of the former type was proposed by Selove.[124] The reference was a band-pass filtered noise source of equal bandwidth to the signal but of different frequency. The two signals were separated at the receiver output by filtering and detected separately. Measurements were obtained from a comparison of the two outputs.

Time domain multiplexing was first employed by Dicke[117] who interrupted the incoming radiation with a rotating resistive vane. Since the vane was at room temperature, the receiver input was chopped into a series of discrete pulses separated by room temperature noise. Phase sensitive detection of the detected receiver output then enabled the input noise temperature to be compared with room temperature. Stewart[125] and Mayer[126,127] describe radiometers of this type using ferrite modulators in place of the rotating vane. Square wave modulation was used at frequencies higher than those attainable by mechanical means. The method provides good sensitivity and has been much used by radio-astronomers. Fischer[128] des-

cribes a radiometer operating at 8.7 GHz intended for terrestrial and meterological studies and other workers have used radiometers for radio mapping,[129] all weather navigation[130] and the detection of icebergs.[131]

The radiometer used in this study was similar to those used by Stewart and Mayer but with the addition of a low noise parametric amplifier prior to mixing. Its operation will now be described.

4.3 Construction of a sensitive microwave radiometer

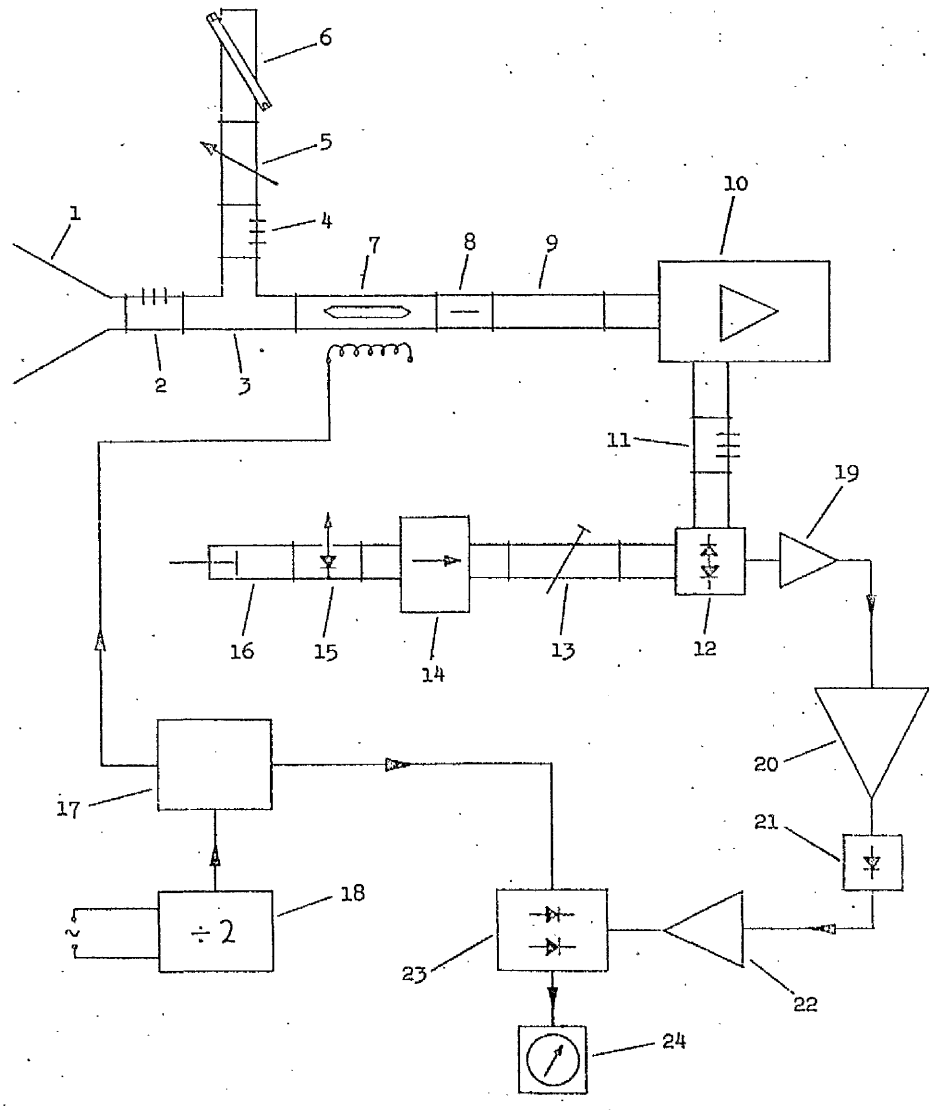

Figure 4.3-1 Schematic diagram of sensitive X-band radiometer

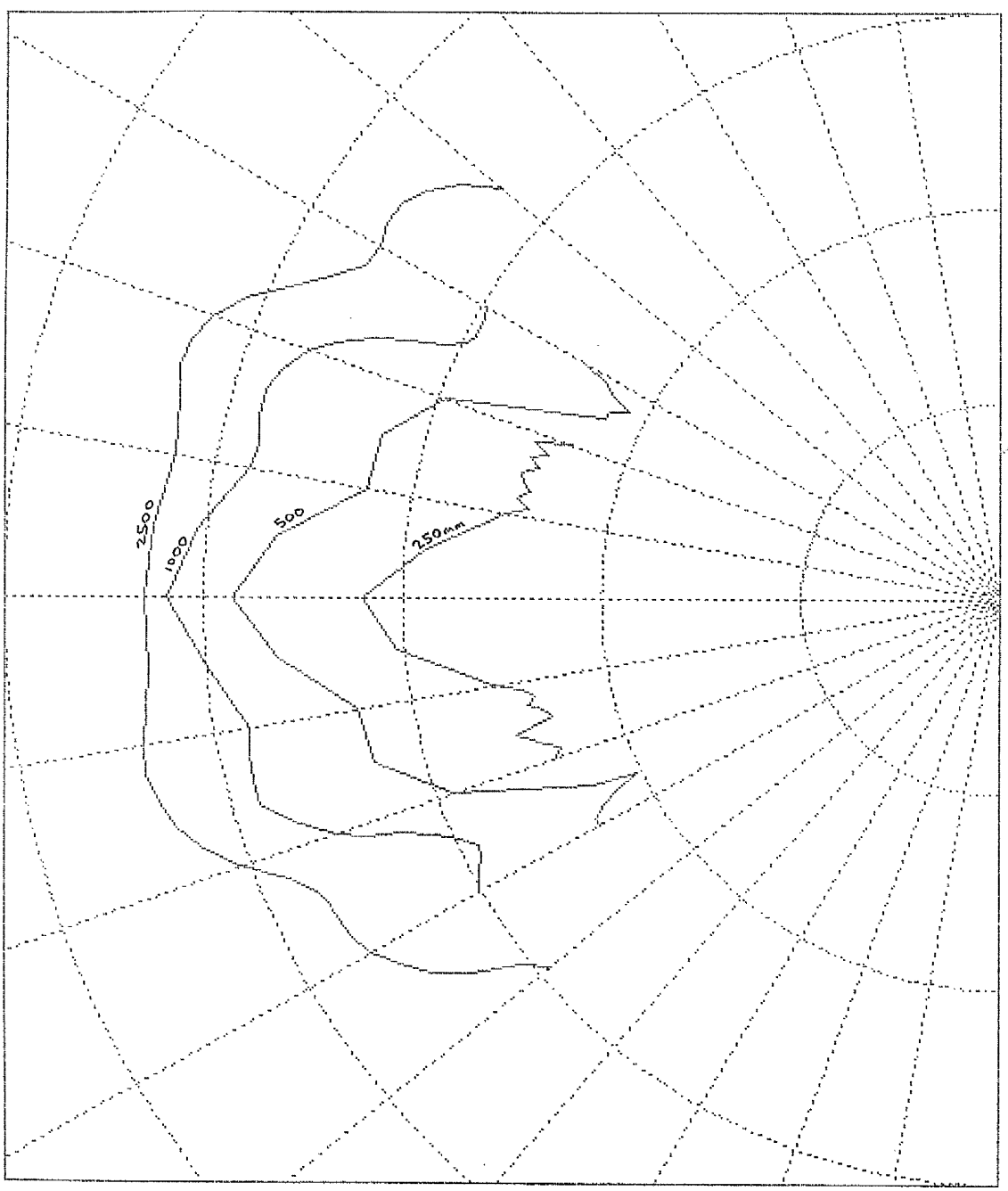

Figure 4.3-2(a) Polar plot of receiving horn (E-plane)

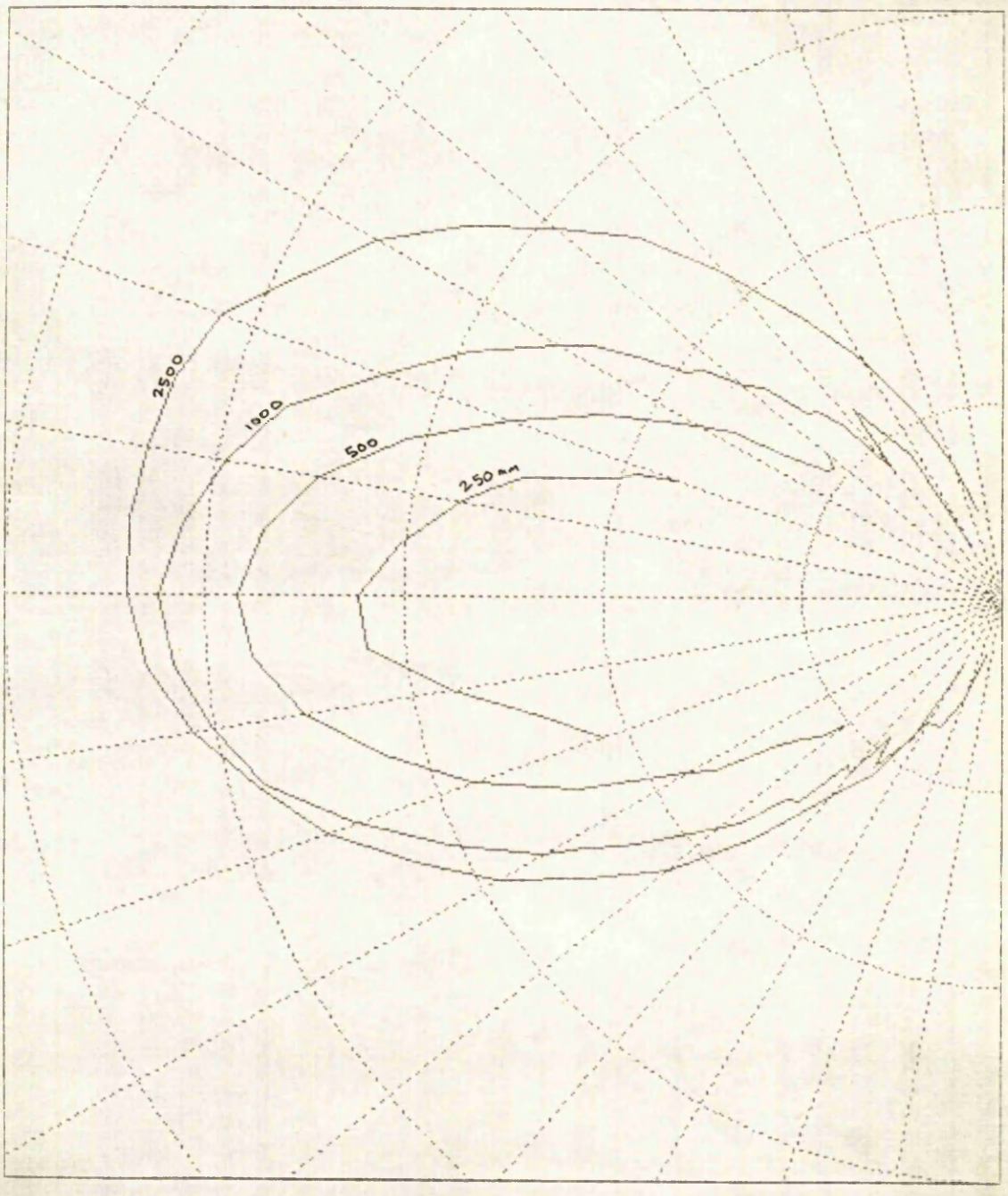

Figure 4.3-2(b) Polar plot of receiving horn (H-plane)

The receiving horn

Details of the radiometer are shown in figure 4.3-1 . The receiving horn (1) has an aperture of 195mm by 145mm and guides the thermal radiation emitted by the object into rectangular X-band waveguide. (WG 16) Polar diagrams in both the E and the H planes of the horn are given in figure 4.3-2 for various transmission path lengths. These plots were obtained on a standard test bench using a Gunn diode with isolator as the signal source. To approximate a point source, an open-ended waveguide without flange was used as the transmitting aerial. The curves show the horn to be reasonably directional in the H-plane but only moderate in the E-plane, especially for the larger transmission path lengths. Much improved resolution would be obtained by using a dish aerial.

The reference temperature source

A gas discharge tube (6) with an output of 15.25db provides a reference noise source. To make absolute measurements using the radiometer, the reference noise temperature is reduced using the attenuator (5) until a null output is obtained indicating equality of signal and reference noise temperatures. Since the attenuator is a precision rotating-vane type with direct calibration, the absolute noise temperature of the signal is easily calculated. For signal levels in excess of 15.25db an additional attenuator is required in the signal arm.

Both the signal and reference arms are matched to the thruplexer (3) with triple stub tuners (2 and 4) to reduce the V.S.W.R.'s to the absolute minimum.

The ferrite modulator

The signal and reference are injected into circular waveguide by the thruplexer with their planes of polarization normal to each other and are then fed to the ferrite modulator (7). The modulator is a Faraday rotator arranged to produce rotation of the plane of polarization through 45 degrees in clockwise and counter clockwise directions alternately.

Since the input of the waveguide twist (9) is set at 45 degrees relative to both planes of polarization, the rotator directs either the signal or the reference into the receiver depending on the direction of rotation. The other signal is absorbed by the resistive vane (8).

The insertion loss and isolation obtained with the Faraday rotator were determined using the arrangement shown in figure 4.3-3 . Measurements were made at the centre frequency of the parametric amplifier pass-band (9.47 GHz) and the input to the rotary vane attenuator was maintained at 1mW throughout the experiment.

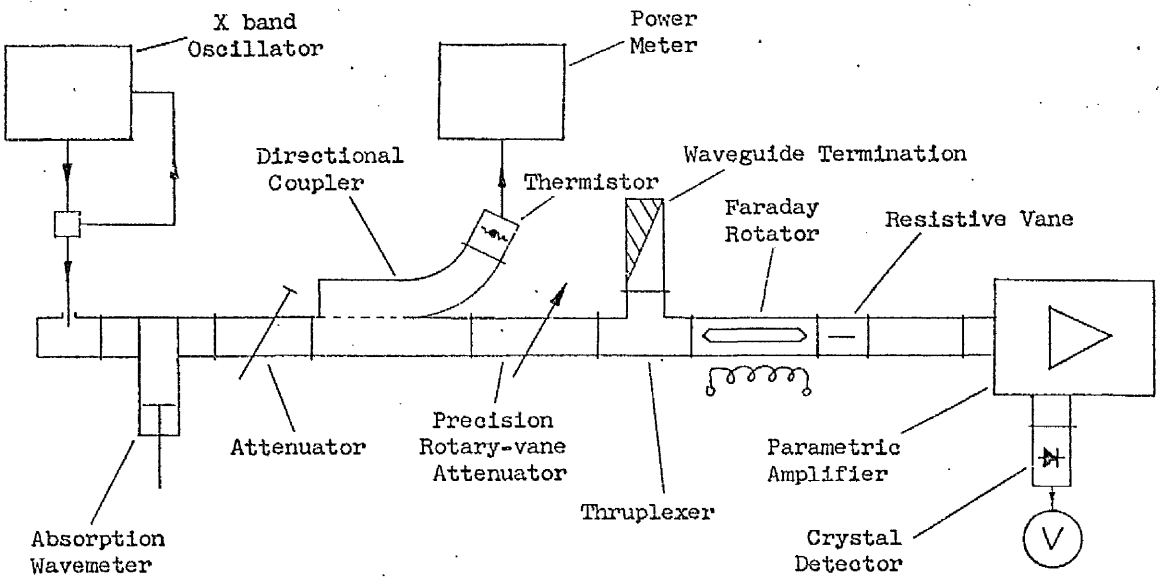

Figure 4.3-3 Set-up used for the determination of the insertion loss and isolation of the Faraday rotator.

Initially the Faraday rotator and its associated components were removed from the set-up to ascertain the total attenuation required for a given crystal output. The Faraday rotator was then refitted and the attenuator adjusted to restore the crystal output. The reduction in the attenuator setting could be identified with the insertion loss or isolation of the Faraday rotator.

Prior to the first measurement with zero current, the ferrite was

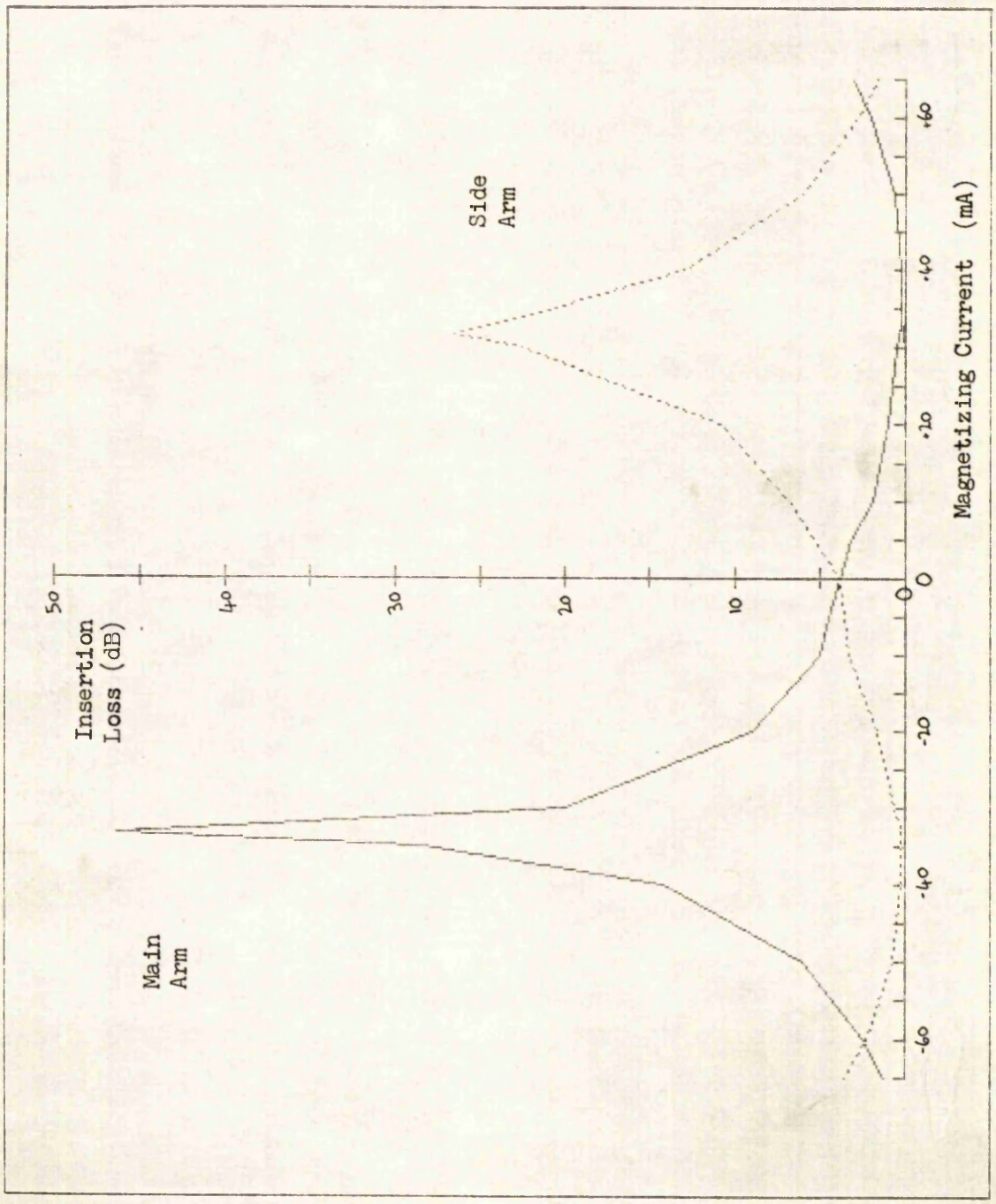

Figure 4.3-4 Variation in the insertion loss / isolation of the Faraday rotator with magnetizing current.

demagnetized. As the ferrite displayed hysteresis subsequent measurements were obtained by monotonically increasing the magnetizing current to that required and then reversing it several times before making the readings. This method was considered the most representative of the actual conditions of use. The parametric amplifier was included in the circuit for the same reason but the ensuing radiometer components were not required as any reflected power from them would have been absorbed in the matched termination of the four-port circulator contained within the parametric amplifier.

The variations in the insertion loss / isolation with current for the main arm and the side arm are shown in figure 4.3-4. These and other results are summarized in table 4.3-1 .

Table 4.3-1

Insertion loss of main arm	0.3 db
Insertion loss of side arm	0.3 db
Isolation of main arm	46 db
Isolation of side arm	26 db
Isolation between main and side arms (I = 0)	30 db
Isolation between main and side arms (I = +32mA)	24 db
Isolation between main and side arms (I = -32mA)	22 db
V.S.W.R. of main arm (I = $\pm$32mA)	1.04
V.S.W.R. at input to parametric amplifier	1.03

Parametric amplifier

After modulation, the incoming noise to the radiometer is amplified at X-band by a low noise, parametric amplifier (10). This is of the non-degenerate type employing two varactor diodes mounted in push-pull and has a bandwidth of 50 MHz centred around 9.47 GHz with a maximum amplification of 22.5 db. The average pump power is 15 mW att25 GHz. The onset of saturation causes the gain of the amplifier to fall by approximately 1 db at an input signal level of -40 dbm and at input levels in excess of -30 dbm

a sharp discontinuity was noticed in the gain / frequency plot.

Balanced mixer

The output of the parametric amplifier is fed to the series arm of a 'magic tee' hybrid junction. In the side arms of the junction, mixer crystals are mounted to form a balanced mixer (12). Local oscillator power enters through the shunt arm. A balanced mixer was chosen as changes in the r.f. impedance at the input are not converted to i.f. impedance changes at the output. As the noise figure of the i.f. amplifier is a function of the i.f. driving impedance, it is important that this remains constant otherwise synchronous noise variations may be generated. Additionally the balanced mixer eleminates converted local oscillator noise and minimizes the local oscillator power leakage into the signal arm.

The V.S.W.R. at the input to the balanced mixer was found to be 1.47 with no local oscillator drive increasing to 2.09 with local oscillator drive. However this could be reduced to 1.03 using the triple stub tuner (11).

Local oscillator

A Gunn diode source (15) is used for the local oscillator and is tuned by the movable short circuit (16). As the oscillator is sensitive to reflected power a ferrite isolator (14) is included. A 50 ohm stabilizing resistor is necessary in series with the diode. At a diode current of 160 mA with the isolator in circuit, the output power is 14.0 mW at 9.425 GHz.

The attenuator (13) adjusts the local oscillator drive to the balanced mixer. A setting of 6.2 db was found to give the optimum signal to noise ratio in the mixer and produced a crystal current of 1.5 mA.

Intermediate frequency amplification and detection

The balanced mixer crystals operate in push-pull and their outputs are coupled to the input of the 45 MHz head amplifier (19) via a double tuned transformer. Over-coupled, this produces a bandpass characteristic with a bandwidth of 5.8 MHz and a ripple of 0.5 db. The i.f. output imped-

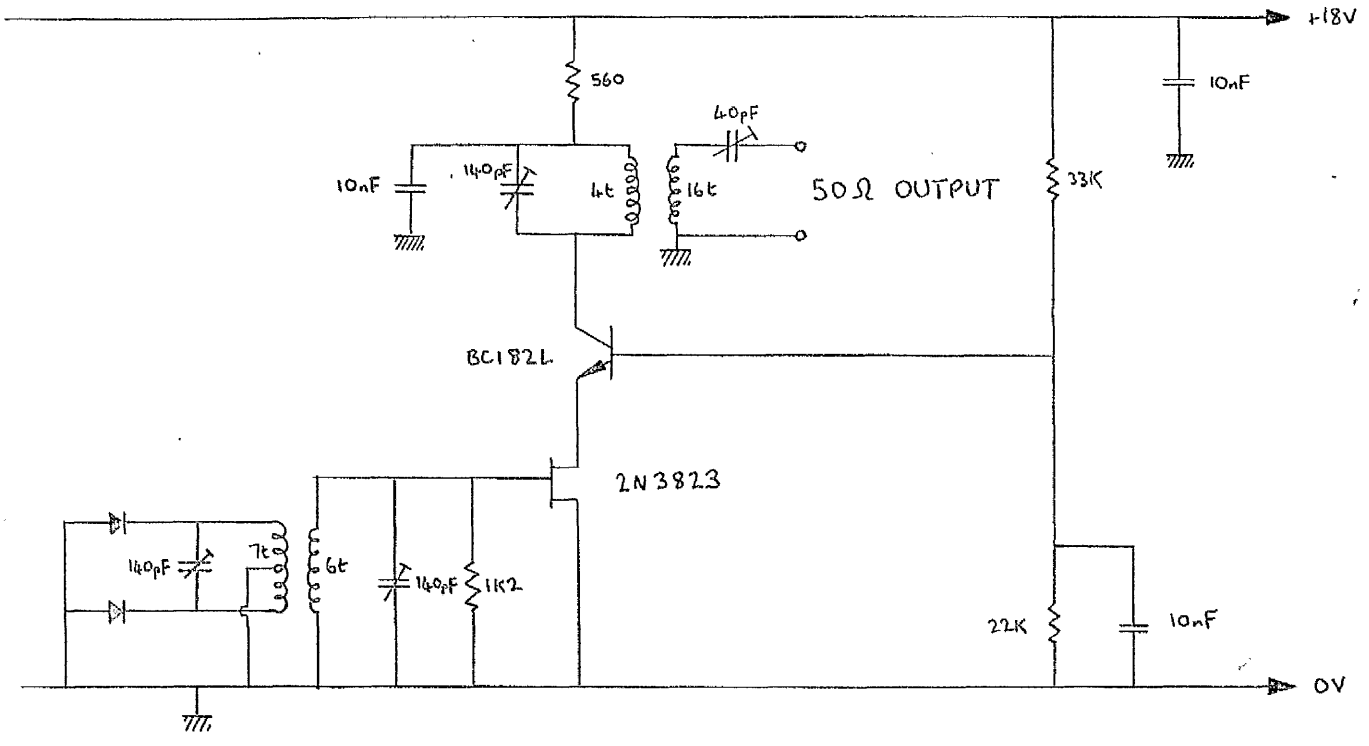

Figure 4.3-5 F.E.T. head amplifier

ance of the crystals is 170 ohm. The head amplifier consists of a field effect transistor and bipolar transistor operating in cascade. They drive a double tuned i.f. transformer operating into 75 ohm. The output transformer is below critical coupling and reduces the overall bandwidth of the head amplifier to 4.7 MHz.

The gain of the head amplifier is 10.1 db and the overall loss, when combined with the mixer, is 1.3 db. This indicates a mixer loss of 11.4 db.

The main 45 MHz i.f. amplifier (20) with integral second detector (21) has a bandwidth of 3 MHz. The second detector current is displayed on a 0 - 100 μA meter and, on maximum sensitivity, full scale deflection is obtained with an i.f. input of 20.9 μV.

Low frequency, narrow-band amplifier

Viewing the output from the second detector with an oscilloscope, an input signal level of -118 dbm was just detectable with the system described so far. To extend measurements below this level, the output is

fed to a phase sensitive detector (23) via an amplifier (22) tuned to the modulating frequency. In this instrument the modulating frequency is half that of the mains supply.

Initially an amplifier employing a parallel-tee feedback network tuned to 25 Hz was used. It had a minimum 3 db bandwidth of 0.35 Hz and a sensitivity of 10 μV. However the circuit rendered the radiometer sensitive to mains frequency variations as it was not readily adjustable in frequency. It was therefore discarded in favour of a second-order, positive feedback, band-pass filter of the type described by Hilburn and Johnson.[132] The circuit of this is shown in figure 4.3-6 and is analysed in appendix 2.

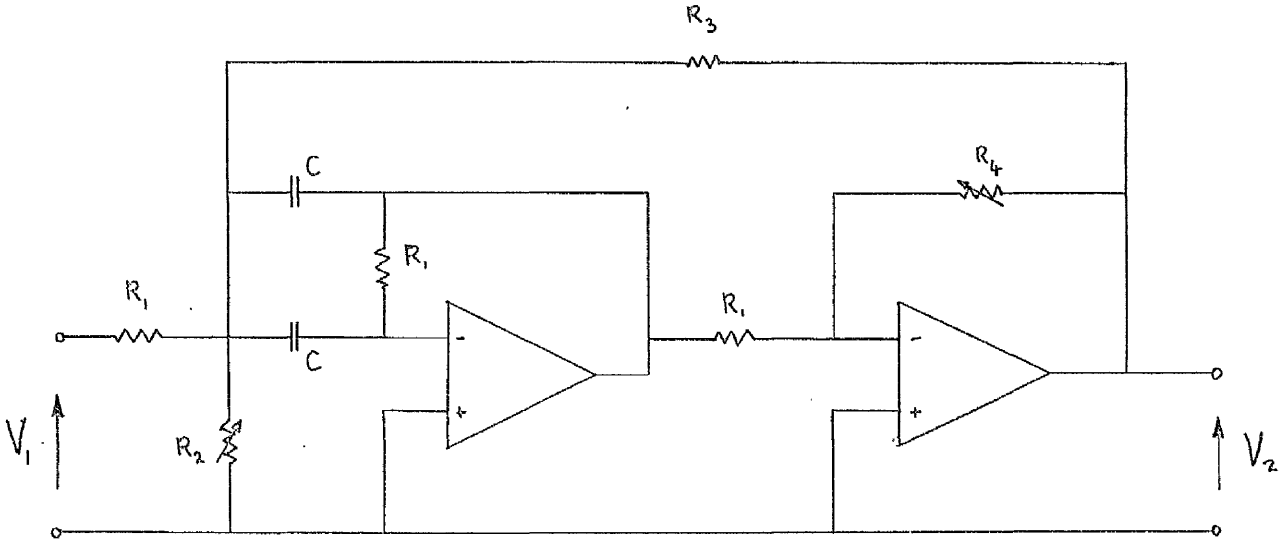

Figure 4.3-6 Second-order positive feedback band-pass filter

The pass-band centre frequency f_o is given by

$$f_o^2 = \frac{1}{4\pi^2 R_1 C^2}\left(\frac{1}{R_1} + \frac{1}{R_2} + \frac{1}{R_3}\right) \qquad (4.3\text{-}1)$$

and the bandwidth B by

$$B = \frac{1}{2\pi R_1 C}\left(2 - \frac{R_4}{R_3}\right) \qquad (4.3\text{-}2)$$

It is clear from these equations that the amplifier can be tuned, without

altering the bandwidth, by varying R_2 and that the bandwidth can be varied without altering the tuning frequency by adjusting R_4. The circuit is thus eminently suited to this application.

The amplifier was designed to be tunable over the range 24.5 - 25.5 Hz with a bandwidth adjustable from 0.6 - 3.3 Hz. The voltage gain at resonance is given by

$$\frac{V_2}{V_1} = \frac{R_4}{R_1(2 - R_4/R_3)} \qquad (4.3\text{-}3)$$

and, depending on the setting of R_4, ranges from 1.25 to 10.7 . For low level signals a standard operational amplifier circuit with a gain of 40 dB is appended.

Phase sensitive detector

The phase sensitive detector (23) measures the degree of correlation between the output of the low frequency tuned amplifier and a reference signal obtained from the modulator drive circuit (17). The output is displayed on the meter (24). At low signal levels the correlation may be poor, requiring averaging over many cycles. To cater for this situation the time constant of the output meter is adjustable upto ten seconds.

Modulator drive circuit

Since discharge testing of high voltage equipment is commonly performed using mains frequency energisation, synchronous modulation at half mains frequency is used in the instrument. This avoids the possibility of beating effects occurring between the modulator and the noise source.

To outline the circuitry used, the mains input to the 'divide by two' circuit (18) is transformed down and then 'squared' by a comparator. (This is arranged to have a finite degree of hysteresis to avoid oscillations at the zero crossing points.) The resulting 50 Hz square wave is used to clock a D-type 'flip-flop'. By connecting the D and $\overline{Q}$ terminals together,

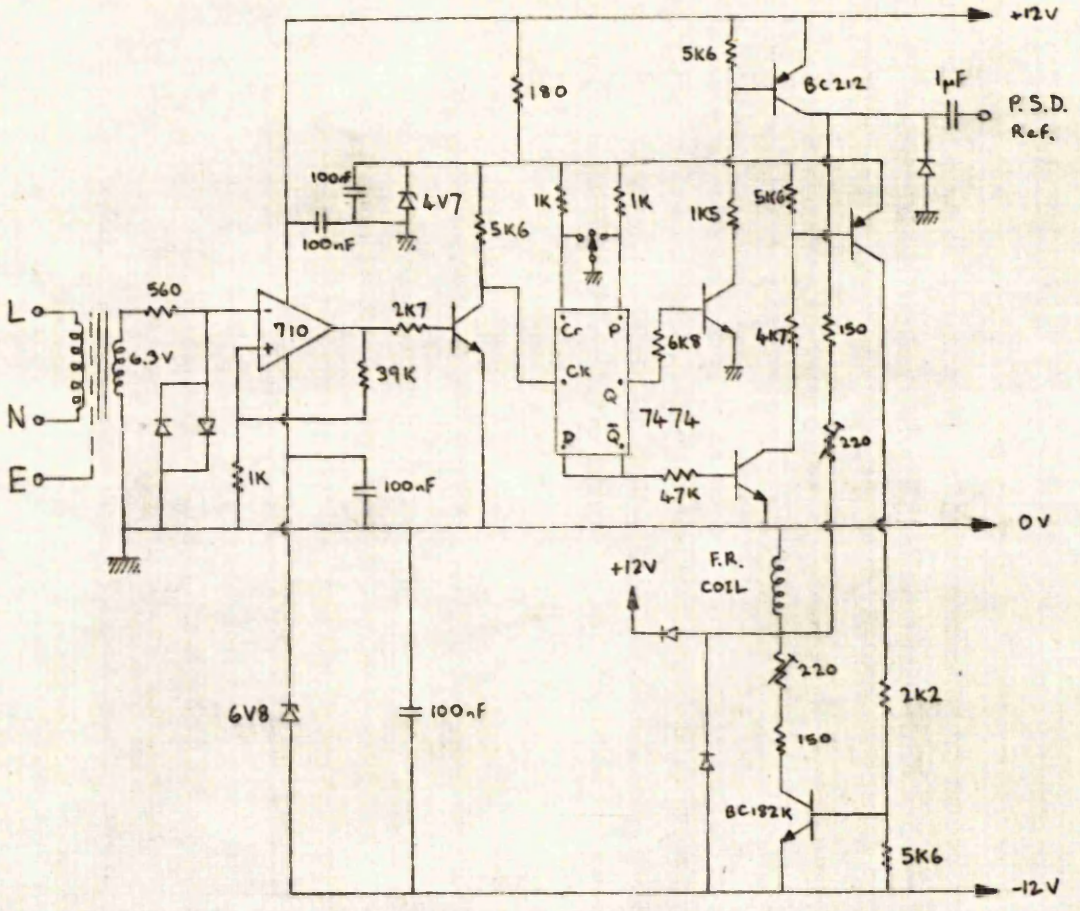

Figure 4.3-7 Circuit diagram of the modulator drive circuit

the edge triggered 'flip-flop' performs the required frequency division and its output controls the modulator drive circuit.

The modulator drive circuit utilizes bipolar transistors and provides independent control of the positive and negative magnetizing currents. Relatively large driving voltages are employed in the output stage to minimize the time taken for current reversal. The current reaches 90% of its final value in less than 850 μseconds.

Radiometer performance

The noise figure of a system is commonly defined as the signal to noise power ratio at the output divided by a similar ratio at the input. The input noise power is taken as the thermal noise originating from a resistor at 290°K. For a multistage system consisting of n elements the

overall noise figure is given by

$$F = F_1 + \sum_{i=2}^{n} \frac{F_i - 1}{\prod_{j=1}^{i-1} G_j} \qquad (4.3\text{-}4)$$

where F_i and G_i are the noise figure and gain of the i^{th} stage respectively.

Noise measurements were made using the method given by Harvey.[133] He points out that if P_1 is the output power obtained from a system when the input power is zero, except for thermal noise, and P_2 is the output power when the input power is increased by P_s, then the noise figure is given by

$$F = \frac{P_1 P_s}{(P_2 - P_1)kT_oB} \qquad (4.3\text{-}5)$$

If $P_2 = 2P_1$ this reduces to $F = P_s / kT_oB$. For radiometer applications it is preferable that P_s should itself be derived from a noise source.

Measurements were made using a low pressure, gas discharge, noise tube. It was mounted obliquely in a section of waveguide to reduce the V.S.W.R. (1.1). The noise tube had an output power of 15.25 db relative to a resistor at 290°K.

For the purpose of noise measurements the radiometer was considered to be a four stage system as shown in figure 4.3-8 . To determine F_a, the

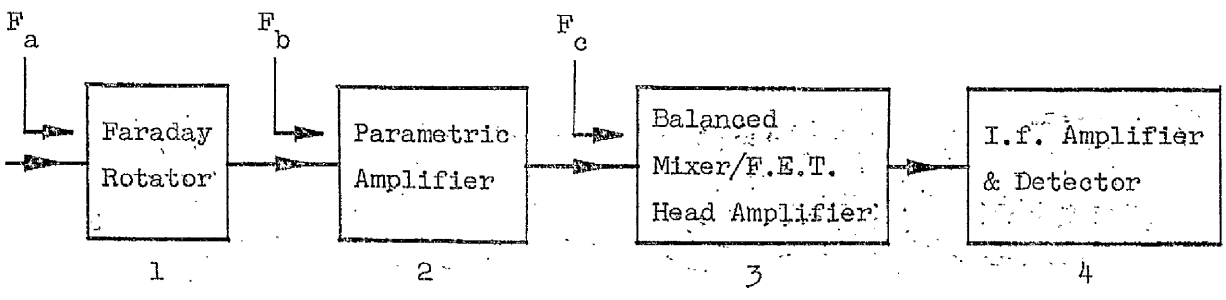

Figure 4.3-8 Representation of radiometer for noise figure evaluation

noise tube was connected to the Faraday rotator via a precision rotating vane attenuator and the second detector output was noted with the noise tube cold. The i.f. gain was then reduced, the noise tube was struck

and the attenuator adjusted to restore the second detector current to its previous value. F_a could then be calculated using equation (4.3-5). This procedure was repeated to obtain F_b and F_c.

From the results obtained and using equation (4.3-4), the performance of the radiometer and its constituent parts was found. The overall results are summarized in table 4.3-2 .

Table 4.3-2 Results of noise measurements

F_a =	6.85 db	F_b =	6.10 db	F_c =	15.8 db
F_1 =	1.41 db	F_2 =	5.87 db	F_3 =	14.3 db
F_4 =	9.84 db				
G_1 =	-0.5 db	G_2 =	22.5 db	G_3 =	-1.27 db
G_{mixer} =	-11.4 db	$G_{head\ amp}$ =	10.1 db		
F_{mixer} =	8.5 db	$F_{head\ amp}$ =	2.44 db		

The results show the contribution of individual components to the overall radiometer performance. The effective noise temperature of the radiometer, given by $(F_a - 1)T_o$, is 1114°K. This disappointingly high figure can be seen to be due to two causes. Firstly the noise figure of the parametric amplifier is high, (it is well outside the manufacturer's specification of 3.3 db) and secondly the conversion loss in the mixer stage is excessive. Nevertheless on testing the complete radiometer with the noise tube, the sensitivity was found to be approximately $\frac{1}{2}$°K with the time constant of the phase sensitive detector set to 10 seconds. This clearly demonstrates the advantages of the Dicke system.

4.4 Results of radiometric measurements

To test the effectiveness of the radiometer as a detector of partial discharges an artificial discharge source was constructed consisting of a spark gap connected in series with a capacitor. The spark gap was formed using two 38mm 0 B.A. brass machine screws each with a tungsten wire mounted concentrally in its tip. The tungsten wires were 1.0mm in diameter and projected 5mm from the screw tips. The electrode ends were ground square and arranged to butt end to end, their separation being adjustable by means of the screws. The capacitor was mounted directly above the upper electrode and consisted of 50mm square aluminium plates with radiused corners. Its initial capacity was chosen to be small and was then, for subsequent measurements, increased by reducing the plate separation, interleaving addition plates or interposing dielectric slabs. The energizing high voltage was supplied via a coaxial cable (type RG 214U) with the unscreened length kept to a minimum. The energizing transformer was mounted in a screened box and decoupled from the discharge source by a chain of ten, 68Kohm resistors connected in series. The transformer could either be energized from the mains supply or from an inverter operating at 116 Hz. In the latter case, as the inverter and its battery were also contained in the screened box, external interference could be minimized. To further reduce the chances of extraneous interference during the measurements, the radiometer was installed in a screened room with only the receiving horn and a short length of waveguide projecting externally. The mains supply to the room was also filtered. The effectiveness of these measures against external interference was checked by blanking-off the input to the radiometer and generating spark discharges nearby. The results were satisfactory, the interference having no noticeable effect with the high voltage transformer energized from either the battery or the mains supply.

Table 4.4-1 Radiometric noise levels obtained with discharge source.

Series Capacitance C_a pF	Noise Temperature ^oK	Number of Discharges sec^{-1}	Charge Transferred pC	Discharge Energy J	Normalized Noise Temperature $^oK \times 10^{-3}$
Electrode separation 0.05mm					
5.0	44	700	4403	2.091	62.9
9.1	41	1000	7265	3.451	41.0
17.1	53	1100	12495	5.935	48.1
37.8	113	2450	24015	11.41	46.1
70.0	149	2400	38085	18.09	62.1
Electrode separation 0.10mm					
5.0	22	425	5517	3.174	51.8
9.1	19.4	575	9143	5.260	33.7
17.1	28	675	15694	9.028	41.5
37.8	64	1300	30362	17.47	49.2
70.0	75	1500	48175	27.71	50.0
Electrode separation 0.20mm					
5.0	10	187.5	10708	10.98	53.3
9.1	10.9	400	17769	18.22	27.3
17.1	15.4	400	30488	31.25	38.5
37.8	31	700	59089	60.57	44.2
70.0	45	900	93795	96.15	50.0
Electrode separation 0.40mm					
5.0	4.3	100	16464	25.11	43.0
9.1	7.7	200	27343	41.70	38.5
17.1	7.5	225	46911	71.54	33.3
37.8	17	400	91001	138.8	42.5
70.0	23	450	144467	220.3	51.1

The noise levels obtained with the discharge source positioned 250mm from the horn are given in table 4.4-1 for four different spark gap settings, namely 0.05, 0.1, 0.2 and 0.4 mm. The actual charge transferred during each discharge and the energy dissipated are also given these having been calculated from measured values for the series capacitance C_a, the capacitance of the spark gap C_b (C_b varies between 0.91 and 1.00 pF), the shunt capacitance C_c, the gap breakdown voltage and the extinction voltage. (Approximately 100 volts) In all cases the source was energised at 50 Hz with the transformer output set at 3.2 kV and it is evident that, under these conditions, the noise temperature fell as the spark gap was increased but increased as the series capacitance C_a was increased.

These observations suggest that the measured noise temperature is primarily dependent on the number of discharges rather than their individual magnitudes and so, in each case, the noise temperature has been divided by the number of discharges occurring per second in order to calculate a 'normalized noise temperature'. (This represents the noise temperature that would be obtained if the discharging rate were to reduced to one per second without altering the discharge magnitude.) The results support the hypothesis, by showing the normalized noise temperatures to be effectively unrelated to the discharge magnitude within the limits of this investigation. This is a surprising finding as it would be expected that the radiation from a discharge channel would intensify with increase in the energy dissipated due to either increased charge transfer or breakdown voltage. Similarly, if the metal electrodes are primarily responsible for launching the microwave radiation, increasing the gap size (and thereby increasing the discharge magnitude) would increase the voltage transient occurring at breakdown and would, as a consequence, be expected to increase the measured noise temperature. The results show neither of these to be true and so it is concluded that the microwave noise emitted by a spark discharge is primarily determined by the noise temperature of the constituents of the arc.

The normalized noise temperature is a measure of the energy radiated by the discharges rather than the instantaneous power. The conclusion that the radiated energy is independent of the discharge magnitude therefore appears to be at variance with the results given in figures 4.1-2 and 4.1-3 where a definite increase is shown. To resolve this inconsistency the microwave rig of figure 4.1-1 was set up again but with a crystal detector that could be coupled to a high speed 50 ohm measurement circuit. By this means the fine temporal structure of the microwave emissions from the spark discharge could be studied. For the measurements of section 4.1 coaxial cable was used as the high voltage capacitor and different lengths were used to obtain different capacitances. On examining the crystal output it became apparent that what had previously been assumed to be single discharges were in fact damped trains of discharges, the individual discharges being separated from each other by twice the travel time along the coaxial cable. This behaviour can be explained by taking the breakdown of the gap to be equivalent to suddenly applying a virtual short circuit to the end of the cable. This causes the voltage across the gap to fall rapidly resulting in a voltage step of inverted polarity being launched into the cable. This travels to the far end of the cable where it reflects, without inversion, off the effective open circuit presented by the high voltage series resistors. It then travels back to the spark gap arriving with inverted polarity and reduced amplitude one return travel time after the initial breakdown. Because breakdown causes the voltage across the gap to fall rapidly, the sparks cannot be maintained and are therefore of only short duration (of the order of a nanosecond). For this reason, by the time the reflected pulse returns the initial spark will have extinguished and the gap will be open circuited. However when the reflected pulse attempts to reflect off this mismatch, the voltage doubling that would normally occur at an open circuited termination, causes the gap to breakdown a second time. This transforms the termination to an effective short circuit once more resulting in the voltage across the

gap falling rapidly almost to zero thereby launching a further voltage step into the cable. Hence, by this mechanism, a train of short sparks of alternately positive and negative polarity are generated. The train will continue until the travelling voltage step-waves are attenuated to approximately half the breakdown voltage. The rate at which the spark train decays for a given spark gap will decrease as the length of the coaxial cable increases because the energy stored in the cable will be greater. For the longer cables there will therefore be more sparks per train and it is for this reason that the curves of figures 4.1-2 and 4.1-3 show an increase in the microwave energy emitted as the discharge magnitudes increase.

Figures 4.1-5 and 4.1-6 show the instantaneous power emitted by the discharges as measured using a spectrum analyser with a bandwidth of 30 kHz. With this bandwidth the spectrum analyser would be unable to resolve the fine temporal structure of the discharges and so these curves should also be considered as a record of the discharge energy emitted rather than the instantaneous power though with a much reduced integration period. For this reason they also show an increase in microwave energy emitted with increased discharge magnitude. The figures also show three different curves for the three different electrode separations used. From these it is apparent that, for a given length of coaxial cable, the microwave energy emitted decreases as the spark gap (and hence the discharge magnitude) is increased. This apparent anomaly arises because the breakdown voltage, and hence the energy dissipated per spark, is increased resulting in a shorter spark train and therefore less microwave energy radiated.

Some measurements were also conducted with 0.5mm diameter tungsten electrodes to ascertain if the electrodes were shielding the radiometer from the discharges but no discernable differences between the results were found. However the surface condition of the electrodes was found to have an effect for cleaning the electrode surfaces by hand using a fine carbor-

undum stone produced an increase in the normalized noise temperature. This could then be further increased by continued discharging.

All the results given so far relate to measurements made on discharges between metal electrodes. The next step was to make measurements on discharges between a metal electrode and a dielectric so a point plane system was set up with the plane covered by a dielectric film. This arrangement gave corona type discharges centred around the negative peak of the energizing waveform of about 50pC magnitude. Disappointingly no microwave noise emission could be detected. This indicated an equivalent noise temperature of less than $\frac{1}{2}^{o}$K. The 'point' used for these measurements had the form of a truncated cone with the end face domed. The diameter of the end face was 0.125mm and the radius of the 0.108mm. To generate larger discharges (100 - 200pC) the point was replaced by a 1mm diameter tungsten wire with a square end. The measurements were then repeated using separations between the electrode and the dielectric surface in the range from 0.05mm to 1.25mm and with polythene, P.T.F.E. and empire tape as the dielectric. In all cases the measured noise temperature did not exceed 1^{o}K.

The considerable reduction in the microwave energies emitted by discharges when one electrode (or both) is non-metallic is attributed to the change from breakdown by a series of avalanches produced by the Townsend mechanism[134,135] and the more energetic breakdown by streamer formation. It is generally considered that there are two mechanisms of streamer formation. The first relates to the formation of cathode directed streamers and was originally proposed by Meek[136,137]. The second relates to the formation of anode directed streamers and was originally proposed by Raether[138,139]. These mechanisms are described by Tedford in the book edited by Alston[140] and extracts from the original papers are included in the collection of papers contained in the volume by Rees.[141] Raether deduces that, at the very minimum, 10^{8} electrons are required per avalanche if field enhancement due

to space charge is to be adequate for streamer propagation. As the electronic charge is 1.602×10^{-19} Coulomb, a charge transfer of at least 16pC per avalanche is, as a consequence, required for streamer breakdown. Streamer formation cannot therefore be expected in the case of the corona type discharges.

The results would have been improved if a high gain dish aerial had been used in place of the receiving horn. However it was considered, in the light of the results obtained so far, that the technique did not merit further investigation as a possible method of detecting and locating partial discharges in high voltage insulation structures.

CHAPTER 5

The location of partial discharges by a travelling wave method

In this chapter a technique will be described that is particularly suitable for locating partial discharges in high voltage metal-clad switchgear and short cables. The location of partial discharges in switchgear is of particular interest because the most common causes of faults due to insulation failure during service are erosion and carbonization resulting from prolonged partial discharge activity. The process is slow at the relatively low electric stress levels typically employed and so the equipment has, in some instances, operated for upwards of fifty years before failing. However, in many cases, failure has occurred much earlier, this being particularly true in the case of some compound filled busbar chambers. As many of the older switchboards are not fitted with busbar protection the damage resulting from a fault can be extensive particularly as the fault current levels to which the busbars are exposed are normally high. The problem has in many cases been exacerbated because the fault level has been steadily increased over the years to cope with increases in system demand.

It is evident therefore that a method of detecting incipient faults in metal-clad switchgear is required in order to reduce the hazards to personnel and to improve system reliability. Of the test methods available, the detection of partial discharges has proved the most satisfactory. Following several faults in 33 kV compund filled busbar chambers, Hill and Creswell[142] of the London Electricity Board initiated an extensive programme of discharge testing on the switch-boards within their jurisdiction and their results showed that, when significant partial discharge activity was detected, it could invariably be traced to localized insulation defects. Thus, by refurbishing the insulation of a limited number of components, the switch-boards could be reinstated. In this way it was possible to defer

the replacement of several older switch-boards thereby achieving a considerable saving in capital expenditure.

Once it has been established that the discharge levels exhibited by an item of equipment are unacceptable the positions of the various discharge sites must be determined before remedial action can be taken. A rough location can be effected by repeated sectioning of the test specimen followed by discharge testing but, in the case of compound filled busbar chambers, this is a laborious procedure. For many other test specimens it is impossible. Metal-clad switchgear is not amenable to standard location techniques such as radio interference or acoustic measurements but successful locations have been reported by Mole[143] using an X-ray method. However, as X-rays capable of penetrating appreciable thicknesses of steel are required the radiation hazards posed render the technique unsuitable for most applications. In the case of the short cable lengths that occur frequently in generating stations and substations, ultrasonic detectors have been used with considerable success. However scanning along the sheath of a cable is not always convenient as the cable may lie in ducting, be buried or rise high above the working area.

This chapter describes a travelling wave method of location that overcomes these limitations be measuring the time taken for the discharge transients to travel along the equipment under test from the discharge site to detection points at either end of the equipment. Travelling wave methods are well established for longer cables. Kreuger[110] describes several circuit arrangements using a single-beam oscilloscope and claims an accuracy of 3 metres. Mason[7] however considers the achievable accuracy to be around 10 metres for a cable insulated with a low-loss dielectric such as polythene. Such an accuracy would render measurements, on cables of less than 100 metres, of only limited value. Furthermore, the techniques described are quite unsuitable for switchgear measurements where gross distortion of the discharge transients occur as the result of multiple

internal reflections. If, however, the transients from each discharge are detected at both ends of the equipment and displayed on the separate beams of a wide-band dual-beam oscilloscope, their waveshapes become less important for the difference in their arrival times can be obtained from their respective leading edges. This method is inherently capable of greater spatial resolution than the single beam technique being ultimately limited only by the rate of current build-up in the discharges.

Spatial resolution achievable under ideal conditions

Previous work by the author[109] to assess the resolution likely to be achievable using such a technique includes the measurement of the rise-time of the current pulses produced by discharges in artificially created voids using a test cell similar to that described by Bailey.[144] Using a fast sampling oscilloscope the risetime of the overall measurement system, including the delay line, was better than 200 pS and, as this risetime was considerably less than those obtained for the discharges, it could be discounted. Polythene, P.T.F.E. and empire cloth insulation discs were tested of thickness from 0.13mm to 1.35mm with centrally disposed cylindrical voids of 0.5 and 1.0mm radius and having depths ranging from 0.04mm to 0.57mm. Within these limits the risetimes of the discharge current pulses were found to be dependent on the void depth and the duration of stressing but independent of the sample thickness and material. After 15 minutes stressing using 50 Hz high voltage excitation at 20% above the inception voltage the discharge current was found to rise from 10% to 90% of its peak value in a time given approximately by

$$t_r = 22 \times d \times 10^{-9} \text{ seconds} \qquad (5\text{-}1)$$

where d is the void depth in millimetres. The risetimes were found to increase markedly if the stressing time was extended and, after 2 hours, could reach a value as much as four times that given by (5-1). A corresponding reduction in the peak current was also noted. These finding are in agreement with the results obtained by Salvage et al[145,146] using voids of 0.13mm

and 0.05mm depth in polythene.

The effect of increasing the conductivity of the upper and lower surfaces of the voids was investigated by interposing two small discs of graphite coated paper (3400 ohms/square) between the dielectric discs. An increase in the magnitude of the output pulse was observed which was indicative of the increased charge transfer but otherwise the results were similar. However the discharges proved less dependent on the stressing time with little change even after 4 hours.

To obtain an idea of the spatial resolution that the method is inherently capable of realizing the transient from a typical discharge produced in the test cell was recorded together with the same transient delayed by travelling along an additional 0.5 metre length of polythene insulated cable. The result obtained is reproduced in figure 5-1. The traces each had a risetime of approximately 10nS and the additional 2.5ns delay of the latter pulse is clearly apparent. From the traces it would appear that a time difference of 0.5ns would just be discernable corresponding to a path difference of 0.1 metres. This would be sufficient to resolve two discharge sites 50mm apart. The traces were obtained using a sampling oscilloscope coupled to an X - Y pen recorder and their irregular nature results from sampling successive pulses of slightly differing amplitude.

Propagation of discharge transients in metal-clad switchgear

The largest single item in a switch-board utilizing metal-clad switchgear is the busbar chamber and, though this can be sectioned, the operation is expensive, especially if the chamber is compound filled. Its physical dimensions combined with the multitude of branch points and other discontinuities along its length cause it to have the poorest performance as a pulse transmission line encountered when discharge testing switchgear. Since also some busbar chambers are currently giving cause for concern, a study of their high frequency transmission properties was considered necessary.

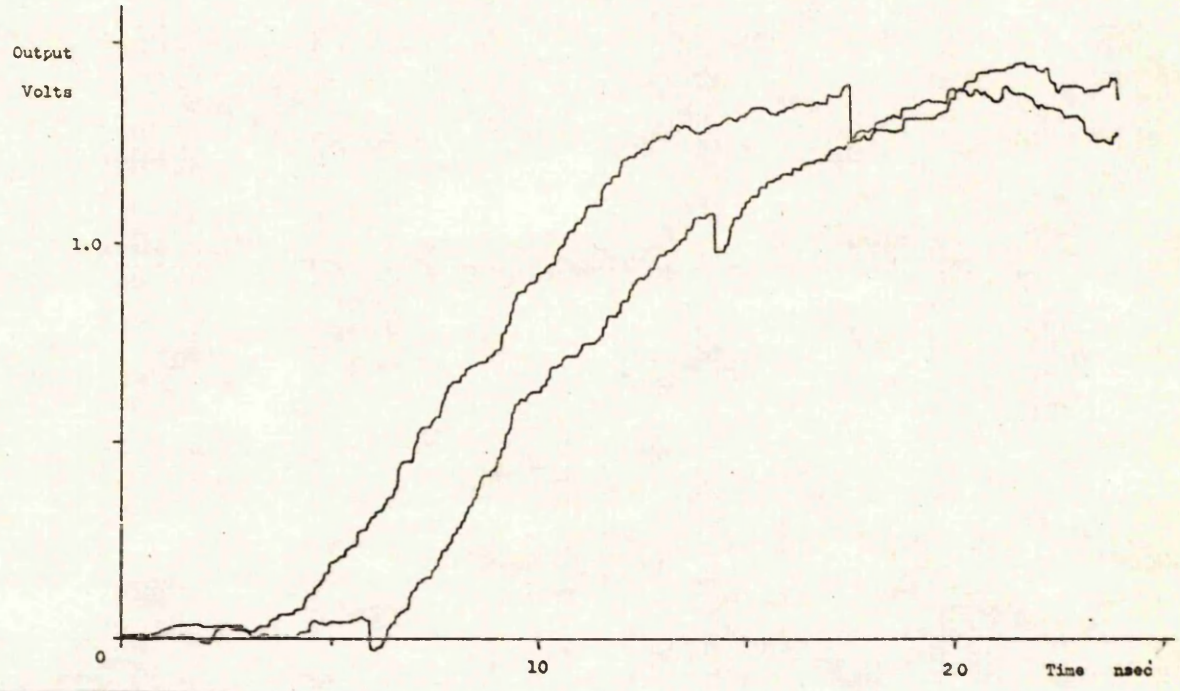

Figure 5-1 Displacement of discharge transients obtained by a change of 0.5 metres in transmission path length

The initial work was centred on a theoretical study, using Fourier techniques, of the propagation capabilities of metal-clad, compound filled busbar chambers. The transients considered had waveshapes similar to those produced by discharges and the parameters of the high frequency busbar model used were obtained, where possible, by measurement. Where this was not possible or practicable, they were obtained by calculation. One parameter, for example, that was not amenable to measurement was the characteristic impedance of the three phase busbar chamber. An estimate of this was therefore obtained by calculating the capacitance per unit length using an electric stress field plot produced numerically by a finite difference routine. To determine the inductance per unit length the program was re-run with the relative permittivities of all the insulation components set equal to unity. This yielded the capacitance per unit length of the chamber if it had been totally vacuum insulated and, knowing the velocity of propagation to be that of light in vacuo for this case, the inductance per unit length could be calculated. The values of capacitance and inductance

so obtained were then used to calculate the characteristic impedance of the chambers. The work has been previously reported by the author[109] but, in summary, the output waveforms obtained served to emphasize the complexity of the transient waveforms that were to be expected in practice. More important though they showed that the leading edge of the waveforms should be adequately steep fronted to allow the accurate location of partial discharge sites.

Following this theoretical study, time domain reflectometry measurements were made on a single 33 kV compound filled busbar chamber to ascertain the severity of the multiple reflections that would arise. From the traces obtained it was possible, but with difficulty, to identify the reflections from various constituent parts of this single chamber. The measurements however confirmed that considerable distortion of the discharge transients could be expected and ruled out any possibility of identifying the component of a discharge transient resulting from reflection off the remote end of a busbar section. This therefore closed any chance of locating discharges by observing the multiple reflection pattern obtained at a single measurement point - a technique commonly used for cables when the remote end is distant from the measuring equipment.[110]

Transmission measurements were next made on four busbar chambers temporarily linked together and the results confirmed the predictions of the theoretical study that good locations should be possible using the double ended measurement technique to ascertain the difference between the times taken by the transients from each discharge to traverse the busbar in their respective directions.

This completed the previously reported feasibility study[109] with the exception of an initial attempt to locate discharges in a compound filled busbar. The location was successful but of low accuracy because only a single beam oscilloscope with sufficient bandwidth was available.

To obtain a dual trace on this instrument at the required sweep speed necessitated operating it in the 'alternate sweep' mode whereby one channel was displayed during the first sweep and the other channel was displayed during a second. This necessitated the time-base of the instrument being triggered twice to obtain both traces and, though triggering in each case was effected by the same channel, variations in the magnitude and shape of the pulse from successive discharges at the same site resulted in variations of the trigger point. As a consequence the differential time delay between the two traces exhibited some degree of jitter thereby considerably reducing the achievable accuracy of location. Work was halted at this stage pending the acquisition of a suitable dual-beam oscilloscope.

5.1 Location technique

The method of locating partial discharges is shown in figure 5.1-1 .

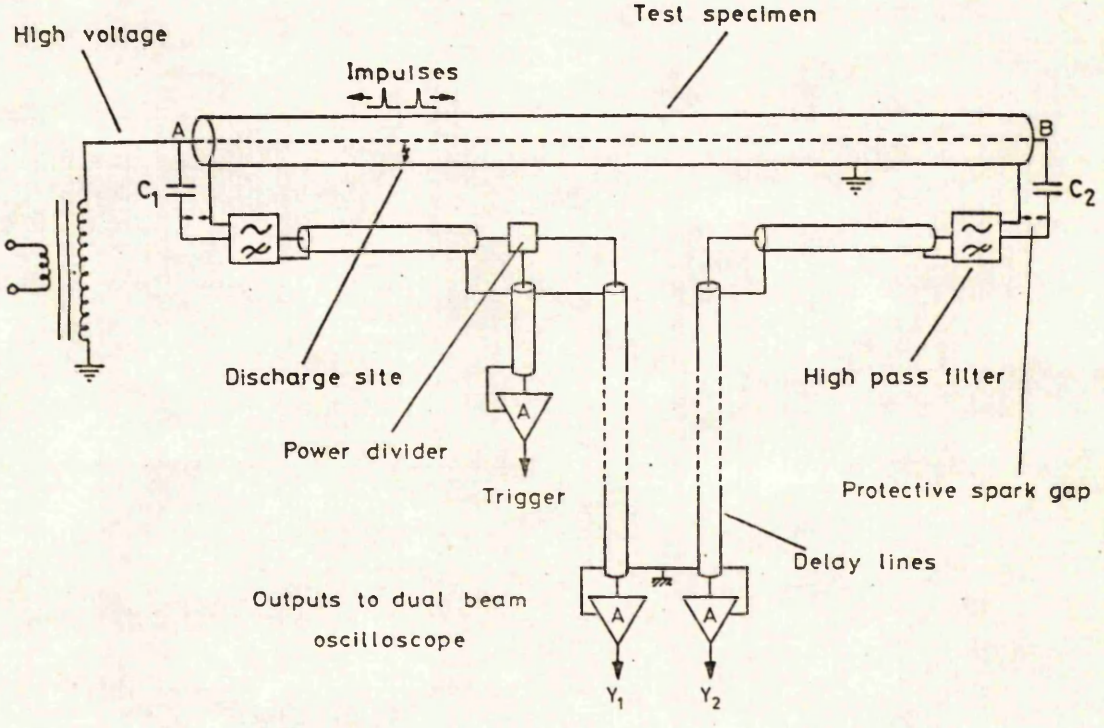

Figure 5.1-1 Travelling wave method of partial discharge location

The discharge transients arriving at the detection points A and B are transmitted via the high voltage blocking capacitors C_1 and C_2 to high-pass filters. The latter serve to reject any residual power frequency components and to reduce other interference. The filtering requirements are modest and a simple resistor - capacitor type of circuit with a cut-off frequency of 30 MHz has proved satisfactory. The transients are fed to the measuring equipment through low-loss coaxial cables and a triggering signal is extracted from one channel using a power divider for matching purposes. The transients are then passed along delay lines to the Y inputs of a dual-beam oscilloscope. The wide-band video preamplifiers extend the sensitivity to 100 microvolts. The delay lines serve two purposes. Firstly they enable the initial part of the transients to be displayed regardless of the point at which triggering occurs. This has the advantage that the triggering level can be set relatively high for more consistent triggering and greater noise immunity. Secondly, should the transient with the greater delay be on the triggering channel, both transients can still be displayed. A delay of 150 ns with a band-width of 100 MHz has proved adequate. Figure 5.1-1 also shows details of the earthing arrangements. It is important that the lengths of the live and earthy sides of each transmission path are matched as closely as possible if detail is not to be lost from the transients.

Results obtained

Figure 5.1-2 shows the traces obtained with a corona source of 50 pC as it was moved along a model busbar consisting of two parallel 28mm O.D. copper tubes spaced at 150mm between centres. The overall length was 11.87 metres and the traces shown were obtained with the discharge source placed at the left-hand end, an intermediate position and the right-hand end respectively. The differential time delay in each case has been measured (a positive value indicates that the upper trace leads the lower) and it can be seen that the change is appreciable between the

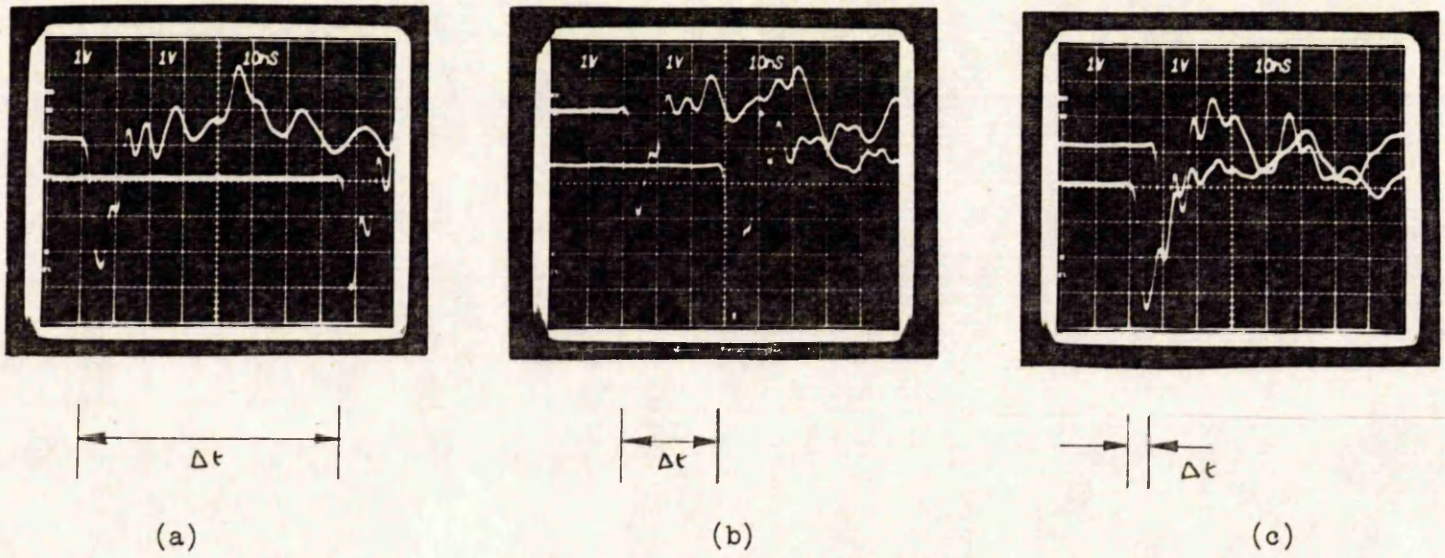

Figure 5.1-2 Traces obtained with a corona source for three positions on a model busbar.

Discharge position:
a) Left hand end (Δt = +75nsec.)
b) Intermediate position (Δt = +28nsec.)
c) Right hand end (Δt = -7nsec.)

Y sensitivity (both beams) 1 volt/div. Sweep speed 10nsec./div.

Upper trace - left-hand end

Lower trace - right-hand end

three sites. Had the delays in the measurement system been equal, the value of Δt for case (c) would have been simply the negative of (a). However it has been found more convenient in practice to make initial measurements with an artificial discharge source placed at each end of the test specimen in turn for, once the system has been calibrated in this way, all subsequent locations are derived as a percentage of the overall system length and the precise values of the circuit delays become irrelevant. Applying this to figure 5.1-2(b) the calculated discharge position is 6.80 metres from the left-hand end, a figure which compares favourably with the actual value of 6.88 metres.

These traces were obtained from an idealized system having few discontinuities and little attenuation or dispersion. As a consequence the traces have clearly defined leading edges and their magnitudes are almost independent of the discharge position. The results obtained in practice are demonstrated in figures 5.1-3(a) - (c). Figure 5.1-3(a) shows the traces obtained when an artificial discharge of 2300 pC was connected to one end of a busbar section consisting of six chambers. The discharge source was provided by a spark gap in series with an air spaced 5 pF capacitor. The spark gap consisted of two 0.5 mm diameter tungsten wires rigidly mounted end to end with a spacing between them of 0.05 mm. The attenuation of the upper trace relative to the lower is apparent but the leading edges of the transients remain sharply defined. The traces shown in figure 5.1-3(b) were obtained for an internal discharge of 200 pC on an 11 kV compound filled busbar chamber. The traces have been expanded to show the leading edges in more detail and it can be seen that, though some rounding has occurred, the time resolution remains good. Figure 5.1-3(c) shows the traces obtained with an internal discharge of 225 pC in a 6 metres long 11 kV transformer feeder cable. The oscilloscope sensitivities and sweep speed are shown in the photographs, the left-hand value in each case denoting the upper trace sensitivity.

Figure 5.1-3 Sample of traces obtained from installed equipment

a) 2300 pC artificial discharge source connected to 33 kV busbar

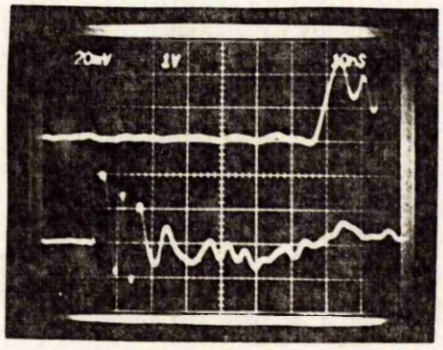

$\Delta t = -63$ nsec.

b) 200 pC internal discharge on 11 kV busbar

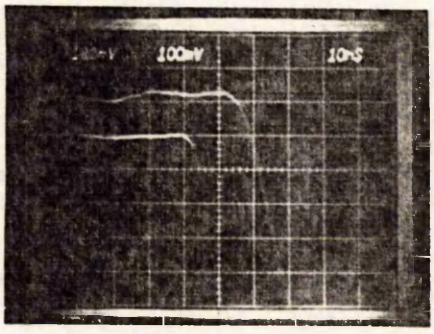

$\Delta t = -12$ nsec.

c) 225 pC internal discharge in short length of 11 kV cable

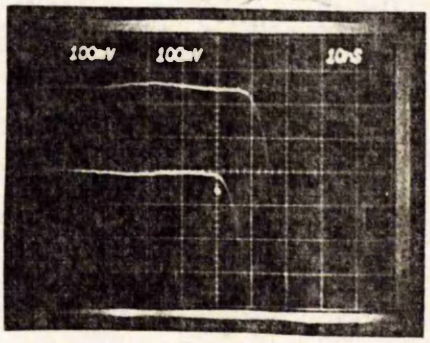

$\Delta t = -8$ nsec.

It should be noted that in figures 5.1-3(b) and (c) the signal has been fed through a wide-band pre-amplifier having a voltage gain of fifty.

Multiple discharge sites

When more than one discharge site is present various techniques are available for obtaining the positions of the individual discharges. The site with the lowest inception stress can be identified by adjustment of the energizing voltage, whilst the largest discharge at any given test voltage can be singled out by raising the triggering level. By applying the latter method with the triggering signal derived firstly from one channel and then the other, two discharge sites at well separated locations can be individually selected. This technique has proved particularly useful when testing 33kV busbars with discharge sites located in more than one end cap. A further means of separating multiple discharge sites is gained by the use of a double timebase where the delaying timebase is set to inhibit triggering of the delayed timebase until a particular point in the energizing high voltage cycle. By adjusting the delay, discharges occurring at different points in the cycle can be separated. As an example this method enables small corona discharges to be located in the presence of much larger internal discharges.

If the above methods fail to separate the individual discharge sites resort must be made to either random 'single-shot' triggering or multiple exposures. Figure 5.1-4(a) demonstrates the latter applied with three corona sources attached to the model busbar. The triggering signal was obtained from the lower channel and so the lower impulses are coincident on the screen. It is evident from the upper traces that the discharges were located at three distinct positions. The intensities of the separate traces are indicative of their relative frequencies of occurrence. Figure 5.1-4(b) shows the same technique applied to a short cable length containing multiple discharge sites. In this case the upper channel has been used for triggering.

Figure 5.1-4 Traces obtained when multiple discharge sites present

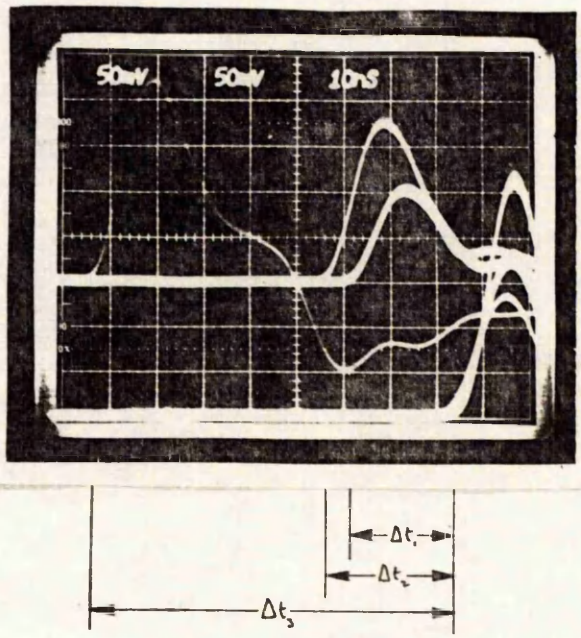

a) Three corona sites on model busbar

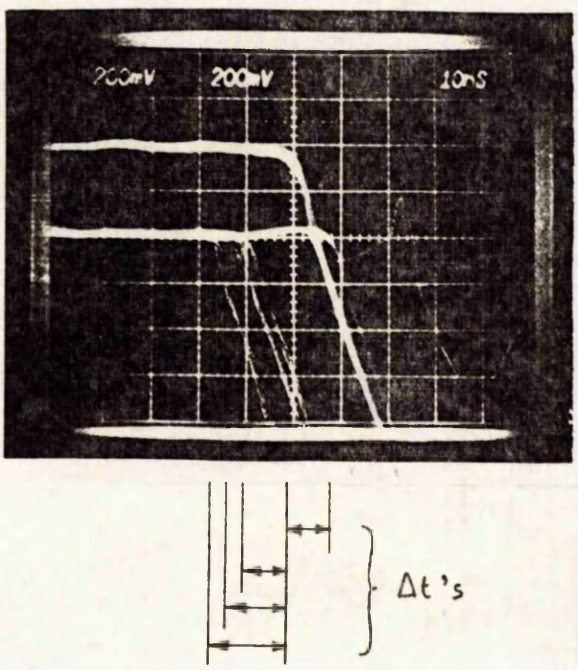

b) Multiple internal discharge sites in a short cable

Anomalous results

If discharges occur on a branch of the test specimen off the main timing circuit, the apparent location will be at the branching point. This arises because only time differences can be measured and the time taken for the discharge transients to travel along the branch is common to both channels. However, once the branch point has been reached, the paths of the two channels will diverge and their time difference will be such that the discharges appear to be located at the branch point. If this situation arises the ambiguity can be resolved only by re-defining the timing circuit to include the branch.

A further instance of anomalous results arises when testing equipment where the timing circuit is substantially two or three dimensional. This situation applies when testing items such as single busbar chambers, current transformer chambers, switches and circuit breakers. In these cases alternative shorter routes are available for the transients either along neighbou ing conductors or by propagation through the insulating medium. As a result the received transients display a preamble and this must be recognised and allowed for if satisfactory locations are to be effected. To illustrate this point, in figure 5.1-5(a) the lower trace has a preamble and it could be construed that the leading edge starts at point 'p' especially if the sensitivity is increased as shown in figure 5.1-5(b). In reality the leading edge starts at 'q' and it is from this point that the time difference must be measured.

Figure 5.1-5 Pulse preamble as a result of alternative, shorter propagation paths

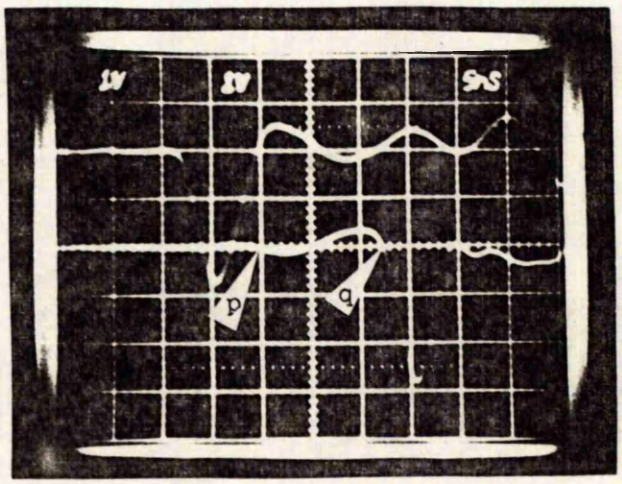

a) Typical trace showing preamble on lower trace

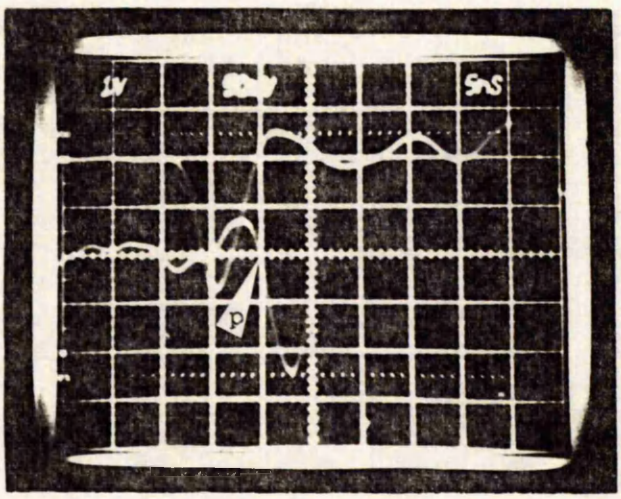

b) As per a) but with lower beam sensitivity increased to 50mV/div.

5.2 An instrument for both measuring and locating partial discharges

So far in this chapter, a technique has been described that enables partial discharges to be located in switchgear and short cables. The technique however provides only the most approximate measure of the magnitude of the discharges located and so resort to an alternative means of measuring their magnitude must be made. This is currently effected by using an E.R.A. type discharge detector[36] connected to the test system concurrently with the location equipment. This arrangement however presents difficulties if there is more than one discharge site within the test specimen because it is not always easy to correlate the location traces obtained on the dual-beam oscilloscope with the discharge pulses observed on the discharge detector. As a result, some doubt can exist when interpreting the results as to which of the identified sites is responsible for a particular discharge. To overcome this difficulty, a discharge detector capable of being synchronized with the location measurement has been developed that can measure the magnitude of a discharge from a single event. This instrument will now be described.

A schematic diagram of the instrument is given in figure 5.2-1 and from this it can be seen that the location is effected using the travelling-wave method described in section 5.1 . The left and right channel outputs and trigger output are fed to a fast dual-beam oscilloscope (a Tektronix type 7844 is currently used) to display the high speed transients in the usual way. At the same time the gate output from the oscilloscope's time-base is used to trigger the magnitude measuring circuits with the result that the magnitude of the actual discharge displayed is measured. The magnitude of the discharge is measured essentially by opening an analogue gate and allowing the step voltage on the test specimen resulting from the discharge to build up a charge on a capacitor. The voltage on this capacitor is then sampled and the result indicated on a digital panel instrument. By

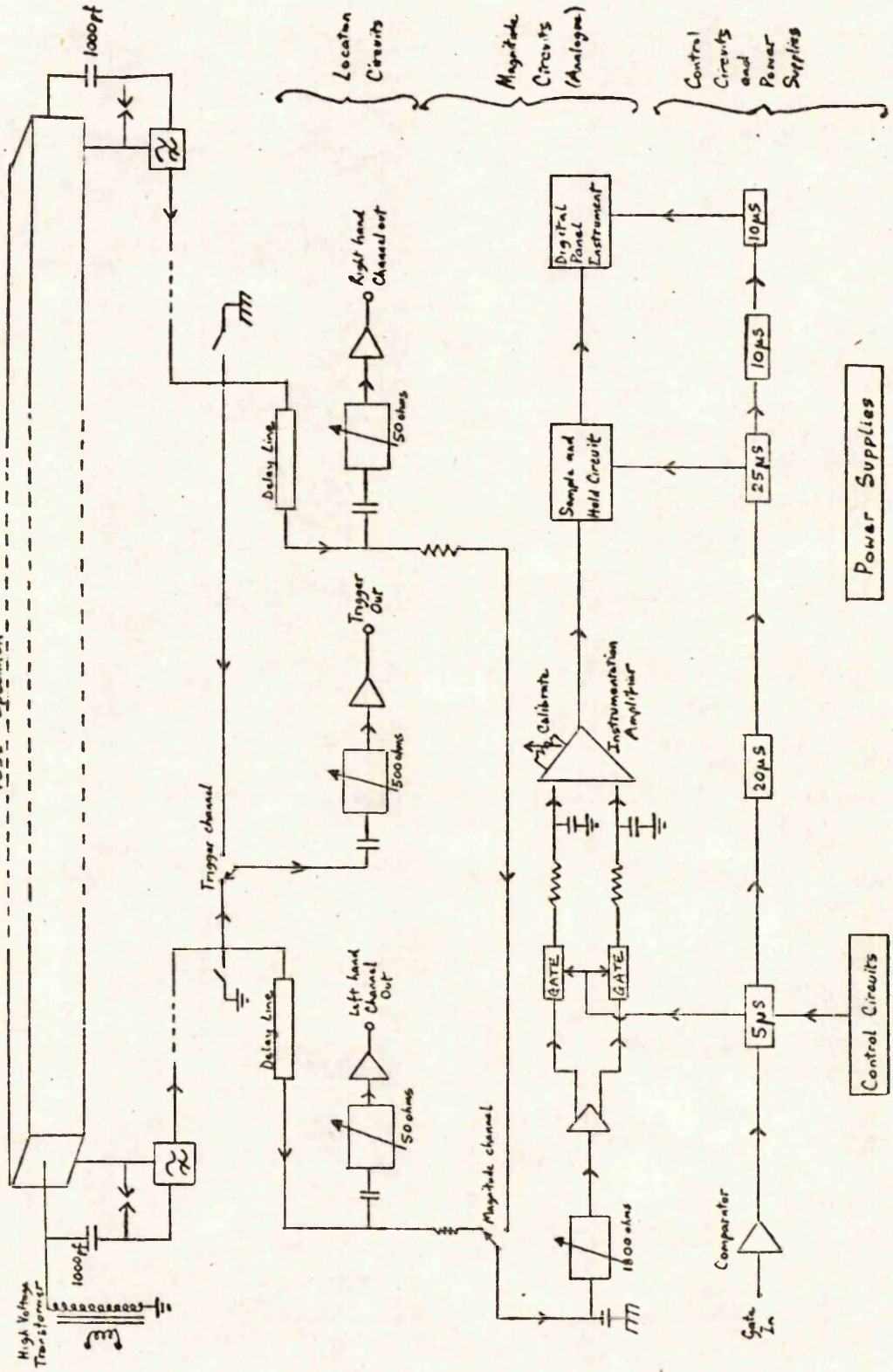

Figure 5.2-1 Schematic diagram of instrument

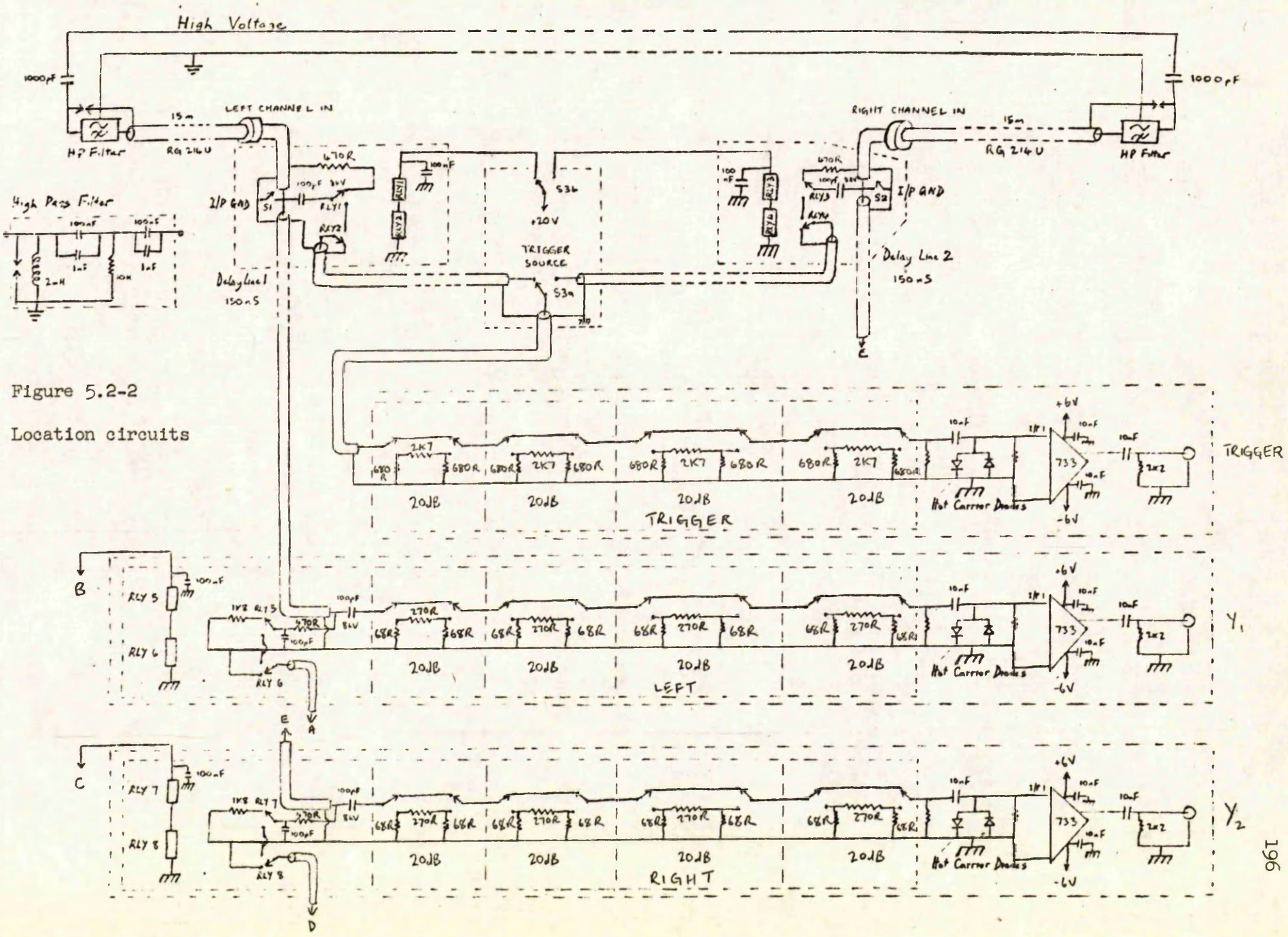

Figure 5.2-2

Location circuits

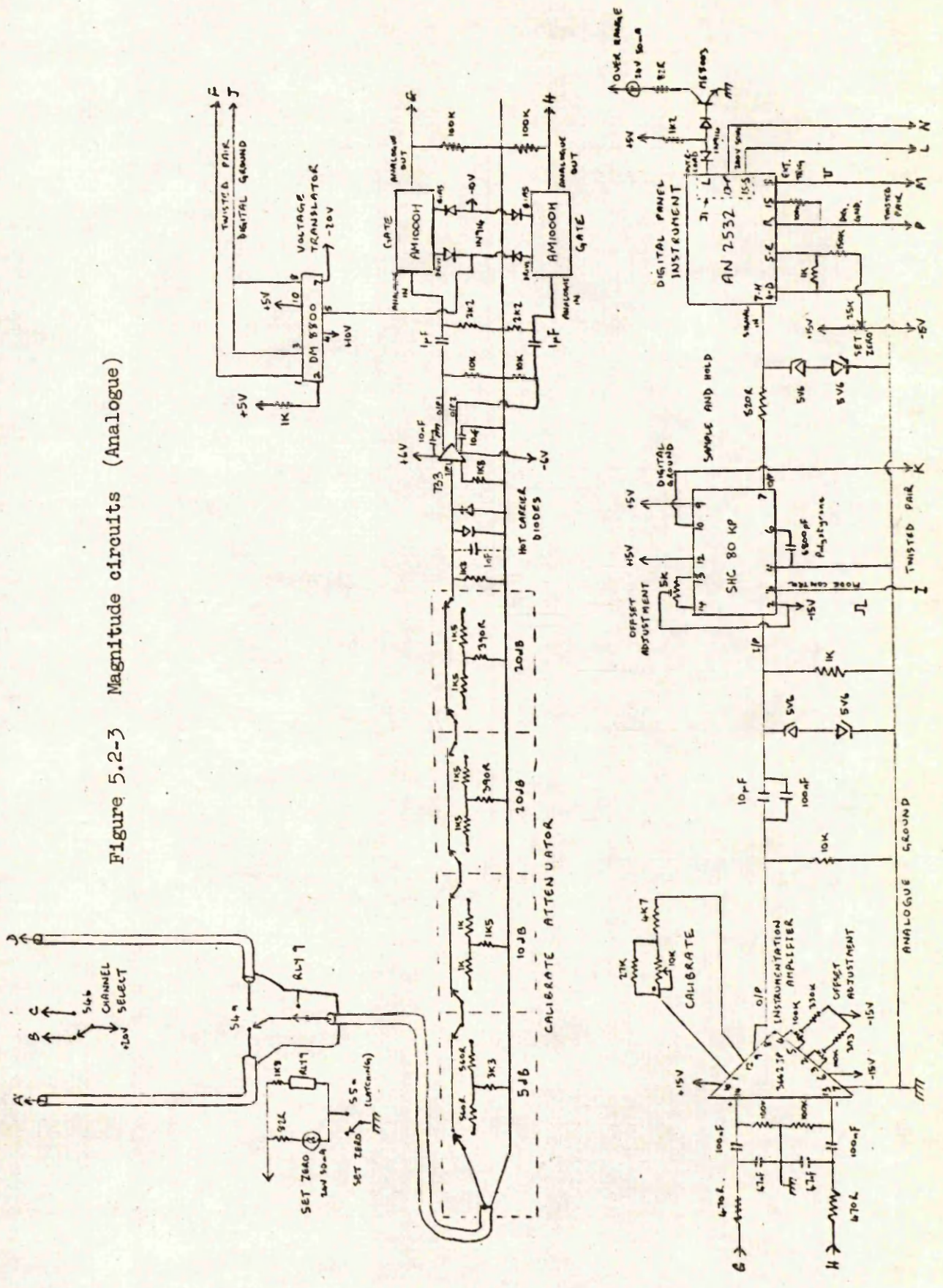

Figure 5.2-3 Magnitude circuits (Analogue)

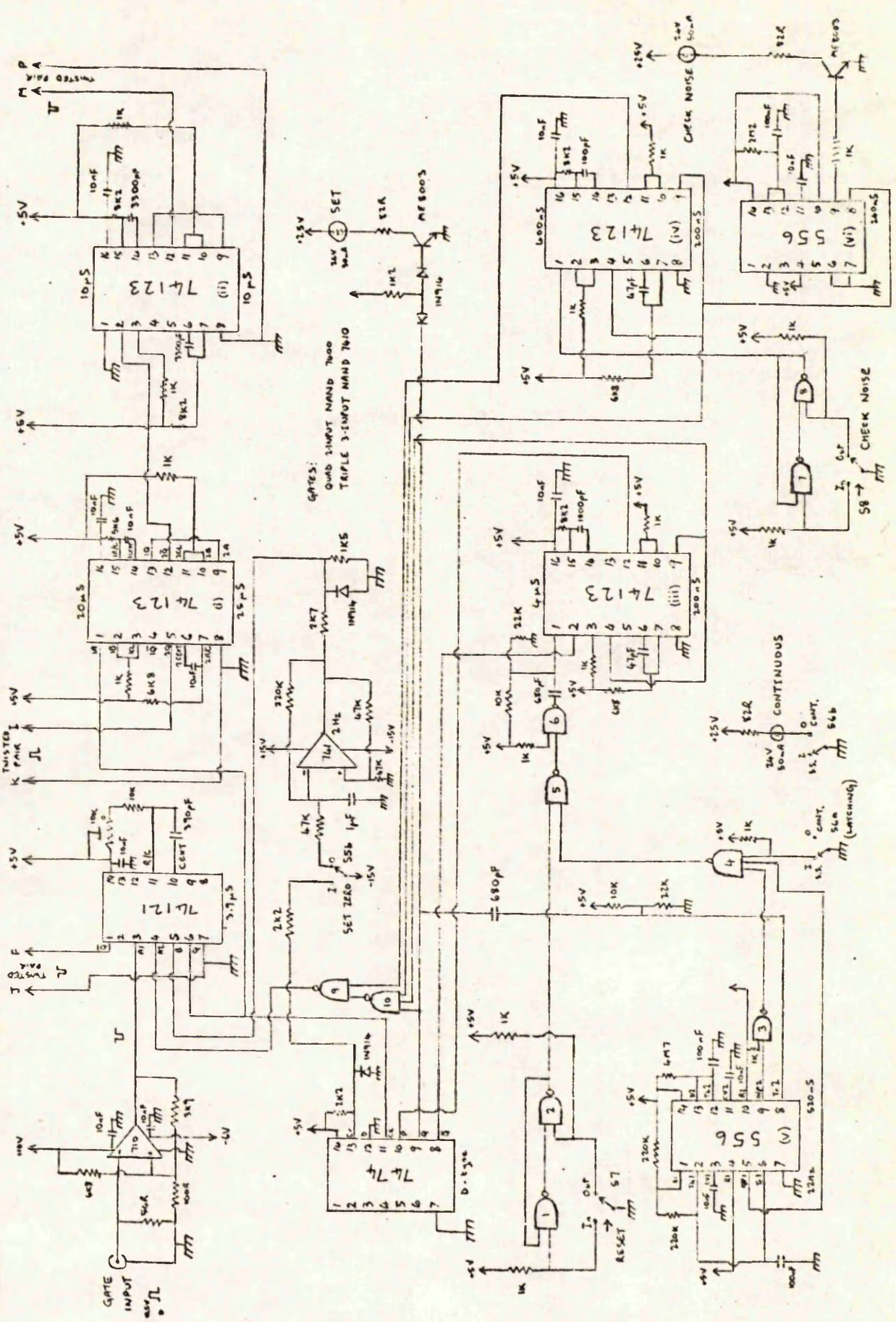

Figure 5.2-4 Magnitude circuits (Digital)

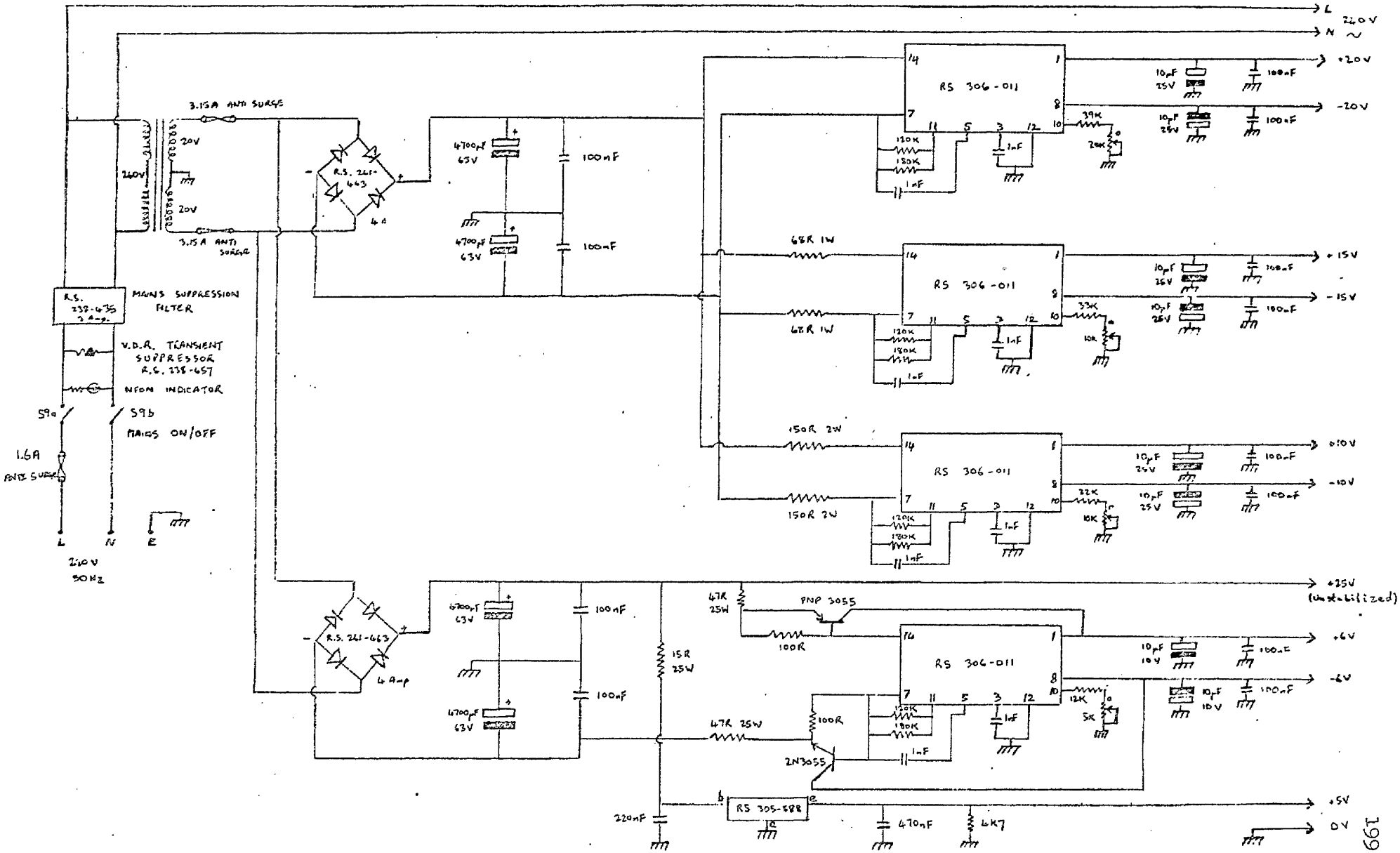

Figure 5.2-5 Power supply circuits

this means a direct readout of the discharge magnitude can be made. By designing the circuitry to have a wide dynamic range, it is intended that discharge magnitudes from 10 - 20,000 pC can be accommodated without recourse to range changing. This has the advantage that, when locating very intermittent discharges of unknown magnitude, readings will not be lost due to the discharge magnitude being off scale for the particular range selected. The various parts of the circuitry will now be described in greater detail.

Input circuits

From figure 5.2-1 and figure 5.2-2 giving the location circuitry, it can be seen that connection is made to each end of the test specimen via a 1000 pF discharge-free high voltage capacitor. The units currently used have an oil impregnated paper dielectric and are constructed to have a reasonably low inductance but it is hoped to further reduce the inductance by using high voltage ceramic capacitors. For the measurements described in section 5.1, 100 pF mica dielectric capacitors were used for the location but such a capacitance is inadequate in this application. The low voltage ends of the capacitors are connected to high-pass filters as shown and for safety reasons the input to each filter is protected by an irradiated, low pressure spark gap. The outputs from the filters are fed to the instrument via 15 metre lengths of high quality, low loss coaxial cable type RG 214 U having a characteristic impedance of 50 ohms. Connections are made at the rear of the instrument to deter the operator from disconnecting these leads whilst a test is in progress as, should the earthing of the high pass filter be defective, an electric shock could be sustained.

Each input circuit serves four functions:-

a) To act as a low loss transmission path for the high frequency (30 - 100 MHz) transients utilized to effect the location of discharge sites.

b) To provide an anticipatory trigger signal for initiating subsequent circuits before the transients reach them.

c) To respond to the (slower) step change in the voltage across the specimen under test in order that a measurement of the apparent discharge magnitude may be effected.

d) To adequately attenuate the energizing high voltage.

Discussing the requirements of a) and b), the high pass filters will result in only minimal attenuation, especially as low inductance ceramic capacitors of 1 nF are connected in parallel with the 100 nF series capacitors, and so most of the input signal power will be conveyed at 50 ohms impedance to the instrument. On entering the instrument, 9% of the signal power from one channel is fed to the trigger circuit whilst a similar amount is dumped from the other channel to maintain equality. The remaining signal power is then, in each case, launched into a 50 ohm delay line. The outputs from the delay lines are fed via 100 pF capacitors to 50 ohm pi-section attenuator networks which satisfactorily terminate the lines at these frequencies.

The delay lines are required to provide a delay of 150 ns with a band-width in excess of 100 MHz and minimal attenuation whilst being reasonably small in size and weight. Lumped parameter delay lines are not suitable for this application and so screened cables, preferably with a solid screen, are used. In the prototype instrument two delay lines intended for use in oscilloscopes are utilized. As in this application a delay line for differential signals would be required, the screen is of oval cross secion with two inner conductors each having a characteristic impedance of 50 ohms to the screen. One conductor only is therefore used in the discharge locator with the other terminated at both ends in its characteristic impedance.

Moving on to requirement c) when a discharge occurs in the specimen under test, some charge is rapidly but locally removed from the high voltage conductor system. As the specimen is physically large, it will behave as

a transmission line initially, the transients taking a finite time to travel to the ends of the specimen. It is as a consequence of this that discharges may be located by the travelling wave method. As has been previously discussed, the transients undergo multiple reflections which, particularly in the case of switchgear measurements, prevent interpretation of the main part of the transient waveforms. However, when the high frequency transients have died away, the voltage across the specimen will settle to a value ΔV lower than the pre-discharge value where $\Delta V = \Delta Q_a / C$. This treatment assumes that the high voltage energizing source is unable to significantly replenish the charge lost during the measurement time.

From the point of view of the discharge magnitude measuring circuitry, the coaxial input leads and delay lines can be represented by a single lumped capacitance of 4.7 nF and so the input circuit is approximated by the equivalent circuit shown in figure 5.2-6 . An apparent discharge magnitude of 10 pC would result in an input step voltage (ΔV) to the 1 nF blocking capacitor (C_b) of 1 mV assuming the specimen capacitance (C_x) to be 10 nF and this step would be attenuated to 137 μV at the output. The response of the circuit after the initial step can be assessed by treating the circuit as the simple parallel R - L - C circuit shown in figure 5.2-7 with R_p equal to 2270 and 10,000 ohms in parallel (1850 ohms) and C_p equal to the series combination of 4.7, 101 and 101 nF in parallel with the series combination of 1 nF and C_x. Thus $C_p = 5.21$ nF with $C_x = 10$ nF and, as a limiting case, $C_p = 4.30$ nF with $C_x = 0$. The value of the inductance L_p is 2 mH. This simplified circuit would be less heavily damped than the actual circuit but nevertheless it provides a reasonable approximation.

From Scott[147] (section 12.5) the response of the parallel R - L - C circuit is governed by a second-order differential equation of the form

$$\frac{d^2y}{dt^2} + 2\alpha\frac{dy}{dt} + \omega_o^2 y = 0 \qquad (5.2\text{-}1)$$

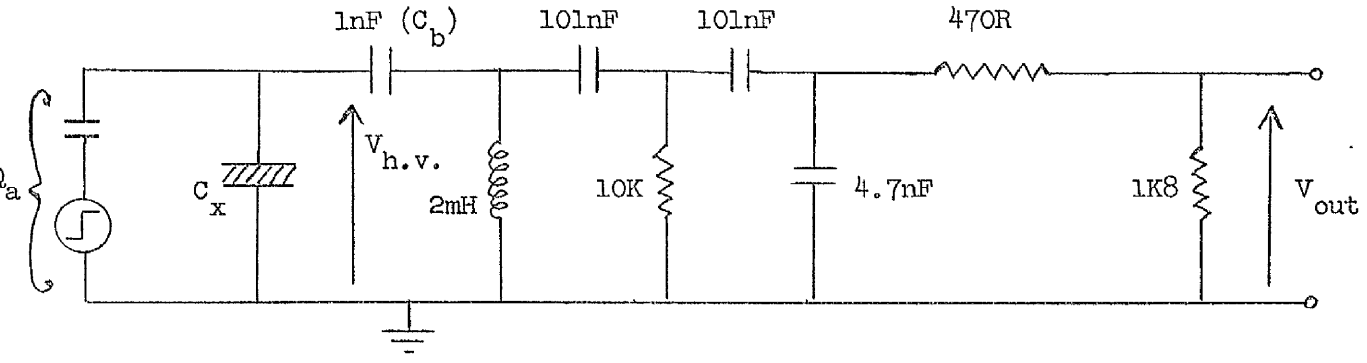

Figure 5.2-6 Equivalent input circuit for the measurement of discharge magnitudes

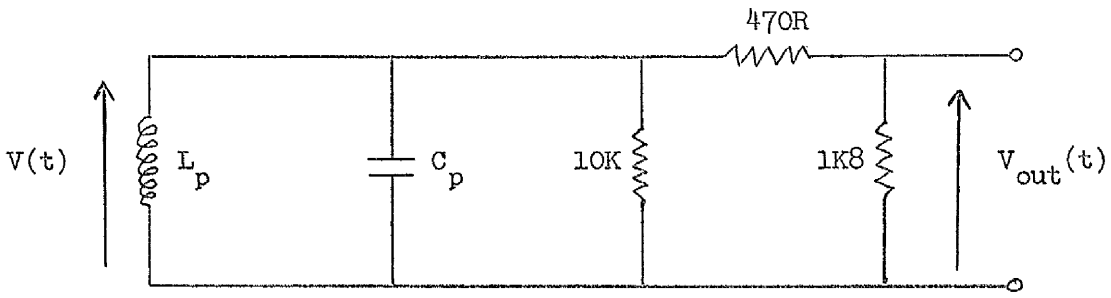

Figure 5.2-7 Simplified equivalent input circuit

where $\omega_o = 1 / (L_p C_p)^{\frac{1}{2}}$ (5.2-2)

and $\alpha = 1 / 2 R_p C_p$ (5.2-3)

For the case with $C_x = 10$ nF, $\omega_o = 309.8 \times 10^3$ and $\alpha = 51.89 \times 10^3$ whereas with $C_x = 0$ these values are 341.0×10^3 and 62.85×10^3 respectively. In both cases $\alpha < \omega_o$ and so the circuits are underdamped with a response of the form

$$v(t) = A e^{-\alpha t} \cos (\omega_d t + \theta) \quad (5.2-4)$$

for $t > 0$. The damped natural frequency ω_d is given by

$$\omega_d = (\omega_o^2 - \alpha^2)^{\frac{1}{2}} \quad (5.2-5)$$

From consideration of the initial condition values $v(0^+)$ and $dv(0^+)/dt$

it is easily shown that

$$\theta = \tan^{-1}(\alpha/\omega_d) \qquad (5.2\text{-}6)$$

and

$$A = v(0^+) / \cos\theta \qquad (5.2\text{-}7)$$

Substituting the parameter values into equation (5.2-4) gives

$$v_{out}(t) = 0.1388\,\Delta V\, e^{-51.89\times10^3 t} \cos(305.4\times10^3 t + 0.1683) \qquad (5.2\text{-}8)$$

with C_x = 10 nF and

$$v_{out}(t) = 0.1393\,\Delta V\, e^{-62.85\times10^3 t} \cos(335.2\times10^3 t + 0.1853) \qquad (5.2\text{-}9)$$

with $C_x = 0$. ΔV is the voltage step developed across the high voltage test specimen. The moduli of the damped wave-trains described by equations (5.2-8) and (5.2-9) fall to 1% of their initial values in 88.75 and 73.27 microseconds respectively so provided the discharges are separated temporally by greater than these amounts, the instrument will be able to resolve them with minimal error due to super-position.

If the 470 ohm resistor were to be reduced in value to zero, $v_{out}(t)$ would be increased by 26.1% . However this would not be an acceptable circuit because the 100pF capacitor would degrade the rise-time of the pulses entering the location attenuator / amplifier. This capacitor is required to limit the amplitude of the fast transients fed to the magnitude amplifier. Also connection to the channel select switch must be made using coaxial cable to provide adequate screening. The coaxial cable is mis-matched at the far end and, as a consequence, constitutes a potential source of multiple reflections that would further degrade the performance of the location circuitry. The 470 ohm resistor is therefore needed to decouple the location and magnitude circuits.

Considering requirement (d), the input circuit must also adequately attenuate the 50 Hz energizing high voltage. The attenuation can be ascer-

tained from the circuit of figure 5.2-6 for which $|v_{out} / v_{h.v.}|$ = 2.966×10^{-9} . With $v_{h.v.}$ equal to 30 kV r.m.s. there is consequently a residual 50 Hz component in v_{out} of 88.98 microvolts. This level would be unacceptable if it were not for the a.c. coupling after the video amplifier (733) which reduces it by a further factor of 14.5 .

Either channel can be selected as a source for the trigger signal, this facility being especially useful when it is necessary to differentiate between two discharge sites of similar magnitude but reasonable spatial separation. In this case triggering off the left channel will favour the discharge site nearest to the left-hand end whilst triggering off the right channel will favour the other. To effect this change a D.P.D.T. switch mounted adjacent to the trigger amplifier is used. One contact is used to select the required coaxial feeder and the other is used to operate reed relays located in the screened boxes of the two channels' inputs. Two change-over relays are used per channel to provide maximum isolation between channels and to connect a dummy load to the non-selected channel to maintain symmetry. A similar arrangement enables the discharge magnitude to be measured using either the left or the right channel. This facility was provided on the prototype instrument as a check but may be dispensed with in later instruments.

Wide-band attenuators and amplifiers

Four sets of wide-band attenuators with amplifiers are used in the instrument: one in the location circuitry of each channel, one in the trigger circuitry and one in the magnitude measurement circuitry. The first three utilize switchable pi-section attenuators whereas the fourth utilizes T-sections. The characteristic impedances of the attenuators are nominally 50, 50, 500 and 1800 ohms respectively. The resistance values required for the shunt and series elements of the pi-sections are given by

$$R_a = R_c = R_o (N + 1) / (N - 1)$$
$$R_b = R_o (N^2 - 1) / 2N \qquad (5.2\text{-}10)$$

respectively where R_o is the characteristic impedance and $N = (P_{in} / P_{out})^{\frac{1}{2}}$. The corresponding series and shunt elements of the T-sections are respectively

$$R_a = R_c = R_o (N - 1) / (N + 1)$$
$$R_b = R_o (2N) / (N^2 - 1) \qquad (5.2\text{-}11)$$

The attenuators are required to reduce the input signals to within the working range of the instrument. Following the attenuators the signals are amplified by broad-band integrated circuit amplifiers, type 733, set to give a differential voltage gain of 10 in the magnitude measuring circuit and a single ended gain of 50 in the others. These circuits have a band-width of upto 120 MHz and so care must be taken in the component layout. Also, to obtain a satisfactory pulse performance, the circuit inductance must be reduced to the minimum and so these circuits are constructed on a ground-plane. The hot carrier diodes on the inputs to the video amplifiers are provided to afford a degree of protection from transient overvoltages. The outputs from the amplifiers are, in each case, a.c. coupled. This is necessary as the 733 can have an output offset voltage of upto 1 volt. (1.5 volts in the case of the lower specification 733C version.)

Figure 5.2-2 shows that some connections are made using screened leads. These serve two purposes. Firstly they provide immunity from extraneous interference and secondly they provide a well defined signal path for both the live and the earthy side of the signal circuit. This is important because, if the latter is ill-defined, the leading edges of the discharge pulses will lose definition thereby preventing accurate location of the discharges. For the same reason, care must be taken with all high frequency connections to ensure that the live and earthy sides of the transmission path are kept as near equal as possible and also abrupt changes of direction should be avoided.

Measurement of discharge magnitude

Integrator circuit

The damped cosine wave appearing at the output of the video amplifier following a partial discharge in the test specimen is applied to the input of a high speed analogue gate. (National Semiconductors AM1000H) Using the pre-trigger facility, this gate is arranged to be switched on prior to the arrival of the required discharge transient and so this signal will begin to charge the 47 nF integrating capacitor. Charging continues for most of the first quarter cycle of the oscillatory transient, the gate being closed at, or just prior to, the first zero of the current through the 470 ohm charging resistor. Thus a voltage is developed across the integration capacitor that, for any given test specimen capacitance, is proportional to the apparent charge transferred by the discharge.

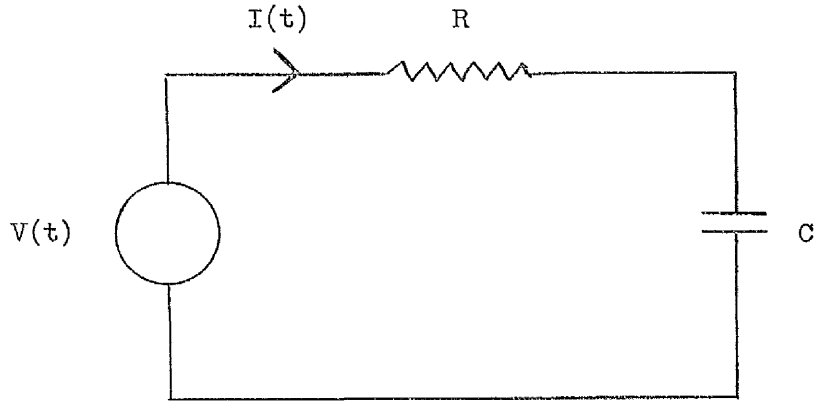

Figure 5.2-8 Simplified equivalent circuit of integrator

A simplified equivalent circuit of the integrator is given in figure 5.2-8 and this will now be used to determine when the charging current I(t) first falls to zero with $t > 0$. C is the series combination of 47 nF and 1 μF (44.89 nF) and R is the series combination of the charging resistor (470 ohms), the amplifier output impedance (20 ohms) and the ON resistance of the gate. (25 ohms) The driving voltage is given by

$$V(t) = \frac{V_o}{\cos(\theta)} e^{-\alpha t} \cos(\omega_d t + \theta) \qquad (5.2\text{-}12)$$

for $t > 0$ where $V_o = V(0^+)$ and the other constants are identical with those of equation (5.2-4). V_o depends on the value of ΔV, the attenuator setting and the amplifier gain. Now

$$V(t) = R \cdot I(t) + Q / C \qquad (5.2\text{-}13)$$

and so differentiating and rearranging

$$\frac{dI(t)}{dt} + \frac{I(t)}{RC} = \frac{1}{R}\frac{dV(t)}{dt} \qquad (5.2\text{-}14)$$

Using an integrating factor this gives

$$I(t)\, e^{\frac{t}{RC}} = \frac{1}{R}\int e^{\frac{t}{RC}} \frac{dV(t)}{dt}\, dt + K \qquad (5.2\text{-}15)$$

where K is a constant. Integrating by parts

$$I(t)\, e^{\frac{t}{RC}} = \frac{1}{R}\left[e^{\frac{t}{RC}} V(t) - \int \frac{e^{\frac{t}{RC}} V(t)}{R\,C}\, dt \right] + K \qquad (5.2\text{-}16)$$

Let $$t_o = t + \theta / \omega_d \qquad (5.2\text{-}17)$$

Then $dt_o = dt$ and

$$V(t_o) = \frac{V_o\, e^{\alpha\theta/\omega_d}}{\cos\theta}\, e^{-\alpha t_o} \cos(\omega_d t_o) \qquad (5.2\text{-}18)$$

Thus

$$\int e^{\frac{t}{RC}} v(t)\, dt = \frac{V_o\, e^{k\theta/\omega_d}}{\cos\theta} \int e^{-kt_o} \cos(\omega_d t_o)\, dt_o$$

$$= \frac{V_o\, e^{-k(t_o - \theta/\omega_d)}}{\cos\theta} \left\{ \frac{\omega_d \sin(\omega_d t_o) - k\cos(\omega_d t_o)}{\omega_d^2 + k^2} \right\} \qquad (5.2\text{-}19)$$

where $k = \alpha - 1/RC$. Substituting this into equation (5.2-16) and rearranging yields the following expression for the current:

$$I(t) = \frac{V_o\, e^{-\alpha t}}{R\,(\omega_d^2 + k^2)\cos\theta}\left\{(\omega_d^2 + \alpha k)\cos(\omega_d t + \theta) - \frac{\omega_d}{RC}\sin(\omega_d t + \theta)\right\} + K\, e^{-t/RC} \qquad (5.2\text{-}20)$$

The constant K can be evaluated from the initial current given by (5.2-20) namely

$$I(0^+) = \frac{V_o}{R\,(\omega_d^2 + k^2)\cos\theta}\left\{(\omega_d^2 + \alpha k)\cos\theta - \frac{\omega_d}{RC}\sin\theta\right\} + K \qquad (5.2\text{-}21)$$

But $I(0^+) = V_o / R$ so

$$K = \frac{V_o}{R}\left\{1 - \frac{1}{\omega_d^2 + k^2}\left[\omega_d^2 + \alpha k - \frac{\omega_d}{RC}\tan\theta\right]\right\} \qquad (5.2\text{-}22)$$

The time taken for I(t) to fall to zero was calculated using a numerical tabulation method and found to be 4.20 μs with C_x = 10 nF. For the limiting case with C_x = 0, I(t) reaches zero after 3.81 μs. At these points in time, the voltage on the capacitor C will be equal to the driving voltage and so can be calculated using equations (5.2-8) and (5.2-9). 95.5% of this voltage will be across the integration capacitor and so the integrator output voltage will be given by

$$V_c = 0.1388 \times \Delta V \times B \times 0.0918 \qquad (5.2\text{-}23)$$

for C_x = 10 nF and

$$V_c = 0.1393 \times \Delta V \times B \times 0.0813 \qquad (5.2\text{-}24)$$

with C_x = 0 . The multiplying factor B is dependent on the attenuator setting and the gain of the video amplifier but, with no attenuation inserted and a single ended amplifier gain of five, equation (5.2-23) gives V_c = 63.71 μV with ΔV = 1 mV. Similarly, from equation (5.2-24), V_c = 56.63 μV with C_x = 0 . In the light of the preceding calculations and allowing for the difference in the propagation times through the signal and trigger circuits, the gate

is arranged to be switched on for 3.9 microseconds. As the charging current does not quite fall to zero in this time for most test specimen capacitances, the integrator output voltage is less than the optimum value. However the reduction is small being approximately 1% with C_x = 10 nF.

Referring to figure 5.2-3, it can be seen that two analogue gates are used one operating on each side of the differential output from the video amplifier. This arrangement was chosen to provide, in conjunction with the differential input instrumentation amplifier, high immunity to common mode noise originating from either the gates or the supply rails. Analogue gates are notorious for injecting voltage spikes into the signal circuit during switching and so it was considered a worthwhile precaution to adopt a differential signal path at this point in the circuit despite the, claimed, relative freedom from such spikes in the particular gates used. It has the further advantage of doubling the signal applied to the input of the instrumentation amplifier thereby improving the signal to noise ratio. To realize the immunity to commutation spikes, both gates are controlled from the same drive source. The drive required is -20 V when OFF and +10 V when ON and these drive levels are provided by one half of the T.T.L. compatible, dual level-translator. (National Semiconductors DM 8800) The analogue gates each contain three N-channel junction field-effect transistors and require, in addition to the drive signal, a biassing supply of -10 V. Both the drive and bias connections require external diodes.

The instrumentation amplifier (Burr Brown 3662 JP) has a maximum input bias current of 300 nA and could therefore develop a bias voltage of upto 30 mV across each 47 nF integrating capacitor with its 100 kohm discharge resistor. This situation would clearly be unacceptable so the amplifier inputs are a.c. coupled to the integration capacitors. Though the bias currents are still drawn through 100 kohm resistors, the resultant 30 mV common mode signal is now of no consequence. The difference between the two input bias currents of upto 80 nA can, however, produce a differential signal of upto 8 mV with the result that the output from the amplifier

generally exhibits an offset. This offset can be reduced to some extent by the two offset adjustment potentiometers. Two potentiometers are utilized for this adjustment in order that both input and output offsets may be annulled. The latter is effected first with the amplifier at minimum gain by means of the potentiometer between pins 4 and 5. The gain is then set to its maximum and the potentiometer between pins 2 and 3 used to adjust the input offset.

The gain of the instrumentation amplifier used is adjustable and given by $10^5/R_g$. The minimum allowable gain is dictated by the maximum guaranteed output voltage swing achievable by the video amplifier. This is 1.5 V which will therefore correspond to the full scale value of 20,000 pC. The resultant differential input voltage to the instrumentation amplifier is 244 mV and this must result in a 2 V output. Thus the minimum gain is 8.20 for which R_g = 12.2 K. The maximum gain is that required to allow calibration of the instrument when C_x is large. Taking the maximum value of C_x equal to 20 nF, ΔV = 0.5 mV for a 10 pC discharge. From equation (5.2-23) this results in a differential input signal to the instrumentation amplifier of approximately 64 μV and, as this must be amplified to 1 mV, the maximum gain required is 15.7 . This corresponds to a value of 6.37 K for R_g. The circuit shown gives a variation in R_g from 12.0 to 4.7 K corresponding to gain values of 8.34 and 21.3 respectively. This allows some leeway in the upper gain value yet remains within bounds at the lower. When operating with the instrumentation amplifier gain towards the upper end, noise will degrade the instrument's sensitivity. For this reason the calibration attenuator must always be set to the minimum value at which a calibration can be obtained. The instrument is calibrated by adjusting the calibration attenuator and calibration potentiometer with a charge source of known magnitude connected to the high voltage system. This can be either an artificial discharge, such as the one described in section 5.3, or any conventional direct calibrator. (Low or high voltage)

'Sample and hold' and digital display circuits

The instrumentation amplifier has a settling time of 20 μs. After this time has elapsed, the output is sampled by the 'sample and hold' circuit (Burr Brown SHC 80KP) which has an acquisition time of approximately 25 μs when used with an external capacitor of 6800 pF. Now, after 45 μs, the input to the instrumentation amplifier will have fallen by 2.33% (determined numerically) and this fall is increased to 2.77% at the input to the 'sample and hold' circuit by the a.c. coupling. However such a droop rate is quite acceptable but the figures do highlight the need for the 'sample and hold' circuit as the digital display has a maximum conversion time of 9.9 ms. With an external capacitor of 6800 pF, the 'sample and hold' circuit has a droop rate of 65.8 mV/s which is equivalent to less than one unit on the display during the conversion time. The external capacitor also serves to reduce the charge offset of the 'sample and hold' circuit to an acceptable level. The need for a.c. coupling between the instrumentation amplifier and the 'sample and hold' circuit arises as a result of the offset at the amplifier output as previously discussed. Because the input bias current of the 'sample and hold' circuit is 400 nA, a d.c. source resistance of 1 kohm is provided in order to keep the input bias to well below 1mV, the voltage equivalent to one unit on the digital display. As a consequence a large coupling capacitor is required to avoid further increasing the droop rate.

The output voltage from the 'sample and hold' circuit is measured to obtain the discharge magnitude. This is displayed digitally thus enabling the wide dynamic range of the instrument to be handled directly without recourse to an analogue display with a logarithmic scale. The display used is a commercially available digital panel instrument (Analogic AN 2532) with an input range from -1.999 to +1.999 volts in 1 mV steps. By using the unit in its externally triggered mode, it can be arranged to trigger 10 μs after the 'sample and hold' circuit has reverted to the

'hold' state. This allows a generous time for the output from the 'sample and hold' circuit to settle. The digital panel instrument has a bipolar floating differential input and so use is made of the other input to provide a null facility. This control is mounted on the front panel of the instrument and is used to annul any overall residual offset voltage. In figure 5.2-3 an analogue ground connection is shown linking the instrumentation amplifier, the 'sample and hold' circuit and the digital display. This ground rail is connected to the main instrument ground at one point only to avoid errors arising from potential differencies between separate points on the latter. Finally the digital panel instrument has a digital output to signify an overload condition. When this output goes high a transistor is arranged to illuminate a lamp on the front panel of the instrument to indicate that the signal was outside the measurement range - either positive or negative.

Control circuits

These are shown in figure 5.2-4 .

Main timing circuit

The circuitry is triggered by the leading edge of the time-base gate output from the oscilloscope. In the case of the Tektronix type 7844 oscilloscope, this pulse is of 10 volts amplitude with a source impedance of 1 kohm so the signal developed across the 56 ohm input resistor is 530 mV. The pulse is applied directly to the inverting input of a voltage comparator (710) to produce a sharp, well defined, T.T.L. compatible trigger pulse. The resistor network connected to the non-inverting input gives the comparator a threshold level of +220 mV with 91 mV hysteresis and so ensures that the output is normally high with good noise immunity and freedom from 'chatter' during transitions.

The negative going leading edge of the comparator output is used to trigger the 74121 monostable via its A1 input. This monostable provides

an accurately timed 3.9 μs negative-going pulse at its $\overline{Q}$ output which is used to operate the DM 8800 voltage translator and hence switch on the analogue gates of the integrator. At the end of 3.9 μs, the falling edge of the Q output is used to trigger the first monostable in the number (i) dual-monostable circuit type 74123. This monostable provides a delay of 20 μs to allow the instrumentation amplifier to 'settle' before triggering the second monostable set to give an output pulse of 25 μs duration. The positive going pulse from the Q output of this is used to actuate the 'sample and hold' circuit. The $\overline{Q}$ output, however, is applied to the B input of the first monostable of the number (ii) 74123 and this is therefore triggered by the positive-going trailing edge. Set for a delay of 10 μs, this enables the 'sample and hold' circuit to 'settle' before the digital panel instrument is triggered by the second monostable of (ii). The duration of the trigger pulse is non critical within the limits 1.5 μs to 2 ms and so is set to approximately 10 μs for convenience. Connections between the controlling monostables and their associated circuits are made using twisted pairs of wires to provide reasonable transmission paths without incurring the high capacitance loading of coaxial leads.

Single-shot operation

If a repetitive discharge site with little variation in magnitude between successive discharges is being investigated, viewing of the transients will be eased considerably if the oscilloscope time-base is operated in its normal mode rather than the single-shot mode. In this mode, however, the discharge magnitude measurement circuitry would be retriggered in quick succession giving erroneous results which would, in any case, be over-written before the operator could take a reading. To overcome this difficulty, the instrument is provided with a single-shot facility whereby, on arming the circuitry, the next trigger pulse causes a reading to be taken and, at the same time, inhibits the circuitry from retriggering. This reading will, as a consequence, continue to be displayed until the instrument is manually reset.

Referring to figure 5.2-4, single-shot operation is achieved as follows. The reset switch S7 is normally biassed to hold one input of NAND gate No. 2 at zero and so the output of this gate will normally be high. On depressing the change-over switch S7, the output from gate 4 will fall but the changeover will not occur until first contact is made with the 'normally-open' contact. Similarly the bistable, consisting of gates 1 and 2, will not revert to its normal state until contact is re-established with the 'normally-closed' contact. Thus, by using a 'break-before-make' type of change-over switch, a 'bounce-free' transition can be effected. This is applied to one input of gate 5, of which the other input is held high in the single-shot mode by shorting one input of gate 4 to ground. The resultant positive going edge at the output of gate 5 is inverted by 6 and then a.c. coupled to the 1A trigger input of the 74123 No. (iii). This generates a negative going pulse at the $1\overline{Q}$ output of 4 μs duration which serves two purposes. Firstly it ensures that the output of gate 10 remains high during the resetting time and therefore the A2 trigger of the 74121 remains low. (The other input of gate 9 is normally high.) This means that the 74121 (and hence the rest of the main timing circuit) cannot be triggered during the reset time. Secondly, the negative going leading edge is used to trigger the second monostable of this integrated circuit via the 2A trigger input. This monostable generates a negative going 200 ns pulse at its $2\overline{Q}$ output which is applied to the preset input of the 7474 dual D-type flip-flop causing its Q output to go high. As a result, when the negative going 4 μs pulse returns to the 1 state again, the output of gate 10 goes low and the A2 input of the 74121 goes high. Since the B input of the 74121 is normally high, the circuit can now be triggered. This condition is indicated on the front panel by the 'SET' lamp driven from the Q output of the 7474. (Lamp on when Q high.) With all three trigger inputs of the 74121 high a negative transition on the A2 input would result in a spurious trigger, a situation that could arise if the 400 ns monostable of (iii) were to be retriggered. To prevent this happening the $\overline{Q}$ output of the

7474 holds the 1B input of this monostable low to inhibit it from retriggering when the instrument is 'set'.

When the 74121 is triggered by the 710 comparator the positive-going leading edge of its Q output clocks the 7474 causing the Q output of the latter to fall to the 0 state because the D input is at 0. The output of gate 10 consequently goes high and the A2 trigger input is taken low by gate 9 thereby preventing further triggering. At the same time the 'SET' lamp is extinguished and the 1B input of (iii) is returned to the 1 state to permit re-setting. This single-shot operation would be prevented from operating if the preset input to the D-type flip-flop were to be held low. In this situation, therefore, multiple shots could take place and so it is to prevent this from happening, that triggering of the instrument is arranged to be inhibited by the 4 μs monostable of (iii) whilst the 200 ns reset pulse is applied to the flip-flop.

When the instrument is 'armed', the next gating pulse from the oscilloscope will result in triggering. This will cause the D-type flip-flop to revert to the 'non-armed' state thereby preventing further triggering. However this reversion will result in the 1B input of the No. (iii) 74123 executing a positive-going transition which would retrigger the monostable if the 1A input were wtill in the low state. To avoid this situation, the negative-going trigger input to 1A is a.c. coupled with a decay time of less than 4 μs.

Multiple shot (or continuous) operation

The first timer (pins 1 - 6) of the 556 dual timer integrated circuit No. (v) is connected in an astable mode to produce an approximately square wave output with a repetition frequency of 22 Hz. This is applied to one input of the triple-input NAND gate No. 4 . The output of gate 3 is normally high and the third input of 4 is also high when the latching switch S6(a) is set to the continuous mode, so the square wave is transmitted, inverted, to gate 5 . This similarly transmits the square wave

because the output of gate 2 is normally high. Thus the square wave is applied to the 1A input of (iii), each negative edge behaving as if it were a negative edge derived from the manual reset circuit used in the single-shot mode. The ensuing reset procedure is identical to that in the single-shot mode, the circuit, once set, remaining so until a trigger pulse is received.

When the instrument is triggered, the D-type flip-flop changes state as before to prevent further triggering. However this situation would be short lived with the 556 oscillator attempting to issue a reset command twenty two times every second. As a result, if trigger pulses were to be received by the instrument in quick succession, each display would be held for a time far too short for the operator to take a reading. To overcome this difficulty, the Q output of the 7474 is a.c. coupled to the trigger input of the second timer of the No. (v) 556. (Pins 8 - 13) This timer is connected as a monostable circuit with an output pulse width of 0.52 seconds and is triggered by the falling edge of the Q output of the 7474. The output pulse from the timer causes the output of gate 3 to go low thereby forcing the output of gate 4 high and preventing the 22Hz oscillator from resetting the circuit. By this means a display time of at least half a second is ensured. On a point of detail, the Q output of the 7474 must be a.c. coupled to the trigger input to prevent the timer from being continuously held on by the Q output in its zero state. As the trigger voltage level is 1.9 V maximum for this circuit with V_{cc} = 5 V, the normal bias voltage could be reduced significantly below 5 V to ensure consistent triggering by the 5 V edge. A bias level of 3.4 volts was adopted.

With the continuous mode selected, the instrument can be used in two ways. Firstly, if the oscilloscope is triggering repetitively, the magnitude of approximately two discharges will be measured per second. If the discharges all originate from the same site a measure of the spread in their magnitudes will thus be afforded. Alternatively, if the oscillo-

scope is set to trigger on discharges from a number of different sites, their magnitudes and relative discharging rates will be obtained. The second purpose of the continuous mode is to avoid the necessity for retriggering the instrument when using the oscilloscope in its single-shot mode. This is the normal mode of use, the operator instigating single-shot recordings of the discharge transients from the oscilloscope with the discharge magnitude measurement circuit operating under a 'master-slave' hierarchy. With this arrangement a measurement of the discharge magnitude will be made each time the oscilloscope is triggered provided that more than half a second has elapsed since the previous trigger. To indicate that the instrument is in the continuous mode, a lamp is illuminated by switch S6(b).

Adjusting the zero setting

The digital panel instrument is adjusted to zero by means of the 'SET ZERO' potentiometer. This, like the 'CALIBRATE' potentiometer, is a multi-turn type for fine adjustment with a locking device to prevent inadvertent adjustment once set. To actuate the 'set zero' circuitry, switch S5 is depressed. This is a latching, two pole type. S5(a), shown in figure 5.2-3, operates reed relay No. 9 which shorts the input to the magnitude measurement circuitry to prevent any extraneous pick-up. S5(a) also illuminates the SET ZERO indication lamp. S5(b), shown in figure 5.2-4, normally prevents the 741 operational amplifier circuit from oscillating but, when the switch is changed over, the latter commences to oscillate at approximately 2 Hz with a square-wave output. Meanwhile the switch holds the clear input of the 7474 in the zero state thereby holding the Q output at 0. As a result the A2 input of the 74121 is held low preventing the 710 from triggering the monostable. The output from the 741 in normal operation is held high but now alternates between the high and low states with the result that each upward transition results in the circuit being triggered. A new indication on the digital panel instrument is therefore displayed every 500 mS enabling the operator to make a zero adjustment.

In the normal mode the inverting input of the 741 is held negative with respect to the non-inverting input and so the output remains permanently in the high state. When, however, the 47 kohm connection between the inverting input and the -15 V supply rail is broken, the 1 μF capacitor starts to charge positively through the 220 kohm resistor. This charging continues until the voltage on the inverting input exceeds the voltage on the non-inverting input, namely half the output voltage of the amplifier. At this point the amplifier output will swing fully negative with positive feedback ensuring a swift, chatter-free transition. The capacitor will now start to discharge and then charge negatively resulting in a positive transition of the 741 output when the voltage on the inverting input reaches half the negative output voltage. These oscillations will continue indefinitely with a period of 2.2 RC.

Noise checking circuitry

On depressing the momentary change-over switch S8, a magnitude measurement is immediately initiated. This serves as a check of the noise present on the high voltage and can be used either prior to energising the test system or, alternatively, with the system energised but below the discharge inception voltage. The circuitry is similar to that used to reset the instrument when it is in the single-shot mode with the exception that the $\overline{Q}$ output from the 200 ns monostable is applied to one input of gate 9 instead of the 7474. Once again the $\overline{Q}$ output from the first monostable (400 ns) is applied to one input of gate 10 forcing the output of the latter high if is is not so already. The $\overline{Q}$ output of the 200 ns monostable causes the output of gate 9 to go high but this will fall to the 0 state at the end of the pulse, thereby triggering the 74121. At the end of the 400 ns pulse the output of gate 10 will be held high by the Q output from the 7474 to prevent further unwanted triggering. To indicate that the noise checking circuitry has been activated, the $\overline{Q}$ output from the 400 ns

monostable is also used to trigger one half of a 556 timer. This generates an output pulse of 240 ms which is utilized to momentarily illuminate the 'CHECK NOISE' lamp. The other half of this 556 dual timer circuit and the other half of the 7474 dual D-type flip-flop are not used.

Power Supplies

These are shown in figure 5.2-5. The mains input is fitted with a suppression filter and, to further reduce interference, a voltage dependent resistor is fitted prior to this to suppress transients. With the exception of the +25 volt d.c. rail, all supply rails are stabilized, most of them using the adjustable dual polarity voltage regulator type RS 306-011 . In the case of the two 6 volt supply rails, this integrated circuit is not capable on its own of supplying the required current and so a complementary pair of power transistors are appended in a current sharing configuration. The series resistors fitted on the supply side of all but the 20 volt regulator serve to reduce the power dissipated in the regulators.

Performance during commissioning

Location circuits

The instrument is currently being commissioned and the following traces were obtained from tests in the laboratory on a 2 metre length of 33 kV single-core cable with a sealing end attached. This was a conventional oil impregnated paper type with a porcelain weather shield. From the point of view of the discharge location circuits, this was a difficult test specimen because the sealing end lacks the earth conductor required for the propagation of the high frequency transients.

To verify that the internal high frequency signal circuits of the instrument are capable of handling fast pulses without undue loss of definition, a square wave with transition times of less than 1.6 ns (the rise-time of the oscilloscope) was injected into each high-pass filter in turn via a

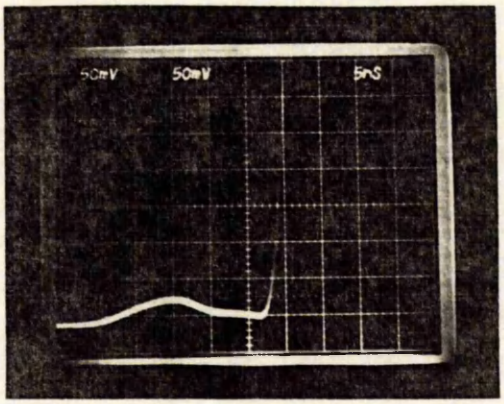

a) Low voltage 'ideal' coupling capacitor

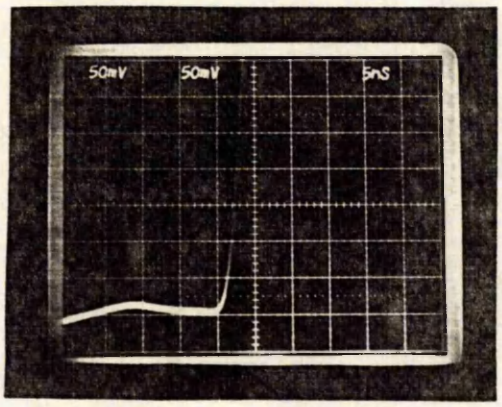

b) High voltage ceramic coupling capacitor

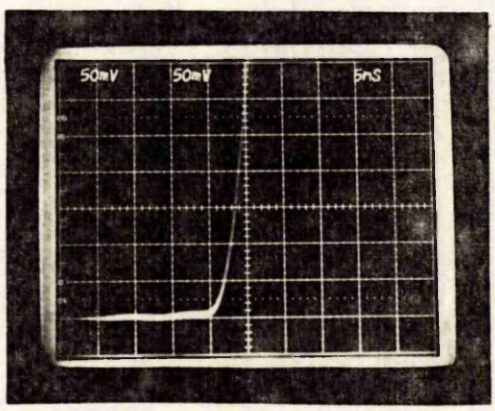

c) High voltage oil impregnated paper coupling capacitor

Figure 5.2-9 Transient response of discharge location circuits

1000 pF coupling capacitor. Figure 5.2-9(a) shows the result obtained using a low voltage, low-inductance, ceramic capacitor and figures 5.2-9(b) and 5.2-9(c) show the equivalent performance obtained with two different types of high voltage (40 kV r.m.s.) capacitor. The first is a ceramic type intended for high frequency applications and the second has an oil impregnated paper dielectric. It can be seen that the performance of the former is almost indistinguishable from the low voltage 'ideal' capacitor but that a small loss of definition in terms of rounding of the 'knee point' and increase in risetime occurs in the case of the latter. Nevertheless the position of the 'knee point' can be resolved to an accuracy of 1 ns in all three cases. (N.B. For all three traces the oscilloscope sweep speed is 5 ns per large division.) Unfortunately the high voltage ceramic capacitor used for this test cannot be used in practice because it is not discharge free but the manufacturer confidently expects to be able to supply suitable units in the near future.

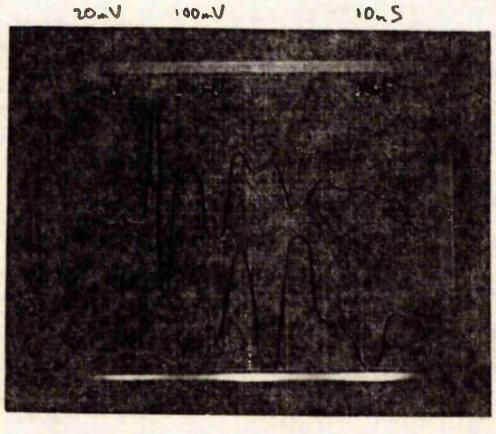

Figure 5.2-10 'Location' measurement made on test sample

Figure 5.2-10 shows the result of a 'location' made on the test specimen. The transients in this case (and figures 5.2-11 to 5.2-14) were derived from an artificial discharge source of 1600 pC connected to the bare end of the cable. (Upper trace) The test voltage was 5 kV and Δt = +17 ns. The large preamble on the lower trace is a consequence of the poorly defined

high frequency propagation path. A resolution of 1 ns is achieved representing a spatial resolution of approximately 100 mm.

Magnitude circuits

To limit the ringing that was found to be present at the input to the 733 wide-band amplifier, a 1 nF shunt capacitor was added. This also produced a small increase in the period of the damped oscillatory wave-train but this was not of consequence. The differential output waveforms from the wide-band amplifier are shown in figure 5.2-11 .

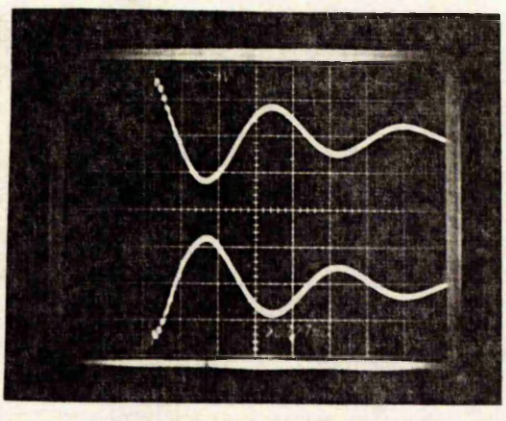

Figure 5.2-11 Output waveforms from wide-band amplifier. (Both traces 50 mV/div and 5 μs/div)

The corresponding waveforms across the two integration capacitors are shown in figure 5.2-12 . The charging period whilst the analogue gates are open is clearly apparent, as is the negative step change that occurs when the gates turn off. These steps indicate that the gates are removing charge from the integration capacitors as they turn off and the magnitude of this effect is, at present, excessive. Fortunately, because the waveforms are handled differentially, their effect is much reduced as a consequence of the high common-mode rejection ratio of the instrumentation amplifier. However the steps differ slightly in their magnitude and this difference will not be rejected. Provided the difference remains constant though, this can be offset using the 'set zero' control but any variability will cause

inconsistent results. This factor is, at present, limiting the resolution to 50 pC. The decay rate of the charge on the capacitors after the step can just be seen from the traces of figure 5.2-12 .

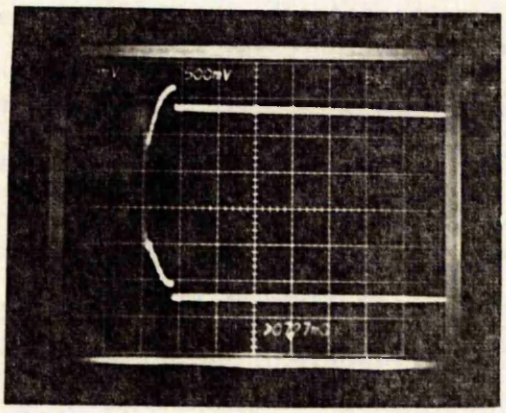

Figure 5.2-12 Waveforms across integration capacitors. (5 mV/div, 5 μs/div.)

The resulting input waveform to the 'sample and hold' circuit is shown in figure 5.2-13 . This demonstrates the common mode rejection capabilities of the instrumentation amplifier, the resultant step being the result of the difference between the two input steps. Also it can be seen that the instrumentation amplifier settles well within the 20 microseconds allowed.

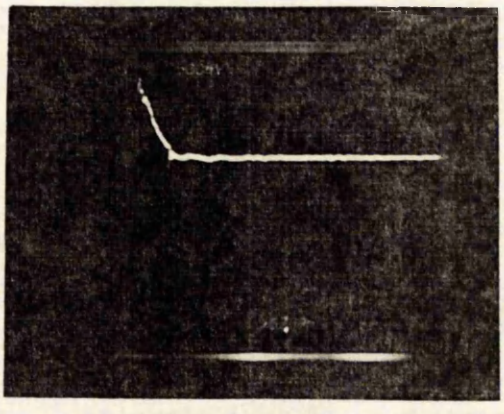

Figure 5.2-13 Input waveform to 'sample and hold' circuit.
(100 mV/div, 5 μs/div.)

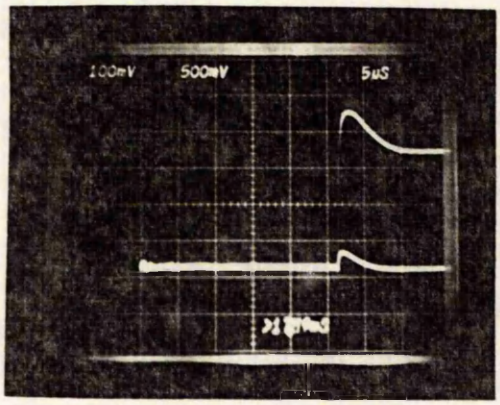

Figure 5.2-14 Two output wave-forms from 'sample and hold' circuit. (100 mV/div., 5 μs/div.)

Figure 5.2-14 shows two output wave-forms from the 'sample and hold' circuit. The lower resulted from sampling a discharge of the same polarity and magnitude as its predecessor whereas the upper resulted from sampling a discharge of similar magnitude but opposite polarity. (The centre of the oscillogram represents zero volts.) The first 26.5 μs of each trace relates to the delay before the 'sample and hold' circuit is triggered. On receipt of the trigger pulse, the output can be seen to make a considerable voltage excursion even in the case of the lower trace. However the voltage settles to its final value well within the 25 μs allowed. No noticeable transient occurs at the end of the trigger pulse.

In its present form the instrument requires a minimum of 100 μs between successive discharges if super-position errors are not to arise. However this could easily be reduced by increasing the damping of the input circuits. This would also improve its noise immunity.

A photograph of the prototype instrument is shown in figure 5.2-15 . It can be seen that the front panel has been designed with ease of use in mind. All the separate circuit functions are clearly grouped on the front panel and, internally, they are all separately contained in screened enclosures.

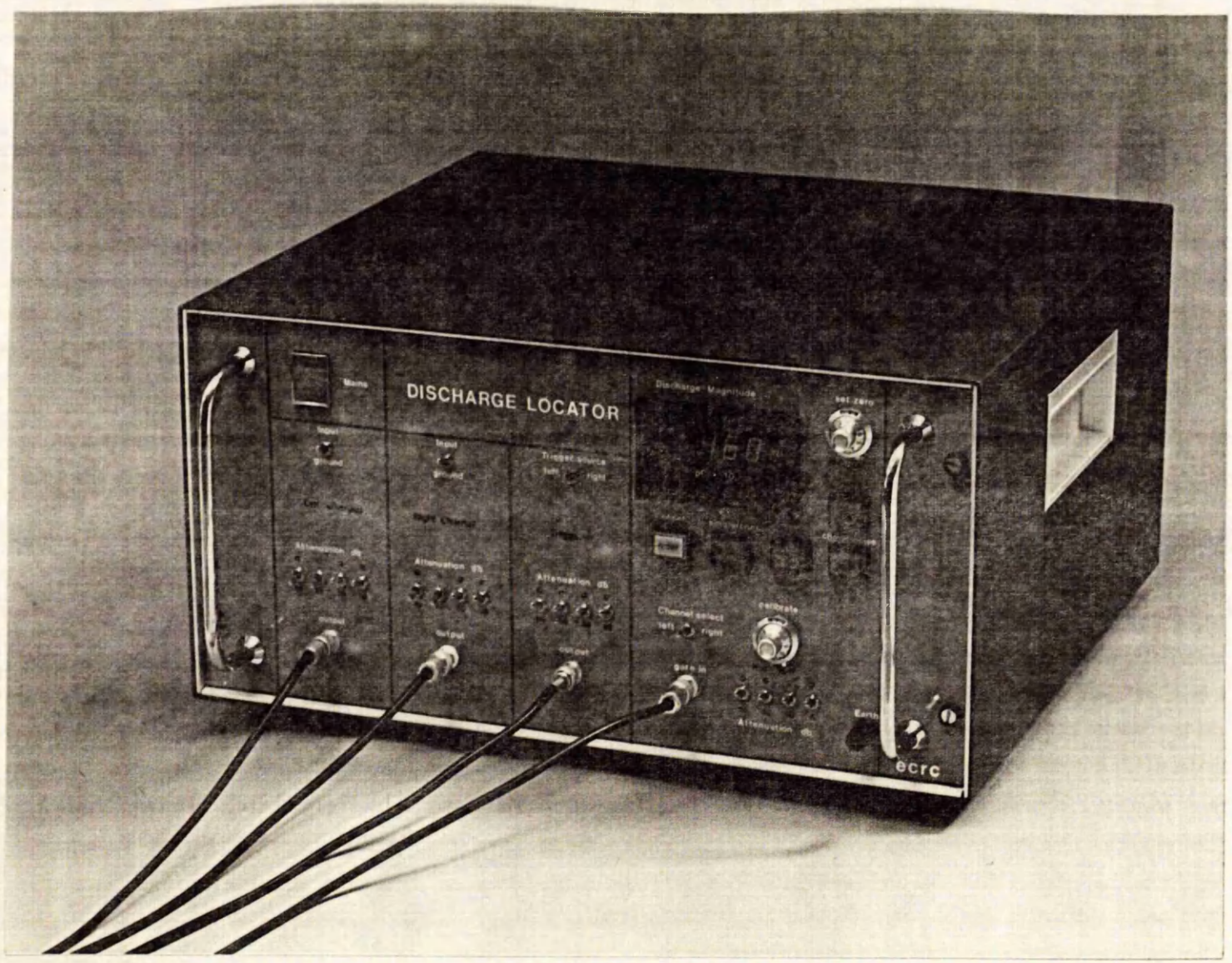

Figure 5.2-15 Prototype discharge measurement / location instrument

5.3 Artificial discharge source

This is required for two reasons. The first is to provide a discharge of known magnitude for calibration purposes. The second is to provide a means of injecting short rise-time pulses into the measurement system at a known location in order to establish the relative travel times from that site for the two location channels.

To satisfy the first requirement, the electrodes must be resistant to oxidation and erosion. Tungsten has been found to be satisfactory. Also the electrodes must be contained in a dust tight enclosure to prevent bridging of the gap. It is helpful if the electrodes can be viewed without dismantling the discharge source and so the body of the unit is made of Perspex which also serves as the insulation structure. However, this has a large coefficient of thermal expansion which could produce unacceptable variations, with temperature, in the electrode gap setting. To avoid this the low voltage, moveable electrode is controlled by three 5 mm diameter brass screws via a brass bridge piece and the screws are tapped into the Perspex body in the plane of location of the centre (electrically floating) electrode. By this means the thermal expansion of the Perspex is rendered irrelevant. The residual thermal variation in the gap setting results from the thermal expansion of the brass. As this is exacerbated by the almost zero expansion coefficient of the tungsten tips, the length of these must be kept to the minimum (but without unduly increasing the inter-electrode capacitance which would increase the discharge inception voltage.) The electrode gap setting is adjusted by tightening the three brass screws against the compression forces of a neoprene washer and a gap of 0.15 mm has proved satisfactory. The electrodes are made from 0.5 mm diameter, high purity, tungsten wire with the ends ground square and polished. Any burrs at the edges were removed using an Arkansas stone.

The apparent discharge magnitude is given by the product of the gap breakdown voltage and the capacitance between the floating electrode

and the high voltage electrode. In order to keep the discharge magnitude in the required range of 1000 - 2500 pC, the series capacitance must be kept small, but not too small, or the inception voltage will exceed 2 kV, the maximum value considered acceptable. The arrangement shown has proved satisfactory, yielding an apparent discharge magnitude of 1600 pC. Also the high voltage electrode adequately shields the floating electrode thereby avoiding errors due to stray capacitance. The minimum spacing between the electrodes is 10 mm giving a breakdown voltage of approximately 10 kV r.m.s. This is well in excess of the required maximum withstand voltage of 5 kV r.m.s. Inlet and outlet vents plus internal drillings are provided to enable the whole assembly to be filled with high purity nitrogen.

To satisfy the requirement for short risetime pulses, a simple concentric construction is adopted to keep the inductance small. The inductance of the connections are also kept small by restricting the overall dimensions of the assembly, by fitting a clip on the high voltage electrode suitable for hanging the source directly onto the high voltage test system and by connecting a short copper-braid tail (not shown) to the low voltage electrode to provide a simple, but effective, method of keeping the earth connection as short as possible. Also the electrode gap must be small in order to generate steep fronted discharge transients.

The prototype discharge source is shown in figure 5.3-1 and an exploded view of the components is shown in figure 5.3-2 .

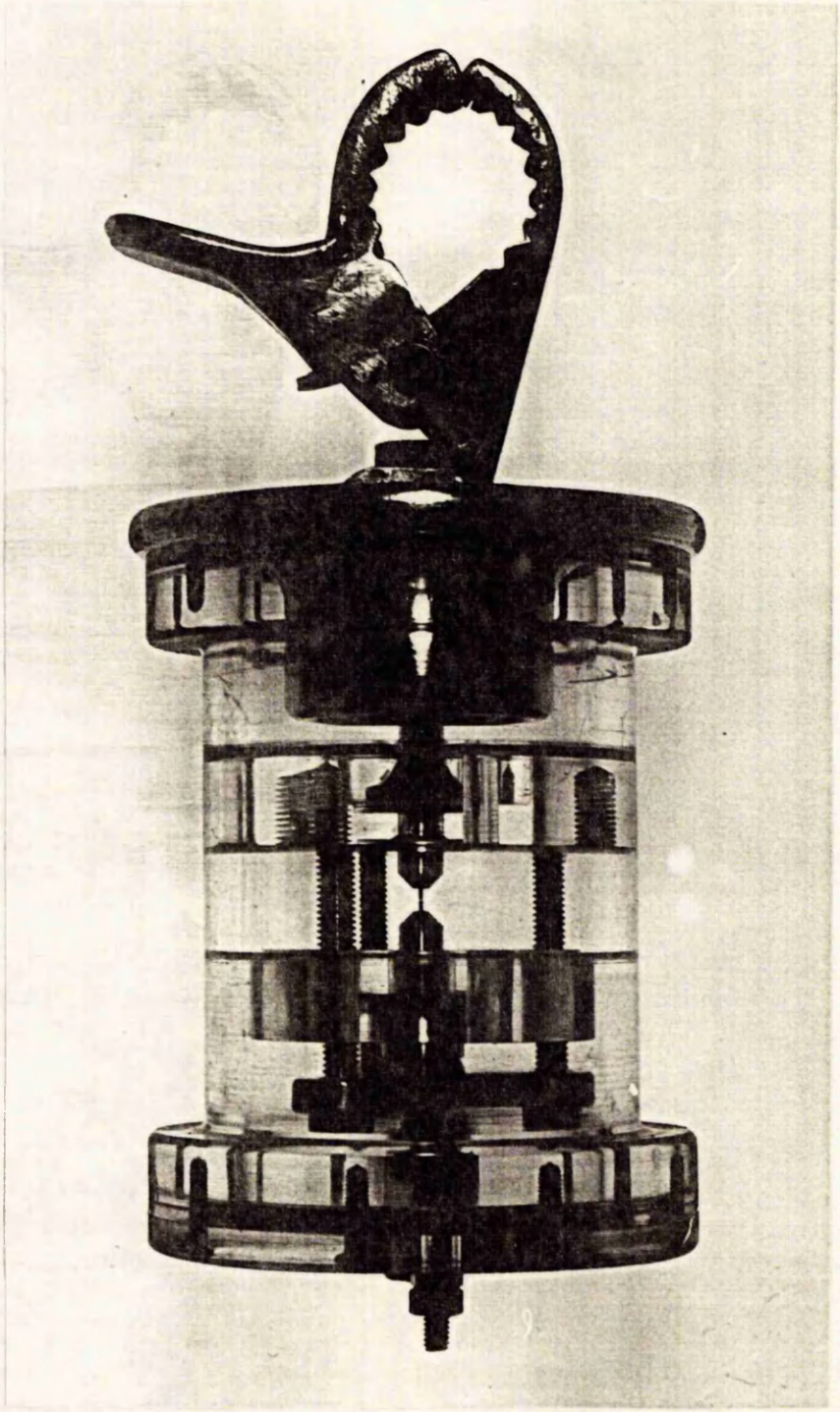

Figure 5.3-1 Prototype discharge source

Scale:- approximately full size

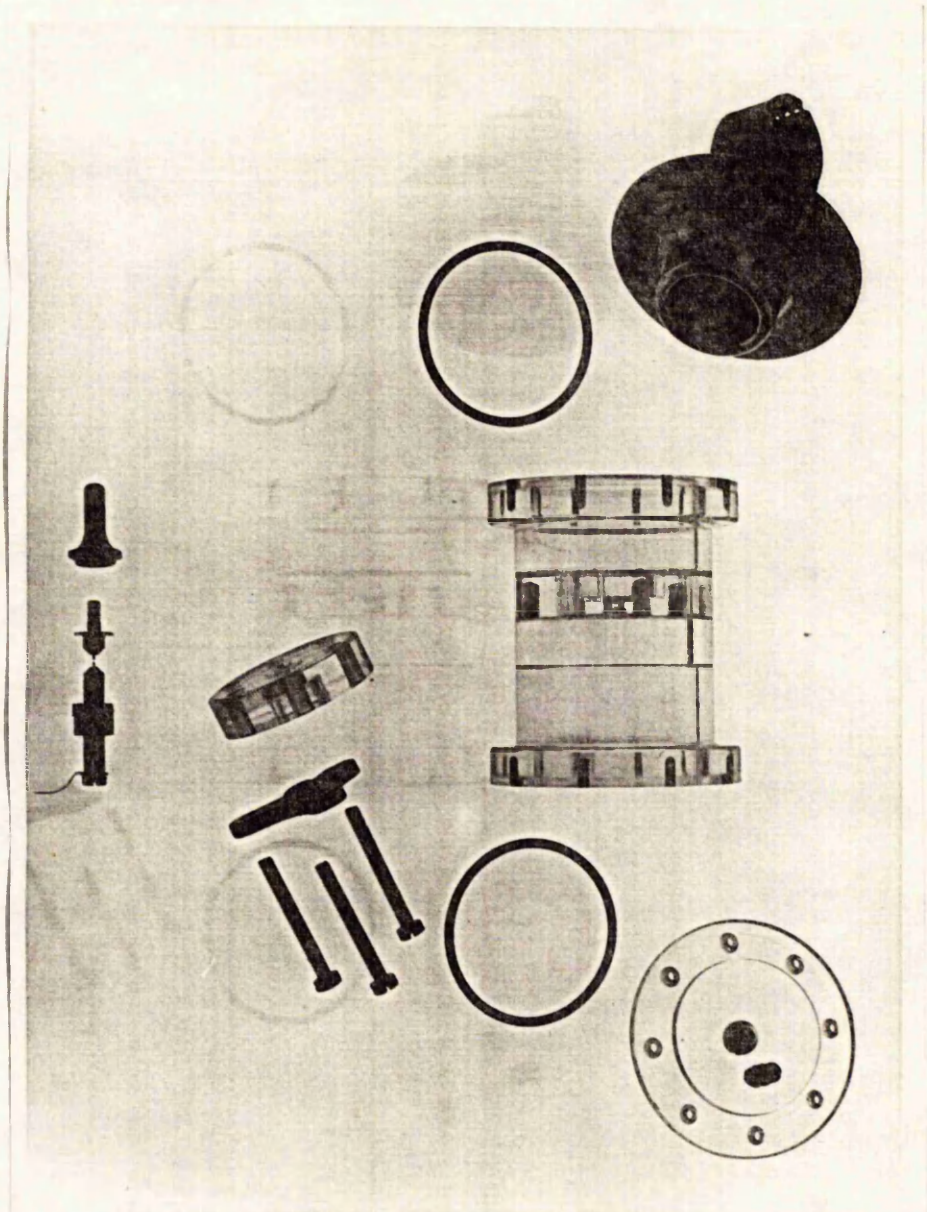

Figure 5.3-2 Exploded view of the prototype discharge source

CHAPTER 6

Conclusions

The numerical analysis demonstrates that both loss-less and lossy fields can be accurately modelled by first-order finite difference equations and that these can be efficiently solved by a Gaussian elimination scheme that takes full advantage of the banded nature of the coefficient matrices so generated. The work also shows that such fields can be modelled by finite elements defined using higher order interpolatory polynomials and that the representation can be reasonable even for relatively coarse element structures. By this means considerable savings in the time and effort required to define a field region can be realized. The finite element method is also particularly suitable for the calculation of capacitance in problems involving two electrodes.

Applying these techniques to dielectric regions containing 'pill box' shaped voids, it is concluded that considerable stress enhancement can take place across voids of small dimensions parallel to the field and large dimensions perpendicular to it, especially if the dielectric has a high relative permittivity. Though the mean stress across a 'pill box' shaped void is greatest at the centre, the maximum is not pronounced. However the mean stress can fall rapidly towards the periphery of the void resulting in appreciable surface stress across the end surfaces in this region. The surface stress down the cylindrical faces is also appreciable but, in contrast, is almost uniform.

The presence of a void can also affect the capacitance of a test specimen. For voids without a conducting surface film there is a significant decrease in the system capacitance whereas for a void with perfectly conducting surfaces there is a significant increase. Intermediate results are obtained with finite conductivities and so this could prove a useful diagnostic test for assessing the surface conductivity of voids.

Adjacent to perfectly conducting 'pill box' shaped inclusions

appreciable enhancement of E_y or E_x is shown to occur, demonstrating the need for concern when a discharge self extinguishes due to effective 'shorting' of the cavity by a conducting surface film. The subsequent complex analysis given shows the critical resistivity for this phenomenum to be around 1 MΩ/sq. at 50 Hz or 500 MΩ/sq. at 0.1 Hz with $\epsilon_r = 4$. At this resistivity the modulus of the electric stress across the void starts to fall and its phase approaches quadrature, leading. Also the void results in virtually no change in the system capacitance but, in contrast, it has its greatest effect on the system loss.

The effect of dielectric anisotropy is also considered and it is shown that, for a given value of $(\epsilon_r)_y$, reducing $(\epsilon_r)_x$ increases the stress enhancement and increasing $(\epsilon_r)_x$ reduces it. Dielectric loss is shown to increase the magnitude of the stress enhancement and to result in it having a lagging phase angle.

The stress enhancements experienced by 'pill box', spheroidal and 'wedge' shaped voids of similar dimensions are compared. It is concluded that the stress enhancements are slightly less for the spheroid, when compared with the 'pill box' but, for the 'wedge', they are appreciable greater at the 'thin end' and appreciabley less at the 'thick end'.

The effect of a partial discharge on the potential and charge distributions in and around a void are assessed for different degrees of discharge. From the results obtained it is concluded that appreciable stress is created on the end faces of the voids following a discharge and that, for the configurations considered, the value of $\Delta Q_a / \Delta Q_r$ can vary from 0.0754 to 0.661 . The values obtained vary from 16.4 to 67.8% of the value predicted by a simple, parallel plate, capacitor model with total discharge of the capacitor representing the void.

The initial microwave measurements were encouraging, demonstrating that spark discharges could easily be detected using a simple, broad-band crystal detector. Coupling such a detector to a dish aerial of, say,

300 mm diameter would give an angular resolution of about 3 degrees. The results obtained with the sensitive radiometer that was subsequently constructed, show that the microwave noise power emitted by a spark discharge is largely independent of the discharge magnitude or energy. It is therefore concluded that the radiated microwave energy is primarily determined by the noise temperature of the constituents of the arc. The insensitivity of radiometric measurements to partial discharges is considered to be the result of the change from gaseous conduction by streamer mechanisms to conduction by Townsend avalanches.

From the work described in chapter 5, it is concluded that discharge sources can be accurately located in switchgear and short cables from double-ended travelling-wave measurements and that the technique possess considerable versatility. For instance the author is now extending the technique to measurements on live apparatus by monitoring the discharge voltage transients appearing on the metal-cladding of switchgear or the sheaths of cables. Though these are solidly earthed, the sudden injection of charge at a point will result in a voltage transient on account of the finite travel time from the site to earth. As, of necessity, any such transient must have a short rise-time, capacitive coupling can readily be used. It is therefore perfectly adequate when making measurements on a cable, for instance, to fit a simple electrode over the serving (e.g. 8 close spaced turns of 20 s.w.g. tinned copper wire) thereby avoiding any disturbance to the cable. This technique is proving invaluable for detecting discharges in 132 kV sealing ends.

The instrument described in section 5.2 demonstrates that both the magnitude and the location of a discharge source can be ascertained from a single discharge.

The artificial discharge source described in section 5.3 for calibrating the discharge measurement / location system has also proved useful for calibrating the discharge alarm referred to in chapter 1. Because the

discharge source has a low inception voltage, a portable transformer can be used to energize the test specimen. The discharge source has also been used to calibrate a test system energized directly from the 132 kV grid by clipping the high voltage electrode to a live conductor and hanging a small metal box from the low voltage connection. A diecast box approximately 100 mm cube in dimensions and suspended by a 150 mm length of wire in free air has proved satisfactory.

BIBLIOGRAPHY

1 Forrest J.S., Lambeth P.J. and Oakeshott D.F.: 'Research on the performance of high voltage insulators in polluted atmospheres', Proc. I.E.E., Vol. 107, 1960, pp. 172 - 196.

2 Alston L.L. and Zoledziowski S.: 'Growth of discharges on polluted insulation', Proc. I.E.E., Vol. 110, 1963, pp. 1260 - 6.

3 Wilkins R.: 'Mechanism of failure of high voltage insulation with surface contamination', Ph.D. Thesis, University of Manchester, 1968.

4 Cobine J.D.: 'Gaseous conductors, theory and engineering applications', Dover 1958.

5 Baker W.P.: 'Electrical Insulation Measurements', Chemical Publishing Co. Inc., New York, 1963.

6 Mayoux C.: ''Corona discharge and ageing proces of an insulation', I.E.E.E. transactions of Electrical Insulation, Vol. EI-12, No. 2, April 1977, pp. 153 - 8.

7 Mason J.H.: 'Discharge detection and measurements', Proc. I.E.E., July 1965, pp. 1407 - 1423.

8 Whitehead S.: 'Dielectric breakdown of solids', Clarendon Press, Oxford, 1953.

9 Edwards D.G.: 'The dielectric breakdown of epoxy resins by thermal instability', M.Sc. Thesis, University of Manchester, 1968.

10 Warren L.: 'Thermal problems of organic outdoor insulators', Ph.D. Thesis, University of Manchester, 1969.

11 Dakin T.W.: 'Electrical insulation deterioration treated as a chemical rate phenomenon', A.I.E.E. trans., Vol. 67, 1948.

12 Allen P.H.G. and Tustin A.: 'The aging process in electrical insulation: a tutorial summary', I.E.E.E. Trans. on El. Insul., Vol. EI-7, No. 3, Sept. 1972, pp. 153 - 7.

13 Clark F.M.: A.I.E.E. Tech. Paper 42-98, Elec. Eng., 1942.

14 Montsinger V.M.: Trans. A.I.E.E. 49, 1930, p776.

15 Clark F.M.: 'Chemical changes affecting the stability of cellulose insulation', J. Electrochem. Soc., 83, 143, 1943.

16 Fabre J. and Pichon A.: 'Deteriorating processes and products of paper in oil. Application to transformers', C.I.G.R.E. Paper No. 137, June 1960.

17 Stannett A.W.: 'Ageing of paper in model transformers', C.E.R.L. Lab. Note No. RD/L/N 31/64, 1964.

18 Reynolds E.H. and Rogers E.C.: 'Discharge damage and failure in 11 kV belted cables', Trans. of the S.A. Inst. of Elec. Engrs., Oct. 1961, pp. 266 - 296.

19 Eichhorn R.M.: 'Treeing in solid extruded electrical insulation', I.E.E.E. Trans. on Elec. Insul., Vol. EI-12, No. 1, Feb. 1976, pp. 2 - 18.

20 Baker W.P.: See reference 5.

21 Daniel V.V.: 'Dielectric Relaxation', Academic Press, 1967.

22 Douglas J.L., Chesney S.J. and Wilson A.: 'CERL bridge predicts insulation deterioration', Electrical Times, 13th August 1970, pp.38-40.

23 Formby J.R. and Reeves J.H.: 'The communication capabilities of 11 kV cable networks', Electricity Council Research Centre, Capenhust, Report No. ECRC/R582, Feb. 1973.

24 Simons J.S.: 'The measurement of integrated discharge energy in high voltage insulation using a dielectric loss analyser with loop - trace display', I.E.E. Conf. on Dielectric and Insulating Materials, April 1964.

25 Mole G.: 'Improved methods of test for the insulation of electrical equipment', Proc. I.E.E., Vol. 100, Part IIA, 1953, p276.

26 Wilson A.: 'Site discharge testing aids plant maintenance', Electrical Times, February 13, 1976, p 13.

27 Wilson A.: 'Discharge testing on site', B.E.A.M.A. International Elec. Insul. Conf., pp. 294 - 9, May, 1978.

28 Allen D.J., Forrest J.A.C., Howitt E.L. and Petchell A.B.: 'Electric

and acoustic location of discharges in transformers', I.E.E. Conf. Publ. No. 94, Diag. test. of h.v. power app. in service, March 73, pp 65 - 70.

29 Harrold R.T.: 'Ultrasonic spectrum signatures of under oil corona sources', ibid., pp 53 - 58.

30 Bashara N.M.: A.I.E.E. Trans. 1961, pp. 115 - 9.

31 Wilson A. and Hogg W.K.: 'Optical studies of gas breakdown between dielectric - covered electrodes', I.E.E. Conf. Publ. No. 118, 3rd International Gas Discharge Conf., Sept. 1974, pp. 443 - 7.

32 Teich T.H.: 'Locating of corona points by detection of their U.V. emission', I.E.E. Conf. Publ. No. 94, Diag. test. of h.v. power app. in service, March 73, pp. 26 - 30.

33 Strong N.G., Davis N.E. and Melville D.R.G.: 'Visual, ultrviolet and ultrasonic display of corona fields in air', Proc. I.E.E., July 1970, pp. 1453 - 9.

34 Daniel T.N.: 'Continuous observation of corona using u.v. sensitive TV camera', C.E.G.B. North Western Region, Report No. NW/SSD/RR/243/72, September 1972.

35 Meats R.J. and Stannett A.W.: 'Degradation of insulating materials by electrical discharges', Electrical Insulation Conf. on materials and application, 1963, p. 104.

36 Mole G. and Robinson F.C.: 'A versatile discharge detector', Conf. on Electrical Insulation, Hershey, Pa., U.S.A., 1962.

37 Wilson A.: 'The application of correlation analysis to partial discharge measurements', I.E.E. Conf. Publ. No. 94, Diag. test. of h.v. power app. in service, March 73, pp. 8 - 13.

38 Wilson A.: 'Discharge detection under noisy conditions', Proc. I.E.E., Vol. 121, No. 9, September 1974, pp. 993 - 996.

39 Black I.A.: 'A pulse discrimination system for discharge detection measurements on equipment operating in a power system', I.E.E. Conf.

Publ. No. 94, Diag. test. of h.v. power app. in service, March 1973, pp. 1 - 7.

40 Black I.A.: 'The pulse discrimination system for partial discharge measurements in electrically noisy environments', B.E.A.M.A. Conf. on elec. insul., May 1978, pp. 300 - 8.

41 Bleys C.A.: 'Floating input, optically isolated, high-voltage measurement probe', Rev. Sci. Instrum., Vol. 47, No. 5, May 1976, pp. 621 - 3.

42 Mole G.: 'Basic characteristics of corona detector calibrators', I.E.E.E. Trans. P.A.S., Vol. PAS-89, No. 2, Feb. 1970, pp. 198 - 204.

43 I.E.E.E. Committee Report: 'Guide for calibration of test equipment and circuits for measurement of corona pulses', Vol. PAS-86, No. 10, October 1967, pp. 1185 - 1191.

44 Mole G.: 'Measurement of the magnitude of internal corona in cables', I.E.E.E. Trans. on Power Apparatus and Systems, Vol. PAS-89, No. 2, February 1970, pp. 204 - 212.

45 Eager G.S. and Bader G.: 'Discharge detection in extruded polyethylene insulated power cables', I.E.E.E., Vol. PAS-86, No. 1, Jan. 1967, pp. 10 - 34.

46 Lukaschewitsch A. and Puff E.: 'Partial discharge measurements on long cables', Energie, Vol. 28, No. 2, pp. 32 - 39, Feb. 1976. (In German.)

47 Beneke, Von Volker: 'Messung von Teilentladungen in langen Kabeln und deren Bewertung', Elektrizitatswirtschaft, Jg. 72 (1973), 18, pp. 636 - 640.

48 Kreuger F.H.: 'Discharge detection in high voltage equipment', Temple Press, London, 1964.

49 Blodgett R.B. and Eigen D.: 'Cable corona signals - their origin and detection', I.E.E.E. Trans., PAS-87, No. 6, June 1968, pp. 1492 - 1507.

50 Eager G.S., Bahder G. and Silver D.A.: 'Corona detection experience in commercial production of power cables with extruded insulation', I.E.E.E. Trans., Vol. PAS-88, No. 4, April 1969, pp. 342 - 364.

51 Shimoguchi S., Miura A., Kusube M., Kawa K. and Koshizuka K.: 'Equipment of testing the underground distribution cables and the result of the field test', Dainichi - Nippon Cables Rev., Nov. 1973, pp. 52 - 62. (In Japanese)

52 Nigol O.: 'The detection and location of internal ionization sources in high-voltage cables', Ontario Hydro Research Quarterly. Reprinted in Transmission and Distribution, October 1971, pp. 47 - 49.

53 Galand J.: 'Localisation des decharges partielles dans les cables par une methode d'ondes stationnaires', R.G.E., Tome 80, No. 5, Mai 1971, pp. 399 - 405.

54 Miller R., Black I.A. and Gray V.N.: 'A variable low-frequency high-voltage generator using valves with fibre-optic light guide control', J. of Physics E: Sci. Instrs., Vol. 8, No. 9, Sept. 1975, pp. 748 - 750.

55 Hilder D.A., Black I.A. and Gray V.N.: 'The application of ramp and low frequency a.c. voltages to discharge detection', I.E.E. Conf. Publ. No. 94, Diag. test. of h.v. power app. in service, March 73, pp. 14 - 19.

56 Virsberg L.G. and Kelen A.: 'Some observations on the very-low-frequency testing of high-voltage machine insulation', C.I.G.R.E. Report 108, June 1964.

57 Miller R. and Black I.A.: 'Partial discharge measurements over the frequency range 0.1 Hz to 50 Hz', I.E.E.E. Trans. on Electr. Insul., Vol EI-12, No. 3, June 1977, pp. 224 - 233.

58 Taylor R.: 'Low frequency (0.1 Hz) bridge measurements on machine insulation', B.E.A.M.A. Int. Elec. Insul. Conf., May 1978, pp. 287 - 293, Brighton.

59 Wilson A.: See reference 27.

60 Wilson A.: 'Detecting incipient insulation faults', Electrical Times, February 9, 1979, p. 11

61 NEMA publication 107: Methods of measurement of radio influence voltage (riv) of high voltage apparatus', National Electrical Manufacturers Association, 1964.

62 Loftness M.O.: 'Locating RFI problem sources: the low-voltage hardware gap', Electric Light and Power, June 1978, pp. 41 - 2.

63 Allan R.N. and Kashani K.: 'Location and measurement of radio noise using an ultrasonic detector', I.E.E. Conf. Publ. No. 94, Diag. test. of h.v. power app. in service, March 73, pp. 20 - 25.

64 Lawson W.G., Simmons M.A. and Gale P.S.: 'Thermal ageing of cellulose paper insulation', I.E.E.E. Trans. on Elec. Insul., Vol. EI-12, February, 1977, pp. 61 - 66.

65 I.E.C. Publication 450: 'Measurement of the average viscometric degree of polymerization of new and aged electrical papers', 1st Edition, 1974.

66 Dakin T.W., Works C.N. and Miller R.L.: 'Utilization of peak-reading voltmeters and recorders for corona measurement', I.E.E.E. Trans. on Elec. Insul., Vol. EI-2, No. 2, August 1967, pp. 75 - 82.

67 Reynolds P.H.: 'Evaluation of insulation systems using a new partial discharge measurement technique', B.E.A.M.A. Int. E.ec. Insul. Conf., Brighton, May 1978, pp. 277 - 286.

68 Bartnikas R.: 'Corona pulse probability density function measurements on primary distribution power cables', I.E.E.E. Trans. on Power App. and Systems, Vol. PAS-94, No. 3, May/June 1975, pp. 716 - 723.

69 Megahed I., Mansfield B.C. and Wootton R.E.: 'Detection and measurement of discharges in cavities in solid dielectrics', Correspondence I.E.E. Proc., Vol 114, No. 11, November 1967, pp. 1822 - 4.

70 Franke E.A. and Czekaj E.: 'Wide-band partial discharge detector', I.E.E.E. Trans. on Elec. Insul., Vol. EI-10, No. 4, Dec. 1975, pp. 112 - 116.

71 Lacoste R., Ai Bui and Giam Hoang the: 'Partial discharge distribution as a function of time between two consecutive discharges', Proc. of Conf. on diel. mat., meas. and appl., Lancaster, July 1970, I.E.E.

72 Constandinou T.E.: 'Effects of internal discharges on prospective life and overvoltage-withstand behaviour of e.h.v. oil-impregnated paper bushings', Proc. I.E.E., Vol. 116, No. 5, May 1969, pp. 834 - 846.

73 I.E.C. Publication 137: 'Bushings for alternating voltages above 1000 V', Second edition, 1973.

74 Mole G.: 'A survey or the severity of internal discharges encountered in installed 11 kV mass-impregnated paper-insulated cables', Electrical Research Association Report No. 5200, March 1967.

75 Toriyama Y., Okamoto H., Kanazashi M. and Horii K.: 'Degradation of polyethylene by partial discharge', I.E.E.E. Trans. on Elect. Insul., Vol. EI-2, No. 2, August 1967, pp. 83 - 92.

76 Reynders J.P.: 'Electrical detection of degradation caused by partial discharges in polythene', I.E.E. Conf. Publ. No. 129, Conference on Diel. Mat., Meas. and Appl., July 1975, pp. 19 - 22.

77 Mason J.H.: 'Breakdown of insulation by discharges', I.E.E. Proc., Vol. 100, Part IIA, March 1953, pp. 149 - 158.

78 Hogg W.K. and Walley C.A.: 'Breakdown of insulation by partial discharges', Proc. I.E.E., Vol. 117, No. 1, January 1970, pp. 261 - 8.

79 Moon and Spencer: 'Field Theory for Engineers', Van Nostrand, 1961.

80 Kober H.: 'Dictionary of Conformal Representations', Dover, New York, 1952.

81 Vitkovitch D. (Editor): 'Field analysis: experimental and computational methods', Van Nostrand, London, 1966.

82 Wensley J.H. and Parker F.W.: 'The solution of electric field problems using a digital computer', Electrical Energy, September 1956, pp. 12 - 16.

83 Wexler A.: 'Finite elements for technologists', Lectures Notes for course given at the Polytechnic of Central London, May 1974.

84 Fox L.: 'Numerical solution of ordinary and partial differential equations', Oxford, Pergamon, 1962.

85 Piper L.A. and Harvill L.R.: 'Applied Mathematics for Engineers and Physicists', International Student Edition, McGraw-Hill, 1970.

86 Forsythe G.E. and Waso W.R.: 'Finite-difference methods for partial differential equations', Wiley, New York, 1960.

87 Frankel S.P.: 'Convergence rates of iterative treatments of partial differential equations', Mathematical Tables and other aids to computation. Volume 4, 1950.

88 Carre B.A.: 'The determination of the optimum accelerating factor for successive over relaxation', Computer Journal, Vol. 4, No. 1, 1961, p. 73.

89 Stoll R.L.: 'Solution of linear steady-state eddy-current problems by complex successive over-relaxation', Proc. I.E.E., July 1970, pp. 1317 - 1323.

90 Galloway R.H., Ryan H.McL. and Scott M.F.: 'Calculation of electric fields by digital computer', Proc. I.E.E., Vol. 114, No. 6, June 1967, pp. 824 - 9.

91 Calahan D.A.: 'Computer aided network design', McGraw-Hill, 1972.

92 Froberg C.E.: 'Introduction to numerical analysis', Reading, Mass., Addison-Wesley, 1965.

93 Reid J.K. (Editor): 'Large sparse sets of linear equations', Academic Press, London, 1971. Extracted from the Proc. of the Oxford Conf. of the I.M.A., April 1970. Joan Walsh:- 'Direct and Indirect Methods', pp. 41 - 56.

94 Zollenkopf K.: 'Bi-factorixation - basic computational algorith and programming techniques', ibid., pp. 75 - 96.

95 Gibson R.C.: 'Bieddy, a computer program for calculating the induction and other heating of long rect. & other reg. shaped slabs and billets', March 1974 , ECRC/MM20.

96 Jennings A. and Tuff A.D.: 'A direct method for the solution of large

sparse symmetric simultaneous equations', as per ref. 93, pp. 97 - 104.

97 Milne W.E.: 'Numerical solutions of differential equations', Wiley, New York, 1953.

98 Metcalf W.S.: 'Characteristic impedance of rectangular transmission lines', Proc. I.E.E., Nov. 1965, pp. 2033 - 39.

99 Finlayson B.A.: 'The method of weighted residuals and variational principles', Academic Press, New York, 1972.

100 Desai C.S. and Abel J.F.: 'Introduction to the finite element method - a numerical method for engineering analysis', Van Nostrand Reinhold, 1972.

101 Strang G. and Fix G.J.: 'An analysis of the finite element method', Prentice-Hall, 1973.

102 Zienkiewicz O.C.: 'The finite element method in structural and continuum mechanics', McGraw-Hill, 1967.

103 Mikhlin S.G.: 'Variational methods in mathematical physics', Pergamon Press, Oxford, 1965.

105 Smythe W.R.: 'Static and dynamic electricity', 2nd Edition, McGraw-Hill, 1950.

106 Salvage B.: 'Electric stresses in gaseous cavities in solid dielectrics', Proc. I.E.E., Vol. 111, No. 6, June 1964, pp. 1162 - 1172.

107 Sakr M.M. and Salvage B.: 'Electric stresses in gaseous cavities in solid dielectrics: experiments with an electrolytic tank', Correspondence, ibid., pp. 1176 - 1179.

108 Mitra G. and Salvage B.: 'Electric stress in a circular cylindrical gaseous cavity in a solid dielectric, the axis of the cylinder being parallel to the field', Proc. I.E.E., Vol. 113, No. 5, May 1966, pp. 931 - 5.

109 Reeves J.H.: 'The location of partial discharges in metal-clad switchgear', M.Sc. Thesis, University of Manchester, October 1972.

110 Kreuger F.H.: See reference 48.

111 Strong N.G., Davis N.E. and Melville D.R.C.: See ref. 33.

112 Lodge, Sir Oliver: Proc. Roy. Inst., Vol. 14, 1894, p.321.

113 von Lang V.: See Ref. 6, Proc. I.R.E., May 62, p. 1200.

114 Drude P.: ibid., Ref. 7

115 Weber R.H.: ibid., Ref. 8

116 Bekefi G., Hirshfield J.L. and Brown S.C.: Phys. Rev., 116, 1051, 1959.

117 Dicke R.H.: 'The measurement of thermal radiation at microwave frequencies', The Rev. of Sci. Instr., Vol. 17, No. 7, July 1946, pp. 268 - 275.

118 Penning F.M.: 'Electrical discharges in gases', Macmillan, Cleaver-Hume Press, 1965.

119 Elenbaas W.: 'The high-pressure mercury-vapour discharge', Amsterdam, 1951.

120 Heaton A.G. and Reeves J.H.: 'Microwave radiation from discharges', 3rd International Gas Discharge Conference, I.E.E. Conf. Publ. No. 118, Sept. 1974, pp. 73 - 77.

121 Nicoll G.R.: 'The measurement of thermal and similar radiations at millimetre wavelengths', Proc. I.E.E., Vol. 104B, 1957, p.519.

122 Gabor D.: 'Communication Theory and Physics', Phil. Mag., Vol. 41, 1950, p. 1161.

123 Goldstein S.J.: 'A comparison of two radiometer circuits', Proc. I.R.E., Vol. 43, 1955, p. 1663.

124 Selove W.: 'A d.c. comparison radiometer', Rev. Sci. Instr., Vol. 25, 1954, p. 120.

125 Stewart C.: 'Some applications and characteristics of ferrites at wavelengths of 0.87 and 1.9 cm', Trans. I.R.E., MTT-3, No. 3, 1955, p. 27.

126 Mayer C.H.: 'Improved microwave noise measurements using ferrites', Trans. I.R.E., MTT-4, 1956, p. 24.

127 Mayer C.H.: 'Improved noise power measurements through the use of ferrites', J. Geophys. Res., 1954, Vol. 59, p. 188.

128 Fischer H.J.: 'A partly transistorized radiometer for the measurement of thermal radiation at 3.4 cm', Proc. 3rd Colloquium on microwave communication, Budapest, April 1966, pp. 899 - 907.

129 Klass: 'Passive radar gives infra-red technique', Aviation Week, 1, 1957, pp. 62 - 68.

130 McCoy: 'An all-weather radio-sextant', I.R.E. Natl. Conv. Rec., 1955, Pt. 5, pp 92 - 101.

131 Seling and Nance: 'Sensitive microwave radiometer detects small icebergs', Electronics, Vol. 12, 1961, pp. 72 - 75.

132 Hilburn J.L. and Johnson D.E.: 'Manual of active filter design', McGraw-Hill, 1973.

133 Harvey A.F.: 'Microwave engineering', Academic Press, London, 1963.

134 Townsend J.S.: 'The theory of ionization of gases by collision', Constable and Co. Ltd., London, 1910.

135 Townsend J.S.: Nature, 62, 340, 1900.

136 Meek J.M.: 'A theory of spark discharge', Phys. Rev., 57, 722, 1940.

137 Meek J.M. and Craggs J.D.: 'Electrical breakdown of gases', Clarendon Press, Oxford, 1953.

138 Raether H.: 'The development of kanal discharges', Archiv fur Electrotechnik, 34, 49, 1940.

139 Raether H.: 'Electron avalanches and breakdown in gases', Butterworth, London, 1964.

140 Alston L.L.: 'High voltage technology', Harwell Post-Graduate Series, Oxford Univ. Press.

141 Rees J.A.: 'Electrical breakdown in gases', MacMillan, London, 1973.

142 Hill J.H.R. and Cresswell R.T.: 'Partial discharge testing of HV metalclad compound filled switchgear in service in London', Diag. test. of h.v. power app. in service, I.E.E. Conf. Publ. No. 94, March 1973, pp. 163 - 170.

143 Mole G.: 'Location of discharging cavity in 33 kV metalclad busbar

by the use of X-rays', Proc. I.E.E., Vol. 114, No. 10, October 1967, pp. 1558 - 1560.

144 Bailey C.A.: 'A study of internal discharges in cable insulation', I.E.E.E. Trans. on Elec. Insul., Vol. EI-2, No. 3, December 1967, pp. 155 - 159.

145 Salvage B. and Tapupere O.: 'Measurement of current pulses due to discharges in a gaseous cavity in solid dielectric', Electronics Letters, Vol. 4, No. 24, 29th November 1968, pp. 529 - 530.

146 Charters J.S.T., Roaldset S.A. and Salvage B.: 'Current pulses due to discharges in a gaseous cavity in solid dielectric', Electronics Letters, Vol. 6, No. 17, 3rd September 1970, pp. 569 - 570.

147 Scott R.E.: 'Linear Circuits', Addison-Wesley Publishing Co., 1964.

APPENDIX 1

Rotation of two dimensional vector coordinates

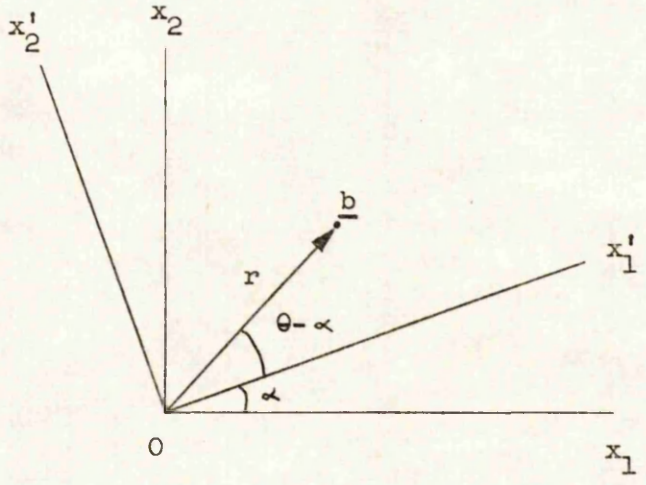

Figure A2-1 Rotation of coordinates

If vector $\underline{b}$ is of magnitude r and is inclined at an angle θ with respect to the unprimed axes, its coordinates are given by

$$x_1 = r \cos \theta \qquad x_2 = r \sin \theta \tag{A2-1}$$

In the primed frame of reference inclined at an angle α to the unprimed axes, the same vector has coordinates

$$x_1' = r \cos (\theta - \alpha) \qquad x_2' = r \sin (\theta - \alpha) \tag{A2-2}$$

Substituting (A2-1) into (A2-2)

$$\begin{aligned} x_1' &= x_1 \cos \alpha + x_2 \sin \alpha \\ x_2' &= -x_1 \sin \alpha + x_2 \cos \alpha \end{aligned} \tag{A2-3}$$

This can be expressed in matrix form

$$\underline{b}' = T \underline{b} \tag{A2-4}$$

where

$$\underline{b}' = \begin{pmatrix} x_1' \\ x_2' \end{pmatrix} \qquad \underline{b} = \begin{pmatrix} x_1 \\ x_2 \end{pmatrix} \tag{A2-5}$$

and

$$T = \begin{pmatrix} \cos\alpha & \sin\alpha \\ -\sin\alpha & \cos\alpha \end{pmatrix} \qquad \text{(A2-6)}$$

Transformation of a set of linear simultaneous equations

If

$$A\,\underline{x}' = \underline{b}' \qquad \text{(A2-7)}$$

a transformation to unprimed coordinates can be effected by substituting

$$T\,\underline{x} = \underline{x}' \qquad T\,\underline{b} = \underline{b}' \qquad \text{(A2-8)}$$

This gives

$$A\,T\,\underline{x} = T\,\underline{b} \qquad \text{(A2-9)}$$

or

$$B\,\underline{x} = \underline{b} \qquad \text{(A2-10)}$$

where

$$B = T^{-1}\,A\,T \qquad \text{(A2-11)}$$

APPENDIX 2

Analysis of second order, positive feedback, band-pass active filter

The circuit of the filter is given in figure A2-1 and, by delta-star transformation, this can be redrawn as shown in figure A2-2 where

$$Z_1 = \frac{1}{2j\omega C - \omega^2 C^2 R} \qquad \text{(A2-1)}$$

and

$$Z_2 = \frac{R_1}{2 + j\omega C R_1} \qquad \text{(A2-2)}$$

The nature of Z_3 is irrelevant if the input impedance of the operational amplifier is assumed to be infinite.

Figure A2-2 can be represented by the equivalent circuit of figure A2-3 if the operational amplifiers are assumed to be 'ideal'. The output voltages of the two operational amplifiers are given by

$$V_3 = Z_2 \times v / Z_1 \qquad V_2 = R_4 \times V_3 / R_1 \qquad \text{(A2-3)}$$

Applying Kirchhoff's Law to the node with voltage v

$$\frac{V_1 - v}{R_1} + \frac{V_2 - v}{R_3} = \frac{v\,(R_2 + Z_1)}{R_2 Z_1} \qquad \text{(A2-4)}$$

By eliminating v from this equation using (A2-3), an expression for the voltage gain of the filter can be derived

$$H(s) = \frac{V_2}{V_1} = \frac{ks}{s^2 + Bs + \omega_o^2} \qquad \text{(A2-5)}$$

where

$$k = R_4/(R_1^2 C) \qquad \text{(A2-6)}$$

$$B = \frac{1}{R_1 C}\left(2 - \frac{R_4}{R_3}\right) \qquad \text{(A2-7)}$$

$$\omega_o^2 = \frac{1}{R_1 C^2}\left(\frac{1}{R_1} + \frac{1}{R_2} + \frac{1}{R_3}\right) \qquad \text{(A2-8)}$$

and $s = j\omega$.

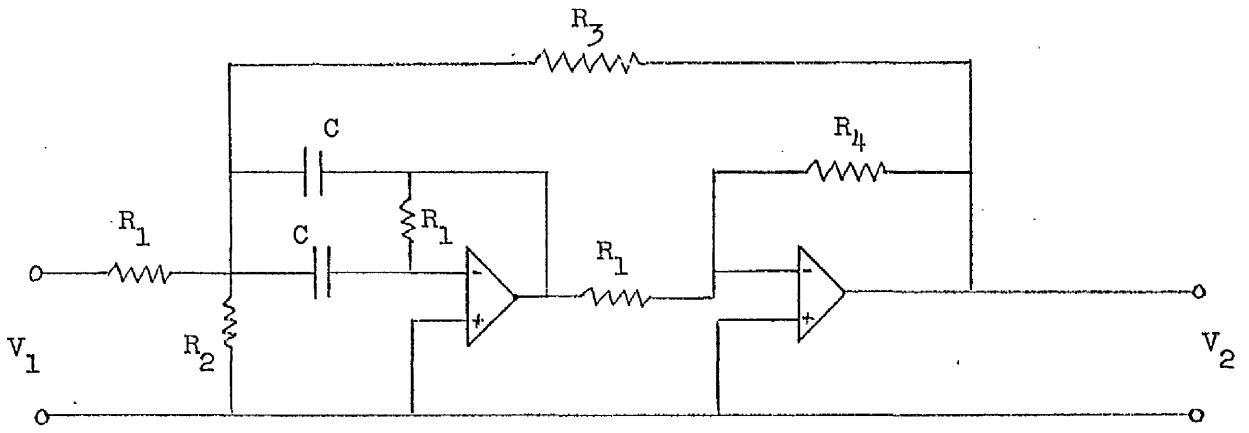

Figure A2-1 Circuit diagram of active, band-pass filter

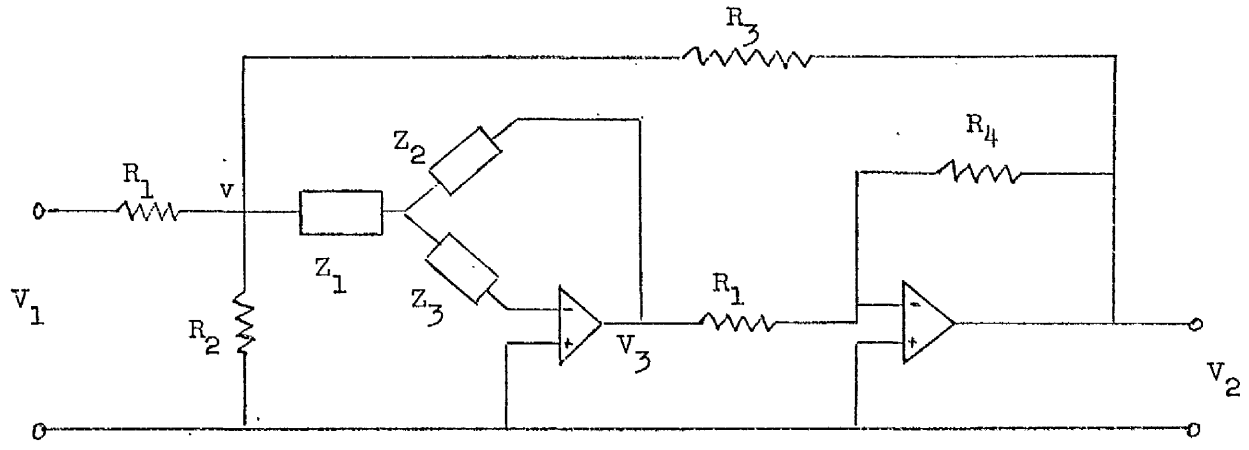

Figure A2-2 Circuit after delta-star transformation

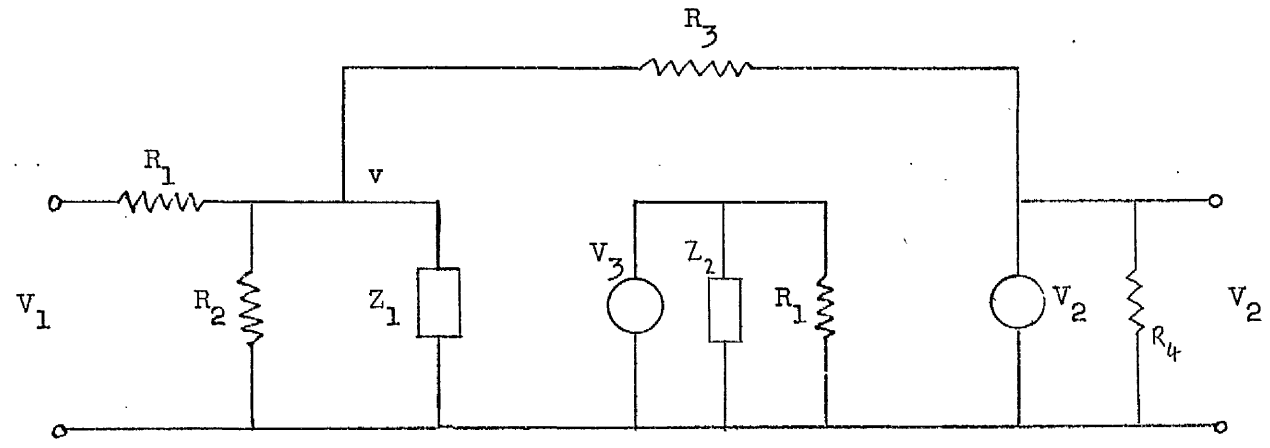

Figure A2-3 Equivalent circuit of figure A2-2

The power gain is, from equation (A2-5),

$$|H(\omega)|^2 = \frac{k^2 \omega^2}{(\omega_o^2 - \omega^2)^2 + B^2 \omega^2} \qquad \text{(A2-9)}$$

and this will be a maximum at the centre frequency of the amplifier's pass-band. This frequency can be ascertained by differentiating (A2-9) with respect to ω and setting the numerator equal to zero. This gives $\omega = \pm\omega_o$ and $\pm j\omega_o$. The stationary response at $\omega = \pm\omega_o$ represents the maximum and at this frequency

$$H(\omega_o) = k / B \qquad \text{(A2-10)}$$

The bandwidth between the half power points can be obtained by solving

$$\frac{k^2 \omega^2}{(\omega_o^2 - \omega^2)^2 + B^2 \omega^2} = \frac{k^2}{2 B^2} \qquad \text{(A2-11)}$$

to give

$$\omega^2 = \tfrac{1}{2}(2\omega_o^2 + B^2 \pm B\sqrt{B^2 + 4\omega_o^2}) \qquad \text{(A2-12)}$$

Since $B^2 << \omega_o^2$

$$\omega^2 \simeq \omega_o^2 \pm B\omega_o + \tfrac{1}{2} B^2 \qquad \text{(A2-13)}$$

and the half power frequencies are approximately given by

$$\omega = \pm (\omega_o \pm B/2) \qquad \text{(A2-14)}$$

Hence B is the 3 dB bandwidth in radians/second.